université de BORDEAUX

THÈSE PRESENTÉE

POUR OBTENIR LE GRADE DE

# DOCTEUR DE

# L'UNIVERSITÉ DE BORDEAUX

ÉCOLE DOCTORALE DES SCIENCES CHIMIQUES

SPÉCIALITÉ : PHYSICO-CHIMIE DE LA MATIÈRE CONDENSÉE

Par Emmanuel O. IDOWU

# FABRICATION DE NANOSTRUCTURES À BASE DE SILICIUM : MODIFICATION DES PROPRIÉTÉS OPTIQUES PAR LA MORPHOLOGIE ET LA COMPOSITION

## FABRICATION OF SILICON-BASED NANOSTRUCTURES: ALTERING OPTICAL PROPERTIES THROUGH MORPHOLOGY AND COMPOSITION

Sous la direction de : Glenna L. DRISKO

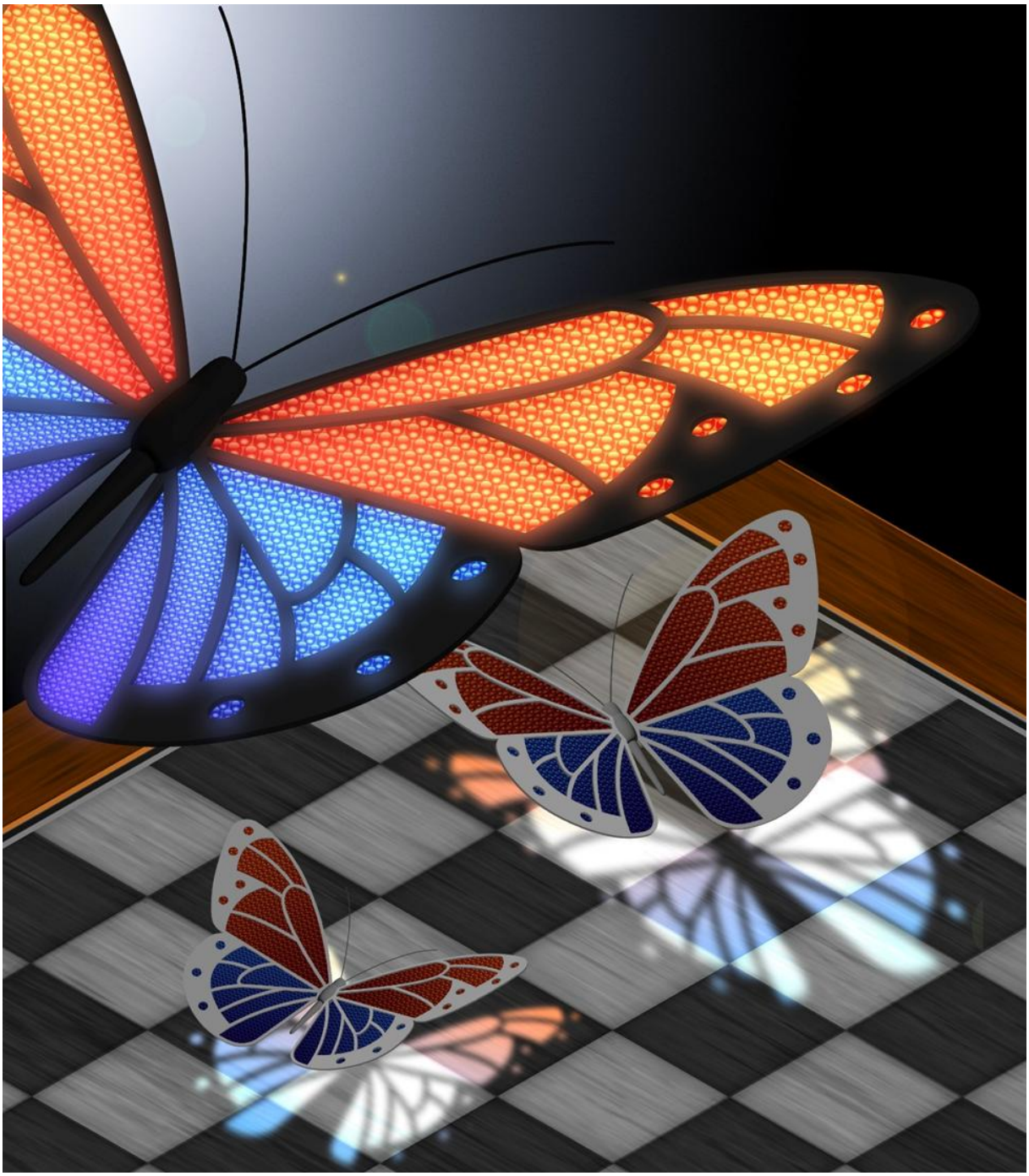
Co-directrice : Virginie PONSINET

Soutenue le : 04 Décembre 2025

Membres du jury :

| | | | |
|---|---|---|---|
| M. Stéphane PAROLA | Professeur | ENS de Lyon, CNRS, UCBL1 | Rapporteur |
| M. Cyrille HAMON | Chargé de Recherche | LPS, CNRS, UPSaclay | Rapporteur |
| M. Gilles R. BOURRET | Maître de Conférences | Univ. P. L. de Salzbourg | Examinateur |
| Mme. Laurence CROGUENNEC | Directrice de Recherche | ICMCB, CNRS, Univ. Bordeaux | Président de Jury |
| Mme. Glenna L. DRISKO | Directrice de Recherche | ENS de Lyon, CNRS, UCBL1<br>ICMCB, CNRS, Univ. Bordeaux | Directrice de thèse |
| Mme. Virginie PONSINET | Directrice de Recherche | CRPP, CNRS, Univ. Bordeaux | Co-directrice de thèse |

**Graphical Abstract**



*Illustrated by: Delphine Bailly*

*Light drifts like a butterfly, gliding forward without a backward glance. Each delicate sphere shapes its own color, scattering light ahead while leaving shadows deep and still. In this quiet dance, color and light become weightless, almost unreal.*

Fabrication de nanostructures à base de silicium : modification des propriétés optiques par la morphologie et la composition

**Résumé**

La recherche en nanophotonique vise à concevoir des nanostructures capables de diffuser la lumière de manière directionnelle afin de contrôler sa propagation à l'échelle nanométrique. Une telle diffusion présente un large éventail d'applications technologiques, notamment les revêtements optiques à transmission ou réflexion parfaite et large bande, l'amplification de la diffusion Raman, et l'optique non linéaire. Les particules de silicium (Si) de taille ous-inférieure à la longueur d'onde (100–200 nm) sont particulièrement prometteuses en raison de leurs faibles pertes optiques et de leurs fortes résonances électriques et magnétiques dans le domaine du visible et du proche infrarouge. Lorsqu'elles sont combinées, ces résonances permettent une diffusion seulement vers l'avant. Cependant, pour des sphères de Si, leur chevauchement spectral n'est que partiel, et les efficacités de diffusion qui en résultent restent relativement faibles.

Pour surmonter cette limitation, plusieurs stratégies ont été proposées, telles que l'introduction de morphologies non sphériques (par exemple ellipsoïdes, nanofils), la fabrication d'architectures cœur–coquille et l'assemblage de particules en métasurfaces. Cette thèse explore différentes approches de synthèse ascendante (bottom-up) pour développer des nanostructures à base de silicium aux propriétés optiques améliorées et étudie leur comportement de diffusion de la lumière.

Dans un premier temps, une approche en deux étapes a été développée pour préparer des particules cœur–coquille Si@Au avec une épaisseur de coquille ajustable inférieure à 10 nm. L'augmentation de la couverture en nanoparticules d'or par des étapes successives de fonctionnalisation/dépôt a permis d'améliorer la continuité de la coquille. La réponse électromagnétique de ces particules a été étudiée par spectroscopie de diffusion sur particule unique et par spectroscopie de pertes d'énergie des électrons (EELS), puis comparée à des sphères de Si de référence et à des structures cœur–coquille $SiO_2$@Au. Des simulations basées sur la méthode T-matrix ont confirmé nos observations expérimentales et mis en évidence le rôle essentiel du rapport des dimensions cœur/coquille et de la continuité de la coquille pour maximiser la diffusion en avant. En parallèle, une voie de synthèse a également été établie pour des particules cœur–coquille Si@Ag, caractérisées avec les mêmes techniques optiques. Ce

travail ouvre la voie à l'élargissement de cette bibliothèque de nanostructures cœur–coquille à des coquilles diélectriques telles que $Si@SiO_2$, $Si@ZrO_2$ ou $Si@TiO_2$.

Dans un second temps, des nanofils de silicium ont été obtenus par réaction de disproportionation thermique d'un oxyde de silicium enrichi en présence de différentes nanoparticules métalliques (Au, Ag, $Fe_2O_3$), qui jouent un rôle catalytique dans la croissance. Les nanofils obtenus présentent un cœur de silicium cristallin recouvert d'une coquille de 10–20 nm d'oxyde de silicium, et leur longueur varie de 1 à 6 µm, leur conférant des propriétés optiques fortement anisotropes. Leur formation a en outre été étudiée in situ en conditions environnementales, offrant une observation en temps réel des mécanismes de croissance. Une telle compréhension est essentielle pour améliorer le rendement, le contrôle morphologique et l'évolutivité des nanofils de silicium.

Enfin, des particules ellipsoïdales de silice mésoporeuse ont été synthétisées par voie sol-gel. Afin d'améliorer leurs performances optiques, nous avons tenté de les réduire en silicium élémentaire par réduction magnésiothermique. Toutefois, des difficultés liées au contrôle de la morphologie, à l'agrégation et à la porosité ont limité leur exploitation.

**Mots clés :** Silicium, nanoantennes, résonances de Mie, diffusion directionnelle, cœur–coquille, nanofil, nanoellipse

---

**Abstract**

Nanophotonics research has sought to create nanostructures with strong directional optical scattering to control light propagation at the nanoscale. This directional scattered light has a range of potential technological applications, such as perfectly transmitting (or reflecting) broadband optical coatings, enhanced Raman scattering, nonlinear optics, etc. Subwavelength-sized silicon (Si) particles (100 – 200 nm) interact with visible and near-infrared light, offering low optical losses and presenting strong electric and magnetic resonances. These resonances can combine to produce pure forward scattering. However, there is only partial spectral overlap of the electric and magnetic responses, resulting in relatively weak total scattering efficiencies.

The different strategies to improve the spectral overlap of these two modes in Si particles include creating non-spherical morphologies (e.g., nanoellipse, nanowires, etc), core-shell architectures, or assembling Si particles into arrays (such as metasurfaces). Hence, this thesis aims to develop such silicon-based nanostructures via different bottom-up synthesis approaches and study their optical properties.

First, we present a two-step solution approach to prepare Si@Au core-shell particles with controllable shell thickness below 10 nm. The Au nanoparticle density around the Si particles can be increased by performing a second functionalization/deposition step. We study the electromagnetic response of the particles using single-particle scattering spectroscopy and electron energy loss spectroscopy (EELS). Our results on Si@Au core-shell particles were compared with reference Si spheres and $SiO_2$@Au core-shell particles, allowing us to establish the contribution of the Au decoration to the optical response of the hybrid particles. To further elucidate the nature of the electromagnetic response of the particles, we performed T-matrix simulations. These simulations replicated our experimental findings and showed the importance of controlling the shell/core dimensions and the need for a continuous shell to maximize forward scattering. Furthermore, a synthesis pathway was investigated for Si@Ag and Si@$SiO_2$ core-shell particles. Future work may extend this library of core-shell nanostructures to dielectric shells such as Si@$ZrO_2$ and Si@$TiO_2$.

Second, we developed a route to fabricate silicon nanowires as potential nanoantennas through the thermal disproportionation reaction of a silicon-rich oxide in the presence of different metallic nanoparticles, which we assume catalyze the wire growth. We used different metal catalysts, such as Au, Ag, and $Fe_2O_3$ nanoparticles, to grow the silicon nanowires. The silicon nanowires have a core of elemental silicon with a shell of 10–20 nm of silicon oxide. The length of the nanowires is between 1–6 μm, rendering them highly anisotropic. To achieve a higher degree of control over the morphology and to compare with other nanowire growth techniques, we performed in situ environmental studies to follow the formation of these nanowires in real time. Such knowledge can help us improve silicon nanowire yield and scalability.

Lastly, we present the sol-gel synthesis of ellipsoidal silica particles. As potential nanoantennas, we explored the reduction of these particles to elemental silicon through magnesiothermic reduction, as they would exhibit improved and asymmetric light scattering properties. However, we encountered challenges with controlling particle morphology, aggregation, and porosity.

**Keywords:** Silicon, nanoantennas, Mie resonances, directional scattering, core-shell, nanowire, nanoellipse

---

**Institut de Chimie de la Matière Condensée de Bordeaux**

[ICMCB (CNRS) – UMR5026, 87, Avenue du Docteur Schweitzer, 33608, PESSAC cedex (France)]

**Acknowledgements**

Finally, it is time to acknowledge the contribution of many lovely people towards this dissertation. If not for their devoted effort and assistance, the completion of this Ph.D. thesis would not have been possible.

First, I would like to express my gratitude to my thesis supervisors, Dr. Glenna L. DRISKO and Dr. Virginie PONSINET, for mentoring and nurturing me throughout my Ph.D. thesis. Thank you for the opportunity and for your confidence in me. You held my hand and pulled me through extremely difficult times. Thank you for your patience and for creating a very good working environment. I sincerely appreciate all you have done.

I would like to thank the members of my jury, Pr. Stéphane PAROLA, Dr. Cyrille HAMON, Dr. Gilles R. BOURRET, and Dr. Laurence CROGUENNEC, for agreeing to review my dissertation, for raising constructive scientific questions, and for the interesting discussion on the day of the defense.

I would then extend my gratitude to Dr. Peter WEICHA, Dr. Lucien ROACH, and Dr. Alexandre BARON for their assistance, especially in the optical simulations section of this thesis. Moreso, I thank them for their immense contributions and discussions during the writing of the manuscript. It would not have been possible without you all, and I really cannot thank you enough.

Furthermore, I would like to thank all the collaborators, starting with Pr. Jonathan G. C. VEINOT, Kevin O'CONNOR, and Abbie RUBLETZ, for always being ready to help whenever called upon. Thank you for being a great host during my visit to your research group in Canada. To Pr. Jérôme PLAIN, Dr. Julien PROUST, Pr. Mathieu KOCIAK, and Dr. Xiaoyan LI, thank you for the tremendous help with the experimental optical characterization and the warm reception during my visits. To Sabrina LACOMME, David MONTERO, and Isabelle LY, thank you for the several microscopy sessions. To Estelle MORVAN, thank you for the help with the NMR analysis. To Thibault CORNIER, thank you for the TGA/MS analysis. To Dr. Virginie PONSINET, thank you for the SAXS and DLS analysis and for the discussions around the interpretation of the results. To Maria Letizia DE MARCO, thank you for the warm welcome, assistance with the challenging in-situ microscopy experiments, your contribution to the manuscript, and your words of encouragement. To Yann LOUYER, Yacine AMAROUCHENE, and Manon BARRIÈRE, thank you for the optical trapping experiments and several scientific discussions. To Nicolas PENIN, thank you for your assistance during my

several heat treatment experiments. Thank you to Éric LEBRAUD for the support in the X-ray diffraction characterization. To Stephane TOULIN, thank you for all the help with data curation and bibliography research during this period.

I would like to thank all the members of the Institute of Condensed Matter Chemistry of Bordeaux – ICMCB, and the Paul Pascal Research Center – CRPP. To everyone I have crossed paths with and who has made these places feel like home. From the research institute directors, Dr. Cyril AYMONIER and Dr. Laurence CROGUENNEC; to the administrative staff, Christine SANZ, Matthieu RENAUDIN, Frédérique BONNET, and Virginie COSSERON-DA COSTA; to the infrastructure service members, Mickaël BARRÉ and Jean-Yves JUANICO; and to the informatics service member, Cyril DUFOUR.

I would like to extend my deepest gratitude to the permanent staff of the research team – Nanomaterials Chemistry (group 5), Pr. Mona TREGUER-DELAPIERRE, Dr. Marie-Hélène DELVILLE, Dr. Stéphane MORNET, Martin ROMANUS, and Lydia ROUDIER. To the non-permanent members, Cynthia, Megan, Anđela, Auriane, and Apolline, thank you for your help and advice when I started. I am especially grateful for the moral support you all showed by being present at the end of this journey. To Safa, Maelys, Liubov, Lina, Annette, Louise, Merlin, Shagun, Kevin, and Ons, thank you for your moral support throughout the journey. To Julien, Eugenie, and Henri, thank you for being lovely friends since the beginning of this journey. The memories we shared through the good and difficult times will remain close to my heart. All I can say is thank you all!

Finally, my deepest and most sincere gratitude goes to my lovely parents, siblings, uncles, aunts, cousins, extended family, and friends. Without your love and support since the start of my master's and doctoral programs, this would not have been possible. This Ph.D. is dedicated to you all.

# Contents

Graphical Abstract ..... i
Résumé ..... ii
Acknowledgements ..... v
Contents ..... vii
General Introduction ..... 1
References ..... 12
**CHAPTER 1**. Directional light scattering in silicon-based dielectric nanoantennas ..... 16
1.1 Introduction to optical nanoantennas ..... 17
1.2 Mie resonances ..... 18
1.3 Choice of dielectric materials ..... 21
1.4 The Kerker effect and Kerker conditions ..... 24
1.5 Directional Mie scattering in spherical Si particles ..... 26
1.6 Directional light scattering in Si-based core-shell nanostructures ..... 28
1.6.1 Proposed core-shell geometries ..... 28
1.6.2 Plasmonic shell materials ..... 30
1.6.3 Dielectric shell materials ..... 35
1.7 Directional light scattering in silicon nanowires ..... 41
1.8 Growth mechanisms for silicon nanowires ..... 44
1.8.1 Vapor-Liquid-Solid ..... 44
1.8.2 Solution−Liquid−Solid and Supercritical Fluid-liquid-Solid ..... 45
1.8.3 Solid-Liquid-Solid ..... 45
1.8.4 Vapor-Solid-Solid ..... 46
1.9 Growth techniques for silicon nanowires ..... 46
1.9.1 Metal-assisted chemical etching (MACE) ..... 47
1.9.2 Chemical vapor deposition (CVD) ..... 49
1.9.3 Plasma-enhanced chemical vapor deposition ..... 53
1.9.4 Supercritical fluid decomposition of silicon precursor ..... 54
1.9.5 Thermal decomposition in high-boiling point solvents ..... 57
1.9.6 Thermal disproportionation of silicon-rich oxide ..... 59
1.10 Directional light scattering in silicon nanoellipse ..... 64
1.10.1 Overview of geometry design ..... 64
1.10.2 Theoretical prediction of the directional light scattering ..... 64
1.11 Fabrication of silicon nanoellipses and their directional scattering properties ..... 67
1.11.1 Laser ablation approach ..... 67
1.11.2 Sol-gel method ..... 70

1.11.3 Metallothermic reduction of silica ..... 75
1.12 Objectives of the PhD thesis ..... 78
References ..... 80
**CHAPTER 2**. Experimental methods ..... 96
2.1 Introduction ..... 97
2.2 Dark-field optical microscopy and scattering spectroscopy ..... 97
2.3 Electron energy loss spectroscopy (EELS) ..... 99
2.4 Optical absorption (UV-vis-IR) ..... 102
2.5 Raman spectroscopy ..... 102
2.6 Dynamic Light Scattering (DLS) ..... 104
2.7 Small-Angle X-ray Scattering (SAXS) ..... 107
2.8 X-ray powder diffraction (XRD) ..... 109
2.9 Fourier transform infrared spectroscopy (FTIR) ..... 110
2.10 Solid-state Nuclear Magnetic Resonance (NMR) Spectroscopy ..... 112
2.11 Optical levitodynamics ..... 113
2.12 Transmission Electron Microscopy (TEM) ..... 115
2.13 Scanning Transmission Electron Microscopy (STEM) ..... 118
2.14 Energy-dispersive X-ray spectroscopy (EDS) ..... 120
2.15 In-situ Transmission Electron Microscopy (TEM) ..... 121
2.16 Scanning Electron Microscopy (SEM) ..... 124
2.17 Thermogravimetric analysis (TGA) ..... 126
2.18 Brunauer–Emmett–Teller (BET) ..... 126
2.19 Mie theory, T-matrix simulations, and simulated EELS spectra ..... 126
References ..... 127
**CHAPTER 3**. Directional light scattering in Mie-resonant Si particles with Au shells ..... 130
3.1 Review of the colloidal Si@Au core-shell particles ..... 131
3.2 Experimental section ..... 132
3.2.1 Materials ..... 132
3.2.2 Synthesis of silica particles ..... 132
3.2.3 Synthesis of silicon particles ..... 135
3.2.4 Synthesis of the Au-decorated silicon particles ..... 136
3.3 Results ..... 138
3.3.1 Morphological analysis ..... 138
3.3.2 Electron energy loss spectroscopy (EELS) ..... 140
3.3.3 Single particle darkfield spectroscopy ..... 143
3.3.4 T-matrix/Mie-theory calculations of scattering spectra ..... 148
3.4 Conclusions and Perspective ..... 152

References ..... 153
**CHAPTER 4**. Synthesis of silicon nanowires by thermal annealing of Si-rich oxide precursor containing metal nanoparticles ..... 156
4.1 Introduction ..... 157
4.2 Experimental section ..... 158
4.2.1 Materials ..... 158
4.3 Synthesis of silicon nanowires ..... 158
4.4 Results ..... 159
4.4.1 Formation of the silicon nanowires ..... 159
4.4.2 Formation mechanism of the silicon nanowires ..... 164
4.4.3 In-situ study of the thermal annealing ..... 166
4.4.4 Tailoring the morphology of the silicon nanowires ..... 171
4.4.5 Generalization of nanowire growth to other catalysts ..... 178
4.5 Conclusion and Perspectives ..... 181
References ..... 183
**CHAPTER 5**. L-tyrosine-directed synthesis and 3D characterization of ellipsoidal silica particles via optical levitation ..... 186
5.1 Interest in the colloidal fabrication of ellipse-shaped silicon particles ..... 187
5.2 Experimental section ..... 189
5.2.1 Materials ..... 189
5.3 Synthesis of the ellipsoidal silica particles ..... 189
5.4 Results ..... 190
5.4.1 Formation of ellipsoidal particle suspensions ..... 190
5.4.2 Optical levitation of the ellipsoidal particle ..... 193
5.4.3 Effect of experimental conditions on morphology ..... 194
5.4.4 Formation mechanism of the ellipsoidal silica particles ..... 201
5.4.5 Magnesiothermic reduction of the particles ..... 205
5.5 Conclusions and perspectives ..... 207
Annexe 1. Tumbling time calculation from Perrin's formula ..... 209
References ..... 210
General conclusions and perspectives ..... 214
Annexe 2. Experimental methods for the synthesis of silver and silica shell ..... 221
References ..... 223
Résumé en Français des travaux de thèse ..... 224
Références ..... 237

# General Introduction

## 1.0 Context

### 1.1 Introduction to nanophotonics and metasurfaces

Nanophotonics is the study of light-matter interactions at the nanoscale, combining nanotechnology and optics. It enables the design of nanostructures to generate, control, and detect light across the electromagnetic spectrum. Light is an electromagnetic radiation that plays a significant role in our perceptual cognition through vision, operating within the wavelength range of 400 – 800 nm. Typically, the near ultraviolet and near-infrared ranges are also involved, providing an approximate range of electromagnetic radiation from 100 – 2000 nm, which is the subject of photonics (Figure 1). The control and manipulation of light with optical devices involve altering its amplitude, phase, and polarization states in a desired manner. This results in steering the light propagation direction, shaping the wavefront (e.g., focusing), and imparting information. These have found a wide range of applications in imaging, sensing, optoelectronics, lighting and displays, communication, energy harvesting, computing, etc[1–3].

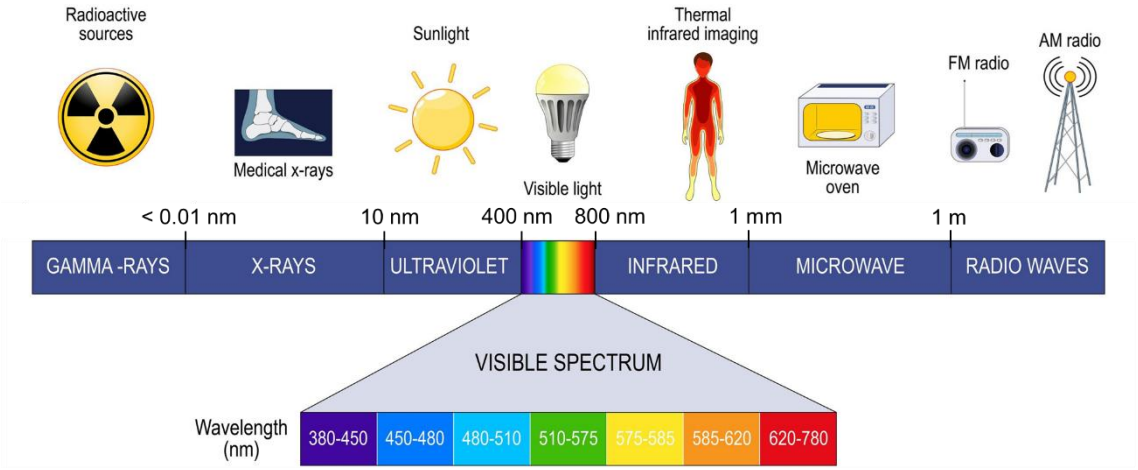



*Figure 1. The electromagnetic spectrum, spanning from short-wavelength gamma rays to long-wavelength radio waves, with visible light occupying the 400 – 800 nm range. Reproduced from ref.*[4]

### 1.2 Metasurfaces/Metamaterials

The branch of nanophotonics that has seen immense and rapid developments in the last few decades is metamaterials. The word *metamaterials* comes from the Greek prefix ‘‘meta-’’ (μετά), meaning *beyond* or *after*, and ‘‘materials’’ - literally meaning materials beyond conventional ones[5]. Metamaterials are artificial materials with regularly arranged subwavelength metal/dielectric structures (known as meta-atoms). These structures couple their resonances to either the electric or magnetic, or both, electromagnetic fields, exhibiting an effective electric and/or magnetic response not found in nature. While natural material

properties are mainly defined by their chemical composition, metamaterials inherit their properties mostly from the geometrical structure of their sub-units. Therefore, the desirable electromagnetic responses and device functionalities are determined by the electromagnetic properties of the subwavelength structures, as well as the integrated functional materials. They have been explored to achieve different physical phenomena such as negative refraction[6,7], which can be used to accomplish super-resolution in optical imaging[8,9], perfect lenses for sub-diffraction-limited imaging[8,10], invisibility cloaking[11,12], and artificial chirality[13,14] at the microwave and optical wavelengths. These potential applications, however, are hindered in realization due to the structural complexity of the 3D fabrication of sub-wavelength units at large scales, which are often expensive and time-consuming. Also, metallic-based metamaterials suffer from high losses, which limit the propagation of light through the bulk of the metamaterial.

However, the two-dimensional (2D) equivalent of the metamaterials, known as metasurfaces, has attracted significant interest because they can be readily fabricated albeit on small areas using existing technologies such as lithography and nanoimprinting techniques. Additionally, they can overcome the challenges encountered in bulk metamaterials, while their interactions with incident waves remain sufficiently strong to achieve useful optical functionalities. The wave propagates through subwavelength thickness, which can suppress undesirable losses by using an appropriate choice of materials and geometric structures. The sub-units are arranged into a planar subwavelength array, which collectively scatter the transmitted wave. Therefore, the control and manipulation of the light wave amplitude, phase, and polarization can be achieved by choosing the sub-unit geometry, material, and organization. These metasurfaces have the potential to be the next generation of optical components for controlling the optical field. They have been widely explored for applications such as metalenses[15,16], holograms[17–19], waveplates[20,21], optical vortex generation[22,23], and beam deflectors[24,25] as illustrated in Figure 2.

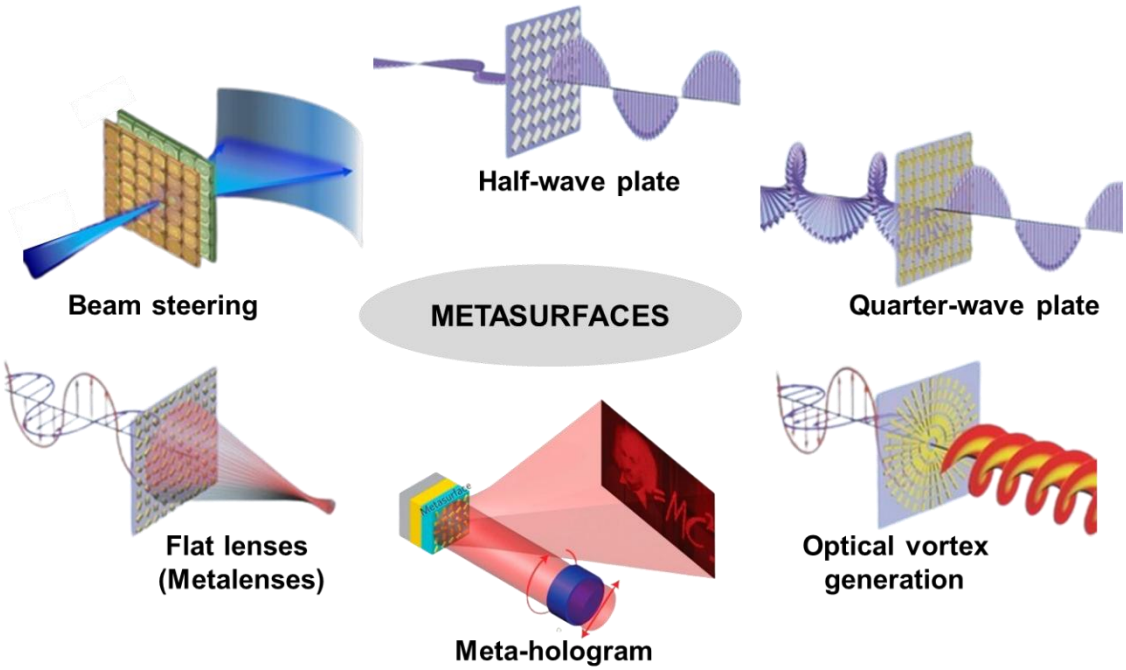



*Figure 2. Examples of applications of metasurfaces. Modified from ref.*[26]

### 1.3 Huygens-Fresnel principle to Huygens metasurfaces

The Huygens-Fresnel principle is a well-established concept in electromagnetism, which forms the foundation for the classic wave theory of light. It was introduced by Christian Huygens in 1690 in his work entitled *Traité de la Lumiére*[27]. It states that every point in space that receives an electromagnetic wave becomes the fictitious source of a new spherical wave spreading in the forward direction, which explains the gradual propagation of light. These point sources are referred to as Huygens sources (Figure 3a). It has been used to describe various phenomena, such as diffraction, refraction (Figure 3b), and interference, that occur in classical wave physics. In comparison to metasurfaces, each nanoantenna is treated as a point source that scatters light waves (Figure 3c). In both transmission and reflection modes, the new wavefronts are regarded as the combination of all the secondary waves. An artificial interface that molds the optical wavefronts into arbitrary shapes can be created by introducing spatial variations in the phase retardation of the optical scatterers. Therefore, a good candidate for wave manipulation is structures sub-wavelength in size that can trap and release the electromagnetic field with a controlled phase shift.

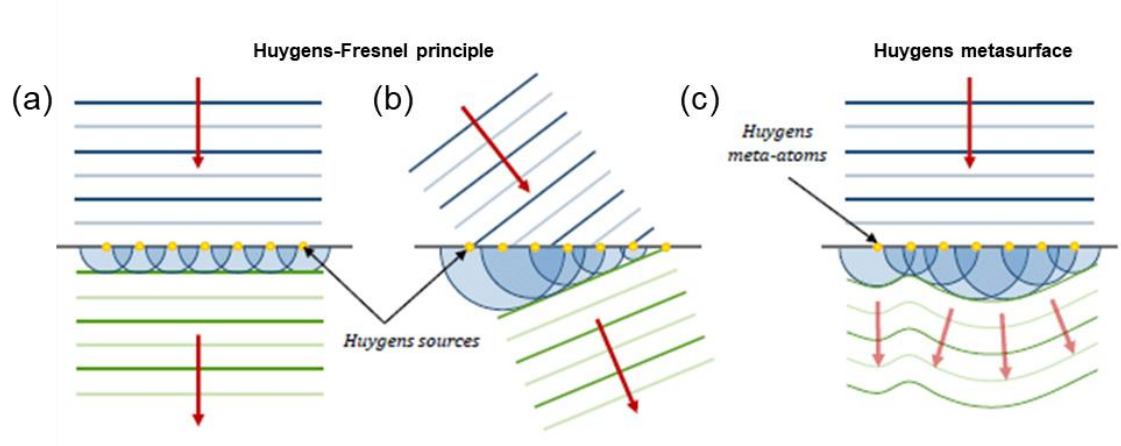



*Figure 3. Schematic illustration of the (a) Huygens-Fresnel principle showing the gradual propagation of a plane wave through the excitation of secondary waves. (b) Huygens-Fresnel principle applied to the phenomenon of refraction. (c) Illustration of the Huygens metasurface concept. The sub-wavelength array exhibits Huygens source features by converting an incident plane wave to an arbitrarily shaped wave. Reproduced from ref.*[28]

The choice of material is critical to the development of a highly efficient metasurface. Most pioneering metasurfaces in wavefront shaping relied on plasmonic resonances of metallic meta-atoms with different geometries, such as V-shaped[20] and C-shaped[29]. These meta-atoms exhibit two orthogonal electric dipole resonances, in which changes to the length, orientation, and angle of the meta-atoms can lead to a phase variation from 0 to $2\pi$ in the infrared region. However, these plasmonic meta-atoms exhibit low transmission efficiency, ranging from 10 – 20%, due to the high intrinsic losses of metallic materials. A patterned array of metallic-based meta-atoms, comprising copper wire and loops stacked on a printed circuit board, has been shown to exhibit both electric and magnetic responses. This metasurface has been demonstrated as a beam deflector with 86% transmittance at microwave wavelengths[30], which has been scaled down to the optical wavelengths[31]. However, these still suffer from limited efficiency due to ohmic losses.

Huygens metasurfaces are essentially based on sub-wavelength polarizable dielectric meta-atoms. The scattering properties of these meta-atoms can be tailored by their size, shape, and composition. They have been widely suggested as optical building blocks capable of scattering light in a forward direction. They exhibit both electric and magnetic resonances that can overlap in the same spectral range, producing a Huygens source in the visible to near-infrared region. For example, silicon (Si), titanium dioxide ($TiO_2$), and gallium phosphide (GaP) are ideal materials for the near-infrared, ultraviolet, and visible regions, respectively. This is due to their

high refractive index, low absorption in the wavelength range, and established fabrication techniques[32]. These dielectric materials can be in various shapes and compositions, such as spheres[33,34], spheroids[35], cubes[36], disks[17,18], cylinders[37,38], core-shell[39,40], particles with holes[41], etc. The periodic arrays of these dielectric nanostructures, fabricated using top-down techniques such as electron-beam lithography, have demonstrated forward light transmission at near-infrared wavelengths[15,17–19,42,43]. These are known as Huygens metasurfaces. They have proven to be a significant advance in achieving full-phase control and high transmission efficiencies[17–19]. Huygens metasurfaces are also advantageous for applications where a surface must reflect as little power as possible. The absorption is achieved by organizing lossy Huygens sources that can dissipate energy. The forward-scattered wave by the lattice cancels the incident wave through destructive interference, resulting in an absence of transmission. For example, electromagnetic absorbers are important for applications such as energy harvesting, sensing, thermal emission control, wave filtering, etc[44,45].

Decker *et al.*[17–19] reported a Huygens metasurface made of silicon nanodisks in the near-infrared (1477 ± 20 nm). They demonstrated a holographic metasurface with ~ 82% light transmittance efficiency and a ~ 40% image efficiency (i.e., the amount of light that ends up in the predefined hologram pattern) (Figure 4). Computer-generated holographic technology already exists. However, most conventional holograms rely on diffractive optics that require multistep lithography processes with limitations such as alignment and fabrication errors. Furthermore, there are limitations with twin image generation, which reduce the holography efficiency, and strong polarization sensitivity due to the holography gratings. The Huygens metasurface, fabricated with silicon nanodisks, is polarization-insensitive.

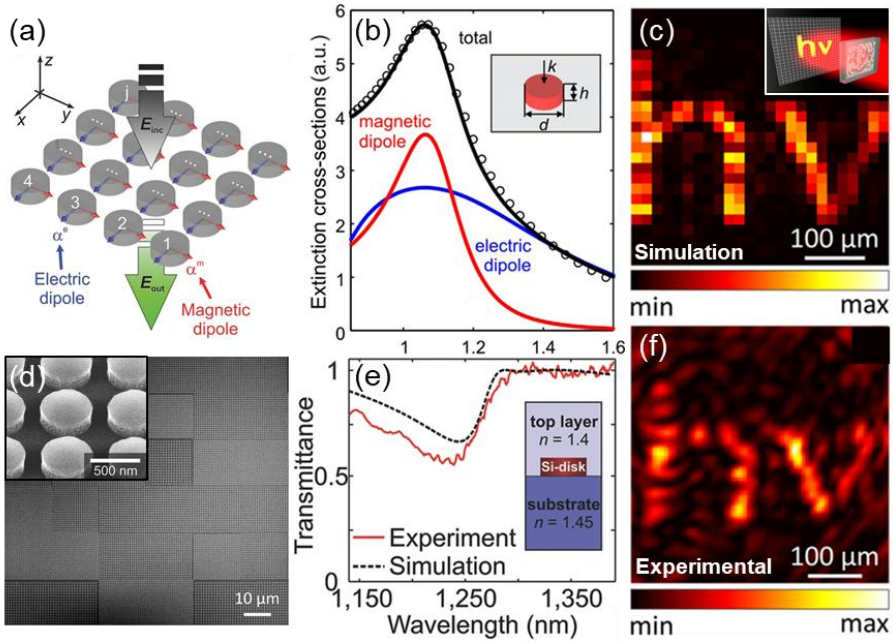



*Figure 4. (a) Schematic diagram of an array of nanodisks supporting electric and magnetic dipole resonances. Calculated extinction cross-sections for a single meta-atom silicon nanodisk with a height of ~ 220 nm and a diameter of ~ 290 nm, showing the overlap of the electric and magnetic dipoles. (c, f) Simulated and experimental holography image realized at a distance of 12 mm behind the sample plane by the fabricated metasurface. (d) SEM image of a region of the typical hologram metasurface sample. Reproduced from ref.*[17–19]

Tseng, E., *et al.*[42] demonstrated a metasurface lens made of silicon nitride nanopillars to achieve a high-quality, polarization-insensitive nano-optics imager for full-color (400 – 700 nm) and wide field-of-view (40°) imaging (Figure 5). With the aid of a neural network, image reconstruction recovers detail comparable to that of a conventional, bulky six-element refractive lens, while being ~550,000× smaller. The fabricated device has an aperture of 0.5 mm. This represents a significant advancement in the miniaturization of the optical components of electronic devices.

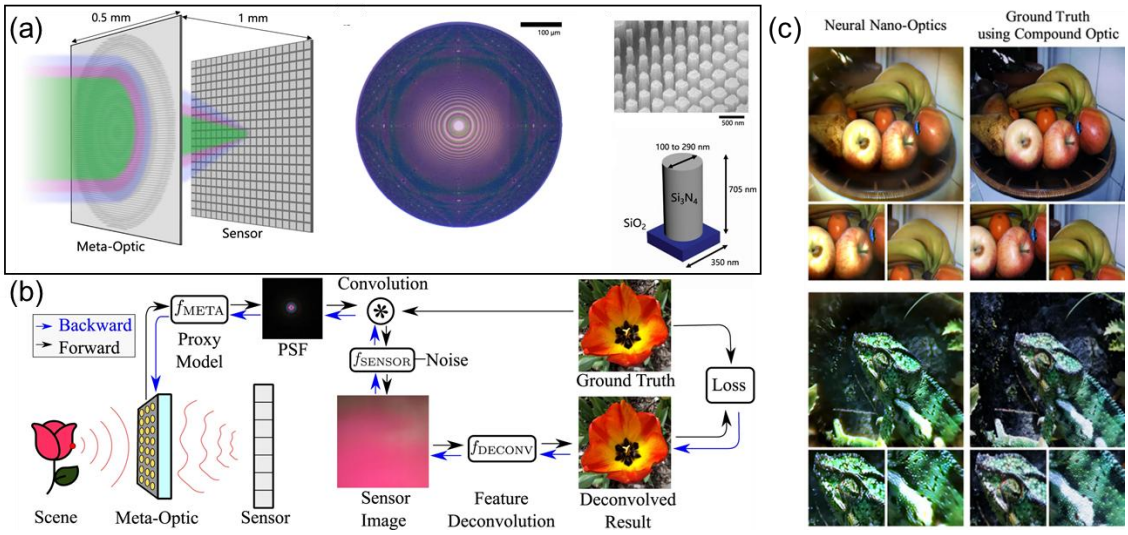



*Figure 5. (a) The ultrathin meta-optic design that enables a miniature camera. (b) The imaging pipeline designed for combining a metasurface image formation model with a deconvolution algorithm. (c) Images acquired with the designed metasurface lens compared to compound optic lens. Reproduced from ref.*[42]

Park, J.-S., *et al.*[15,43] demonstrated the fabrication of an all-glass metalens operating at visible wavelengths. Using deep-ultraviolet (DUV) projection lithography, a metalens with a diameter of 10 mm composed of cylindrical nanopillars of fused silica with diameters ranging from 250 – 600 nm and heights of 1.5 – 2.0 µm, was fabricated. This was used for imaging an AMOLED display, which can be implemented in virtual and augmented reality (Figure 6a-g). They also implemented a reflective scanning setup, similar to confocal microscopy, where the same metalens was used for both focusing and collecting light. This allowed for the reconstruction of resolution targets with good clarity, confirming the metalens imaging capability. However, the metalens faces limitations such as 2π phase coverage and fabrication imperfections, which led to a focusing efficiency of ~ 45.6% and a numerical aperture of 0.1 across the visible wavelength range of 488 – 660 nm under unpolarized light. In the 2024 advancement report, the all-glass metalens was scaled up to a 100 mm diameter. This is ~10× larger than the previous report. Thus, large-area, visible-wavelength metasurfaces are feasible through already existing semiconductor manufacturing techniques. The successful imaging of celestial objects such as the moon, sun, and stars to a magnification of ~ 9.15 suggests the potential use of the metalens in optics, telescopes, and compact imaging systems.

Zhang, L., *et al.*[16] demonstrated an 80 mm diameter metalens made of amorphous silicon nanopillars with a sub-wavelength diameter range of 150 – 400 nm and a height of 1 – 1.5 µm (Figure 6h-k). The metalens achieved a peak focusing efficiency of ~ 80.8% at a wavelength of

1450 nm. This high efficiency, combined with near-diffraction-limited focusing, confirms the practicality of large-area, high-performance metalenses for imaging applications.

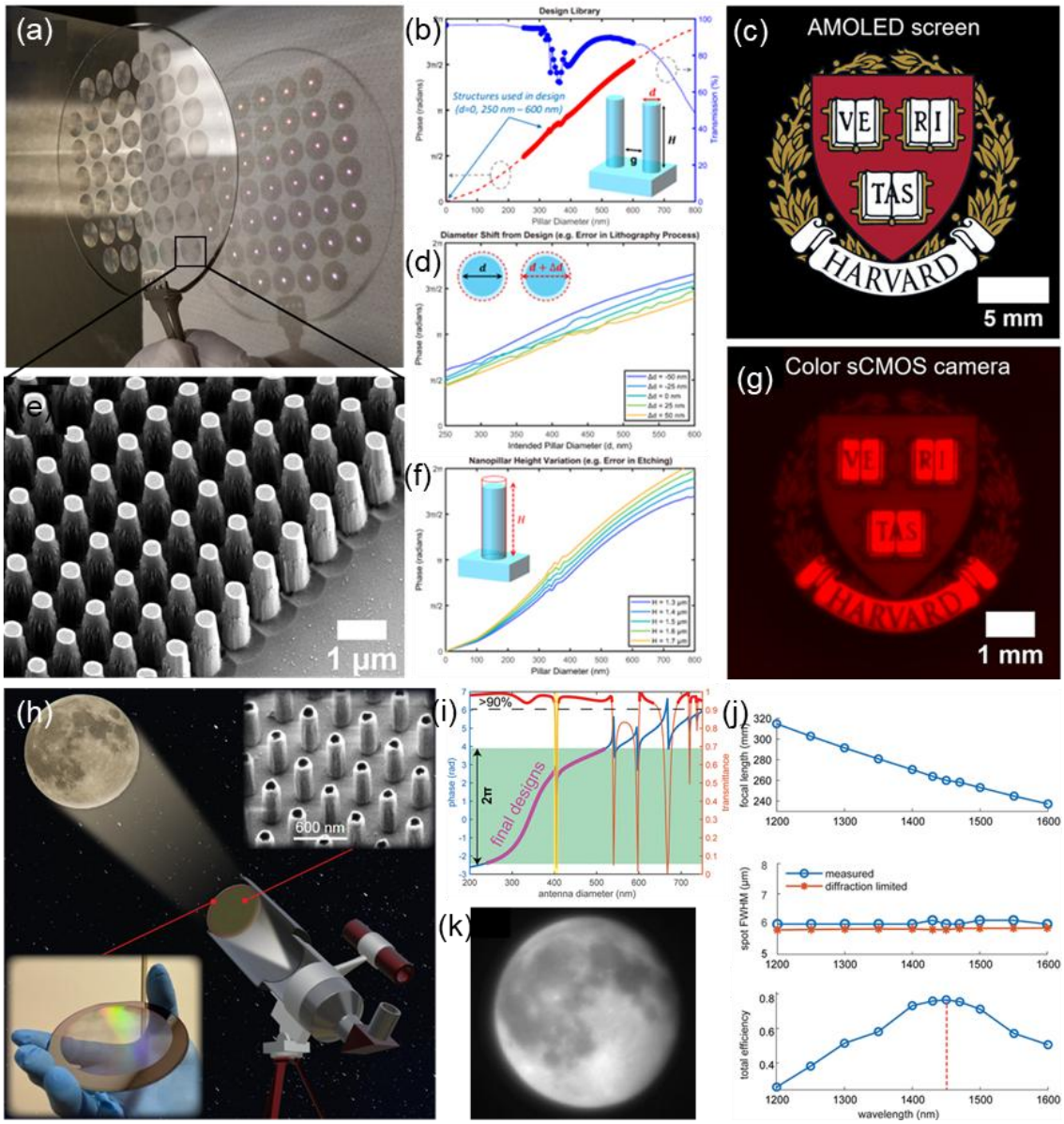



*Figure 6. (a,e) An image of the fabricated all-glass metasurface with an SEM image of a random section. (b,d,f) Simulations of the nanopillars used in the metalens design. (c) Imaging with the metalens on the AMOLED screen. (g) Image obtained from a color sCMOS camera at the metalens focal plane. (h) An image of a telescope with an 80 mm metalens as its objective, with an inset of the corresponding SEM image. (i) Simulation of the phase and transmittance of the amorphous silicon nanocylinders with different diameters ranging from 200 – 800 nm. (j) Measured focusing properties (focal lengths, focal spot, and total focusing efficiency) of the fabricated metalens with the wavelength ranging from 1200 – 1600 nm. (k) An IR image of the moon formed by the metalens. Reproduced from ref.*[15,16,43]

## 1.4 Bottom-up fabrication of optical metasurfaces

Most metasurfaces are fabricated using top-down approaches, such as electron-beam and focused-ion-beam lithography, due to their high spatial resolution, which enables the resolution of nanometer-scale features and the precise organization of nanostructures into a two-dimensional geometry. However, these techniques are expensive, slow, and limited in scalability, making mass production quite challenging. Most of the conventional lenses in our daily life have aperatures at least on the centimeter-scale. However, to date, most metalenses reported have only millimeter-scale apertures (80 – 100 mm). Therefore, there is a need for the metalenses to be fabricated with low-cost, large-aperture, high-efficiency, and scalable methods. The bottom-up fabrication technique is based on the combination of colloidal synthesis of the meta-atoms in large amounts and their self-assembly onto two-dimensional substrates. This could be an alternative for realizing metasurfaces operating in the visible and near-infrared regions.

For example, it has been experimentally demonstrated that spherical silicon particles synthesized by various bottom-up approaches[46,47] exhibit forward scattering of light due to the overlap of the electric and magnetic dipole resonances. By varying the Si sphere diameter between 100 – 200 nm, significant changes are observed in the forward-to-backward scattering ratio. For a 150 nm diameter, the ratio exceeds 6:1 (which is predominantly forward scattering) at a wavelength of ~ 660 nm (Figures 7a and d). Recently, Hu, Y., *et al*.[48] fabricated a metasurface ~100 × 70 mm by the colloidal capillary-force assisted self-assembly process of the monodispersed Si particles with an average diameter of 254 nm (Figures 7b and e). The measurement of reflectance across the visible to near-infrared wavelength range (600 – 1100 nm) yields a reflectance maximum of 25 – 30% at a wavelength of 850 – 900 nm, which decreases to as low as 10 – 15% at wavelengths between 600 and 800 nm. The light transmission exceeds 50% in the near-infrared (1000 – 1100 nm), which is attributed to the overlap of the electric and magnetic dipole resonances (Figures 7c and f). Previously, within the group at the ICMCB, forward scattering of light by subwavelength-size single particles of silicon with a silicon oxynitride ($Si@SiO_xN_y$) shell and their 2D arrays has been experimentally demonstrated at visible to near-infrared wavelengths (as shown in Figure 7g-i). In the single particle, a forward scattering efficiency above 1.3 was observed in the broadband wavelength range of 500 – 750 nm, which rose to 2.8 at ~ 600 nm. The interfacial self-assembly technique was used to fabricate a large-area metasurface (~ 100 $mm^2$), which exhibits a transmission efficiency of approximately 50% across the visible to near-infrared region in solution.

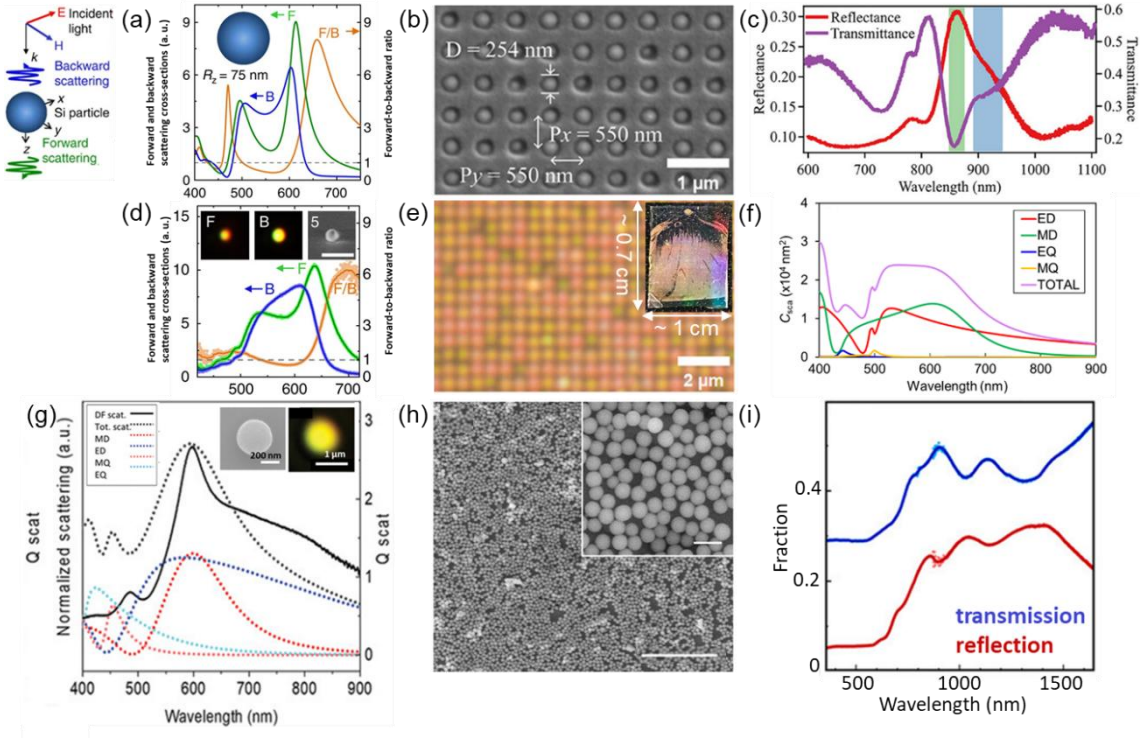



*Figure 7. Theoretical and experimental demonstration of the light scattering by (a,d) a single dielectric Si particle of diameter 150 nm, (g) core-shell Si@$SiO_xN_y$ with diameter of 150 nm and shell thickness of 115 nm. SEM (b,h) and darkfield optical image (e) of the particles in a 2D array. Transmission and reflection spectra of the particles in a 2D array (c,f) and in solution (i). Reproduced from ref.*[33,48,49]

The aim of this thesis was therefore to investigate the bottom-up fabrication and directional light scattering properties of isotropic and anisotropic Si-based nanostructures, which could serve as potential building blocks for Huygens metasurfaces. We focused on theoretically predicted Si-based nanostructures that can be obtained by colloidal synthesis in large quantities. These include spherical silicon particles with a plasmonic shell (Au, Ag), dielectric shell ($SiO_2$), ellipsoidal Si particles, and heterostructure Si nanowires. These different nanomaterials are presented subsequently in 3 results chapters, where optical measurements were made on the most promising materials to determine their potential as meta-atoms. I then conclude with perspectives about where meta-atom synthetic efforts should be oriented in the future.

## References


(1) Gaponenko, S. V.; Demir, H. V. *Applied Nanophotonics*, 1st ed.; Cambridge University Press, 2018. https://doi.org/10.1017/9781316535868.

(2) McGurn, A. *Nanophotonics*; Springer Series in Optical Sciences; Springer International Publishing: Cham, 2018; Vol. 213. https://doi.org/10.1007/978-3-319-77072-7.

(3) Chen, H.-T.; Taylor, A. J.; Yu, N. A Review of Metasurfaces: Physics and Applications. *Rep. Prog. Phys.* **2016**, *79* (7), 076401. https://doi.org/10.1088/0034-4885/79/7/076401.

(4) *The Electromagnetic Spectrum: An Overview. Radiation and Your Health.* https://www.cdc.gov/radiation-health/about/electromagnetic-spectrum.html.

(5) Smith, D. R.; Padilla, W. J.; Vier, D. C.; Nemat-Nasser, S. C.; Schultz, S. Composite Medium with Simultaneously Negative Permeability and Permittivity. *Phys. Rev. Lett.* **2000**, *84* (18), 4184–4187. https://doi.org/10.1103/PhysRevLett.84.4184.

(6) Shelby, R. A.; Smith, D. R.; Schultz, S. Experimental Verification of a Negative Index of Refraction. *Science* **2001**, *292* (5514), 77–79. https://doi.org/10.1126/science.1058847.

(7) Smith, D. R.; Pendry, J. B.; Wiltshire, M. C. K. Metamaterials and Negative Refractive Index. *Science* **2004**, *305* (5685), 788–792. https://doi.org/10.1126/science.1096796.

(8) Pendry, J. B. Negative Refraction Makes a Perfect Lens. *Phys. Rev. Lett.* **2000**, *85* (18), 3966–3969. https://doi.org/10.1103/PhysRevLett.85.3966.

(9) Fang, N.; Lee, H.; Sun, C.; Zhang, X. Sub-Diffraction-Limited Optical Imaging with a Silver Superlens. *Science* **2005**, *308* (5721), 534–537. https://doi.org/10.1126/science.1108759.

(10) Liu, Z.; Lee, H.; Xiong, Y.; Sun, C.; Zhang, X. Far-Field Optical Hyperlens Magnifying Sub-Diffraction-Limited Objects. *Science* **2007**, *315* (5819), 1686–1686. https://doi.org/10.1126/science.1137368.

(11) Cai, W.; Chettiar, U. K.; Kildishev, A. V.; Shalaev, V. M.; Milton, G. W. Nonmagnetic Cloak with Minimized Scattering. *Appl. Phys. Lett.* **2007**, *91* (11), 111105. https://doi.org/10.1063/1.2783266.

(12) Schurig, D.; Mock, J. J.; Justice, B. J.; Cummer, S. A.; Pendry, J. B.; Starr, A. F.; Smith, D. R. Metamaterial Electromagnetic Cloak at Microwave Frequencies. *Science* **2006**, *314* (5801), 977–980. https://doi.org/10.1126/science.1133628.

(13) Plum, E.; Fedotov, V. A.; Schwanecke, A. S.; Zheludev, N. I.; Chen, Y. Giant Optical Gyrotropy Due to Electromagnetic Coupling. *Appl. Phys. Lett.* **2007**, *90* (22), 223113. https://doi.org/10.1063/1.2745203.

(14) Rogacheva, A. V.; Fedotov, V. A.; Schwanecke, A. S.; Zheludev, N. I. Giant Gyrotropy Due to Electromagnetic-Field Coupling in a Bilayered Chiral Structure. *Phys. Rev. Lett.* **2006**, *97* (17), 177401. https://doi.org/10.1103/PhysRevLett.97.177401.

(15) Park, J.-S.; Zhang, S.; She, A.; Chen, W. T.; Lin, P.; Yousef, K. M. A.; Cheng, J.-X.; Capasso, F. All-Glass, Large Metalens at Visible Wavelength Using Deep-Ultraviolet Projection Lithography. *Nano Lett.* **2019**, *19* (12), 8673–8682. https://doi.org/10.1021/acs.nanolett.9b03333.

(16) Zhang, L.; Chang, S.; Chen, X.; Ding, Y.; Rahman, M. T.; Duan, Y.; Stephen, M.; Ni, X. High-Efficiency, 80 Mm Aperture Metalens Telescope. *Nano Lett.* **2023**, *23* (1), 51–57. https://doi.org/10.1021/acs.nanolett.2c03561.

(17) Staude, I.; Miroshnichenko, A. E.; Decker, M.; Fofang, N. T.; Liu, S.; Gonzales, E.; Dominguez, J.; Luk, T. S.; Neshev, D. N.; Brener, I.; Kivshar, Y. Tailoring Directional Scattering through Magnetic and Electric Resonances in Subwavelength Silicon Nanodisks. *ACS Nano* **2013**, *7* (9), 7824–7832. https://doi.org/10.1021/nn402736f.

(18) Decker, M.; Staude, I.; Falkner, M.; Dominguez, J.; Neshev, D. N.; Brener, I.; Pertsch, T.; Kivshar, Y. S. High-Efficiency Dielectric Huygens' Surfaces. *Adv. Opt. Mater.* **2015**, *3* (6), 813–820. https://doi.org/10.1002/adom.201400584.

(19) Chong, K. E.; Wang, L.; Staude, I.; James, A. R.; Dominguez, J.; Liu, S.; Subramania, G. S.; Decker, M.; Neshev, D. N.; Brener, I.; Kivshar, Y. S. Efficient Polarization-Insensitive Complex Wavefront Control Using Huygens' Metasurfaces Based on Dielectric Resonant Meta-Atoms. *ACS Photonics* **2016**, *3* (4), 514–519. https://doi.org/10.1021/acsphotonics.5b00678.

(20) Yu, N.; Aieta, F.; Genevet, P.; Kats, M. A.; Gaburro, Z.; Capasso, F. A Broadband, Background-Free Quarter-Wave Plate Based on Plasmonic Metasurfaces. *Nano Lett.* **2012**, *12* (12), 6328–6333. https://doi.org/10.1021/nl303445u.

(21) Zhao, Y.; Alù, A. Manipulating Light Polarization with Ultrathin Plasmonic Metasurfaces. *Phys. Rev. B* **2011**, *84* (20), 205428. https://doi.org/10.1103/PhysRevB.84.205428.

(22) Shalaev, M. I.; Sun, J.; Tsukernik, A.; Pandey, A.; Nikolskiy, K.; Litchinitser, N. M. High-Efficiency All-Dielectric Metasurfaces for Ultracompact Beam Manipulation in Transmission Mode. *Nano Lett.* **2015**, *15* (9), 6261–6266. https://doi.org/10.1021/acs.nanolett.5b02926.

(23) Chong, K. E.; Staude, I.; James, A.; Dominguez, J.; Liu, S.; Campione, S.; Subramania, G. S.; Luk, T. S.; Decker, M.; Neshev, D. N.; Brener, I.; Kivshar, Y. S. Polarization-Independent Silicon Metadevices for Efficient Optical Wavefront Control. *Nano Lett.* **2015**, *15* (8), 5369–5374. https://doi.org/10.1021/acs.nanolett.5b01752.

(24) Arbabi, A.; Horie, Y.; Bagheri, M.; Faraon, A. Dielectric Metasurfaces for Complete Control of Phase and Polarization with Subwavelength Spatial Resolution and High Transmission. *Nat. Nanotechnol.* **2015**, *10* (11), 937–943. https://doi.org/10.1038/nnano.2015.186.

(25) Yu, Y. F.; Zhu, A. Y.; Paniagua-Domínguez, R.; Fu, Y. H.; Luk'yanchuk, B.; Kuznetsov, A. I. High-transmission Dielectric Metasurface with 2π Phase Control at Visible Wavelengths. *Laser Photonics Rev.* **2015**, *9* (4), 412–418. https://doi.org/10.1002/lpor.201500041.

(26) Hsiao, H.; Chu, C. H.; Tsai, D. P. Fundamentals and Applications of Metasurfaces. *Small Methods* **2017**, *1* (4), 1600064. https://doi.org/10.1002/smtd.201600064.

(27) Huyghens, C. Traite de La Lumière. **1966**.

(28) Romain Dezert. Theoretical Study of Isotropic Huygens Particles for Metasurfaces, Université de Bordeaux, 2019.

(29) Liu, L.; Zhang, X.; Kenney, M.; Su, X.; Xu, N.; Ouyang, C.; Shi, Y.; Han, J.; Zhang, W.; Zhang, S. Broadband Metasurfaces with Simultaneous Control of Phase and Amplitude. *Adv. Mater.* **2014**, *26* (29), 5031–5036. https://doi.org/10.1002/adma.201401484.

(30) Pfeiffer, C.; Grbic, A. Metamaterial Huygens' Surfaces: Tailoring Wave Fronts with Reflectionless Sheets. *Phys. Rev. Lett.* **2013**, *110* (19), 197401. https://doi.org/10.1103/PhysRevLett.110.197401.

(31) Chen, M.; Kim, M.; Wong, A. M. H.; Eleftheriades, G. V. Huygens' Metasurfaces from Microwaves to Optics: A Review. *Nanophotonics* **2018**, *7* (6), 1207–1231. https://doi.org/10.1515/nanoph-2017-0117.

(32) Ollanik, A. J.; Smith, J. A.; Belue, M. J.; Escarra, M. D. High-Efficiency All-Dielectric Huygens Metasurfaces from the Ultraviolet to the Infrared. *ACS Photonics* **2018**, *5* (4), 1351–1358. https://doi.org/10.1021/acsphotonics.7b01368.

(33) Fu, Y. H.; Kuznetsov, A. I.; Miroshnichenko, A. E.; Yu, Y. F.; Luk'yanchuk, B. Directional Visible Light Scattering by Silicon Nanoparticles. *Nat. Commun.* **2013**, *4* (1), 1527. https://doi.org/10.1038/ncomms2538.

(34) Zhang, S.; Jiang, R.; Xie, Y.; Ruan, Q.; Yang, B.; Wang, J.; Lin, H. Colloidal Moderate-Refractive-Index $Cu_2$ O Nanospheres as Visible-Region Nanoantennas with Electromagnetic Resonance and Directional Light-Scattering Properties. *Adv. Mater.* **2015**, *27* (45), 7432–7439. https://doi.org/10.1002/adma.201502917.

(35) Wang, Z.; An, N.; Shen, F.; Zhou, H.; Sun, Y.; Jiang, Z.; Han, Y.; Li, Y.; Guo, Z. Enhanced Forward Scattering of Ellipsoidal Dielectric Nanoparticles. *Nanoscale Res. Lett.* **2017**, *12* (1), 58. https://doi.org/10.1186/s11671-016-1794-x.

(36) Sikdar, D.; Cheng, W.; Premaratne, M. Optically Resonant Magneto-Electric Cubic Nanoantennas for Ultra-Directional Light Scattering. *J. Appl. Phys.* **2015**, *117* (8), 083101. https://doi.org/10.1063/1.4907536.

(37) Wiecha, P. R.; Cuche, A.; Arbouet, A.; Girard, C.; Colas Des Francs, G.; Lecestre, A.; Larrieu, G.; Fournel, F.; Larrey, V.; Baron, T.; Paillard, V. Strongly Directional Scattering from Dielectric Nanowires. *ACS Photonics* **2017**, *4* (8), 2036–2046. https://doi.org/10.1021/acsphotonics.7b00423.

(38) Xu, H.; Pan, H.; Yang, M.; Du, Q.; Lu, Y.; Chen, Y. Strongly Directional Fano Resonance in an Individual Silicon Nanorod. *J. Phys. Chem. C* **2020**, *124* (48), 26486–26492. https://doi.org/10.1021/acs.jpcc.0c09163.

(39) Liu, W.; Miroshnichenko, A. E.; Neshev, D. N.; Kivshar, Y. S. Broadband Unidirectional Scattering by Magneto-Electric Core–Shell Nanoparticles. *ACS Nano* **2012**, *6* (6), 5489–5497. https://doi.org/10.1021/nn301398a.

(40) Liu, W.; Miroshnichenko, A. E.; Oulton, R. F.; Neshev, D. N.; Hess, O.; Kivshar, Y. S. Scattering of Core-Shell Nanowires with the Interference of Electric and Magnetic Resonances. *Opt. Lett.* **2013**, *38* (14), 2621. https://doi.org/10.1364/OL.38.002621.

(41) Sun, Y.; Mu, H.; Liu, C.; Qiao, J.; Sun, T.; Chu, P. K. Enhancement of Unidirectional Forward Scattering and Suppression of Backward Scattering in Hollow Silicon Nanoblocks. *Appl. Opt.* **2021**, *60* (28), 8737. https://doi.org/10.1364/AO.435987.

(42) Tseng, E.; Colburn, S.; Whitehead, J.; Huang, L.; Baek, S.-H.; Majumdar, A.; Heide, F. Neural Nano-Optics for High-Quality Thin Lens Imaging. *Nat. Commun.* **2021**, *12* (1), 6493. https://doi.org/10.1038/s41467-021-26443-0.

(43) Park, J.-S.; Lim, S. W. D.; Amirzhan, A.; Kang, H.; Karrfalt, K.; Kim, D.; Leger, J.; Urbas, A.; Ossiander, M.; Li, Z.; Capasso, F. All-Glass 100 Mm Diameter Visible Metalens for Imaging the Cosmos. *ACS Nano* **2024**, *18* (4), 3187–3198. https://doi.org/10.1021/acsnano.3c09462.

(44) Badloe, T.; Mun, J.; Rho, J. Metasurfaces-Based Absorption and Reflection Control: Perfect Absorbers and Reflectors. *J. Nanomater.* **2017**, *2017*, 1–18. https://doi.org/10.1155/2017/2361042.

(45) Watts, C. M.; Liu, X.; Padilla, W. J. Metamaterial Electromagnetic Wave Absorbers. *Adv. Mater.* **2012**, *24* (23). https://doi.org/10.1002/adma.201200674.

(46) Sugimoto, H.; Fujii, M. Colloidal Mie Resonant Silicon Nanoparticles. *Nanotechnology* **2021**, *32* (45), 452001. https://doi.org/10.1088/1361-6528/ac1a44.

(47) O'Connor, K. M.; Rubletz, A.; Ni, C.; He, Y.; Butler, C.; Veinot, J. G. C. High-Temperature Anomaly in the Synthesis of Large ( $d$ > 100 Nm) Silicon Nanoparticles from Hydrogen Silsesquioxane. *Chem. Mater.* **2023**, *35* (19), 7967–7973. https://doi.org/10.1021/acs.chemmater.3c01200.

(48) Hu, Y.; Probst, P. T.; Habil, M. K.; Sugimoto, H.; Fujii, M. Mechanically Tunable Optical Response in Silicon Nanosphere Metasurface Fabricated via Bottom-Up Process. *Adv. Opt. Mater.* **2025**, 01013. https://doi.org/10.1002/adom.202501013.

(49) De Marco, M. L.; Jiang, T.; Fang, J.; Lacomme, S.; Zheng, Y.; Baron, A.; Korgel, B. A.; Barois, P.; Drisko, G. L.; Aymonier, C. Broadband Forward Light Scattering by Architectural Design of Core–Shell Silicon Particles. *Adv. Funct. Mater.* **2021**, *31* (26), 2100915. https://doi.org/10.1002/adfm.202100915.

# CHAPTER 1. Directional light scattering in silicon-based dielectric nanoantennas


1.1 Introduction to optical nanoantennas ..... 17
1.2 Mie resonances ..... 18
1.3 Choice of dielectric materials ..... 21
1.4 The Kerker effect and Kerker conditions ..... 24
1.5 Directional Mie scattering in spherical Si particles ..... 26
1.6 Directional light scattering in Si-based core-shell nanostructures ..... 28
1.6.1 Proposed core-shell geometries ..... 28
1.6.2 Plasmonic shell materials ..... 30
1.6.3 Dielectric shell materials ..... 35
1.7 Directional light scattering in silicon nanowires ..... 41
1.8 Growth mechanisms for silicon nanowires ..... 44
1.8.1 Vapor-Liquid-Solid ..... 44
1.8.2 Solution−Liquid−Solid and Supercritical Fluid-liquid-Solid ..... 45
1.8.3 Solid-Liquid-Solid ..... 45
1.8.4 Vapor-Solid-Solid ..... 46
1.9 Growth techniques for silicon nanowires ..... 46
1.9.1 Metal-assisted chemical etching (MACE) ..... 47
1.9.2 Chemical vapor deposition (CVD) ..... 49
1.9.3 Plasma-enhanced chemical vapor deposition ..... 53
1.9.4 Supercritical fluid decomposition of silicon precursor ..... 54
1.9.5 Thermal decomposition in high-boiling point solvents ..... 57
1.9.6 Thermal disproportionation of silicon-rich oxide ..... 59
1.10 Directional light scattering in silicon nanoellipse ..... 64
1.10.1 Overview of geometry design ..... 64
1.10.2 Theoretical prediction of the directional light scattering ..... 64
1.11 Fabrication of silicon nanoellipses and their directional scattering properties ..... 67
1.11.1 Laser ablation approach ..... 67
1.11.2 Sol-gel method ..... 70
1.11.3 Metallothermic reduction of silica ..... 75
1.12 Objectives of the PhD thesis ..... 78
References ..... 80

## 1.1 Introduction to optical nanoantennas

Optical nanoantennas that can confine electromagnetic fields to a nanometric volume have been widely used to control light propagation and to enhance light-matter interactions[1,2]. When light interacts with a metal nanoparticle, its conduction electrons can be excited by the electric field of the incident light in collective oscillations, at the particle surface, known as localized surface plasmon resonances (LSPRs). The particle then radiates, so that the LSPRs enable an efficient transfer of electromagnetic energy from the near-field to the far-field of the metal nanoparticles. Hence, such plasmonic nanostructures are considered nanoantennas because they operate in a similar way to radio antennas, but at higher frequencies. The LSPRs give rise to different optical phenomena, including the formation of high-intensity hotspots at the surface of nanoparticles, the directional scattering of light out of the structure, manipulation of the incident radiation pattern, and the subwavelength localization of electromagnetic energy. Moreso, the LSPRs of such a plasmonic nanoparticle can couple to the electromagnetic fields emitted by other materials (dielectric particles, substrates, molecules, quantum dots, etc.), leading to a strong modification of the radiative and non-radiative properties of the emitter. Common plasmonic nanoantennas at the optical wavelengths are made of gold (Au) and silver (Ag) due to their relatively good metallic properties[1,2].

To achieve unidirectional scattering in plasmonic nanoantennas, two or more individual light scattering objects with tailored relative phases and structures are usually required to interfere with each other. Plasmonic nanoantennas mainly support electric dipole resonances. Thus, two or more components are integrated to achieve the directional scattering by the interference between radiating dipoles[3]. For example, an asymmetric nanorod pair can direct the scattered light into the direction perpendicular to the incident light[4,5]. This scattering is known as the unidirectional transverse scattering. Another example is the split-ring resonator, which has been used to generate artificial magnetism at frequencies above the GHz range[6]. The external electric field induces circular current within the nanoantennas, which then results in a magnetic dipole.

Nevertheless, the scattering efficiency is limited by the high optical losses due to absorption by the metal. An alternative to plasmonic nanoantennas is dielectric nanostructures, due to their lower optical losses and high refractive index, which can lead to intense Mie resonances. Moreover, the magnetic response in simple dielectric objects can be leveraged to design functional materials with unidirectional scattering. Due to the unique optical resonances that can combine to produce different interference effects and strong localization of electromagnetic

fields, dielectric nanostructures are expected to complement or even replace various plasmonic components in a range of potential applications.

## 1.2 Mie resonances

The light scattering by nanoparticles and sub-micrometric particles is a fundamental problem in nano-optics and electromagnetism. The earliest solution that addressed this was described in spheres by Gustav Mie in 1908[7] by solving Maxwell's equations in spherical coordinates while analyzing the scattering problem of particles whose dimensions ($a$) are comparable to the electromagnetic wavelength ($\lambda$) in the particle material of refractive index $n$ ($a \approx \lambda/n$). The example studied was gold nanoparticles in a homogeneous water environment, excited by an electromagnetic plane wave. It was used to explain the different colors produced by the Au colloidal nanoparticles. The solution is referred to as the multipolar theory or Mie theory[8–11]. Light scattering by subwavelength particles commonly involves Rayleigh scattering or surface plasmon interaction. These interactions depend only on material properties. In contrast, the Mie-type resonances hinge on both the size and geometry of the particle, as well as its refractive index contrast. Hence, Mie-type resonances are otherwise referred to as morphology-dependent resonances. According to Mie theory[7,10], the light scattering cross section, $C_{sca}$ (Equation 1.1) of a spherical particle can be decomposed into an infinite series of multipole contributions expressed as:

$$C_{sca} = \frac{2\pi}{k^2} \sum_{n}^{\infty} (2n+1)(|a_n|^2 + |b_n|^2) \qquad (1.1)$$

Where $a_n$ and $b_n$ are Mie coefficients of the n$^{th}$-order electric and magnetic modes, and $k$ is the wavenumber. The first four multipolar terms in the Mie expansion are the electric dipole (ED, $a_1^2$), magnetic dipole (MD, $b_1^2$), electric quadrupole (EQ, $a_2^2$), and magnetic quadrupole (MQ, $b_2^2$).

The amplitude of each mode is determined by the scattering coefficient. The coefficients $a_n$ and $b_n$ are functions of the incident wavelength and of the ratio of the refractive index of the dielectric particle, $N_p$ with respect to the surrounding medium, $N_m$ as shown in Equations (1.2 – 1.3):

$$a_n = \frac{m\psi_n(mx)\psi_n'(x) - \psi_n(x)\psi_n'(mx)}{m\psi_n(mx)\xi_n'(x) - \xi_n(x)\psi_n'(mx)} \qquad (1.2)$$

$$b_n = \frac{\psi_n(mx)\psi_n'(x) - m\psi_n(x)\psi_n'(mx)}{\psi_n(mx)\xi_n'(x) - m\xi_n(x)\psi_n'(mx)} \qquad (1.3)$$

The functions ψ and ξ correspond to the Riccati-Bessel functions [10]. The coefficient $n$ = 1 represents the dipolar part of the response, while $n$ = 2 represents the quadrupolar, and so on. As mentioned earlier, the relative refractive index, $m$ is defined as the ratio between the refractive index of the particle, $N_p$ and the refractive index of the medium, $N_m$:

$$m = \frac{N_p}{N_m} \tag{1.4}$$

The size parameter, $x$ is defined as the wavenumber within the particle multiplied by the particle's radius, r:

$$x = \mathrm{k} \times \mathrm{r} = \frac{2\pi n_p}{\lambda_0} \times \mathrm{r} \tag{1.5}$$

The scattering cross section quantifies the scattered power by a dielectric particle, $W_s$ with respect to the irradiance of the incident field, $I$ (Equation 1.1). The scattering cross section has the dimensions of area, and it is often normalized by the geometrical cross section (Equation 1.6), which in the case of a dielectric nanosphere is given as:

$$\text{Geometrical cross section} = \pi \times r^2 \tag{1.6}$$

The ratio between the scattering cross section and the geometric cross section is the scattering efficiency (Equations 1.7 and 1.8)[6]. The scattering efficiency exceeds 1 if the particle scatters light from an area larger than its geometrical form would suggest. The scattering efficiency is a direct measure of the quality of a resonator. The field enhancement observed during a Mie resonance results from the displacement currents induced within the particle by the external electric field, which in turn generates an oscillating electromagnetic field inside and outside the particle. The displacement currents result from the polarization of bound electrons and are free from ohmic losses, which hinder the scattering efficiency of metals in the optical range.

$$\mathrm{C_{sca}} = \frac{W_s}{I} = \frac{2\pi}{\mathrm{k}^2} \sum_{\mathrm{n}=1}^{\infty} (2\mathrm{n}+1)(|\mathrm{a_n}|^2 + |\mathrm{b_n}|^2) \tag{1.7}$$

$$\mathrm{Q_{sca}} = \frac{C_{sca}}{\pi r^2} = \frac{2}{x^2} \cdot \sum_{\mathrm{n}}^{\infty} (2\mathrm{n}+1)(|\mathrm{a_n}|^2 + |\mathrm{b_n}|^2) \tag{1.8}$$

The modes respond according to their scattering coefficient when excited by light. Under specific conditions, the modes exhibit resonances that amplify the electromagnetic field outside and within the particle. Each resonant mode has a specific wavelength. The value of the coefficient corresponding to the excited mode increases significantly during its resonance, and the resonant mode becomes the main contributor to the overall scattering spectrum. To achieve intense Mie resonances, the refractive index of the particle should be high compared to the

index of the medium with minimal absorption. The scattering efficiency is zero when the index of the particle is similar to the index of the medium. This can be observed in Equations 1.2 and 1.3 above. The coefficients $a_n$ and $b_n$ disappear when $N_p = N_m$. When a sphere with a high refractive index traps light, it enhances the electromagnetic field and exhibits resonances at a specific wavelength value. These are the resonant modes supported by the particle. The fundamental mode, corresponding to the scattering from a magnetic dipole, occurs when the wavelength inside the particle is approximately the same as the particle size[12]. The second mode, corresponding to the electric dipole scattering, is when the wavelength is half the size of the particle (Figure 1.1).

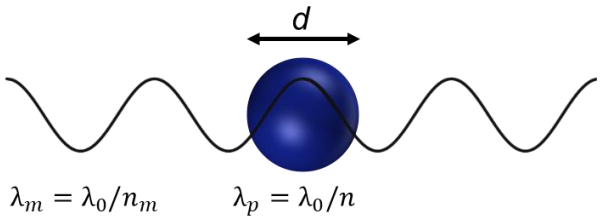



*Figure 1.1 Schematic illustration of the hypothesized condition for the excitation of the magnetic dipole. Reproduced from ref.*[6]

$$\lambda_p \text{ (magnetic dipole)} = \lambda_0/n \approx d \qquad (1.9)$$

$$\lambda_p \text{ (electric dipole)} = \lambda_0/n \approx d/2 \qquad (1.10)$$

The condition under which a nanoparticle has a diameter significantly smaller than the wavelength requires a high refractive index material, as shown in Equations 1.9 and 1.10. For such dielectric particles, the first two dipole modes are the most intense. The fundamental mode is referred to as the magnetic dipole because the scattered field corresponds to the field radiated by an oscillating magnetic dipole, which is perpendicular to the incident electric field. The second resonance is the electric dipole because the scattered field corresponds to the field radiated by an oscillating electric dipole parallel to the direction of the incident electric field. These modes are followed by the electric and magnetic quadrupoles (Figure 1.2). The higher orders, such as the octupole and fourth orders, are almost always extremely weak and are rarely considered for engineering the electromagnetic response of a dielectric nanoantenna[13].

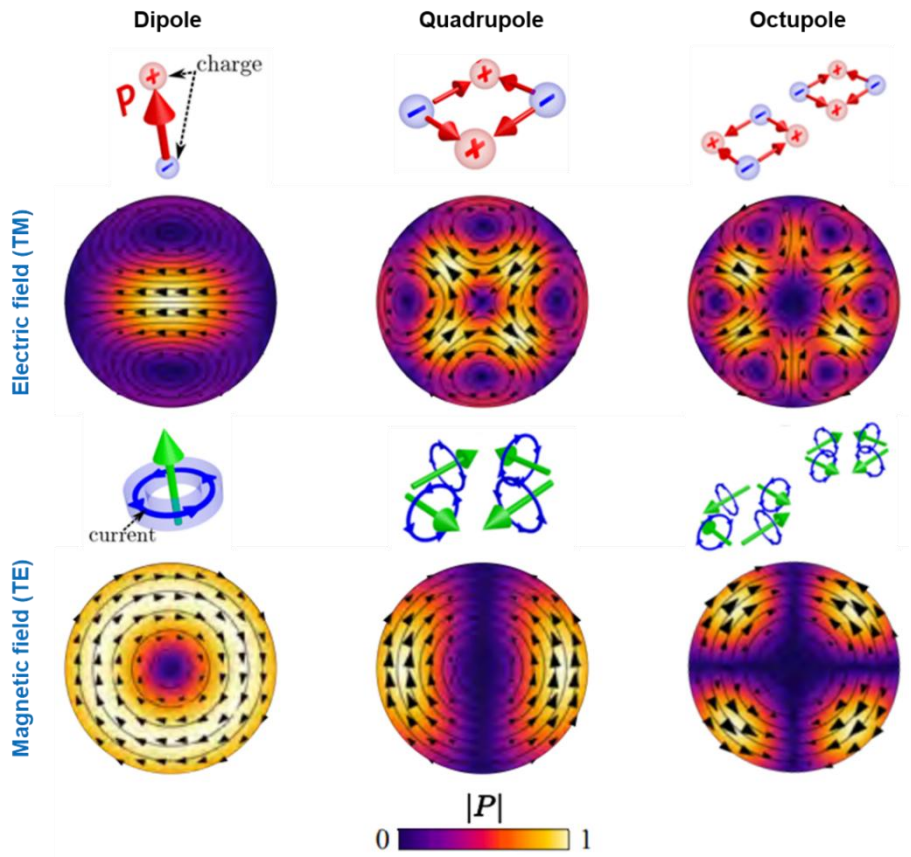



*Figure 1.2 Polarization field distributions of the electric and magnetic field lines and the charge-current distribution of a dielectric particle supporting different electric and magnetic modes. Black arrows point in the direction of polarization currents. Reproduced from ref.*[14]

## 1.3 Choice of dielectric materials

The refractive index, $n$, and the extinction coefficient, $k$, have a significant influence on the Mie scattering of dielectric particles. The refractive index of the material determines the spectral position of the particle's resonances. Therefore, the higher the refractive index of the material, the smaller the particle diameter required to exhibit Mie resonances at the visible/near-infrared wavelength, and vice versa. The field enhancement of Mie resonances increases with a higher refractive index (Figure 1.3a). Also, a large refractive index contrast with the medium (usually $n_{air}$ = 1.0, $n_{water}$ = 1.33, or $n_{oil}$ = 1.52) results in smaller radiation leakage from the particles. A value between 0 and 1 represents the extinction coefficient, $k$, and a low value supports intense light scattering (Figure 1.3b). When $k$ is equal to 0, the particles do not absorb any of the light, thus, the scattering is most intense. When $k$ is equal to 1, there is complete light absorbance, and light scattering is very minimal. Therefore, the higher the refractive index and the lower the extinction coefficient, the more intense the Mie scattering. For efficient directional light scattering, resonances with high-quality (high-Q) are required[15].

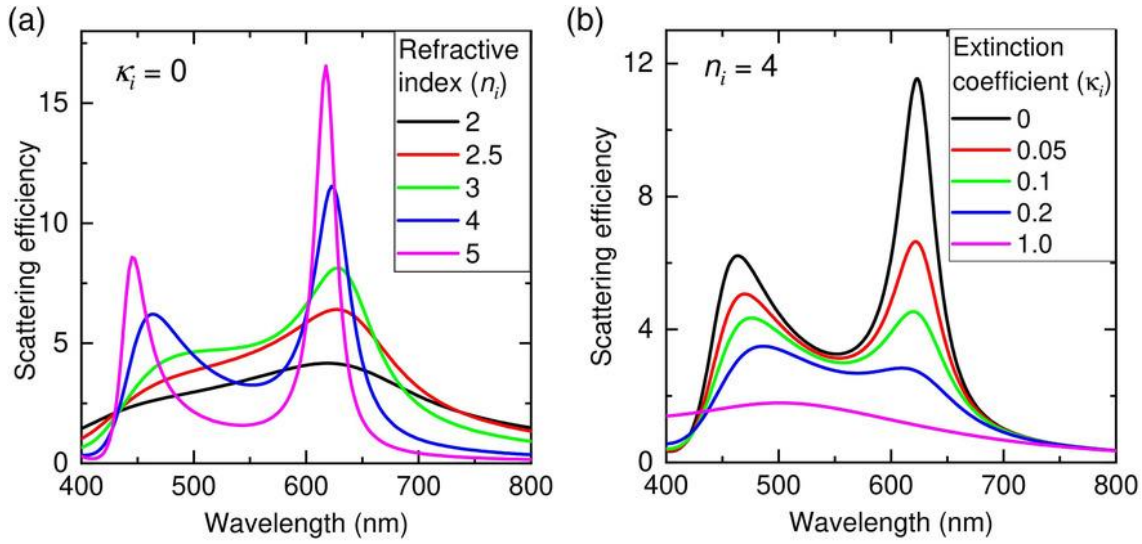



*Figure 1.3 Simulated Mie scattering spectra of spheres with defined n and k values. (a) The diameter is changed depending on n (d = 600/n (nm) (b) The diameter is fixed at 150 nm. Figure reproduced from ref.*[15]

There are several dielectric materials with relatively high refractive index ($n > 4$) in the visible and near-IR range (Table 1.1). For example, silicon (Si), germanium (Ge), tellurium (Te), lead telluride (PbTe), gallium arsenide (GaAs), aluminum gallium arsenide (AlGaAs), etc. However, the optical losses of some of these materials, such as Ge, GaAs, and AlGaAs, are too significant to support high-Q resonances in the visible region (Table 1.1). Materials such as Te, GeTe, PbTe, and SiC have high-Q resonances in the mid-IR region (Figure 1.4).

*Table 1.1 Refractive indices and extinction coefficients for some dielectric materials available in the visible and IR spectral regions. Reproduced from ref.*[12]

| Material | Spectral range (μm) | Refractive index, *n* | Extinction coefficient, *k* |
|---|---|---|---|
| Crystalline Si | 0.50 – 1.45 | 4.293 – 3.486 | 0.045 – 0.001 |
| | 1.45 – 2.40 | 3.484 – 3.437 | ~ 0 |
| Amorphous Si | 0.50 – 1.00 | 4.47 – 3.61 | 1.12 – 0.01 |
| Ge | 0.50 – 0.60 | 4.460 – 5.811 | 2.366 – 1.389 |
| | 0.60 – 0.80 | 5.811 – 4.699 | 1.389 – 0.3 |
| | 0.80 – 1.90 | 4.684 – 4.129 | 0.3 – 0.001 |
| | 1.90 – 2.40 | 4.111 – 4.069 | ~ 0 |
| $TiO_2$ | 0.50 – 1.00 | 2.715 – 2.483 | ~ 0 |
| GaP | 0.50 – 0.80 | 3.590 – 3.197 | ~ 0 |
| GaAs | 0.50 – 0.80 | 4.037 – 3.679 | 0.376 – 0.089 |

| | | | |
|---|---|---|---|
| InP | 0.50 – 0.80 | 3.456 – 3.818 | 0.203 – 0.511 |
| GaSb | 1.00 – 2.40 | 4.140 – 3.846 | 0.225 – 0.001 |
| Te | 4.00 – 14.0 | 4.929 – 4.785 | ~ 0 |
| PbTe | 4.10 – 12.5 | 5.975 – 5.609 | ~ 0 |
| GeTe | 6.20 – 11.8 | 7.3 – 7.278 | ~ 0 |
| SiC | 11.0 – 15.0 | ~ 20 | ~ 15 |

Among these materials, Si, $TiO_2$, and GaP have high refractive indices and low optical losses in the visible region. In the visible to near-infrared region, directional scattering has been experimentally demonstrated in Si[16–20], Ge[21], GaAs[17], and $TiO_2$[22] particles. Dielectric materials, such as AlAs and GaP, have been less explored as nanoresonators for directional scattering compared to Si due to fabrication difficulties. However, Shima, D., *et al*.[23] recently fabricated Mie resonant GaP nanoparticles with uncontrolled shape via a combination of mechanical milling and a pulsed laser melting process in solution. It was demonstrated that the pulsed laser melting process is crucial for imparting a spherical shape and a smooth surface to irregular particles formed through mechanical milling. The fabricated particles were shown to be effective as low-loss nanoantennas in the visible range. However, the batch dispersity, morphology, and homogeneity throughout the samples still need to be improved to achieve efficient scattering[23]. Subwavelength-sized Si particles, with diameters ranging from 70 to 200 nm, interact with visible and near-infrared light, producing strong electric and magnetic resonances. Simple Si spheres offer low optical losses and present strong resonances, while being accessible through bulk syntheses using both chemical[24–26] and physical approaches[27,28]. Hence, crystalline Si particles remain the best choice of material for nanoresonators due to their strong Mie scattering, relatively versatile method of fabrication, and their natural abundance.

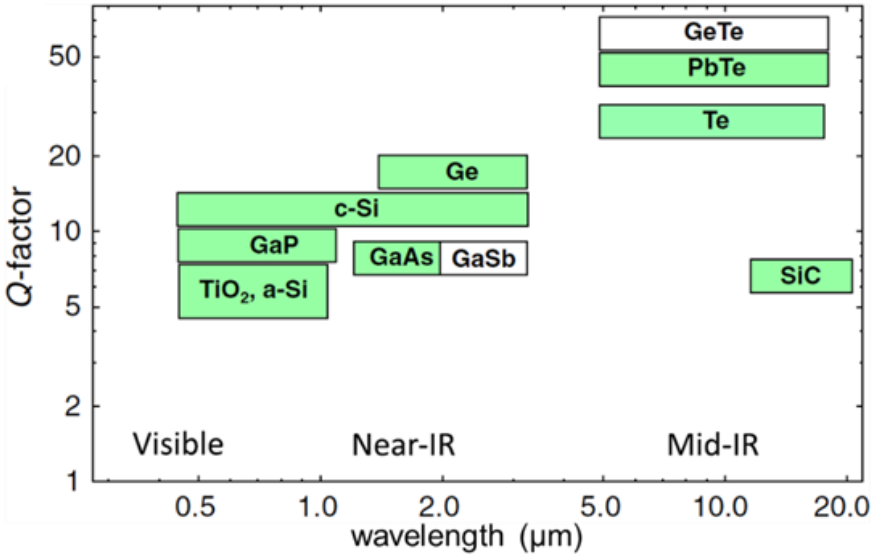



*Figure 1.4 The quality (Q)-factors of dielectric materials. The dielectric materials that can be nanostructured by existing fabrication techniques are marked in green. The figure is reproduced from ref.*[12]

## 1.4 The Kerker effect and Kerker conditions

Kerker, M., *et al.*[29] discovered an interesting effect in the scattering of electromagnetic waves by a spherical particle composed of a magnetic material characterized by magnetic permeability, $\mu$ and dielectric permittivity, $\varepsilon$. This study revealed the possibility of redirecting the scattered radiation to either only forward or backward direction, depending on the wavelength. This unique effect is referred to as the Kerker effect. The discovery was categorized into two conditions known as the first and second Kerker conditions. The first Kerker condition corresponds to the cancellation of the backward scattering while maximizing the forward scattering. The second Kerker condition corresponds to a deep minimum in the forward scattering direction. The scattering along the axis of the incoming waves defines the backward and forward scattering. The optical theorem states that the extinction cross-section of a scatterer can be cast with respect to its forward scattering, which means that the forward scattering cannot be canceled. Hence, the Keker conditions are satisfied under the following conditions:

$$\varepsilon = \mu \qquad (1^{st} \text{ Kerker's condition})$$

$$\varepsilon = -\frac{\mu - 4}{\mu + 1} \qquad (2^{nd} \text{ Kerker's condition})$$

These conditions were later extended to non-magnetic dielectric spheres supporting both electric and magnetic Mie resonances[30–32]. The optical magnetism provided by the Mie

resonances mimics the anomalous scattering properties of magnetic spheres. For a scatterer whose multipolar Mie scattering coefficient, $a_n$ and $b_n$ can be neglected for $n \geq 2$, the first Kerker condition is obtained when $a_1 = b_1$. When the electric dipole and the induced magnetic dipole are in-phase, the backward scattering is suppressed, which leads to the first Kerker condition (Figure 1.5a). On the other hand, when the excited electric and magnetic dipoles are equal in amplitude but out-of-phase, the backward scattering is dominant, which leads to the second Kerker condition (Figure 1.5b).

It has also been demonstrated that the Kerker conditions can be extended to higher-order multipoles, and their interference effects can result in a generalized Kerker effect (Figure 1.5c). This can be based on the two-parity rule, which states that, for example, the electric dipole radiation pattern exhibits even symmetry, while the magnetic dipole radiation pattern exhibits odd symmetry. The overlap of these two dipole resonances at equal magnitude leads to the perfect cancellation of the backward radiation. Based on these parity rules, we can categorize the ED, MQ, EO, and $M_4$ as even parity multipoles and MD, EQ, MO, and $E_4$ as odd parity multipoles (Figure 1.5c). The interference of any even parity multipole with the odd parity multipole gives rise to either forward or backward scattering when they resonate at similar intensities and are in-phase or out-of-phase, respectively. The two-parity rules for the classification of the multipoles based on the phase symmetries of their radiation patterns are stated as[33]:

- Multipoles that are the same (either electric or magnetic) with subsequent orders have opposite parity. For example, ED (n = 1) has even parity and EQ (n = 2) has odd parity.
- Multipoles that are not the same but with the same order have opposite parity. For example, EQ (n = 2) has odd parity, while MQ (n = 2) has even parity.

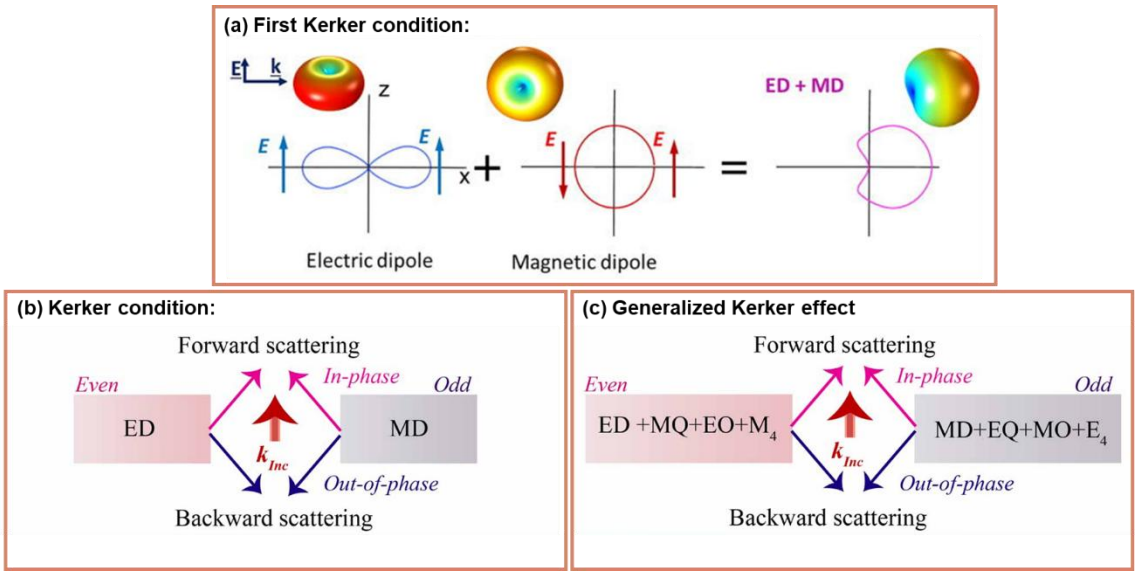



*Figure 1.5 (a) Illustration of the effect of superimposing the electric and magnetic dipoles. (b) Dominance of forward and back scattering based on the Kerker conditions. (c) Generalized Kerker effect for higher-order multipoles. Reproduced from ref.*[33,34]

## 1.5 Directional Mie scattering in spherical Si particles

Spherical Mie resonant particles exhibit directional scattering, but only within a very narrow spectral range. Here, a case study of a Si nanosphere with a diameter of 150 nm illuminated by a plane wave is illustrated. From the decomposition of the total scattering into its different multipoles, it can be seen that the electric and magnetic dipoles dominate the total scattering (Figure 1.6a). An interference can be observed between these dipoles at 564 and 660 nm (Figure 1.6a). Figure 1.6b shows the spectra of the forward and backward scattering over the entire visible range, and the forward-to-backward scattering ratio. At wavelengths higher than 603 nm, forward scattering dominates, while backward scattering is almost zero, resulting in a forward-to-backward ratio of around 8. At wavelengths between 500 – 603 nm, backward scattering dominates with a forward-to-backward scattering ratio below 0.5. The wavelength range less than 500 nm demonstrates scattering in all directions, with a drastic reduction in the total scattering intensity. Figure 1.6c shows the far-field scattering radiation patterns with maximum forward scattering observed at 660 nm, corresponding to the first Kerker's condition. The maximum backward scattering was observed at 564 nm, corresponding to the second Kerker's condition. At the other highlighted wavelength points of 500 and 603, which are the maximum intensity of the electric and magnetic dipole resonances, the scattering is non-directional[35].

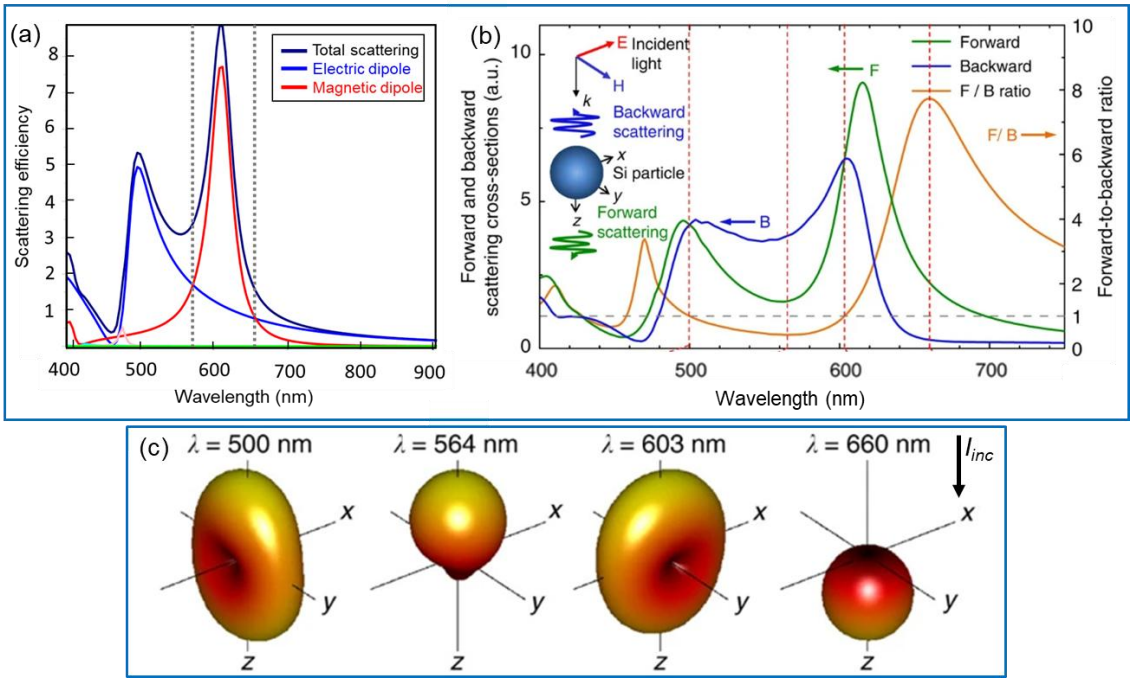



*Figure 1.6 (a) Scattering properties of a silicon (Si) nanoparticle with a diameter of 150 nm in free space calculated by Mie theory. (b) The forward and backward scattering cross-section. (c) The far-field scattering radiation patterns at wavelengths of 500, 564, 603, and 660 nm corresponding to the point of electric dipole, backward scattering, magnetic dipole, and forward scattering, respectively. Modified from ref.*[35]

As shown in Figure 1.6, the partial spectral overlap of the electric and magnetic dipole resonances means that the first Kerker's condition is satisfied off-resonance (dotted lines in Figure 1.6a). This results in relatively weak total scattering efficiencies in the forward direction[35]. Also, the interference or observation of the Kerker effect occurs at the tail end of the visible wavelength. Therefore, different strategies are needed to improve the spectral overlap and increase the forward scattering efficiency, while broadening the directional scattering to lower wavelengths in the visible region. According to the literature, some of the approaches that have been investigated include the creation of non-spherical morphologies (such as nanodisk, nanowires, and nanoellipse)[18,36,37], using a non-homogeneous medium[38,39], and assembling Si particles into arrays[40–42].

Another approach is to superimpose any even multipole (e.g., ED and MQ) with any odd multipole (MD and EQ)[43,44]. For example, clusters of nanoparticles have demonstrated broadband forward scattering due to the spectral overlap arising from the cluster architecture[45–48]. The approach discussed in the next section involves the fabrication of core-shell

architectures. A lower refractive index shell can be used to redshift the ED and/or blueshift the MD to satisfy the first Kerker's condition.

## 1.6 Directional light scattering in Si-based core-shell nanostructures

### 1.6.1 Proposed core-shell geometries

Soun, D., *et al.*[49] simulated the optimized parameters for optimal directional scattering in core-shell particles, based on a Si core with different shell materials (Figure 1.7). The optimization was carried out with a Si core and shell thickness ranging from 2 – 200 nm. The choices of shell material are gold (Au), silver (Ag), silica ($SiO_2$), silicon nitride ($Si_3N_4$), zirconium dioxide ($ZrO_2$), and titanium dioxide ($TiO_2$), based on which material is realistic to fabricate. The analysis revealed the existence of two distinct types of locally optimal forward scattering core Si@shell nanospheres. The structures with lower-index dielectric shells ($SiO_2$, $Si_3N_4$, $ZrO_2$, $TiO_2$) require a large shell thickness, while the plasmonic shells (Au, Ag) have an optimal thickness below 10 nm. In the case of Ag, the shell should even be a bit thinner than for Au, presumably due to its better plasmonic properties and lower dissipation. Figure 1.7 shows the directional scattering spectra for the lowest loss solution of each shell material. These findings agree with studies from Feng, T., *et al.*[50] for Au shells, Tsuchimoto, Y., *et al.*[51,52] for $SiO_2$ shells, and De Marco, M. L., *et al.*[53] for $SiO_xN_y$ shells. In the context of chemical fabrication feasibility, the low-index dielectric shells seem the most interesting choice for the fabrication of Huygen's sources with optimized scattering efficiency. The directionality is very broadband in the visible range. The plasmonic shells made of Au or Ag are also capable of increasing the scattering efficiency at which the Kerker effect occurs. However, the experimental challenge of fabricating thin, crystalline, and continuous shells still needs to be overcome.

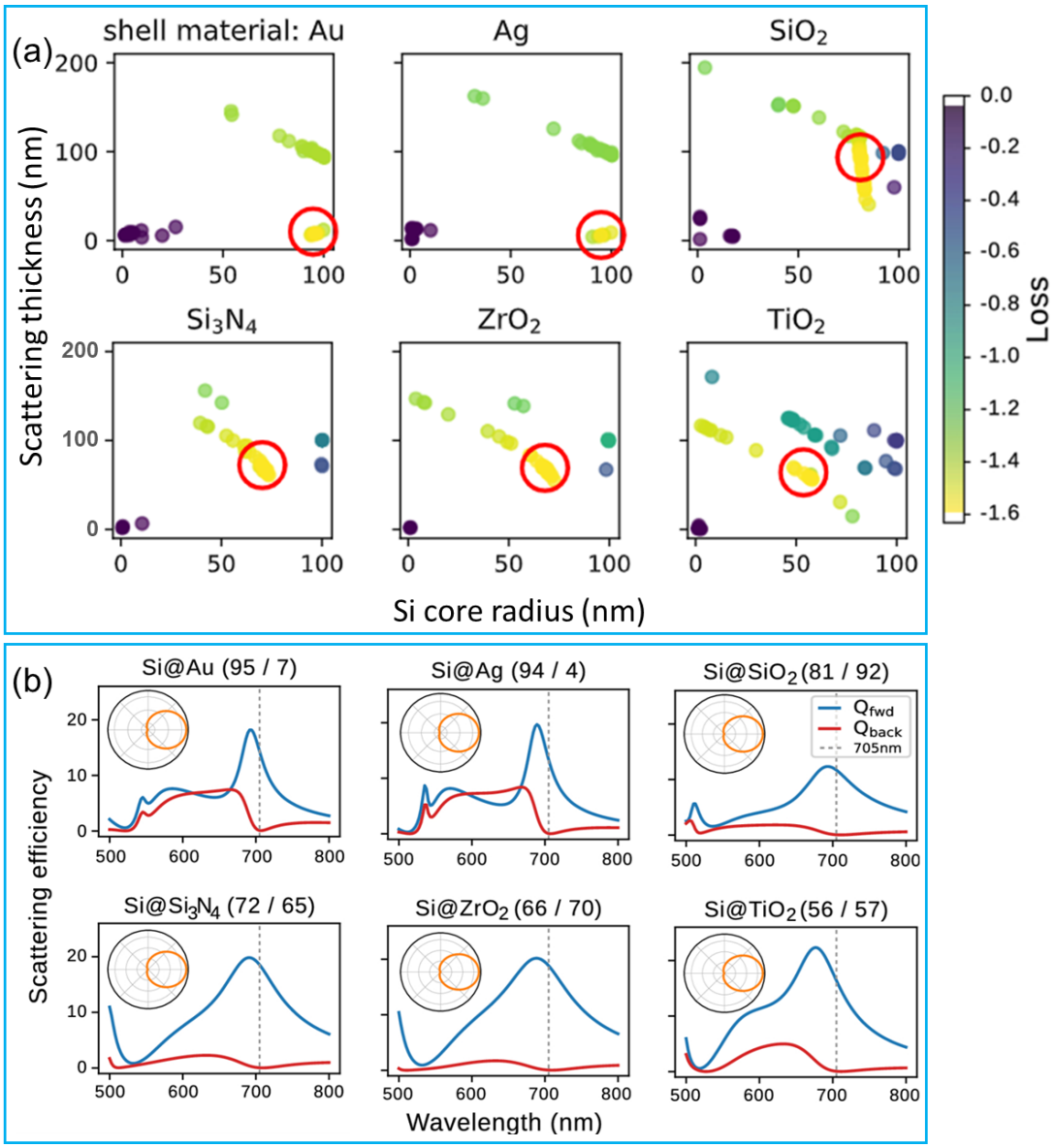



*Figure 1.7 (a) Locally optimal designs for a core-shell sphere with a silicon core as a function of core and shell size. The best solutions for each shell material are highlighted by red circles in the respective subplots. The color scale uses yellow to indicate the best-optimized system and dark-purple for the worst architectures. (b) Best design per shell material (fixed silicon core). The silicon core radius and shell thickness are indicated in parentheses above each subplot (in units of nm). Insets show the polar radiation patterns of the scattering at the design wavelength (nm). Reproduced from ref.*[49]

### 1.6.2 Plasmonic shell materials

This approach to controlling light-matter interactions offers flexibility in shell materials, core diameter, and shell thickness[54,55]. The mode hybridization theory, which considers the hybridization of LSPRs of metal nanospheres and cavities, has been used to qualitatively explain the optical response of a nanoshell at long wavelengths[56,57]. In Figure 1.8a, the resonance frequencies are shown as a function of the core refractive index ($n_c$). A nanosphere with a refractive index less than 2 ($n_c < 2$) has a resonance frequency that is less than that of a cavity. This corresponds to common core materials, such as silica nanospheres ($SiO_2$) or hollow nanoshells. In this case, the lower lying hybridized mode ($\boldsymbol{\omega}_-$) is dominated by the sphere mode ($\boldsymbol{\omega_s}$) which is bright in nature. Hence, the core-shell exhibits intense light scattering in the long wavelength range. However, if the refractive index of the nanosphere is greater than 2 ($n_c > 2$), the resonance frequency of the sphere is greater than that of the cavity. In this case, the hybridized mode ($\boldsymbol{\omega}_-$) is dominated by the lower lying cavity mode ($\boldsymbol{\omega_c}$). Hence, the nanoshell exhibits strong light absorption and is dark in nature (Figure 1.8b). Therefore, the light scattering and absorption properties of the nanoshell are significantly altered. The resonance frequency of a sphere ($\boldsymbol{\omega_s}$) is given as $\boldsymbol{\omega_s = \omega_B/\sqrt{3}}$ in air (where $\boldsymbol{\omega_B}$ is the bulk plasma frequency of a metal), while the resonance frequency of a cavity ($\boldsymbol{\omega_c}$) is given as $\boldsymbol{\omega_c = \omega_B\sqrt{2/(n_c^2+2)}}$ (where $\boldsymbol{n_c}$ is the refractive index of the dielectric cavity).

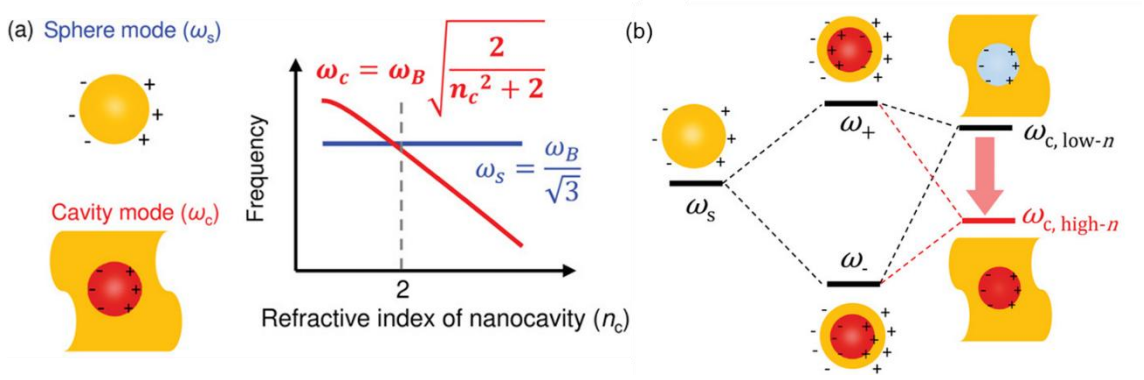



*Figure 1.8 (a) Schematic illustrations of the resonant modes of a nanosphere and cavity in a metal. The resonance energies are shown as a function of the refractive index of a nanocavity. (b) The hybridization model to explain optical resonances of a nanoshell at low and high refractive indices. Reproduced from ref.*[55]

The Mie theory calculations of Feng, T., *et al.*[50] (Figure 1.9a and 1.9b) showed that unidirectional Fano resonant scattering could be achieved with a ~ 9 nm ultrathin Au shell around a Si core with a diameter of 200 nm. This offers the combined advantages of

unidirectional scattering, enhanced forward-to-backward scattering, and a large confinement of electromagnetic energy in the surroundings of the metal[58]. This was compared to a platinum shell material of similar thickness (Figure 1.9c), and it was shown that Au has better overlap properties without total dampening of the resonance intensity. To benefit from the resonant properties of the dielectric core, the plasmonic shell must be thin enough that it does not strongly attenuate light entering the core. However, continuous thin plasmonic shells are challenging to realize due to the difficulty in depositing noble metals such as gold or silver onto Si particle surfaces. The main limitation is that neither of the metals wets the silicon surface sufficiently. This is due to a high lattice mismatch and high surface energy associated with small crystallites[59].

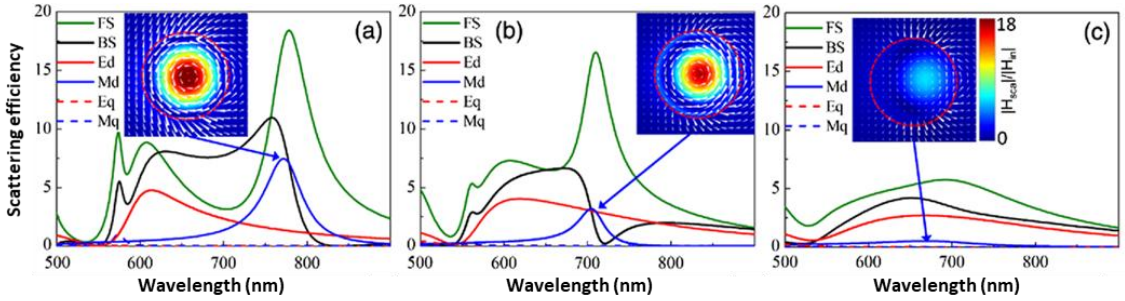



*Figure 1.9 Forward (green) and backward scattering (black) of a (a) spherical Si particle, with a 9 nm (b) Au, and (c) Pt coating, respectively. Reproduced from ref.*[50]

Different studies have produced Si@Au core-satellite particles through laser ablation in liquid. The Si cores are generated from a Si wafer *via* laser ablation in the presence of dissolved chloroauric acid ($HAuCl_4$), which is reduced *in situ* and deposits on the surface of the silicon cores[60–64]. Alternatively, well-formed 10 nm Au nanoparticles present in solution can be electrostatically attracted to Si cores produced *via* laser ablation[65]. Koromyslov *et al.*[66] produced Si cores decorated with Au satellite particles by laser ablation of an Au film deposited on a Si layer. However, none of these approaches has been able to produce ultrathin, homogeneous shells around a silicon core.

Chaâbani, W., *et al.*[54] synthesized Si@Au core-shell nanostructures through a seed-mediated colloidal solution approach. Figure 1.10a shows the procedure for the fabrication of the core-shell particles. As a first step, the small Au particles were attached to the surface of the amine-functionalized Si particles. Then, an Au shell was grown from the particles using an Au growth solution consisting of gold (III) chloride trihydrate, potassium carbonate, and formaldehyde. Whether an Au island or a continuous particulate Au shell was achieved

depended on the level of surface coverage of the Au seeds. Thus, relatively thick shells of around 25 nm were produced. In one case, PVP was added to the solution, which yields a continuous shell of Au and PVP. However, the shell is not more perculating. In the Si core – Au particulate shell particles (Si@Au), in Figure 1.10c, the enhancement of the electric field and Fano-resonances with a strong suppression of the scattering cross-section compared to the bare Si particle (Figure 1.10b) was reported. This is due to the coupling of the Mie modes of the dielectric Si core and the localized surface plasmon resonance (LSPR) of the Au nanoparticles[54]. The near-field enhancement for different excitation wavelengths was confined to the core-shell interface. However, the Au islands/shells were non-uniform and composed of Au nanoparticle diameters between 10 and 25 nm. Moreover, the directional light scattering properties of the synthesized nanostructures have not been clearly studied, likely because the irregular shells and cores are difficult to simulate.

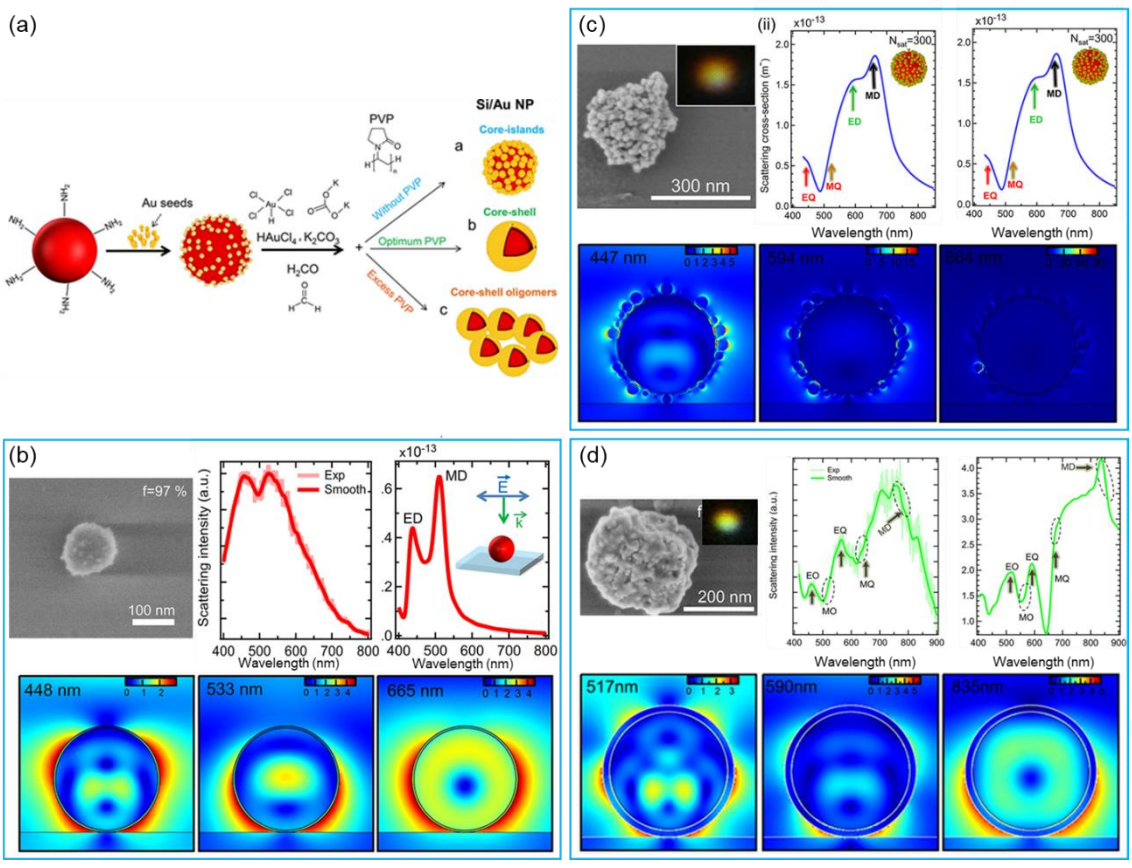



*Figure 1.10 (a) Scheme of the solution synthesis of Si@Au heterostructures. Scattering properties and electric near-field distribution of the (b) Si particles with a diameter of 120 nm (c) Si@Au core–satellite heterostructure, and (d) Si@Au core–shell heterostructure. Reproduced from ref.*[54]

Sugimoto, H., *et al*.[55] fabricated core-shell nanostructures using the same colloidal solution approach. The improvement in this method is that the Si cores are more spherical than the Chaâbani, W., *et al*.[54] particles. Therefore, the complexity of particle anisotropy does not impact the spectral properties. The scattering spectrum of a single particle corresponded better with simulations, showing the dominant ED and MD dipole resonances (Figure 1.11c-d). However, the simulated scattering spectra still failed to capture many spectral features and the relative intensities of different peaks, due to the irregularity of the Au shell. The scattering spectra in Figure 1.11e-f of the core-shell nanostructures predict that the MD blue-shifts by 200 nm, while the ED red-shifts by 150 nm and broadens by the formation of a ~ 25 nm Au shell[55] through the formation of a bright hybridized mode between the Au plasmonic resonance and the ED of the silicon core. The red-shift of the ED mode is extremely strange, as the hybridization is predicted to lead to a lower energy mode occurring, blue-shifted compared to the original peak position. A hybridized ED dark mode appears at ~1150 nm. The dark hybridized mode is predicted to shift to longer wavelengths with an increase in the Si core diameter. At the dip wavelength ~ 620 nm, strong directional scattering to the forward direction occurs due to the overlap of the Si core MD mode with the broad ED ($\omega_+$) mode of the Au shell. The experimental and simulated spectra in Figure 1.11e-f have a number of discrepancies: in the shape, relative intensity of the peaks, and most importantly, the number of spectral peaks. One of the possible origins of the discrepancy is the roughness and discontinuity of the Au shell. Also, the simulations poorly describe the system.

The simulated extinction spectrum in Figure 1.11g showed the contributions of the different multipoles to the total scattering of a typical 200 nm high index (n = 4) sphere, which oddly differ substantially from their simulations of a similar silicon particle shown in Figure 1.11d. The extinction spectrum is dominated by the ED and MD modes at 618 and 832 nm, respectively. The electric field distributions circulate within and around the particle at these wavelengths. In contrast, the metal shell is predicted to have only the electric mode resonances with the spectrum composed of the ED and EQ modes (Figure 1.11h), and the electric field distribution circulates the particle. In comparison, the predicted extinction spectrum of the core-shell particle is very different (Figure 1.11i), impacting both odd and even modes. The MD is substantially dampened and blue-shifts by 100 nm in the core-shell particle, which is explained in that the circulating electric field is more confined within the Si core. The MQ from the high index core is also retained, but also its peak blue-shifts to shorter wavelength with a significant reduction in intensity and width. The broad Au shell ED mode is split into two peaks, which

appear around ~ 620 and 1370 nm. According to the discussed mode hybridization model, the short wavelength peak is assigned to the higher lying mode ($\omega_+$), inheriting the bright nature of the sphere mode. The long wavelength peak is assigned to the lower lying mode ($\omega_-$) inheriting the dark nature of the cavity mode. The electric field distribution of the lower-energy hybridized mode ($\omega_-$ mode) at 1366 nm has a field distribution outside the shell in a similar nature to that of the ED mode in a hollow nanoshell at 732 nm.

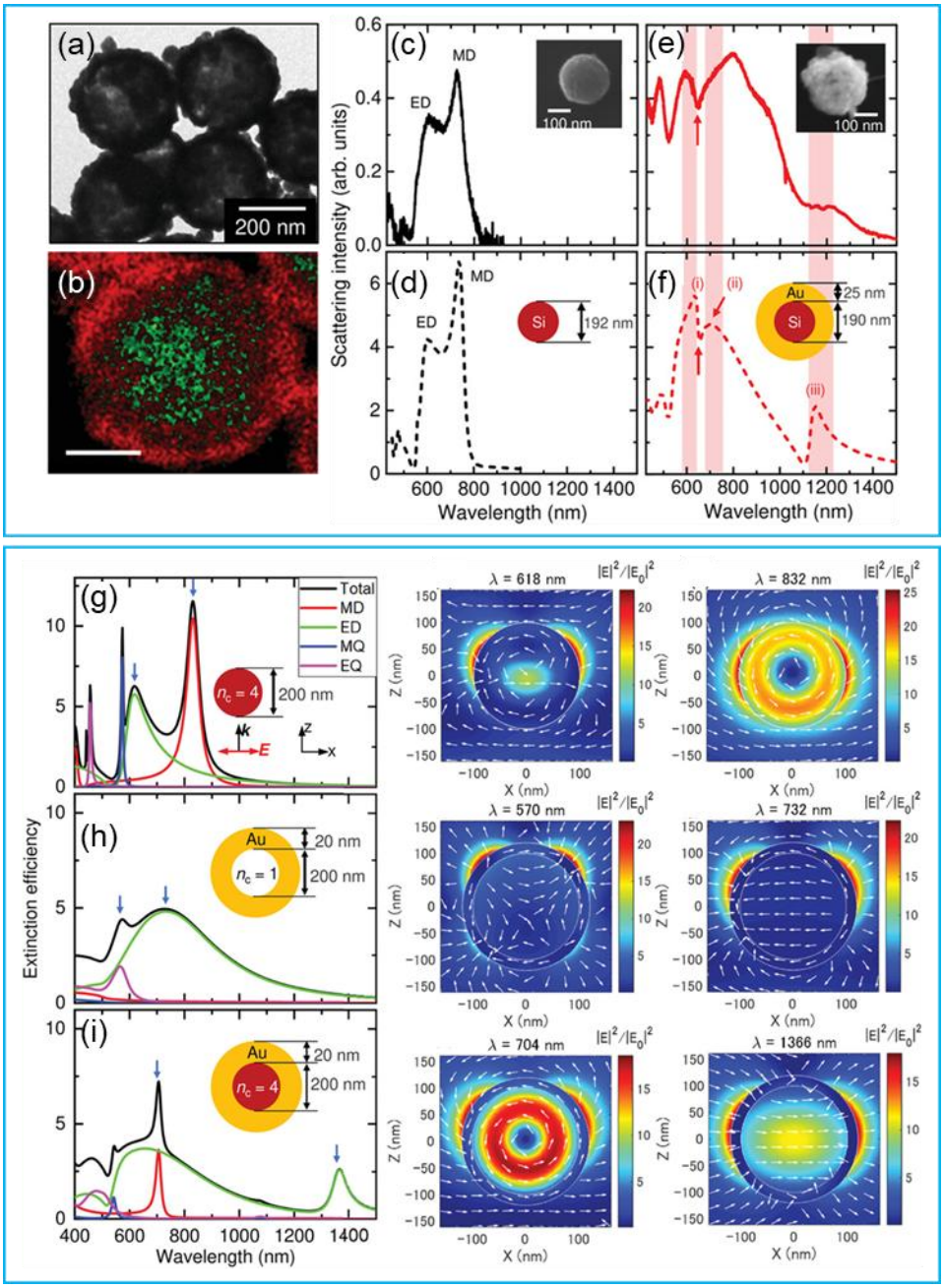



*Figure 1.11 (a) TEM, and (b) EDS elemental mapping image of a single synthesized Si@Au particle. Experimental and measured scattering spectra of a (c-d) single bare Si nanosphere and (e-f) single Si@Au nanosphere. Calculated extinction efficiency spectra and electric field*

*distributions of a (g) high index ($n_c$ = 4) dielectric nanosphere, (h) hollow Au shell, and (i) high index dielectric core–Au shell nanosphere. Reproduced from ref.*[55]

Both the Plain and Fujii groups reported that the core-shell nanostructures were fabricated by surface chemical modification of pre-synthesized Si particles, which are then decorated with Au particles of a specific size that aggregate on the surface to create a particulate shell. Chaâbani, W., *et al.*[54] managed to fit the experimental and numerical simulation spectra roughly, but the fabricated Si and core-shell particles are not spherical. Hence, it is difficult to explain the independent contribution of the Au particles/shell to the total scattering. Sugimoto, H., *et al.*[55] successfully fabricated a spherical Si core, but the Au particles/shell are rough and not continuous. This explained why neither of the reports managed to accurately fit the experimental data with the simulations. In both studies, the Au particles/shell thickness is reported to be around 20 – 25 nm, which exceeds the 9 nm prediction in the earlier discussed theoretical calculation. Hence, further optimization of the colloidal solution approach is needed to achieve an ultra-thin Au shell with a diameter < 10 nm.

### 1.6.3 Dielectric shell materials

A dielectric shell with controlled thickness can be used to control the Mie- or plasmonic resonance properties of the core material. Liu, W., *et al*.[67,68] demonstrated through theoretical calculations that a broadband unidirectional scattering can be achieved with (metal) core-(dielectric) shell nanostructure. Figure 1.12a shows the scattering spectra of a silver (Ag) core with a diameter of 136 nm illuminated by a linearly polarized plane wave, which possesses only the electric dipole. From the scattering pattern at 440 nm, it scatters in both forward and backward directions. However, the scattering efficiency spectra for the core-shell particle with a dielectric shell of refractive index between 2.5 – 3.4 (e.g., Si, Ge, or GaAs) and shell thickness between 60 – 160 nm show an overlap of the electric and magnetic dipoles (Figure 1.12a-d). The scattering patterns show unidirectional scattering in the near-infrared region. The electric dipole of the Ag core, from the localized surface plasmon mode, overlaps at a similar amplitude with the optically-induced magnetic dipole characterized by the cavity mode of the dielectric shell. Also, the scattering efficiency (Figure 1.12b-d) is higher than for the bare Ag core (Figure 1.12a), indicating the existence of superscattering and low loss.

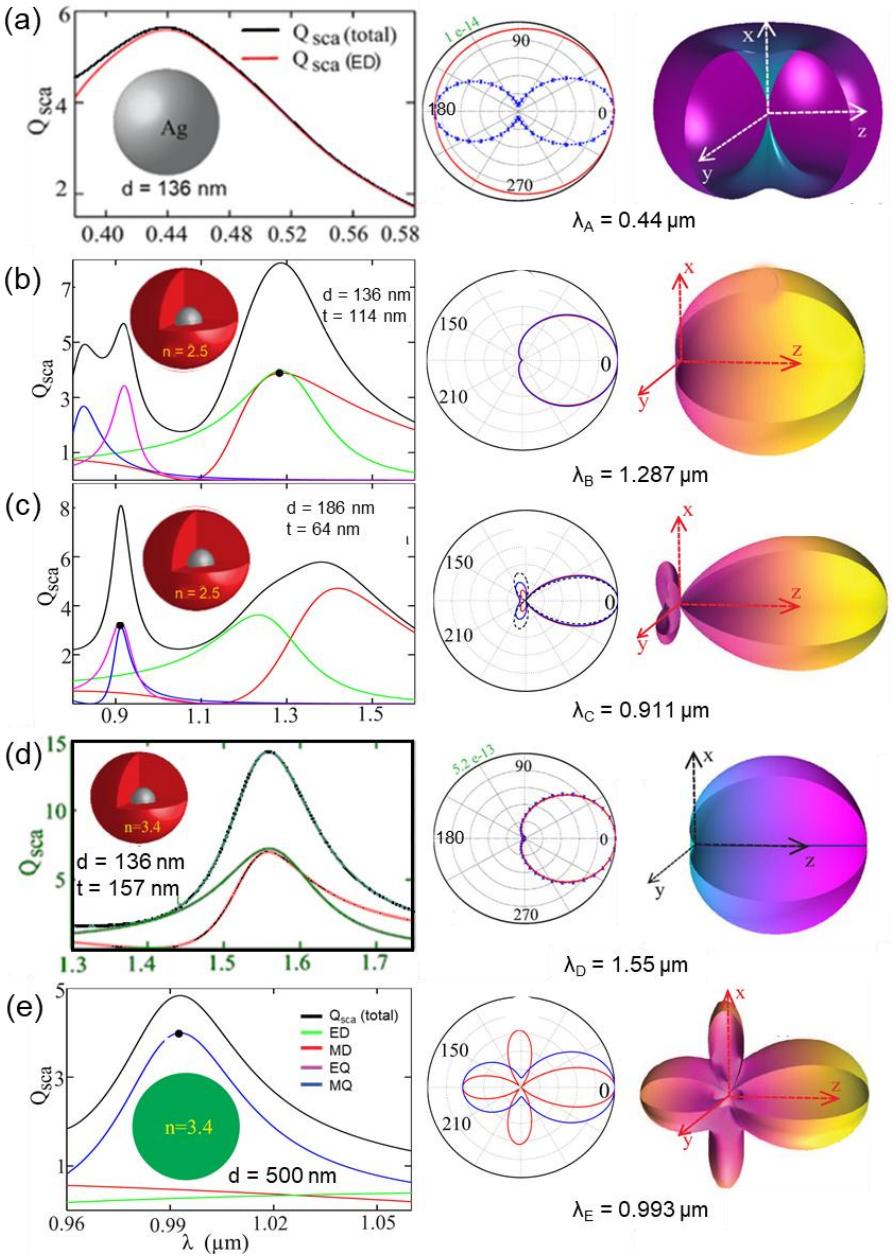



*Figure 1.12 Scattering spectra of core-shell particles showing the contribution of the multipoles, the 2D and 3D far-field scattering patterns at the overlapping resonant wavelength of the ED and MD. The incident plane wave is propagating along the z-axis. Reproduced from ref.*[67,68]

A low-refractive shell does not introduce new functions to the dielectric or plasmonic core particle. However, it has been proposed to help broaden and shift the electric dipole resonance for better overlap with the magnetic dipole. This results in better interference of both dipole resonances, which gives rise to directional light scattering. Tsuchimoto, Y., *et al.*[51,52] demonstrated that a 130 nm Si core with a 75 nm $SiO_2$ shell (Figure 1.13) displayed a forward-to-backward (F/B) scattering ratio five times higher than a bare Si particle of 130 nm diameter.

These polydisperse Si particles were prepared via laser-ablation of a Si wafer and the oxidized core-shell by the thermal oxidation method. The single particle showed very promising results, where the experimental spectra match the simulation quite well.

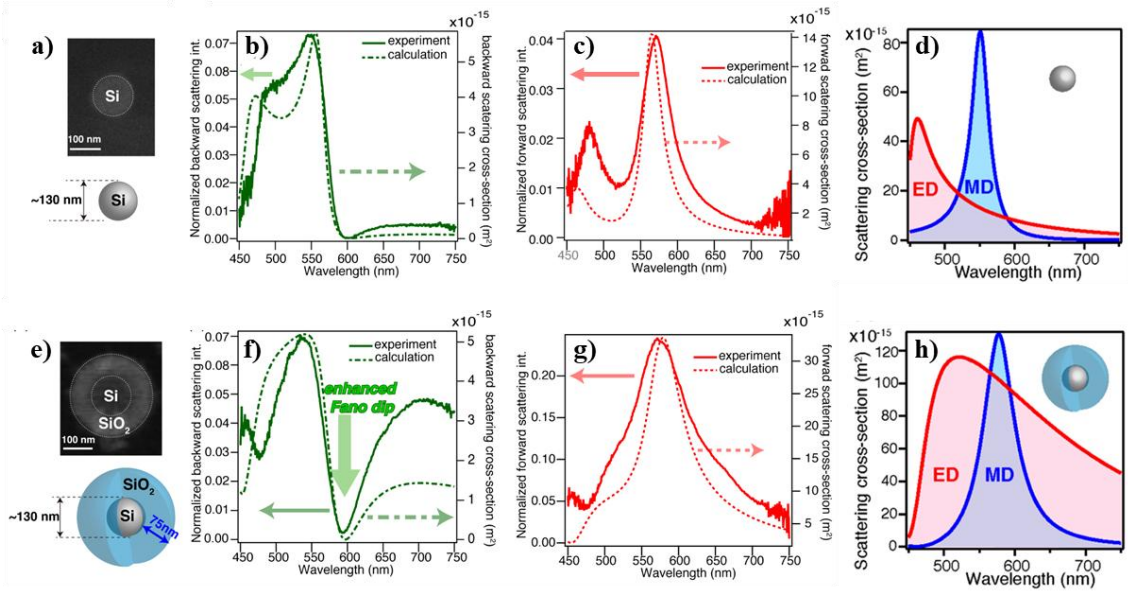



*Figure 1.13 Backward-scattering spectra (green curves) and forward-scattering (red curves). (a, e) SEM image and schematic of the Si and Si@$SiO_2$ particle. The scale bar represents 100 nm. The backward- and forward-scattering spectra of a (b, c) Si, and (f, g) Si@$SiO_2$ particle. Solid and dashed lines indicate experimental and calculated results. The scattering cross sections of ED (red curve) and MD (blue curve) components for (d) Si and (h) Si@$SiO_2$ particles. The diameter of the Si core is 130 nm, and the $SiO_2$ shell is 75 nm thick. Reproduced from ref.*[51,52]

The variation of the shell thickness between 0 – 75 nm for a fixed core diameter of 130 nm showed that the forward scattering intensity increased with the increase in shell diameter (Figure 1.14a-f). The maxima of the forward-to-backward scattering ratio were obtained at a shell thickness of ~ 60 nm. The variation of the silicon core diameter between 100 – 140 nm, at a fixed $SiO_2$ shell thickness of 75 nm, showed that the overlap of the ED and MD dipoles is optimal at a core diameter of 106 nm. Both dipolar modes redshift with increased core diameter. For the backward scattering spectra, the color maps (Figure 1.14e) indicate a yellow region at ~ 580 nm, which is attributed to the ED and MD modes. In comparison, the black region at ~ 590 nm indicates the dip originating from the Fano resonance. At wavelengths greater than 600 nm, the scattering intensity increases gradually with increasing shell thickness. The Fano dip appeared for shell thickness greater than ~ 40 nm. In the forward scattering spectra, the intensity

continues to rise with increasing shell thickness. At the wavelength of the Fano dip, the forward scattering intensity for a 75 nm shell thickness is 12-fold larger than that with no silica shell. Figure 1.14b shows the ratio of the forward- and backward-scattering intensities as a function of the shell thickness. It can be deduced that the ratio remains at a relatively similar level to that of a bare Si particle with a diameter of ~ 130 nm. A drastic increase in the scattering ratio up to $10^5$ was observed at a shell thickness of 57 nm. This means the backward scattering intensity has a minimum value of $10^{-5}$ at this shell thickness. Hence, the forward scattering is 9-fold larger than for a bare Si particle of the same diameter. Therefore, the optimum shell thickness for a core diameter of 130 nm is 57 nm, and the ratio is 5 orders of magnitude greater than that of a Si particle with the same diameter.

Figure 1.14g-i shows the influence of the core diameter on the Fano resonance. For different core diameters (106, 130, and 142 nm) and a shell thickness of 75 nm, the detuning between the ED and MD resonances' wavelengths is 42, 55, and 63 nm, respectively. This means that the detuning of the resonance wavelengths decreases in core diameter, leading to a more symmetric line shape.

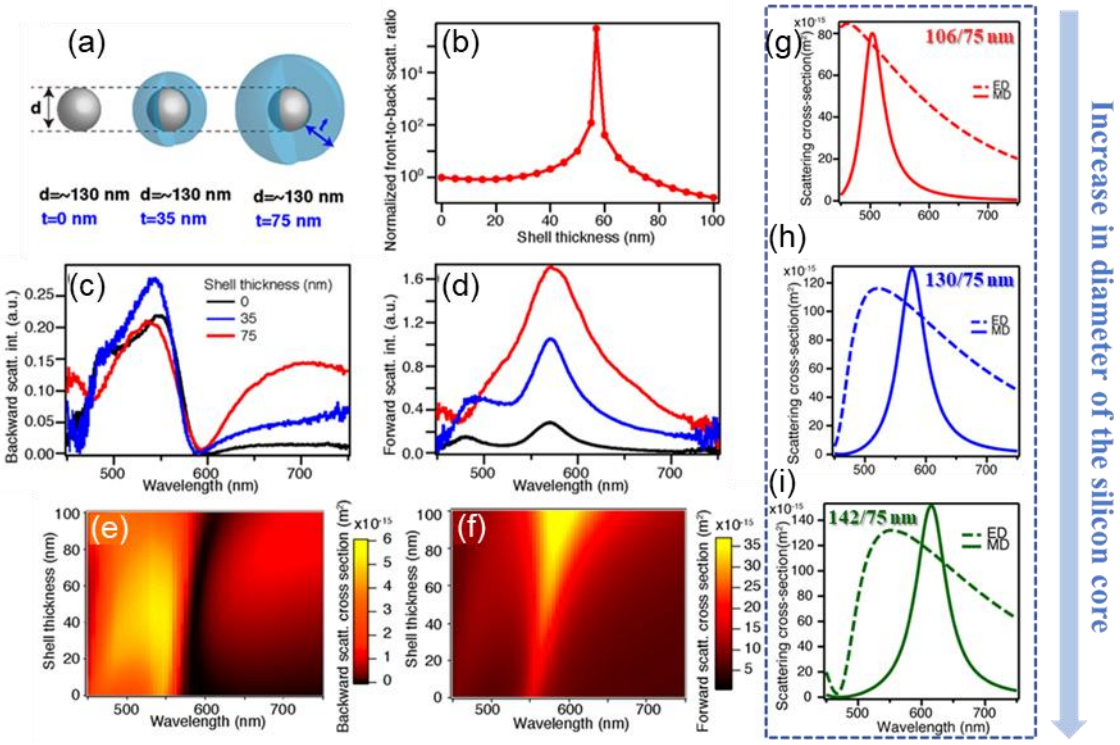



*Figure 1.14 (a) Schematics of Si@SiO₂ particles with a core diameter of 130 nm and various shell thicknesses of 0, 35, and 75 nm. (b) Front-to-back scattering intensity ratio at the wavelength of the Fano dip for the Si@SiO₂ particle with a core diameter of 130 nm as a function of shell thickness. (c, d) Backward- and forward-scattering spectra of the particles*

*illustrated in (a). (e, f) Color maps of the backward- and forward-scattering intensities from a Si@SiO₂ particle with a core diameter of 130 nm and a shell thickness ranging from 0 to 100 nm. (g–i) Calculated scattering cross-sections of the ED (dashed line) and the MD (solid line) resonances for Si@SiO₂ particles with various core diameters (106, 130, 142 nm) and a fixed shell thickness of 75 nm. The red, blue, and green lines, respectively, indicate the results for Si core diameters of 106, 130, and 142 nm. Reproduced from ref.*[51,52]

However, observing individual particles for single-particle optical scattering spectroscopy is quite difficult due to the synthesis approach, which involves the thermal oxidation of silicon particles under controlled temperature and time conditions. The shell thickness is controllable; however, there is little to no control over particle aggregation, and no straightforward synthetic pathway exists for scale-up. Hence, a new synthesis approach, preferably in colloidal solution, needs to be developed for the fabrication of the nanostructures.

Previously, within the group, a one-step batch synthesis method to produce monodisperse core-shell Si@$SiO_xN_y$ particles was reported. The method involved the decomposition of bis (N, N'-diisopropylbutylamidinato)dichlorosilane with trisilane in supercritical n-hexane using a high-pressure reactor[34]. The core size and the shell thickness are controlled by the molar ratio of the two silane precursors. The core diameter is in the range of 130 – 250 nm, and the shell thickness is in the range of 8 – 115 nm. The simulations and experimental results show that the ED and MD resonances of the particles can be superimposed by adjusting the core-to-shell ratio (Figure 1.15). The Si@$SiO_xN_y$ particles with a core diameter of 150 nm and shell thickness of 115 nm displayed three times higher scattering efficiency over a broader wavelength range in the visible region compared to bare Si particles of 150 nm diameter[53]. This makes forward scattering dominant at a specific wavelength and fulfills the conditions of a Huygens source.

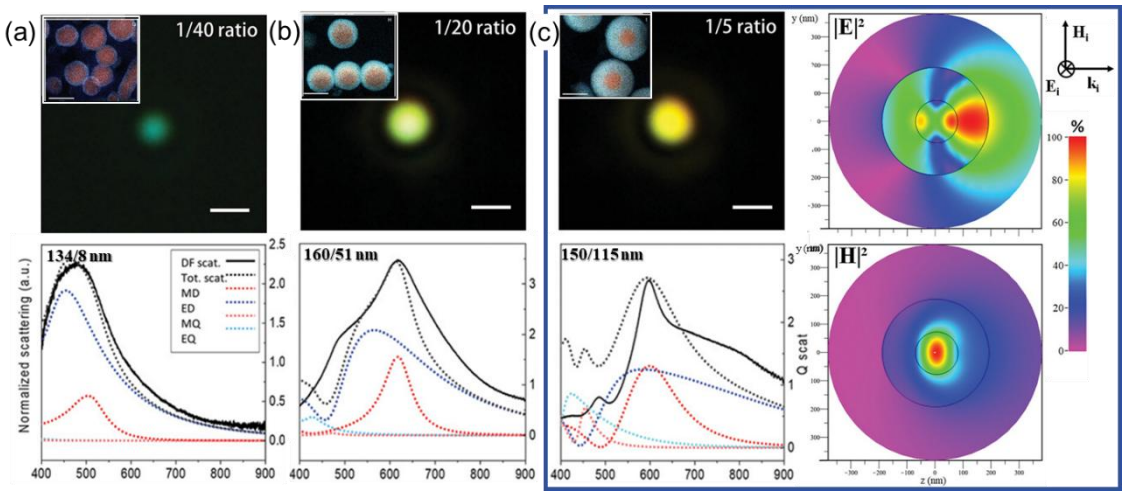


*Figure 1.15 Light scattering properties of single particles. Dark field images of a single particle: (a) Ø = 134/8 nm, (b) Ø = 160/51 nm, (c) Ø = 150/115 nm. The size of the scale bars represents 1 µm. The insets are STEM-EDX mapping of silicon particles. The scale bars represent 200 nm. Experimental (solid black line) and simulated (dotted black line) total scattering and dipolar and quadrupolar scattering (dotted colored lines), for the particles. Reproduced from ref.*[53]

For the optimum shell-to-core ratio, the forward scattering was not only more intense than the pure silicon core, but also broadband (Figure 1.16). The polar plots display the directionality and intensity of the scattering as a function of the incident wavelength. The bare silicon, indicated in red, exhibits intense, non-directional scattering at a wavelength of 500 nm, which then transitions to nearly pure backscattering at 550 nm. It then becomes very intense and non-directional by 600 nm, and subsequently weakly forward-scattering from 656 nm to 750 nm. The core-shell Si@$SiO_2$ particle demonstrates pure forward scattering from 500-750 nm. It is most intense at 600 nm. The maximum intensity of the forward scattering for the pure silicon is only half as intense as the forward scattering for the core-shell at the same wavelength. The superiority of these particles as Huygens sources is thus apparent.

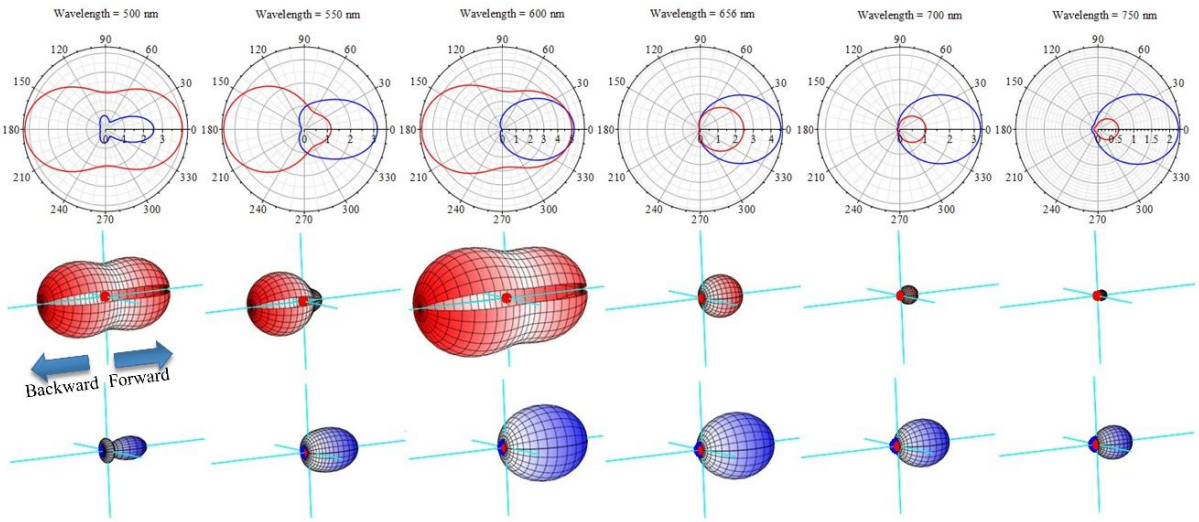



*Figure 1.16 Polar plots of the differential scattering efficiency computed for a core-shell (blue) particle with diameters of Ø = 150/115 nm and a bare silicon (red line) particle with a diameter of Ø = 150 nm. The 3D scattering diagrams of the core-shell (blue) and the bare silicon particle (red). Reproduced from ref.*[53]

## 1.7 Directional light scattering in silicon nanowires

Silicon nanowires (Si NWs) with diameters (70 nm < d < 200 nm) much smaller than the wavelength of visible light (400–800 nm) exhibit optical properties different from those of thin films[69] and spheres. The strong light scattering properties of Si NWs are related to morphology-dependent resonances that arise from their finite size, large anisotropy, and the significant refractive index contrast with their surroundings[69,70]. The intensity of the scattered light is directly proportional to the product of the illuminating light's intensity and the scattering efficiencies. The latter is dependent not only on the wavelength of the incident light, but also on the diameter of the Si NWs[71].

The directional light scattering properties of Si NWs with cylindrical cross-sectional morphology and diameters between 50 – 100 nm were demonstrated by Wiecha, P. R., *et al.*[72]. The NWs were grown in a hot-wall (450 – 650 °C), reduced-pressure (4.5 torr) chemical vapor deposition system through the vapor-liquid-solid process. Au droplets were used as catalysts on a Si (111) substrate with silane ($SiH_4$) as the precursor, diluted in hydrogen as the carrier gas. The rectangular Si NWs were fabricated by a top-down approach through electron beam lithography and subsequent anisotropic plasma etching of a transparent silicon-on-quartz wafer with a 90 nm thick Si overlayer. In Figure 1.17c and 1.17g, the Si NW with a diameter of 50 nm showed a weak directional scattering in both the forward and backward directions for Transversal Electric (TE)- and Transversal Magnetic (TM)-polarized incident light. For the largest Si NW, with a diameter of 100 nm, forward scattering dominates over a broad spectral range of 550 – 700 nm (Figure 1.17e and 1.17i). The backward scattering is stronger at wavelengths less than 550 nm. The increase in the diameter of the Si NW gave a red-shift in both the forward and backward scattering peaks, as occurs in spheres. The intensity of the signal also increases with increasing diameter. The change in the polarization of the incident light from TE to TM allows for the inversion of light scattering direction from forward to backward and vice-versa, as observed at ~750 nm for the 100 nm Si NW. Figure 1.17f and 1.17j showed the Mie theory calculation of an infinitely long Si NW as a function of the diameter. The TE-polarized light revealed that the optimal diameter for achieving maximum forward scattering over a broad wavelength range is ~100 nm, spanning 550 – 700 nm. For TM-polarized light, the optimal diameter for broadband (530 – 750 nm) forward scattering is ~150 nm, although this does not convey the intensity of the scattering[72].

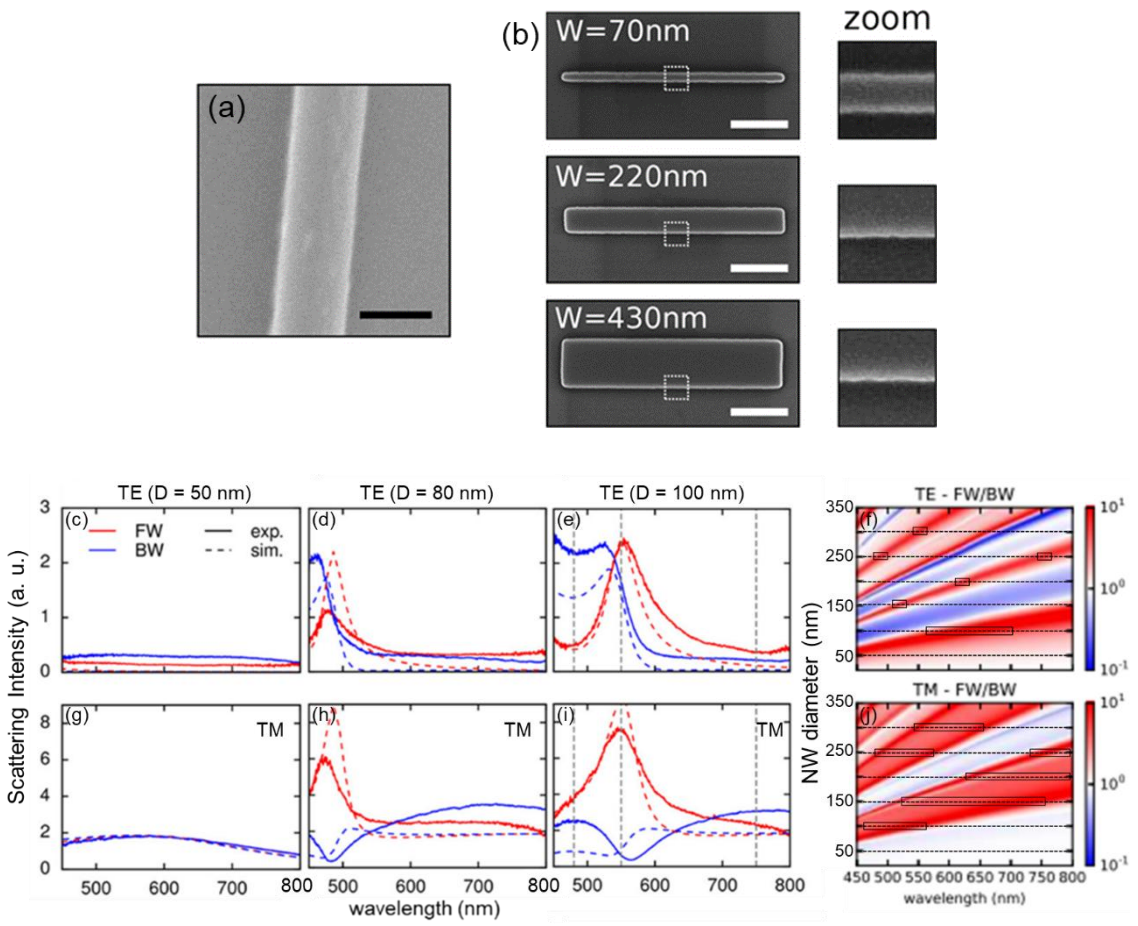



*Figure 1.17 SEM images of the (a) cylindrical (b) rectangular Si NW. (c-e, g-i) Experimental (solid lines) and simulated (dashed lines) FW/BW scattering spectra (red/blue) from cylindrical geometrical cross-section Si NWs with diameters of (c,g) 50 nm, (d,h) 80 nm, and (e,i) 100 nm. (f,j) FW/BW scattering intensities calculated with Mie theory for an infinitely long cylindrical cross-section Si NW as a function of diameter. Reproduced from ref.*[72]

A change in the morphology from a cylindrical to a rectangular cross-section fabricated through electron beam lithography produces significant differences in the directional light scattering properties. The height and length of the Si NWs were respectively fixed at 90 nm and 7 µm, while the width was varied between 60 – 330 nm. The scattering properties were investigated as a function of the changing width (Figure 1.18). The shape of the scattering curve becomes increasingly asymmetrical and more complex, exhibiting multiple peaks due to the anisotropy introduced into the cross-section. Examining Figure 1.18a and 1.18e, the 60 nm width exhibits more forward light scattering for TM-polarized light than occurs for the cylindrical cross-section of similar diameter (50 nm). In Figure 1.18b and 1.18f, the 120 nm width NW exhibits more forward scattering in both TE- and TM-polarized light than the 60 nm width. Specifically, for a 120 nm width, the forward scattering is almost entirely visible from

around 480 – 780 nm. There are relatively narrow spikes of strong forward scattering at ~750 and ~500 nm for both TE- and TM-polarized, respectively. A zone of significant backward scattering was observed only in the case of TE-polarized light at wavelengths less than ~550 nm. The FW/BW ratios in Figure 1.18d and 1.18h are dominated by intense unidirectional scattering, which occurs mostly toward the forward direction in both TE- and TM-polarized light. Hence, the change in the cross-section geometry from cylindrical to rectangular drastically enhanced the forward scattering properties of the Si NWs[72].

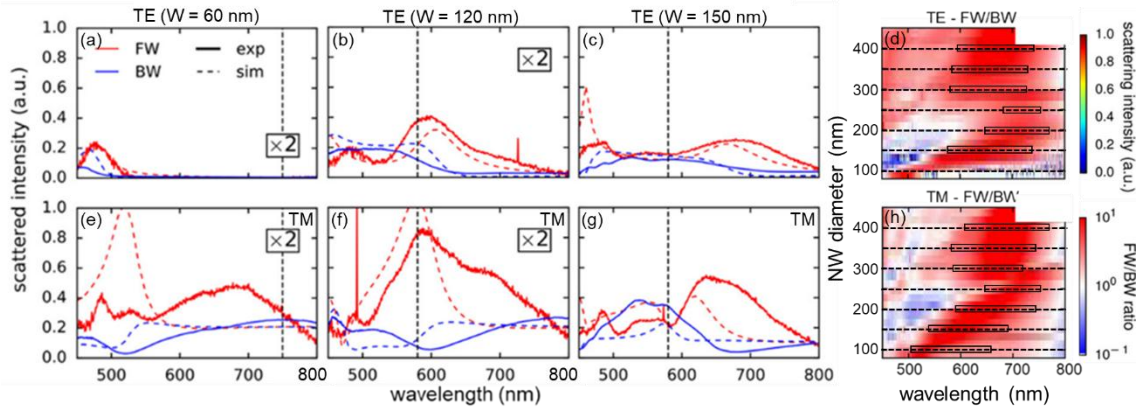



*Figure 1.18 (a-c, e-g) Experimental (solid lines) and simulated (dashed lines) FW/BW scattering spectra (red/blue) from rectangular geometrical cross-section Si NWs with a height of 90 nm and a length of* 7 µm *and different widths: (a,e) 60, (b,f) 120, (c,g) 150 nm. The top row is TE- and the bottom row is TM-polarized light. (d,h) FW/BW scattering intensities calculated with Mie theory for an infinitely long rectangular cross-section Si NW as a function of diameter. Reproduced from ref.*[72]

In summary, silicon nanowires with a symmetric cross-section (cylindrical) or an asymmetric (rectangular, elliptical, hexagonal, square, triangular) can be used to enhance directional light scattering at optical wavelengths. For cylindrical nanowires, the optimal diameter for broadband forward scattering has been reported to be in the range of 100 – 200 nm for TM-polarized light, while for TE-polarized light, the optimal diameter is in the range of 80 – 120 nm. For the rectangular cross-section reported for a fixed height of 90 nm, the optimal width for broadband forward scattering is in the range of 100 – 400 nm, for both TM- and TE-polarized light. In both geometrical cross-sections, the length of the nanowires was considered to be infinite (>7 µm) due to its little effect on the directionality of the scattered light at the optical wavelengths. Unlike in spherical particles, where forward scattering is a result of the overlapping of the electric and magnetic dipole resonances, the directionality in nanowires is a result of the interference between orders of either transverse-electric or transverse-magnetic

modes. In addition to material composition and geometry, as seen in spherical nanostructures, the polarization of light offers an additional degree of freedom in controlling the directionality of light in nanowires.

## 1.8 Growth mechanisms for silicon nanowires

Before explaining the bottom-up synthetic techniques, I will present the generalized mechanisms for the growth of silicon nanowires. The primary difference lies in the method of supplying the silicon precursor: vapor, liquid, or solid state.

### 1.8.1 Vapor-Liquid-Solid

This mechanism of Si NW growth was first reported by Wagner and Ellis[73] for the CVD growth of Si NWs. The concept is that the Au catalyzes the reduction of a silane precursor on its surface, forming an alloyed particle (Figure 1.19). The necessary reaction temperature is determined by the eutectic point of the metal-Si and the thermal degradation of the Si precursor. The eutectic is a mixture of two elements at such proportions that its melting point is at the lowest possible temperature, much lower than the melting point of either of the two elements that compose it. For example, Au melts at a temperature of 1063 °C, while silicon melts at 1414 °C. However, the eutectic temperature for these two elements is 359 °C. To achieve a melting temperature as low as possible, the two elements have to rearrange so that they reach a favorable relative concentration. From the phase diagram of Au-Si, the AuSi alloy must contain 18% Si and 82% Au to reach the liquid state at the lowest possible temperature.

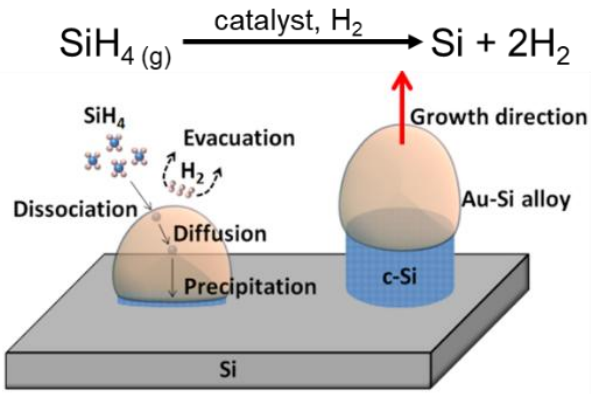



*Figure 1.19 Schematic illustration of the vapor-liquid-solid growth mechanism. Reproduced from ref.*[74]

The role of the metal is to form a liquid solution for the vapor-phase absorption of the Si atoms[75]. This then serves as the preferred site for Si precursor vapor deposition due to its higher sticking coefficient than solid surfaces[76]. The metal liquid droplet becomes supersaturated with

Si atoms due to the continuous gas phase supply of the Si precursor. The precipitation of a crystalline Si seed occurs on the vapor-solid-liquid boundary line after a certain period of crystalline-seed formation. This is located at the interface between the metal catalyst and the substrate[77]. Thereafter, the Si atoms preferentially diffuse towards the formed crystalline Si seed. This is because less energy is needed for crystal growth as compared to secondary nucleation. Therefore, growth is obtained as a steady-state condition between the Si flux and the precipitation of Si on the substrate. This growth occurs at an atomic level in a layer-by-layer approach through a step-flow mode[78]. The Si NW crystal growth continues in length by this mechanism until the metal catalyst is consumed or the growth conditions are changed[77].

### 1.8.2 Solution−Liquid−Solid and Supercritical Fluid-liquid-Solid

Similar to the vapor-liquid-solid growth mechanism in the gas phase is the solution−liquid−solid and supercritical fluid−liquid−solid mechanism. The growth occurs in solution or in the supercritical state rather than in the gaseous phase (Figure 1.20). The growth process involves the decomposition of a Si-rich reactant to form Si, which then forms a eutectic phase with the metal seed and subsequently crystallizes to form a silicon nanowire[79].

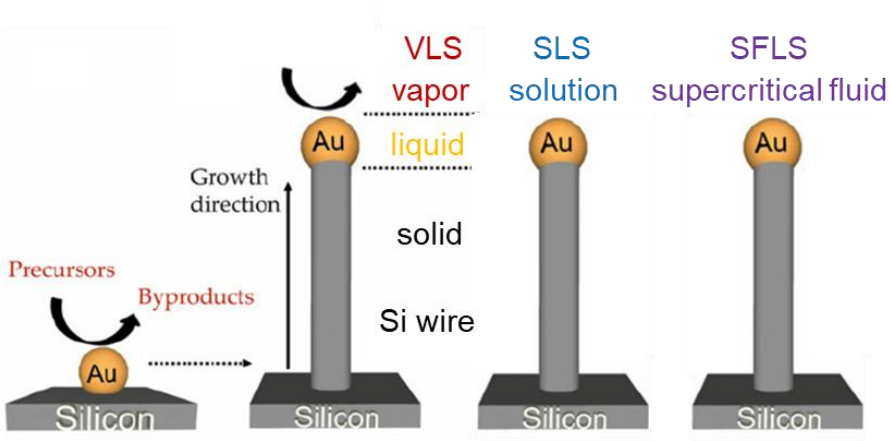



*Figure 1.20 Schematic illustration of different growth mechanisms depending on the nature of the Si precursor. Modified from ref.*[79]

### 1.8.3 Solid-Liquid-Solid

The solid-liquid-solid mechanism of Si NWs growth involves the activation of the lateral in-plane growth by an increase in temperature while maintaining the system in a reactive gas-free environment. The direction of growth is opposite to the out-of-plane growth in the vapor-liquid-solid, solution-liquid-solid, and supercritical fluid−liquid−solid mechanisms (Figure 1.21). One of the earlier reports of the in-plane solid-liquid-solid growth of Si NWs was by Yu,

L., *et al.*[80]. This growth mechanism can be perceived as a nano-liquid-phase epitaxy[81] process or nanoscale metal-induced crystallization[82].

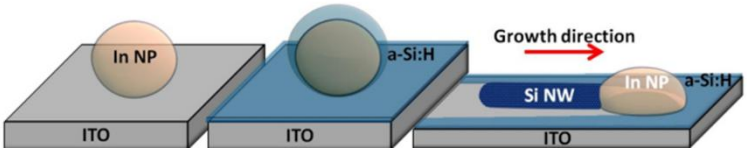



*Figure 1.21 Schematic illustration of the solid-liquid-solid growth mechanism of Si nanowires. Reproduced from ref.*[83]

### 1.8.4 Vapor-Solid-Solid

In the vapor-solid-solid mechanism, the exposure of the metal particles to the vapor phase of the Si precursor results in the formation of a silicide phase. The solid-state silicide phase is expected to form at temperatures as low as ~ 0.35× the eutectic temperature. In the presence of excess reduced Si atoms, the solid Si crystallized at the interface with the silicide because this is energetically favorable. Hence, the significant supersaturation of the catalyst that drives VLS growth may not be required for the VSS growth mechanism, and the solid metal catalyst may not experience the instabilities that lead to branching and diameter changes in VLS. The diffusion of atoms on or through the metal particles, followed by Si atom incorporation at the metal/Si interface, results in nanowire growth[84]. The VSS growth mechanism for Si NWs was first reported by Kamins, T. I., *et al.*[85] for $TiSi_2$-catalyzed Si NWs. The particles at the tip of the Si NWs are $TiSi_2$ and not elemental Ti particles. The VSS growth process has the advantage of growth at much lower temperatures, which is beneficial when a low fabrication temperature is required. In addition, the incorporation of impurities, such as metal catalysts, in the nanowires may be reduced due to the reduction in atom diffusion and solid solubility associated with the lower temperature[86].

## 1.9 Growth techniques for silicon nanowires

Various growth methods for Si NWs have been developed, which can be categorized into top-down (e.g., metal-assisted chemical etching, electron-beam lithography) and bottom-up (e.g., chemical vapor deposition, thermal decomposition in high-boiling-point solvents, and supercritical fluid) approaches. The choice of a growth approach depends on the application, the intrinsic capabilities, and the limitations of the technique. Additionally, it depends on the overall quality of the nanowires and the ability to scale-up the technique. However, the most popular and often successful technique is the metal-assisted growth, which enables control over both the nucleation process and the diameter of the nanowires[87]. More specifically, to the best

of our knowledge, metal-assisted chemical etching is commonly used for the top-down approach, while chemical vapor deposition is widely used for the bottom-up approach. The top-down approach provides control over dimensions, enabling the creation of tailored designs through lithography and etching. One of the advantages of this approach is the preservation of the single-crystalline structure of the Si substrate in the nanowires. In the study of the optical properties of Si NWs, parameters such as size and shape monodispersity, porosity, and defects (such as kinking) must be controlled. Therefore, in this section, metal-assisted chemical etching (MACE) will be used as a benchmark for comparison in the fabrication of SiNWs for optical properties studies. The various bottom-up growth techniques, along with their specific advantages and disadvantages, will be examined.

### 1.9.1 Metal-assisted chemical etching (MACE)

Metal-assisted chemical etching is a wet chemical etching of a Si substrate in the presence of metal catalysts, where silicon etching is selectively in the regions in contact with the metal, typically used to pattern a substrate. This is usually at room temperature, and no metal contamination is observed in the final nanostructures. Li, X., *et al*.[88] was the first to demonstrate this method for the fabrication of porous silicon by etching an aluminum-covered Si substrate in a solution of HF, $HNO_3$, and $H_2O$. The chemical etching reaction occurs at the interface between the Si substrate and the metal. The proposed mechanism for etching involves generating holes due to the reduction of the oxidizing agent on the surface of the metal catalyst. These holes directly penetrate the silicon substrate below the metal, resulting in the oxidation of Si to $SiO_2$. In the presence of HF, the silica rapidly dissolves as $SiF_6$ into solution. This mechanism is responsible for the directional etching of the Si substrate. The process of etching the Si substrate with HF and $H_2O_2$ is shown in Figure 1.22h.

A typical metal-assisted chemical etching process involves a Si substrate partially covered with a noble metal, which is then subjected to an etchant composed of HF and an oxidative agent. The Si beneath the metal gets oxidized and etched much faster than the Si without metal coverage. Therefore, the metal sinks into the Si substrate, generating either pores or Si wires on the substrate[89]. The geometries of the Si nanostructures depend on the initial morphology of the metal coverage. Metals such as Au, Ag, Cu, and Pt are the most frequently used catalysts, which can be deposited on a Si substrate through various methods, including thermal evaporation, sputtering, electron beam evaporation, electroless deposition, electrode deposition, focused-ion-beam-assisted deposition, or spin coating metallic particles[90–96]. The physical vapor deposition methods (thermal evaporation, sputtering, and e-beam evaporation) are the most

common for obtaining patterned structures because the morphology of the metal film can be more easily controlled. Various oxidative agents have been mixed with HF to etch the Si substrates. These include $H_2O_2$, $AgNO_3$, $KAuCl_4$, $K_2PtCl_6$, $H_2PtCl_6$, $Fe(NO_3)_3$, $Ni(NO_3)_2$, $Mg(NO_3)_2$, $KMnO_4$, and $K_2Cr_2O_7$. The metal ions in the oxidative agents are reduced to particles, dendrite structures, or a film, depending on the etching time, parallel to the oxidation and dissolution of the Si substrate[89].

Wendisch, F. J., *et al.*[97,98] fabricated large-scale homogeneous SiNWs through colloidal lithography and metal-assisted chemical etching (MACE). Through this approach, a wide range of diameters (120 – 1050 nm) and lengths up to ~ 10 μm can be achieved. A monolayer of colloidal spherical polystyrene or $SiO_2$ core-PNiPam shell (PNiPam: poly(N-isopropylacrylamide)) particles of a specific diameter transferred onto the Si substrate, either by spin coating or Langmuir-Blodgett (LB) trough, is used to determine the morphology and diameter of the fabricated SiNWs. The latter was also controlled by the plasma or oxygen etching time, which was used to reduce the particle sizes or shrink the particles to obtain hexagonally non-close-packed particle arrays. Figure 1.22b-e shows the SEM images of SiNWs with diameters between 63 – 118 nm as a function of the etching time with KOH solution. The diameter of the NWs varied from top to bottom by ~ 10% with the top section having the smaller diameter. Figure 1.22f shows that the diameter of the NWs decreases with increased KOH etching time. Figure 1.22g shows that the minimum reflectance minima redshift with an increase in the NW diameter from 63 – 118 nm. For NWs with diameters of 63, 77, 87, and 118 nm (Figure 1.22b-e), light transmission is maximum at wavelengths of 390, 440, 525, and 585 nm with measured reflectance values of 4.3, 3.8, 9.4, and 13.7%, respectively (Figure 1.22g).

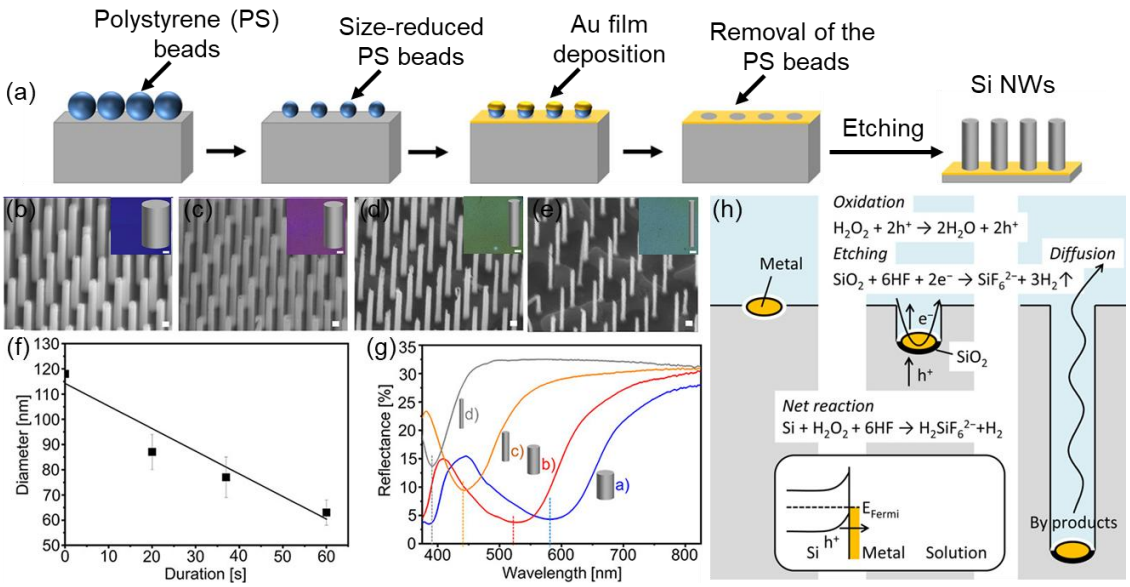


*Figure 1.22 (a) Synthesis of SiNW arrays through MACE and colloidal lithography. SEM images of the SiNWs with a diameter of (b) 118 nm, (c) 87 nm, after 20 s (d) 77 nm, after 40 s, and (e) 63 nm after 60 s of KOH etching. The scale bars represented 100 nm. The inset is the optical microscopy images of the SiNW arrays. The scale bars represented 100 μm. (f) The plot of the SiNW diameter as a function of KOH etching time. (g) The reflectance spectra of the SiNW arrays. (h) The mechanism for the chemical etching of the Si substrate in HF/$H_2O_2$. Reproduced from ref.*[97,98]

The type of metal affects the morphology of the etched structures. Typically, straight pores are formed if isolated Au or Ag particles are used as a catalyst for etching the Si substrate[89]. The concentrations of the $H_2O_2$ and HF affect the etching rate and morphologies of the etched structures. Chartier, C., *et al.*[99] reported that at a relatively high percentage concentration of HF, the etching rate was almost entirely determined by the concentration of $H_2O_2$, and nearly all holes generated at the Si/Ag interface at the pore tip were locally consumed because there was sufficient HF available to dissolve $Si/SiO_x$. At a high $H_2O_2$ concentration, hole diffusion was significant, and the diffused holes came to every exposed surface of the Si substrate. Therefore, oxidation and dissolution of Si occurred everywhere, and the etching was isotropic and independent of the location of Ag particles, resulting in a polished surface. When the ratio of HF concentration to total concentration is less than 70%, the etching rate is determined by the HF concentration. The consumption rate of the holes could diffuse away from the tip to the side wall of the pore. Therefore, microporous Si is formed on the side wall of the pore.

Compared to other bottom-up approaches that will be discussed, metal-assisted chemical etching offers the potential for easy scalability, low cost, and the ability to create ordered and disordered arrays of vertically oriented nanowires, as well as control of the cross-section morphology. Although when not properly optimized, the metal etching mask can bend, break, and delaminate during etching, leading to macroscopic areas where the substrate is not uniformly etched.

### 1.9.2 Chemical vapor deposition (CVD)

CVD is a method for depositing vapor-phase components onto a solid material. The CVD growth of Si NW from a metallic particle has been widely used due to its simplicity and versatility. The first step involved the deposition of metal (e.g., Au[74]) in the form of particles or a thin film on a substrate (e.g., a Si wafer[100] or stainless steel). Thereafter, a molecular silicon precursor in a gaseous state is introduced into the reactor using a carrier gas, while the system is heated to a specified temperature. When a halogenated (*e.g.,* $SiCl_4$[74]) precursor is used, a

reducing carrier gas (Ar + 5% $H_2$[75]) is employed to form $SiH_4$ *in-situ*. Typically, CVD is used to create thin films and nanowires by selecting silane precursors and a metallic substrate. CVD offers a high degree of control over material characteristics and architectures. It was first applied to fabricate Si NWs by Wagner, R. S., *et al.*[73] via the thermal decomposition of a gaseous mixture of $SiCl_4$ and $H_2$ on the surface of a (111) Si substrate coated with Au particles at 950 °C. As earlier stated, the precursor nature and the temperature of the eutectic phase formation usually determine the annealing temperature. The chlorine-substituted silanes are more chemically stable and require higher temperatures to decompose than hydrogenated silanes[100]. Hence, the CVD method can be divided into two classes based on the reaction temperature:

### Low-temperature CVD:

The low-temperature CVD usually occurs between 400 – 600 °C with the hydrogenated Si precursors such as monosilane ($SiH_4$) and disilane ($Si_2H_6$)[101,102]. Hydrogenated silane decomposes at ~ 350 °C. Therefore, the growth of nanowires that use an Au metal occurs within the Si-Au eutectic temperature range (360 – 700 °C)[103]. These reactions are carried out at a low pressure or ultrahigh vacuum environment, and cold-wall reactors using different metal catalyst particles (Figure 1.23a). Wang I.T., *et al.*[102] carried out the growth of Si NWs through the VLS growth mechanism on a (111)-oriented hydrogen-terminated Si wafer using Au film with a thickness of 0.8 nm as catalyst material. The Si precursor (disilane) is supplied at a flow rate of 10 sccm into a chamber with a pressure of $1.0 \times 10^{-4}$ torr (system base pressure of $10^{-9}$ torr). The growth temperature is 450 °C, and the sample is annealed for a period of 1h. The Si NWs produced have a length of 1.0 – 1.5 µm and a width of 40 – 80 nm. The cross-sectional shape of the wires is truncated-triangular with a rough sidewall surface attributed to precipitated Si atoms from Si-Au liquid droplets.

Chan, C. K., *et al.*[104] used a 2% silane gas in a carrier gas of Ar (98%) and a stainless-steel substrate coated with Au particles of 50 – 75 nm in diameter. The reaction temperature is 530 °C, with a precursor flow rate of 80 sccm, and a chamber pressure of 30 torr. The difference to the previously discussed method is the use of Au particles instead of an Au thin film, which enables better control of the diameter of the nanowires. Hainey, M., *et al.*[105] also used silane gas as a Si precursor in a low-pressure chemical vapor deposition process. However, the metal was changed to a 10 nm aluminium-coated Si (110) substrate, whose immediate effect is to change the growth temperature to 550 - 575 °C due to the eutectic temperature of Al-Si (577 °C) (Figure 1.23b-c). The diameter of the nanowires ranges from 100 – 230 nm with an average

length of ~ 9 μm at a growth temperature of 550 °C. Lastly, it was observed that the increase in reaction pressure (> 300 torr) improved the Si nanowire yield by suppressing vapor-solid film wire deposition on the sidewalls during growth, which promoted wire kinking[105].

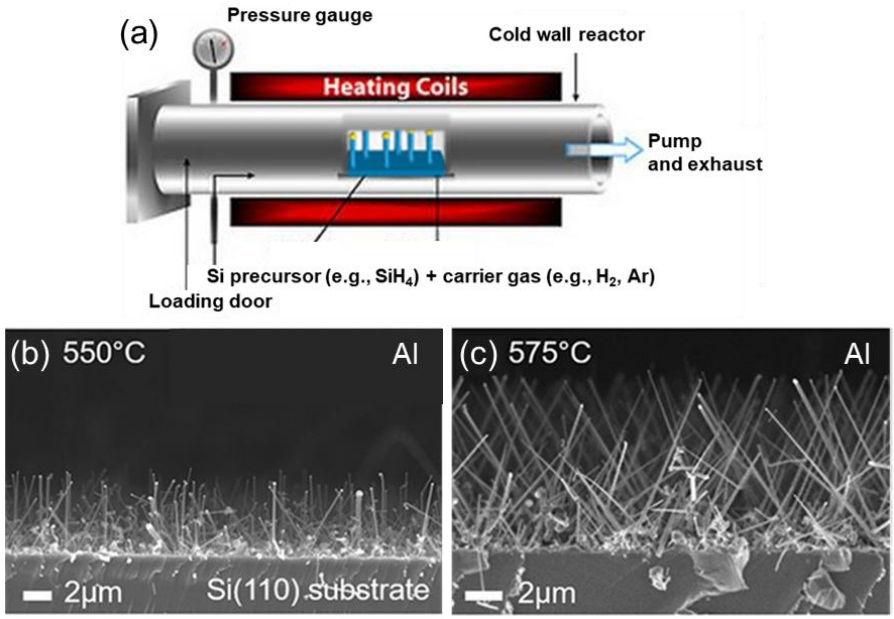



*Figure 1.23 (a) Schematic diagram of the CVD fabrication of Si NWs at low pressure. (b-c) SEM images of the Si NWs as a function of growth temperature. Reproduced from ref.*[104,105]

### High-temperature CVD:

High-temperature CVD occurs between 800 – 1000 °C, using more chemically stable Si precursors such as dichlorosilane ($SiH_2Cl_2$) and tetrachlorosilane ($SiCl_4$). The chemical stability of these precursors affects the choice of metal catalyst, as some metals evaporate below this temperature range. The reactions are usually carried out at atmospheric pressure (760 torr) and in hot-wall reactors (Figure 1.24a). The Si precursor is supplied into the reactor by a carrier gas ($H_2$ or a mixture of $H_2$/inert gases, such as Ar or $N_2$). Once the precursor is delivered to the hot region of the reactor, it decomposes to Si, which then preferentially dissolves in the metal droplet. Wagner, R. S., *et al.*[73] reported the fabrication of Si NWs via the thermal decomposition of a gaseous mixture of $SiCl_4$ and $H_2$ on the surface of a (111) Si substrate coated with Au particles at 950 °C (Figure 1.24b). The Si wires were ~100 nm in diameter in the presence of ~ 100 nm liquid Au droplets. Hence, the diameter of the wire was dependent on that of the catalytic metal particles. The growth mechanism was reported to be a vapor−liquid−solid (VLS) process.

Linh, Q. L., *et al.*[106] used different sizes of platinum (Pt) particles (17, 27, and 72 nm) to grow crystalline, long, and dense Si wires (diameter = 126 ± 52 nm, 223 ± 119 nm, and 261 ±

98 nm, respectively) at temperatures between 800 – 1000 °C for a reaction period of 15 min (Figure 1.24c). The wires produced with Pt NPs ~ 17 nm had a growth rate ~ 7 times faster than the rates of the other two sizes of Pt particles. The mechanism of growth was hypothesized to be VLS. The Pt particles at the tip of the wires are spherical with smoother surfaces, and the nanowires have few defects. On the contrary, the wires from the other two sizes of Pt NPs have more defects (such as kinks, twinning, and dislocation), and the growth mechanism was hypothesized to change to a VSS, with the Pt particles having faceted surface morphology. There is a transition in the growth direction observed between the wires grown using the Pt NPs with sizes of ~ 17 nm and those of 27 – 72 nm[107,108]. This is attributed to the interplay between the liquid catalyst-solid Si wires interfacial energy and the surface energy of Si wires[74]. This transition diameter is ~20 nm for an Au-catalysed vapor-liquid-solid growth[75,76].

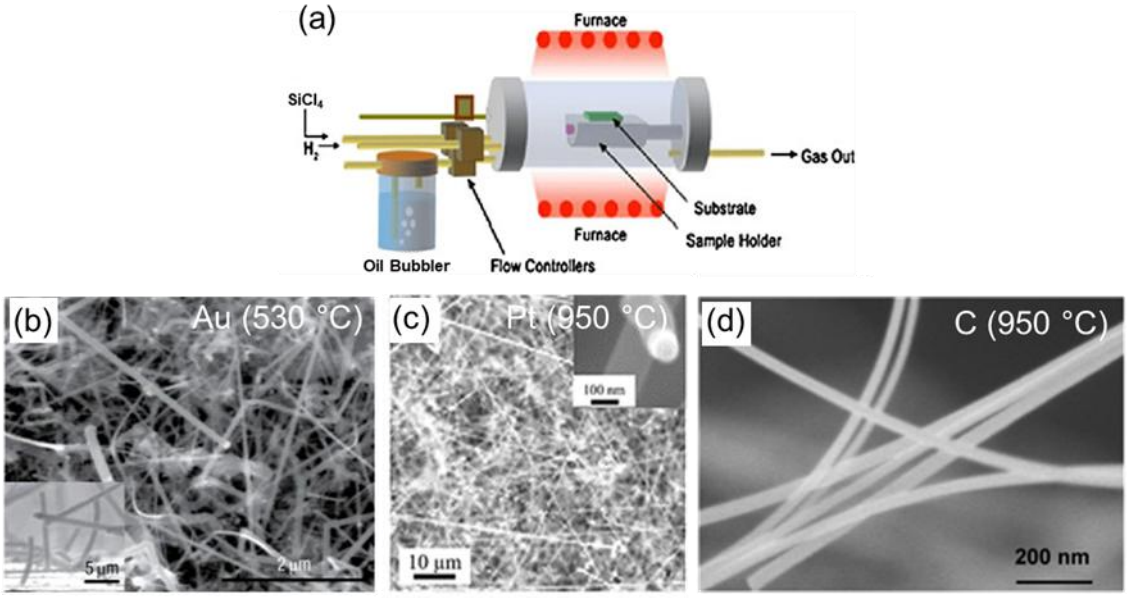



*Figure 1.24 (a) Schematic diagram of the high-temperature CVD growth of Si NWs. SEM images of the Si NWs fabricated with (b) Au particles at a minimum temperature of 530 °C, (c) Pt particles at a minimum temperature of 900 °C, and (d) carbon microbeads at a minimum temperature of 950 °C. Reproduced from ref.*[77,106,107]

Li, W. N., *et al.*[77] reported a *''catalyst-free''* growth of Si nanowires with an average diameter of ~ 50 nm and several micrometers long at a temperature of 950 – 1100 °C (Figure 1.24d). A mixture of 2.5% $SiCl_4$, carried by pure $H_2$, was used as a Si precursor, and mesophase carbon microbeads served as a substrate. After a 60 mins reaction period at 1000–1100 °C, high-density wires with lengths of several micrometers were formed. In contrast, a small fraction of wires was deposited over the substrate when the reaction was carried out at 950 °C.

The diameters and yields of the wires increase with temperature, resulting in round tips at the end of the wires. A more extended reaction period results in a higher yield and a larger diameter of Si wires from 26 to 46 nm, with increased worm-like structures observed after 10 min, in contrast to the long-straight structures after 60 min. The crystallinity of the wires increased with higher reaction temperatures.

The report of catalyst-free growth might not be entirely accurate, as the carbon microbeads could be acting as a catalyst. The carbon microbeads were reported to act as both a reducing agent and a substrate. However, the eutectic temperature of C-Si (~ 2500 °C) is relatively higher than the nanowire growth temperature. Also, the average diameter of the carbon microbeads (~ 6 μm) is much larger than the diameter of the nanowires (50 - 100 nm). To the best of our knowledge, the reports on this approach did not mention the growth of Si NWs without the carbon microbeads. The use of $SiH_4$ (diameter of Si NWs is 10 nm) yields much thinner nanowires than $SiCl_4$ (diameter of Si NWs is 50 – 100 nm).

### 1.9.3 Plasma-enhanced chemical vapor deposition

In a plasma-enhanced CVD growth, a plasma is used to pre-dissociate the precursor, which is then transported to the substrate and catalyst material. An advantage of this approach over conventional CVD is that it broadens the choice of metal catalysts that can be use compared to available materials used in conventional CVD, such as indium[109]. Iacopi, F., *et al.*[110] reported using indium and aluminum liquid precursors as metal catalysts with $SiH_4$ as precursor gas, mixed with Ar and/or $H_2$ carrier gas in a plasma-enhanced CVD growth of Si NWs (Figure 1.25a). The plasma exposure was performed *in-situ* with growth at the annealing temperatures. Indium and aluminum nanoparticles with a diameter range of 40–80 nm were deposited on a Si (001) substrate. The growth of Si NWs was observed at 500 °C for indium catalysts, with an increase in the quality (such as higher wire density, more regular shape, and free of kinks) when the temperature was increased to 600 °C (Figure 1.25b). Aluminum catalysts are not active at 500 °C, and only limited growth was observed at 600 °C (Figure 1.25c). The failure to produce Si NWs with aluminum could be due to the high Al-Si eutectic temperature of 577 °C. Hence, the Aluminum is not active at the annealed temperatures of 500 – 600 °C (Figure 1.25d). On the other hand, Indium is a low-melting point metal, and the eutectic temperature of the In–Si binary system coincides with the melting temperature of indium, which is around 157 °C. Figure 1.25e shows that the yield of the Si NWs could be improved when an Al catalyst is used by adding $H_2$, which decreases the deposition rate of amorphous Si. This allows more time for the solid particle to reach the necessary Si concentration to form a supersaturated liquid alloy. The

nanowire diameter corresponds to the diameter of the Indium particles (40 – 80 nm), with lengths of several micrometers. The Si NWs obtained by this method are monocrystalline, appear regular in shape, and are free of kinks. However, twinning defects are observed.

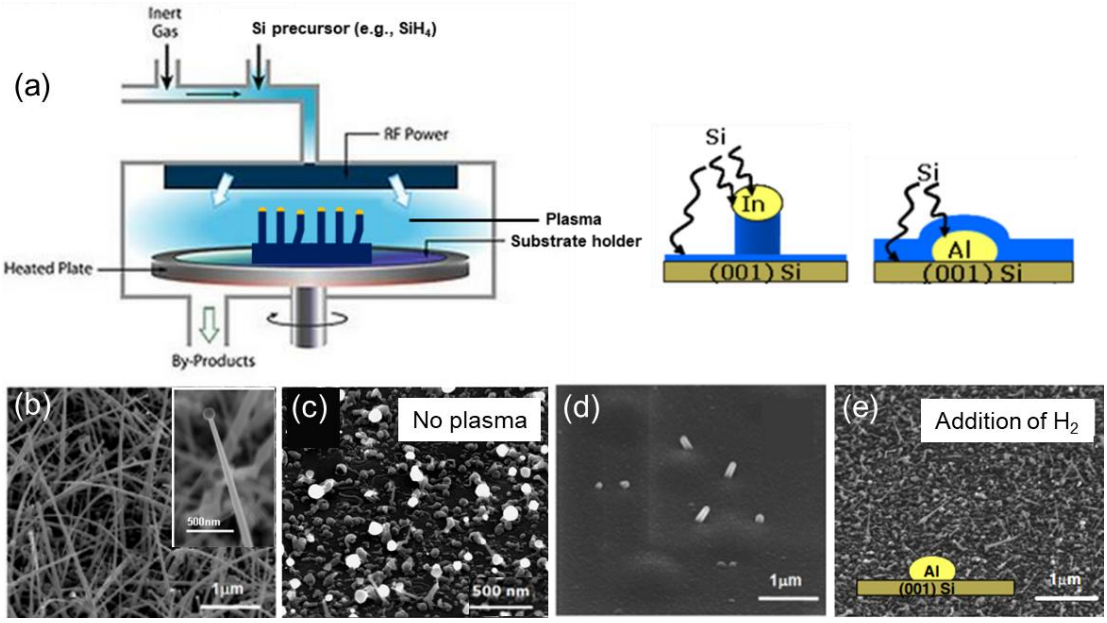



*Figure 1.25 (a) Schematic diagram of plasma-enhanced CVD growth of Si NWs. SEM images of the Si NWs fabricated with In catalyst at 600 °C with (b) plasma treatment, (c) no plasma treatment. SEM images of the product from Al catalyst at 600 °C with (d) plasma treatment, (e) addition of $H_2$ gas. Reproduced from ref.*[109,110]

### 1.9.4 Supercritical fluid decomposition of silicon precursor

In this approach, a Si precursor decomposes in a supercritical fluid rather than a gas or liquid medium (Figure 1.26a). The process of applying pressure to the solvent raises the reaction temperature beyond the metal/Si eutectic temperature[111,112]. At high Si precursor and metal particle concentrations, diffusion coefficients approach those of a gas phase, enabling fast nanowire growth rates. Lu, X., *et al.*[112] reported the degradation of diphenylsilane in supercritical cyclohexane at 500 °C and 24.1 MPa, which is above the solvent critical point ($T_c$ = 281 °C; $P_c$ = 4.1 MPa) and the Si/Au eutectic temperature of 363 °C. The nanowire diameter corresponds to the diameter of the Au particles (5 – 30 nm), with lengths of several micrometers. The reactions were carried out in both the batch and flow reactors. In the batch reactor, at a constant temperature of 500 °C and a diphenylsilane concentration of 0.9 M, straight Si nanowires with a length of several micrometers and Si nanoparticle by-products were observed. Lowering the diphenylsilane concentration results in a decrease in the amount of Si nanoparticles, but in turn shortens the nanowire length and forms a tortuous morphology due to

defects in the crystal lattice. The variation in temperature (400 - 450 °C) at a specific diphenylsilane concentration also resulted in a decrease in Si nanoparticles and more tortuous nanowires. In the flow reactor, the formation of Si nanoparticles increased at higher reactant flow rates. Thus, it seems necessary to carefully control the Au:Si precursor ratio and their absolute concentrations.

The role of Si precursor has been investigated with different precursors, including trisilane, diethylsilane, tetraethylsilane, phenylsilane, diphenylsilane, and octylsilane at 450 – 500 °C, 7.2 MPa, supercritical hexane, and the presence of dodecanethiol-coated Au NCs (~ 4 nm)[113]. In the supercritical system, the Si-Si bonds are very stable at 450 – 500 °C. The substitution of the solvent from cyclohexane to hexane has been studied because the dehydrogenation of trisilane formed a Si trimer, which does not dissolve in the Au catalyst. The Si-H bond is relatively reactive and labile. The homolytic cleavage of the alkyl Si-C bond is too slow to provide sufficient Si atoms for the Au catalyst to sustain crystalline nanowire growth. Instead, micrometer-sized amorphous Si colloids were produced[114]. Diethylsilane produced curly amorphous wires at 450 °C (Figure 1.26d). The more stable tetraethylsilane does not decompose below 500 °C, with only amorphous particulates formed (Figure 1.26e). At 350 °C, the aryl silanes of phenylsilane and diphenylsilane yielded no significant solid products. In the reactions carried out at 400 °C, only poorly defined particulate materials were formed. This was attributed to the slow precursor-degradation kinetics, which limit the Si NWs growth at temperatures just above the Au/Si eutectic temperature. At 500 °C, phenylsilane produced NWs with a relatively high proportion of carbon-containing amorphous Si by-products (Figure 1.26g). The NWs formed by using diphenylsilane are crystalline with a diamond cubic structure and few defects (Figure 1.26f). With octylsilane, there is an extremely low yield of crystalline Si NWs with large amounts of oligomeric silicon- and carbon-containing impurities (Figure 1.26b). The growth direction of nanowires is predominantly (111), although a few NWs with (110) or (112) orientations were observed with a diameter of less than 10 nm. In each of the reactions, the Au/Si molar ratio was 1:1000 with 5 min reaction time[113].

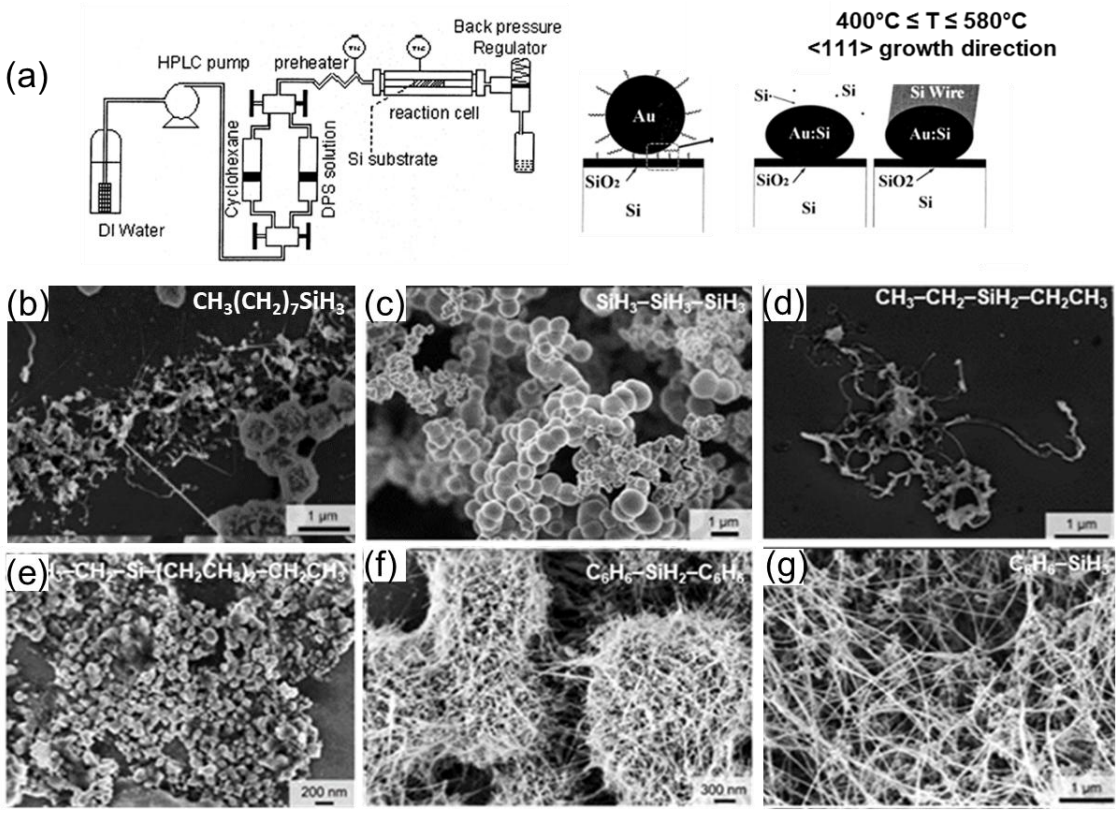



*Figure 1.26 (a) Schematic diagram of the supercritical fluid setup for the growth of Si NWs. (b-g) SEM images of Si NWs fabricated using Au metal catalyst and different Si precursors. Reproduced from ref.*[113]

Summarily, the aryl silanes (phenylsilane and diphenylsilane) are effective precursors for the growth of crystalline Si nanowires by Au-nanocrystal-seeded supercritical fluid-liquid-solid. In contrast, alkyl silanes (diethylsilane, tetraethylsilane, and octylsilane) and trisilane are not good precursors. The quality of the Si product is related directly to the decomposition chemistry of the precursor. The precursor must be sufficiently reactive to saturate the Au-nanocrystal seeds with Si atoms and promote nanowire growth, but not so reactive that homogeneous particle nucleation and sidewall deposition overcome the metal-particle-directed crystallization.

The role of different aromatic solvents, such as benzene, toluene, and hexane, for phenylsilane at 460 °C and 6.9 MPa in the presence of dodecanethiol-capped Au catalyst was investigated[115]. In benzene, 63% of the Si precursor was converted to nanowires, 38.4% in toluene, and 1.4% in hexane. The reaction yield in toluene possessed the most amorphous and particulate by-products. It was proposed that benzene better stabilizes the intermediate species involved in the homogeneous bimolecular disproportionation of phenylsilane to enhance phenylsilane decomposition relative to hexane. The atomic conversion of phenylsilane to Si

nanowires or the yield of the reaction is also affected by temperature, with ~ 50% conversion at 460 °C and ~63% conversion at 500 °C. At 460 °C, a carbon-containing amorphous layer (5–18 nm) was observed, while at 500 °C, only a very thin (< 2 nm) rough surface layer was observed[115]. Chockla, A. M., *et al*.[116] reported a thin polyphenylsilane shell. The NWs are more than 20 µm long with aspect ratios greater than 1000. The NWs are crystalline with a diamond cubic system. There are a few extended defects and little variation in length[115].

In conclusion, it appears that a C-Si bond is necessary to produce high-quality wires. One of the limitations of this approach is the sophisticated reaction setup, which involves the use of a high-pressure titanium grade-2 reactor and the use of highly dangerous precursors that necessitate low concentrations and thus small yields[112]. This approach exhibits a high degree of nanowires. Although an excellent aspect ratio can be achieved, the nanowire diameters have only been demonstrated up to 30 nm. No nanowires large enough to support Mie resonances have been formed using this method.

### 1.9.5 Thermal decomposition in high-boiling point solvents

In this approach, the organic solvents used have a higher boiling point than the decomposition temperature of the Si precursor (Figure 1.27a). This addresses the possible challenge of a lower boiling point ($T_b$) associated with conventional solvents ($T_b$ <400 °C). The reaction temperature influenced by the choice of solvents affects the nanowire formation and size. The reactions are usually carried out in a long-necked, round-bottomed flask within a three-zone furnace, allowing thermally localizable NW growth on the substrate incorporated within the vapor region of the high-boiling point solvent. The structure growth mechanism could be by a vapor–liquid–solid or a vapor–solid–solid approach. Trisilane is a good precursor for synthesizing Si NWs /nanorods as it rapidly decomposes to Si at temperatures below the boiling point of the solvent of choice (e.g., squalene). However, trisilane is a highly dangerous precursor[117,118].

Apart from trisilane, other Si precursors such as isotetrasilane, neopentasilane, or cyclohexasilane have been experimented with using Sn seeds as a catalyst[119]. The decomposition of the precursors to Si NWs using squalene ($C_{30}H_{50}$) as the solvent occurs at varying reaction temperatures depending on the reactivity of the precursors. The lowest growth temperature occurs at 200 °C, as the cyclohexasilane precursor is the most reactive. This is slightly below the Si−Sn eutectic temperature of 232 °C. At 380 °C, all four silane precursors produced Si NRs with an average length of 200 nm (Figure 1.27b-e). At temperatures below 340 °C, trisilane decomposition did not occur to a large extent. At this point, very few NRs

were produced, and the average length of Si NRs produced using isotetrasilane and neopentasilane was reduced to 65 nm. Further reduction to 320 °C resulted in the production of very few NRs using isotetrasilane and neopentasilane. The acyclic silane reactants (trisilane, isotetrasilane, neopentasilane) yield less product than cyclic reactants (cyclohexasilane). This is because the decomposition of acyclic reactants gives lower silanes (such as mono- and di-silane) that are not used in NRs solution growth. The reactants with a higher Si atom content yield better results. At 380 °C, the product yield is as follows: trisilane (28.8%) < isotetrasilane (32.2%) < neopentasilane (32.8%) < cyclohexasilane (54.6%)[119].

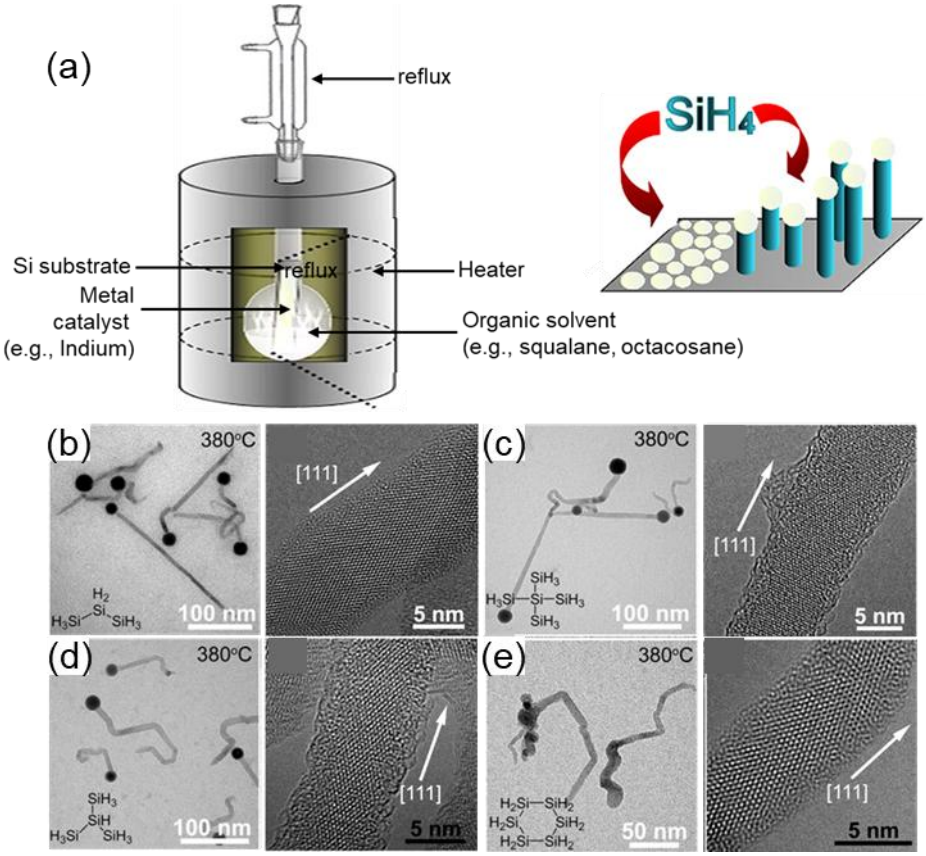



*Figure 1.27 Schematic diagram of the high-boiling point solvent setup for the growth of Si NWs. TEM images of the Si NWs fabricated with different Si precursors. Reproduced from ref.*[119]

Heitsch, A. T., *et al.*[117] synthesized Si nanowires by the decomposition of trisilane ($Si_3H_8$) in octacosane ($C_{28}H_{58}$; $T_b$ = 430 °C) or squalane ($C_{30}H_{62}$; $T_b$ = 423 °C). They used either gold (Au) or bismuth (Bi) nanocrystals as seeds. The reaction occurs at atmospheric pressure within a temperature range of 410 – 430 °C, which is above the eutectic temperatures of Si-Au ($T_E$ = 363 °C) and Si-Bi ($T_E$ = 264 °C). The NWs growth was found to be insensitive to the Si/metal eutectic temperature, as no NWs were observed at reaction temperatures below 410 °C. The minimum molar ratio for the formation of Si wires is 1:300 and 1:650 for Au:Si and Bi:Si,

respectively. The Si NWs produced are 25 – 30 nm in diameter and 2 – 3 μm in length. It was hypothesized that the decomposition of trisilane ($Si_3H_8$) is the limiting process in the NW growth. The decomposition proceeds through the formation of various intermediates (polysilane, silylene, silyl radicals) at lower temperatures (~300−310 °C), which eventually reduce to silane, which decomposes to Si at a temperature greater than 400 °C. A significant yield of crystalline NWs was observed only when reactions were carried out at temperatures higher than 410 °C. At a lower temperature (390 – 400 °C), only an amorphous matrix was observed. Moreso, the NWs are kinked. Heitsch, A. T., *et al*.[118] controlled the diameters (5 – 10 nm) and lengths (15 – 75 nm) of the Si nanorods by tuning the Si/Au molar ratio. The reactions carried out in squalene or octacosane yielded Si nanorods with diameters of about 7−9 nm. The change in the solvent to trioctylamine ($T_b$ = 380 °C) increased the average diameter of the Si nanorods by 2 – 3 times larger than when Au seeds were used (~ 2 nm). The choice of dodecylamine as the Au metal capping ligand was found to be critical in the formation of Si nanorods, as other ligands (such as dodecene, tridodecylamine, and dodecanthiol) did not yield Si nanorods. The ligand was found to help stabilize the Au NPs and prevent Si nanorod aggregation and oxidation.

This technique is not promising for optical applications. The objects are both too narrow and too short, and they are highly kinked. The yield is low (in milligrams per batch), and the precursors are dangerous to handle. But, among the reported nanowires produced in high boiling point solvents, cyclohexasilane should be favored at 380 °C.

### 1.9.6 Thermal disproportionation of silicon-rich oxide

The disproportionation of a Si-rich oxide is an alternative approach to fabricating Si nanowires (Figure 1.28a). In the thermal evaporation of silicon monoxide (SiO), two different growth modes - with or without a metal catalyst are possible. In the approach without a metal catalyst, nucleation of Si occurs on the substrate through the decomposition of SiO. After Si nucleation, growth into larger particles occurs by continuous adsorption of SiO in the vapor phase. For effective adsorption, the Si tips should be in or near their molten states. The growth temperature limits the size of the Si tips.

The sublimation of SiO has been reported to yield different morphologies, sizes, and compositions of Si nanowires under a flow of 5% $H_2$ – Ar (50 sccm) at temperatures between 890 – 1320 °C for a period of 5 h under a pressure of 300 torr (Figure 1.28e-g)[120]. The sublimed precursor is disproportionated and redeposited downstream in a tubular furnace on a substrate to form nanowires. The different morphologies (wire-, octopus-, pin-, tadpole-, and chain-like

structures) are attributed to the temperature distribution in the furnace. Crystalline Si balls at the tips of the wires were reported to act as the energetic site for absorption of the gaseous Si precursor. In the high-temperature region (1230 – 1250 °C), wires with pin-like structures, having diameters of 30 – 100 nm, and lengths of 2 – 10 μm, were formed. The wires with diameters > 50 nm are crystalline and sheathed with a thin amorphous silicon oxide layer, while those with diameters < 50 nm are completely amorphous silicon oxide. In some of the wires, the length of the Si core is one-third to one-half of the entire length of the wire, and the rest is amorphous silicon oxide. In the lower temperature region (890 – 930 °C), the wires are completely oxidized. It has been reported that the decomposition of SiO vapor into Si and $SiO_2$ occurs above the critical temperature of 800 °C. Below this temperature, the SiO vapor directly condenses to form a homogeneous, amorphous, solid silicon oxide[121]. The $Si/SiO_x$ nanowires with similar diameters (10 – 30 nm) were prepared at 735 – 955 °C without any catalyst. The increase in reaction temperature resulted in a corresponding increase in diameter, from ~ 11 nm to ~ 27 nm, with the sheathed amorphous layer increasing from ~ 2 nm to 6 nm[122]. Also, the yield of the Si nanowires increased with reaction temperature and pressure[123].

Another silicon-rich oxide recently reported is hydrogen silsesquioxane (HSQ), which was impregnated with a molecular tin precursor ($SnCl_4$) and thermally disproportionated at a temperature of 450 °C under the flow of 5% $H_2$ – 95% Ar (Figure 1.28b-d)[124]. It was hypothesized that at 250 – 450 °C, the Sn precursor chemically reduced to elemental Sn, which then melted to Sn nanocrystal seeds above the melting point of Sn (~231 °C). Also, the Si precursor was reported to disproportionate to $SiH_4$. The nanocrystal seeds were hypothesized to act as a crystallization promoter surface to decompose diffused $SiH_4$ into elemental Si and $H_2$. The variation in the concentration of the tin precursor varied the diameters (8 – 17 nm) and lengths (50 – 120 nm) of the wires. The advantage of this approach is that it does not require making the metal particles before the formation of the NWs. This is an alternative to all the other methods that require making metal particles before the formation of the NWs[124].

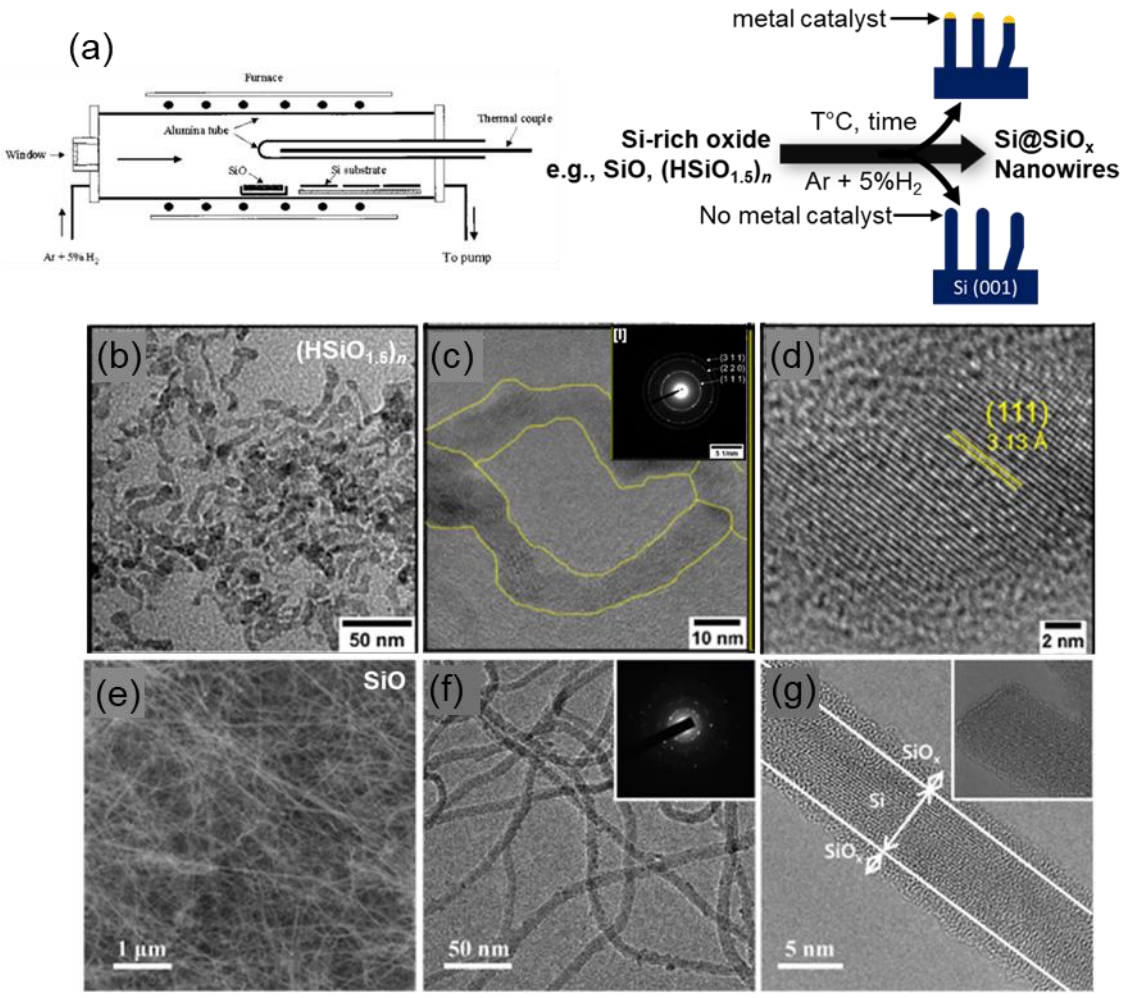
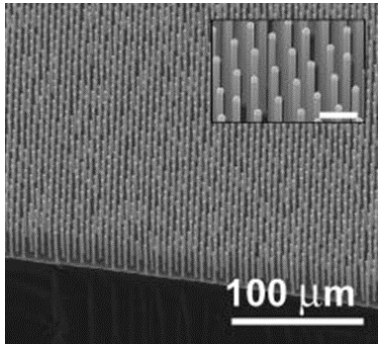
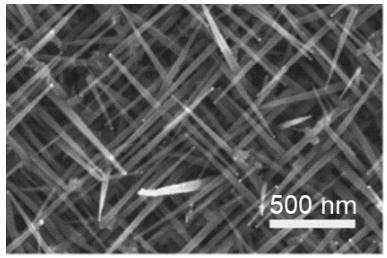
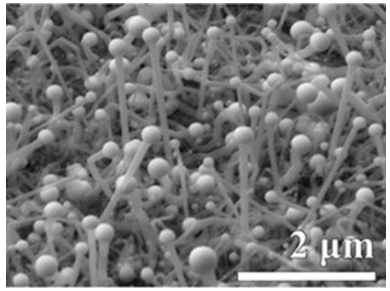
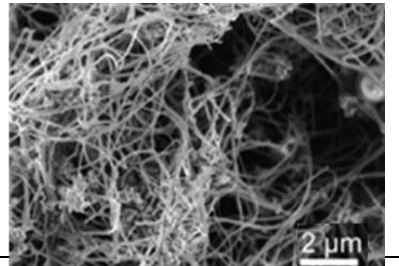
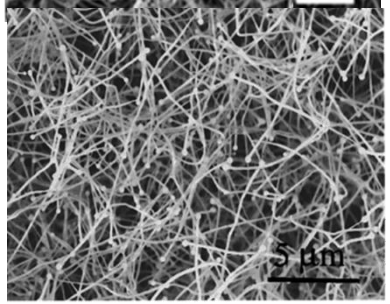



*Figure 1.28 Schematic diagram of the thermal disproportionation of a silicon-rich oxide to fabricate Si NWs. TEM/SEM images of the fabricated Si NWs using (b) $(HSiO_{1.5})_n$ (c) $SiO_x$. Reproduced from ref.*[120,124]

In conclusion, the choice of a fabrication technique depends on the application of the silicon nanowires. The only currently known bottom-up approach that successfully produces silicon nanowires with suitable morphology and size range for optical light scattering studies is chemical vapor deposition (CVD). Every other bottom-up approach suffers from either low-yield production or low-quality Si NWs. These include control of the diameter of the nanowires for Mie-scattering (70 – 200 nm), well-dispersed arrays, defect-free (kinking and twinning of nanowires), and monocrystallinity. These parameters are important in the study of the optical properties. Hence, the top-down approach (such as metal-assisted chemical etching) is still the most optimal approach to make Si NWs for the study of the optical properties.

*Table 1.2 Bottom-up fabrication methods of silicon nanowires*

| Method | Advantages / Limitations | Morphology/Size range | Representative TEM image | Ref. |
|---|---|---|---|---|
| Chemical vapor deposition (CVD) | • Controlled Si NWs dimensions.<br>• Si NWs growth at low - high temperature (450 - 1000 °C) – Au, Pt, Pd, Cu, Ag, Ni.<br>• Required atmospheric pressure (~760 Torr).<br>• Self-igniting precursors when in contact with air ($SiH_4$).<br>• Chlorine-substituted Si precursors ($SiCl_4$) result in etching of Si, substrates, and reactors. | • ~ 5 nm to several hundreds of nanometers (~ 1500 nm).<br>• The metal-catalyst particle size controls the diameter.<br>• Crystalline Si core.<br>• Amorphous oxide layer (~ 2 nm).<br>• Mostly defect-free<br>• Suitable for single particle optical study. |  | 36,37,106,125–131 |
| Plasma-enhanced CVD | • Lower growth temperature<br>• Si NWs growth at 240 °C (Sn, In); 350 - 390 °C (Au, Ga)<br>• Broadened the choice of metal catalysts<br>• Plasma treatment (e.g., $H_2$)<br>• Required vacuum system (380 mTorr – 5 Torr) | • ~ 5 nm to several hundreds of nanometers (~ 180 nm)<br>• Crystalline Si core<br>• Amorphous oxide layer (~ 2 nm)<br>• Kink-defect observed |  | 132–137 |
| Decomposition of silicon precursors in high-boiling-point solvents | • Lower reaction temperature (450 – 500 °C) in solution chemistry<br>• No specialized apparatus<br>• Control over reaction parameters (concentration, growth kinetics)<br>• Si NWs growth at 200 °C (Sn); 410 - 420 °C (Au), 450 °C (In).<br>• Different silane precursors can be used. | • Average diameter of 2 ~ 100 nm<br>• Lower crystallinity / partial amorphous structures<br>• Amorphous oxide layer (~ 2 nm)<br>• Intermittently straight with defects (e.g., kink, twin planes, and stacking faults). |  | 79,117–119,138,139 |

| | | | | |
|---|---|---|---|---|
| | • Organic solvents with high-boiling points.<br>• Defects with amorphous regions. | | | |
| Decomposition of Si precursors in supercritical fluids | • Relatively moderate reaction temperature (450 – 500 °C)<br>• Scalable and wide choice of catalysts<br>• Ligand passivation during growth<br>• Sophisticated setup for high pressure | • Average diameter of 5 – 120 nm<br>• Crystalline Si core<br>• Amorphous layer (e.g., oxide, polyphenylsilane) of 2 – 7 nm.<br>• Significant defects (e.g., kinking and twin planes). |  | 112,113,115,140–145 |
| Thermal annealing of Si-rich oxide | • Simple and scalable process (no vacuum or gas precursor)<br>• High annealing temperature (450 – 1350 °C)<br>• Limited control over oxygen stoichiometry. | • Average diameter of 6 – 1350 nm<br>• Crystalline Si core<br>• Amorphous $SiO_x$ layer up to 260 nm.<br>• Nanowires, Nanorods, chain-like, pin-like, etc structures<br>• Significant defects (e.g., kink, twin planes, and stacking faults). |  | 120,122–124,146,147 |

## 1.10 Directional light scattering in silicon nanoellipse

### 1.10.1 Overview of geometry design

Typical spheroidal particles can be classified into two categories based on the relative length of the three principal axes (*a*, *b*, and *c*), where lengths are taken as the semi-major axis. The particle shapes vary from a sphere (a = b = c; a/b =1) to disk-like oblate spheroids (*a* = *b* > *c*), and cigar-like prolate spheroids (*a* = *b* < *c*). The aspect ratio is defined as the ratio of the major semi-axis (*c*) to the minor semi-axis (*a*).

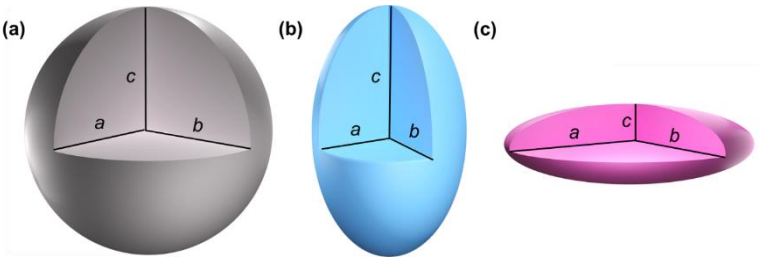



*Figure 1.29 Schematic diagram of (a) spherical, (b) prolate, and (c) oblate spheroidal particle.*

### 1.10.2 Theoretical prediction of the directional light scattering

Wang, Z., *et al.*[148] showed through theoretical calculation that an oblate ellipsoid (major axis = 480 nm; refractive index = 2.5) with an optimum aspect ratio of 1.6 in free-space (refractive index = 1.0) possesses near-zero backward scattering and enhanced forward scattering at the resonant wavelength of total scattering due to the overlapping of the electric and magnetic dipole resonances (Figure 1.30a-d). For a prolate ellipsoid, the forward scattering is also enhanced at an optimum aspect ratio of 4.2, while the backward scattering is not zero due to the existence of higher-order multipolar modes (Figure 1.30e-h).

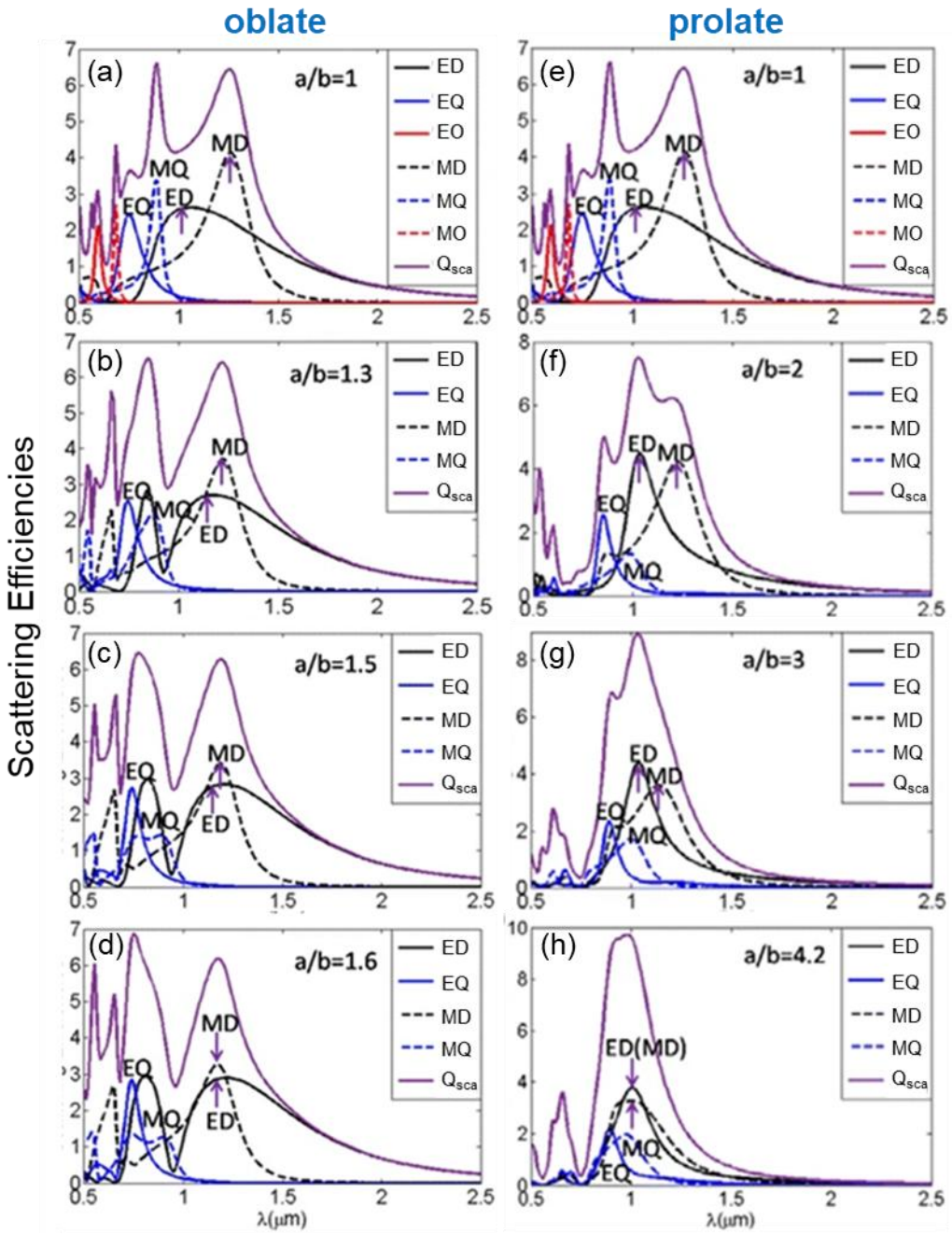



*Figure 1.30 The total scattering efficiency with corresponding multipole contributions of (a-d) oblate ellipsoid particles for different aspect ratios, a/b ranging from 1 to 1.6. (e-h) prolate ellipsoid particles for different aspect ratios, a/b, ranging from 1 to 4.2. Reproduced from ref.*[148]

The polar scattering patterns further showed the radiation patterns for a sphere (a/b = 1), an oblate ellipsoid (a/b = 1.6), and a prolate ellipsoid (a/b = 4.2) corresponding to λ = 1380, 1180, and 1000 nm, respectively (Figure 1.31). From the polar radiation pattern, the forward-to-backward scattering ratio is maximum in the optimized aspect ratio of oblate and prolate

particles at a wavelength closer to the visible region. In contrast, the spherical particle scattered the light in both forward and backward directions.

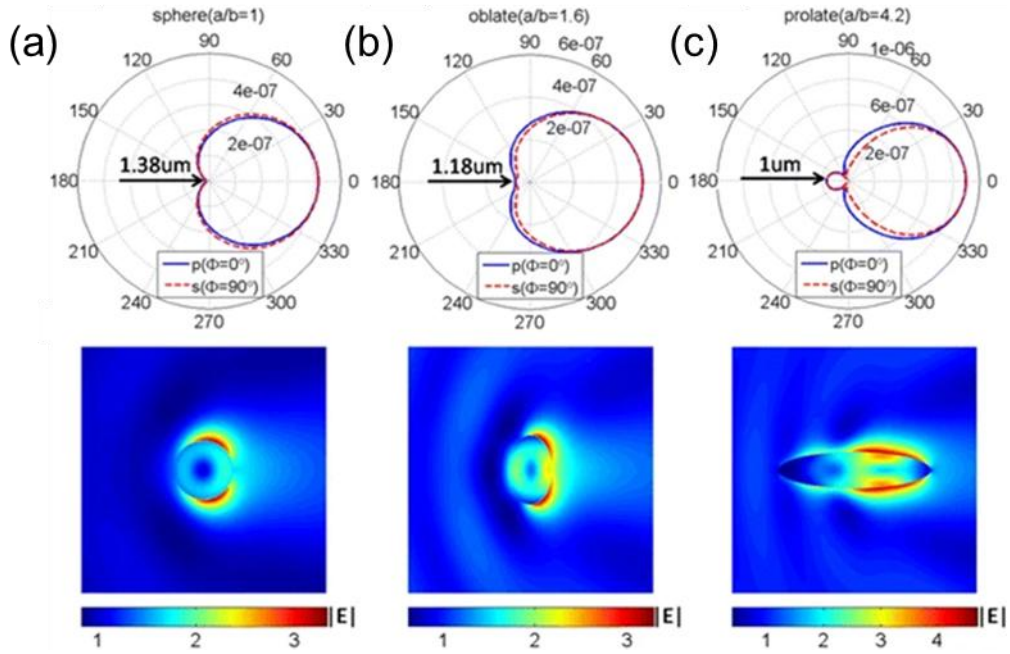



*Figure 1.31 The polar scattering patterns for (a) sphere (a/b = 1), (b) oblate ellipsoid (a/b = 1.6), and (c) prolate ellipsoid (a/b = 4.2). It displays both p-polarized and s-polarized components, along with the corresponding near-field electric field distributions around the particles. Reproduced from ref.*[148]

Luk'yanchuk, B. S., *et al*.[149] showed the optimum aspect ratio for an oblate particle which gives minimum backward scattering efficiency together with maximum forward scattering for each value of refractive index, *n*, between 2.0 and 4.0 (Figure 1.32). The comparison made with spherical particles showed that a spherical particle with a refractive index of 2.4 has a maximum forward-to-backward scattering ratio of ~ 12.3. Whereas, an optimized oblate spheroidal particle with the same refractive index and dimension aspect ratio ~ 1.7 has about 1.4× higher forward scattering efficiency. In fact, the differences in the directional scattering become more pronounced with increased refractive index of the material. A spheroidal particle with a refractive index of ~4 and an aspect ratio of ~2.25 permits a forward-to-backward scattering ratio up to a magnitude of 30-fold, with the back scattering close to zero.

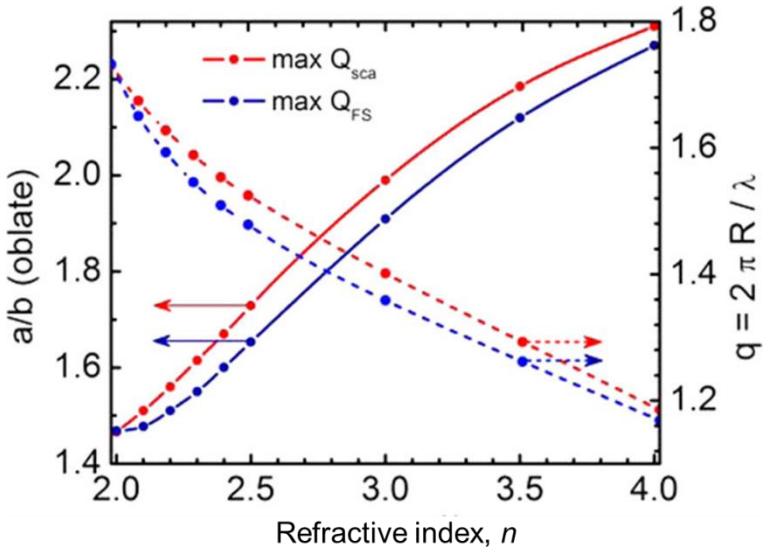



*Figure 1.32 The optimum aspect ratio, a/b (solid line) and size parameter, q for oblate spheroidal particles plotted against the value of refractive index, n. Reproduced from ref.*[149]

## 1.11 Fabrication of silicon nanoellipses and their directional scattering properties

### 1.11.1 Laser ablation approach

Spheroidal Si particles have been fabricated via femtosecond laser ablation of a silicon donor (Figure 1.33b), which can be bulk crystalline silicon[150,151], a silicon-on-insulator wafer[152], or an amorphous silicon film[153]. In this method, a single femtosecond laser pulse focused on a donor substrate causes the material to melt and form a droplet with momentum directed away from the substrate. The droplet then detaches, falls onto another substrate, and solidifies. Depending on the direction of particle transfer relative to the direction of the laser beam propagation, laser-induced backward and forward transfer techniques are distinguished. Based on the choice of donor substrate and the laser beam parameters, the range of optical power providing the creation of single particles varied. In most cases, a huge effort is necessary to achieve the conditions for single particle transfer.

Zywietz, U., *et al.*[150] reported dimer Si particles squeezed along the direction normal to the surface (Figure 1.33a), with the radii of the c-Si cores varying from $r_z$ = 93 nm (top plots) to $r_z$ = 54 nm (bottom plots), the in-plane radii constant at $r_x$ = 93 nm, and a homogeneous 4 nm silica coating. It can be observed from these spectra that the light polarized perpendicularly to the axis of the dimer (Figure 1.33b) showed two dominant peaks that both blue-shift with an increasing anisotropy of the particles. A similar blue-shift of the dominant modes was observed for the incident light polarized along the axis of the dimer (Figure 1.33c). These observations are quite different from the calculated spectra for the spherical particle (Figure 1.33d) and

instead follow the responses of the single oblate scatterer (Figure 1.33e). Lastly, the change in the angle of illumination modifies the relative intensity of the resonances (Figure 1.33f). For instance, it is possible to eliminate the scattering resonance mode at 525 nm (quadrupolar magnetic) by changing the angle of incidence to 67°.

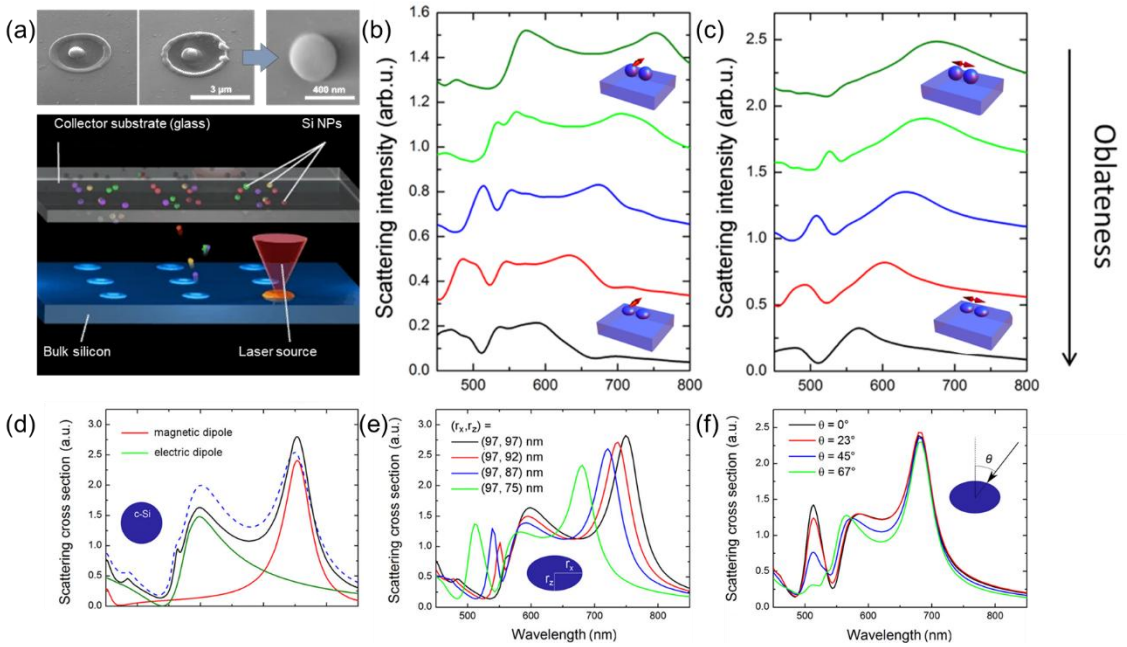



*Figure 1.33 (a) Schematic diagram of the laser generation process of Si particles. (b-c) The dependence of the scattering cross-section on the oblateness of the particles. Two polarizations of the incident light with the electric field (b) perpendicular, and (c) parallel to the dimer axis. Calculated scattering cross sections of single dielectric scatterers. (d) Scattering by a c-Si nanosphere of 97 nm radius (black solid line) (e) Contraction of the c-Si scatterer along the illumination direction (z-axis) selectively blue-shifts magnetic resonances. (f) By modifying the illumination angle, we can selectively tune the strengths of higher-order resonances for the oblate spheroid described by ($r_x$, $r_z$) = (97, 75) nm. Reproduced from ref.*[150]

Fu, Y. H., *et al*.[35] reported Si particles squeezed between aspect ratios of 1.0 – 1.875 in the vertical direction, as shown in the SEM images in the inset of Figure 1.34a–f. It can be observed that the electric dipole resonances in the particles are less pronounced and located closer to the magnetic dipole resonance. It was inferred that this difference arises from the anisotropy of the particles. The calculated spectra properties of the particles with spheroidal shape are shown in Figure 1.34g–k, with the *x*- and *y*-axes diameter fixed at 150 nm and the diameter in the *z*-axis direction varied from 150 to 80 nm. From the calculated spectra, the scattering electric and magnetic resonances are also less pronounced and shift closer to each other. This leads to

overlap of the ED and MD dipole resonances when the diameter in the *z*-axis is less than 120 nm (aspect ratios ~ 1.25). Another interesting feature that arises from the calculated spectra is that the maximum in the forward-to-backward ratio shifts to shorter wavelengths and approaches the maximum of forward scattering when the particles are squeezed in the z-axis direction. Hence, the result of increased overlap of the electric and magnetic dipole resonances leads to an increase in the total scattering in the forward direction[35].

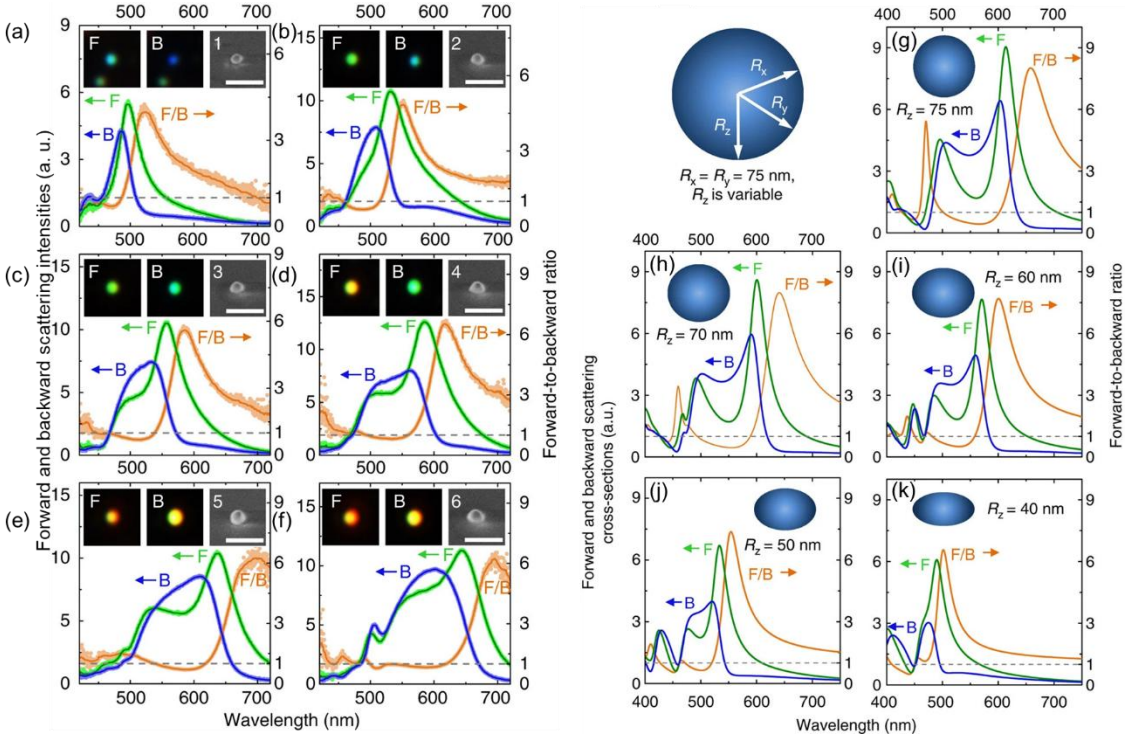



*Figure 1.34 (a-f) The scattering intensities of spheroidal Si particles. The left axes show forward (green) and backward (blue) scattering intensities, and the right axes show the forward-to-backward ratio (orange curves). The dashed lines represent the forward-to-backward ratio equal to unity. The dots represent experimental results fitted with the solid lines. The insets show close view transmitted (F) and reflected (B) dark-field microscope images, and SEM images taken at an angle of 52° different particles labelled 1–6. The scale bar in the SEM images is 500 nm. (g–k) Calculated results of forward (green curves) and backward (blue curves) scattering, and forward-to-backward ratio (orange curves) for silicon particles with $R_z$ = 75, 70, 60, 50, and 40 nm, respectively. The $R_x$=$R_y$=75 nm. Calculations are done in free space using the finite-difference time-domain method. Reproduced from ref.*[35]

However, this fabrication method has several practical and fundamental limitations. There is a variation in particle density and the formation of undesired irregular shapes due to poorly optimized laser source parameters. Achieving stable laser power and pointing over an extended period is challenging. Therefore, it is very tedious to fabricate a large number of particles. Also, unless multiple laser sources are used, scaling to large throughput is quite difficult. The ablation and particle transfer depend on pulse energy, which must be tuned to avoid either incomplete transfer or excessive splashing. Hence, an alternative method for fabricating ellipsoidal silicon particles is needed.

### 1.11.2 Sol-gel method

There are no bottom-up techniques known at this time capable of forming ellipsoidal silicon particles. The combination of the sol-gel strategy with magnesiothermic reduction might provide an alternative method to produce ellipsoidal silicon particles. Therefore, this section will be devoted to the synthesis of ellipsoidal silica particles through a sol-gel approach, and their possible reduction to elemental Si particles via magnesiothermic reduction will be discussed in the next section. A colloidal approach to fabricating solid material from a solution is the sol-gel technique. It is very useful and widely used in the fabrication of spherical silica particles. A solution (sol) slowly changes into a solid state (gel) through regulated chemical processes. The size, shape, and composition of the particles could be precisely controlled with this technique. However, the synthesis of ellipsoidal particles in solution is a big challenge because of the minimization of surface free energy that favors simple spherical shapes[154]. Based on the literature, earlier methods to fabricate ellipsoidal particles rely on deformation strategies such as ionic irradiation[155,156], chemical ion etching[157], mechanical stretching[158,159], and microfluidics processing[160]. However, the limitations of these approaches include low yield of deformed particles, the need for sophisticated equipment, and multi-step preparation procedures.

There are only a few known methods to generate ellipsoidal silica particles via sol-gel chemistry, and these do not generate monodisperse particles. Obtaining ellipsoidal silica particles via a sol-gel approach can be grouped into two broad categories: the hard-templating methods and the use of organic molecules to incur an anisotropic particle growth. The hard-templating method uses spindle-like haematite or gold nanorod particles as templates to control the shape of a growing silica coating. However, this typically requires selective etching of the templates, producing hollow ellipsoidal particles[161–169]. Ellipsoidal particles have been obtained using organic molecules as surfactants to give mesoporous silica particles without an inner

cavity[170–173]. The fabrication of anisotropic silica particles via a surfactant templating approach requires a deep understanding of the different parameters that play a role during the material synthesis.

Zhang, H., *et al.*[170] reported an oil (ethylene glycol)-in-water micellar system as a way to prepare ellipsoidal silica particles (Figure 1.35a-b). This is based on the crucial role of solvents in controlling the morphologies and compositions of the silica particles. A mixture of water/ethanol has been reported to control the diameters of spherical silica particles[174], prepare ordered mesoporous silica spheres[175], and convert silica particles from solid to hollow structures[176]. Other solvent mixtures, such as water/acetone, water/methanol, ethylene glycol, and poly(vinyl alcohol), have been used to modify the size and morphology of mesoporous, spherical silica particles[170]. The appropriate volume ratios of water/ethylene glycol, TEOS, ammonia, and CTAB produced anisotropic surface tension forces at the water-oil interface. The silica nuclei are reported to coalesce and form self-assembled clusters during the reaction. The imbalance in surface tension at the water/oil interface caused the coalesced particles in the water phase to elongate relative to their dimensions in the oil phase. This was stated to be due to the surface tension in the water-phase being greater than the surface tension in the oil-phase. Hence, an asymmetric pull is generated on the particles in the direction perpendicular to the water/oil interface. The hydrophilic nature of the condensed silica particles further facilitates their elongation, as there is increased growth in the water phase due to a larger water phase surface force. At a water/ethylene glycol volume ratio of 1.43, an elliptical growth of the silica particles was induced with an aspect ratio of 1.33 and a pore size of ~ 3 nm (Figure 1.35c). The reduction of the water/ethylene glycol volume ratio from 0.89 to 0.55 resulted in spherical particles with a size range of 124 – 375 nm (Figure 1.35d). However, this approach yields little control over particle size, aspect ratio, and degree of aggregation.

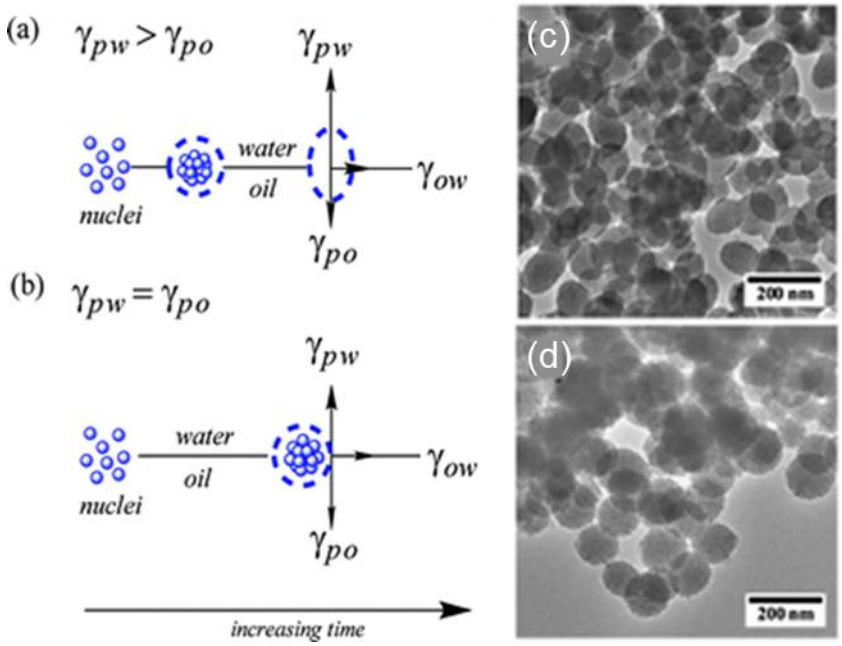



*Figure 1.35 (a-b) Schematic illustration of the formation mechanism (c-d) TEM images of the particles. Reproduced from ref.*[170]

Han, L., *et al.*[172] reported the use of dodecanol/CTAB as surfactants to control the fabrication of ellipsoidal silica particles (Figure 1.36). The volume ratio of dodecanol/CTAB is 1:5 to obtain ellipsoidal silica particles with an average major axis of 200 nm and a minor axis of 100 nm (Figure 1.36b). It is reported that the change in morphology of the silica particles is related to the interaction between the dodecanol, CTAB, and silica oligomers during the aqueous reaction. Anions that are less hydrated than $Br^-$ (e.g., $OH^-$) can replace the former and bind tightly to the head group of the CTAB molecule. Therefore, the repulsion between the cationic head groups is mitigated, and the micelle structure is stabilized. The hydrophobic molecules insert into CTAB through electrostatic interaction to generate the dodecanol/CTAB mixture micelles, or act as an oil core to form an oil-in-water microemulsion with the assistance of CTAB. The change in morphology from sphere to ellipsoid changed the pore size of the silica particles from 3.56 nm to 3.2 nm.

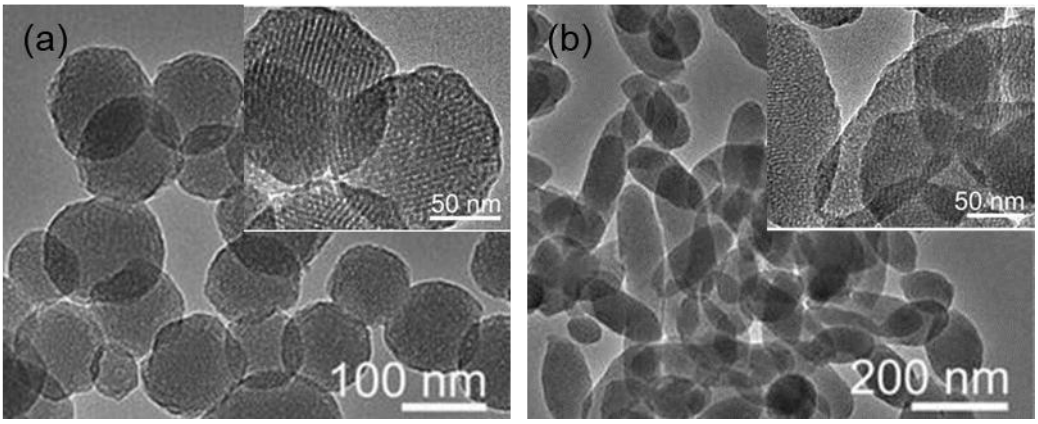



*Figure 1.36 TEM images of the particles formed (a) without dodecanol, (b) with a dodecanol/CTAB volume ratio of 1:5. Reproduced from ref.*[172]

Shen, S., *et al.*[171] reported the use of a polymer template (Pluronic P123) in the presence of an additive (KCl) and solvent (ethanol) in an acidic medium of HCl (Figure 1.37a). The molar ratio of a typical reaction of the reactants, P123:Ethanol:KCl:HCl:$H_2O$:TEOS is 1:142:272:435:11200:27, respectively. It was reported that polymeric surfactants can spontaneously organize into spherical micelles and then transition to non-spherical rod-like micelles in the presence of ethanol and KCl. The ellipsoidal particles have an average major axis of 1.38 ± 0.15 μm and a minor axis of 0.61 ± 0.07 μm, resulting in an aspect ratio of 2.26 from the addition of 2.53 mass% of ethanol (Figure 1.37c). In the absence of ethanol or when the ethanol used is smaller than 1.97 mass%, only rod-like mesoporous silica is generated (Figure 1.37b). The increase in the amount of ethanol between 1.97 – 3.09 mass% decreases the aspect ratio from 2.94 – 1.91 (Figure 1.37d). When the amount of ethanol is greater than 3.09 mass%, curled pseudospherical shape particles are formed. Hence, the aspect ratio of the ellipsoidal silica particles can be systematically tuned by controlling the ethanol concentration. The proposed mechanism for particle formation is that the polymer template tends to form spherical micelles, with the hydrophobic block situated in the core and the hydrophilic block forming the corona. The addition of a silica precursor and KCl induced the formation of hexagonal patterned rod-like micelles with equal length. The ethanol shortens the length of rod-like micelles and delays the colloid phase separation, which favors a spherical morphology due to the minimization of surface area. Therefore, the ellipsoidal morphology is formed as an intermediate state during the rod-to-sphere transition. However, the particles have an average size of several microns, which makes this technique not directly useful for our project.

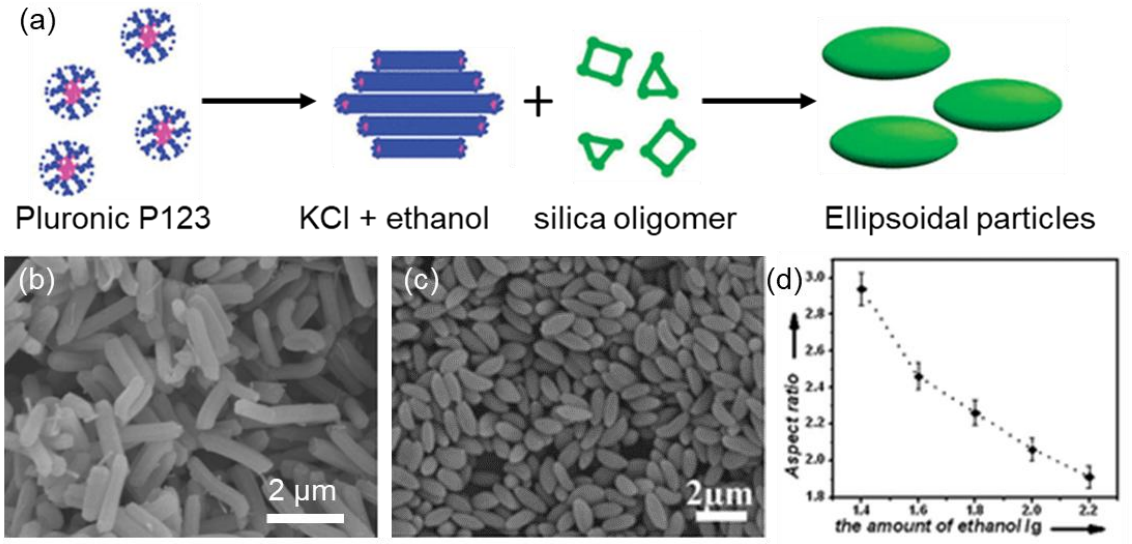



*Figure 1.37 (a) Schematic illustration of the formation mechanism. TEM images of the silica (b) rod with ethanol of 0.5 g, (c) ellipse with ethanol of 1.8 g. The dependence of the aspect ratio on the amount of ethanol. Reproduced from ref.*[171]

Han, L., *et al.*[173] reported using a mixture of CTAB/SDBS surfactants as a soft template with TEOS as silica precursor and aqueous ammonia as the catalyst (Figure 1.38a). The oblate ellipsoidal silica particles were formed with short channels running parallel to the short axis. The average major axis is 200 nm, and the average minor axis is 100 nm (Figure 1.38b). The mesoporous particles possessed a hexagonal cylindrical porosity with a pore size of 2.67 nm. In the absence of the SDBS, rod-like particles with pore channels along the long axis were obtained (Figure 1.38c). It was proposed that the SDBS alters the self-assembly behavior of CTAB by introducing electrostatic interactions between oppositely charged surfactants (Figure 1.38a). This changes the packing characteristics of the mixed micellar templates, leading to the formation of an elongated micelle. The same author[177] reported using L-tyrosine instead of SDBS as a co-surfactant to CTAB to fabricate ellipsoidal particles having an average major axis length of ~150 nm and an average short axis width of ~80 nm. The pore size was determined to be 2.78 nm. The L-tyrosine was reported to play a dominant role in the formation of the ellipsoidal particles, with only spherical particles formed in its absence.

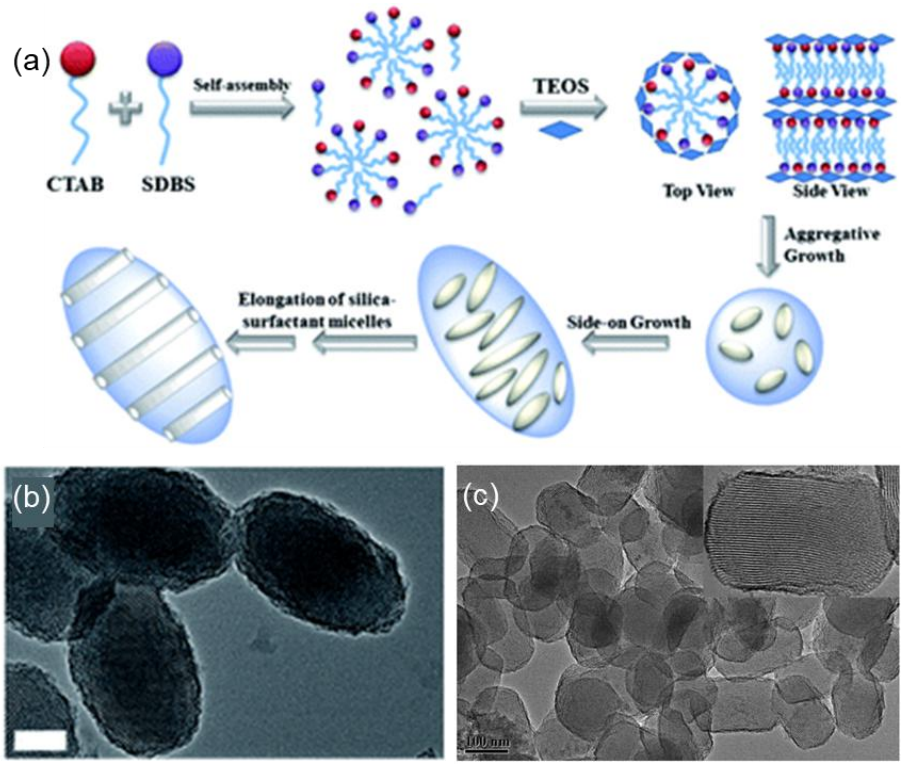



*Figure 1.38 (a) Proposed mechanism for the formation of the ellipsoidal silica particles (b-c) TEM image of the particles. Reproduced from ref.*[173]

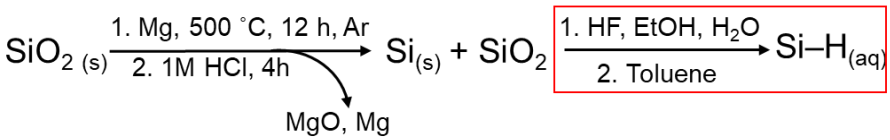
Travaglini, L., *et al.*[178] reported a dual-surfactant system of CTAB and cholate acid, to produce oblate particles having an average minor axis ranging from 180 to 350 nm and an average major axis of ~423 nm. The choice of cholate acid influenced the interaction between the $CTA^+$ cationic micelles and growing silicates. The two surfactants associate into mixed micelles driven by strong attractive charge interactions. The cholic acid tends to insert into the micelle so that the steroidal skeleton stays in the core. At the same time, the carboxylate group interacts electrostatically with $CTA^+$ head groups at the surface level. These strong, attractive interactions lead to a screening of the positive charges, which decreases the charge density and lowers the micelle curvature. Thus, at high concentrations, the transition from spherical to cylindrical micelles is favored, which then controls the morphology of the particles. However, the challenges common to all of these methods are improving experimental reproducibility.

### 1.11.3 Metallothermic reduction of silica

Metallothermic reduction has gained significant attention for the straightforward and scalable synthesis of porous elemental Si from inexpensive precursors such as silica. This approach is attractive because the morphology and dimensions of the silica particles can be relatively controlled. Silica can be reduced to elemental Si using vapors of magnesium (600 –

800 °C)[179], aluminum (700 – 800 °C)[180,181], or sodium (300 °C)[182]. The choice of reducing metal should be cheap, convenient to handle, produce an easily removable byproduct, have a relatively low melting point, and possess appropriate redox properties. Magnesium has been the most widely used reducing metal for silicon oxide and suboxides. However, the removal of the alkali metal oxides can be quite hazardous due to the violent reaction with water. Therefore, Mg and Al are more favorable for the metallothermic reduction of silica.

Upon reaction, a composite of Si and metal oxide (e.g., MgO, $Al_2O_3$) is produced. The reduction with magnesium proceeds through the following reaction:[183]




The metal oxide is typically washed away using 1M HCl, and silica is removed using HF. Significant porosity is formed by removing the metal oxide (Figure 1.39). However, the porosity can be reduced by backfilling with $Si_2H_6$ through chemical vapor deposition[184].

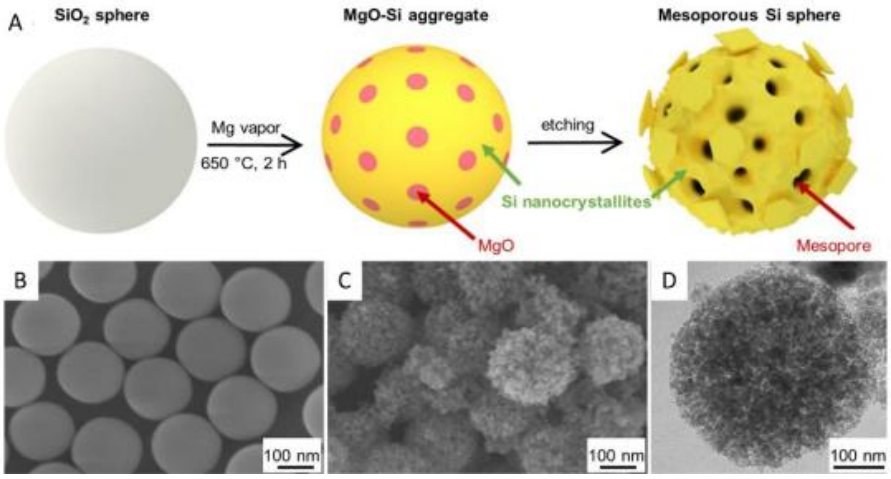



*Figure 1.39 (a) Schematic illustration of the magnesiothermic reduction mechanism. (b) SEM images of the (b) silica spheres (c) elemental Si spheres. (d) TEM image of the elemental Si spheres. Reproduced from ref.*[184–186]

However, this approach presents several challenges. First, the magnesium vapors are inhomogeneously distributed within the reactor. Undesirable by-products such as $Mg_2Si$ and MgO can be formed[187]. If the sample is too far from the magnesium powder during thermal treatment, the silica does not reduce because it is not exposed to a sufficient amount of magnesium vapor. At the end of the reaction, the sample is typically composed of ~ 64 vol%

MgO, ~ 34 vol% Si[188]. Upon magnesium removal, the pore volume is too high for meta-atoms. Thus, several technological barriers must be overcome before metallothermic reduction can be used to produce silicon meta-atoms.

## 1.12 Objectives of the PhD thesis

This first chapter reviewed some of the achievements and progress in the development of silicon-based nanostructures with directional light scattering properties. As incident light hits these nanoscale objects, many of its properties change, such as the intensity and direction of propagation. Optical phenomena basically involve controlling the amplitude, phase, and polarization of the light. Subwavelength-sized Si particles (100 – 200 nm) interact with optical wavelengths, offering low optical losses and exhibiting strong electric and magnetic resonances. These resonances can combine to produce interesting optical effects, such as pure forward light scattering. For this to occur efficiently, the electric dipole (ED) and magnetic dipole (MD) modes must have similar amplitudes and phases. At wavelengths where this happens, the particles act analogously to the forward-propagating point sources of light used in Huygens' principle. Various strategies to improve the spectral overlap of these two modes in Si particles, including the fabrication of core-shell architectures, non-spherical morphologies (e.g., nano-ellipses, nanopillars, nanowires, etc), or assembling Si particles into arrays (e.g., metasurfaces), have been studied theoretically and experimentally. The main optical phenomena employed in these nanostructures are the Mie and plasmon resonances. How can they combine to improve directional light scattering?

The main objectives of this thesis were to fabricate hetero or anisotropic nanostructures through a scalable bottom-up approach and to investigate their directional light scattering properties, thereby validating the theoretical predictions. This fundamental study clearly suggests that bottom-up strategies can be used to fabricate some of these nanostructures as potential building blocks for metasurfaces. Generally, bottom-up approaches do not provide as much control over the spatial arrangement of the nano-objects into metasurfaces as top-down techniques do. However, they remain unrivaled in terms of scalability.

In Chapter 2, the optical and nanostructure characterization techniques used in this thesis will be briefly presented.

Chapter 3 describes the colloidal synthesis of Si@Au core-shell nanostructures with sizes large enough to control optical light scattering. Here, our first objective was to investigate enhancing the directional light scattering efficiency of sub-wavelength spherical silicon particles using a plasmonic shell. By constructing a composite system of both dielectric and metallic materials, one can retain low losses while achieving stronger mode confinement. The fabrication for the Au shell was carried out in a two-step aqueous approach: (i) surface

amination of the silicon particles, followed by the first deposition of Au nanoparticles; (ii) polymerized aminosilane functionalization of the first coating samples, followed by a second deposition of Au nanoparticles. The experimental optical scattering was compared with the simulations, and a perspective study on how to better enhance directional scattering was proposed.

Chapter 4 describes a novel bottom-up synthesis of silicon nanowires. Here, our second objective was to investigate enhancing the directional light scattering efficiency of sub-wavelength silicon nanowires combined with a plasmonic particle in the form of metal-dielectric nanostructures. Silicon nanowire fabrication was achieved with different metal particles in a two-step synthesis: (i) sol-gel synthesis of silicon-rich oxide incorporated with different metal particles; (ii) thermal annealing of the silicon-rich oxide under different experimental conditions. The second part of this chapter examines the growth mechanism of the nanowires through an *in-situ* TEM experiment to gain a deeper understanding of how to control their morphology and size.

Finally, Chapter 5 describes the colloidal synthesis of ellipsoidal silica particles and their reduction to elemental Si particles. Here, our third objective was to investigate enhancing the directional light scattering efficiency of sub-wavelength ellipsoidal silicon particles. Ellipsoidal silicon particles were fabricated in a two-step approach: (i) sol-gel synthesis of ellipsoidal silica particles; (ii) metallothermic reduction of the ellipsoidal silica particles to elemental silicon particles. The mechanism of ellipsoidal morphology formation is a topic of debate in the literature. Therefore, this was investigated by varying different reaction parameters. Beyond the optical effects of controlling light, the mechanical driving forces exerted by light on the elliptical particles were studied through vacuum optical trapping. This was used to measure the three-dimensional axes of the ellipsoidal silica particles.

The fabrication of anisotropic silicon nanomaterials through bottom-up chemistry is very challenging, and thus, there are limited experimental approaches to such meta-atoms in the literature. Working with silicon has a set of challenges that require patience and preservation. We have made small advances in understanding how to make silicon nanomaterials through this thesis, which will help guide further efforts. Due to limited time, not all materials could be optically characterized in terms of their directional scattering capabilities.

## References


(1) Giannini, V.; Fernández-Domínguez, A. I.; Heck, S. C.; Maier, S. A. Plasmonic Nanoantennas: Fundamentals and Their Use in Controlling the Radiative Properties of Nanoemitters. *Chem. Rev.* **2011**, *111* (6), 3888–3912. https://doi.org/10.1021/cr1002672.

(2) Novotny, L.; Hecht, B. *Principles of Nano-Optics*, 1st ed.; Cambridge University Press, 2006. https://doi.org/10.1017/CBO9780511813535.

(3) Matsumori, A.; Sugimoto, H.; Fujii, M. Unidirectional Transverse Light Scattering in Notched Silicon Nanosphere. *Laser Photonics Rev.* **2023**, *17* (8), 2300314. https://doi.org/10.1002/lpor.202300314.

(4) Evlyukhin, A. B.; Bozhevolnyi, S. I.; Pors, A.; Nielsen, M. G.; Radko, I. P.; Willatzen, M.; Albrektsen, O. Detuned Electrical Dipoles for Plasmonic Sensing. *Nano Lett.* **2010**, *10* (11), 4571–4577. https://doi.org/10.1021/nl102572q.

(5) Curto, A. G.; Volpe, G.; Taminiau, T. H.; Kreuzer, M. P.; Quidant, R.; Van Hulst, N. F. Unidirectional Emission of a Quantum Dot Coupled to a Nanoantenna. *Science* **2010**, *329* (5994), 930–933. https://doi.org/10.1126/science.1191922.

(6) De Marco, M. L.; Semlali, S.; Korgel, B. A.; Barois, P.; Drisko, G. L.; Aymonier, C. Silicon-Based Dielectric Metamaterials: Focus on the Current Synthetic Challenges. *Angew. Chem. Int. Ed.* **2018**, *57* (17), 4478–4498. https://doi.org/10.1002/anie.201709044.

(7) Mie, G. Beiträge Zur Optik Trüber Medien, Speziell Kolloidaler Metallösungen. *Ann. Phys.* **1908**, *330* (3), 377–445. https://doi.org/10.1002/andp.19083300302.

(8) Van De Hulst, H. C.; Twersky, V. *Light Scattering by Small Particles*. *Phys. Today* **1957**, *10* (12), 28–30. https://doi.org/10.1063/1.3060205.

(9) Lagendijk, A.; Van Tiggelen, B. A. Resonant Multiple Scattering of Light. *Phys. Rep.* **1996**, *270* (3), 143–215. https://doi.org/10.1016/0370-1573(95)00065-8.

(10) Bohren, C. F.; Huffman, D. R. *Absorption and Scattering of Light by Small Particles*, 1st ed.; Wiley, 1998. https://doi.org/10.1002/9783527618156.

(11) Horvath, H. Gustav Mie and the Scattering and Absorption of Light by Particles: Historic Developments and Basics. *J. Quant. Spectrosc. Radiat. Transf.* **2009**, *110* (11), 787–799. https://doi.org/10.1016/j.jqsrt.2009.02.022.

(12) Baranov, D. G.; Zuev, D. A.; Lepeshov, S. I.; Kotov, O. V.; Krasnok, A. E.; Evlyukhin, A. B.; Chichkov, B. N. All-Dielectric Nanophotonics: The Quest for Better Materials and Fabrication Techniques. *Optica* **2017**, *4* (7), 814. https://doi.org/10.1364/OPTICA.4.000814.

(13) Kuznetsov, A. I.; Miroshnichenko, A. E.; Brongersma, M. L.; Kivshar, Y. S.; Luk'yanchuk, B. Optically Resonant Dielectric Nanostructures. *Science* **2016**, *354* (6314), aag2472. https://doi.org/10.1126/science.aag2472.

(14) Sergei, L. Theoretical Investigations of Mie Scattering and Virtual Excitations in Nanophotonics. Technical University of Denmark., Technical University of Denmark, 2023. https://findit.dtu.dk/en/catalog/68b4ca8d6064878f0ff48b71.

(15) Sugimoto, H.; Fujii, M. Colloidal Mie Resonators for All-Dielectric Metaoptics. *Adv. Photonics Res.* **2021**, *2* (4), 2000111. https://doi.org/10.1002/adpr.202000111.

(16) Fu, Y. H.; Kuznetsov, A. I.; Miroshnichenko, A. E.; Yu, Y. F.; Luk'yanchuk, B. Directional Visible Light Scattering by Silicon Nanoparticles. *Nat. Commun.* **2013**, *4* (1), 1527. https://doi.org/10.1038/ncomms2538.

(17) Person, S.; Jain, M.; Lapin, Z.; Sáenz, J. J.; Wicks, G.; Novotny, L. Demonstration of Zero Optical Backscattering from Single Nanoparticles. *Nano Lett.* **2013**, *13* (4), 1806–1809. https://doi.org/10.1021/nl4005018.

(18) Staude, I.; Miroshnichenko, A. E.; Decker, M.; Fofang, N. T.; Liu, S.; Gonzales, E.; Dominguez, J.; Luk, T. S.; Neshev, D. N.; Brener, I.; Kivshar, Y. Tailoring Directional Scattering through Magnetic and Electric Resonances in Subwavelength Silicon Nanodisks. *ACS Nano* **2013**, *7* (9), 7824–7832. https://doi.org/10.1021/nn402736f.

(19) Sugimoto, H.; Okazaki, T.; Fujii, M. Mie Resonator Color Inks of Monodispersed and Perfectly Spherical Crystalline Silicon Nanoparticles. *Adv. Opt. Mater.* **2020**, *8* (12), 2000033. https://doi.org/10.1002/adom.202000033.

(20) Eslamisaray, M. A.; Wray, P. R.; Lee, Y.; Nelson, G. M.; Ilic, O.; Atwater, H. A.; Kortshagen, U. R. A Single-Step Bottom-up Approach for Synthesis of Highly Uniform Mie-Resonant Crystalline Semiconductor Particles at Visible Wavelengths. *Nano Lett.* **2023**, *23* (5), 1930–1937. https://doi.org/10.1021/acs.nanolett.2c05084.

(21) Ma, C.; Yan, J.; Huang, Y.; Yang, G. Directional Scattering in a Germanium Nanosphere in the Visible Light Region. *Adv. Opt. Mater.* **2017**, *5* (24), 1700761. https://doi.org/10.1002/adom.201700761.

(22) Zhang, Y.; Chen, S.; Han, J. Broadband and Highly Directional Visible Light Scattering by Laser-Splashed Lossless TiO2 Nanoparticles. *Molecules* **2021**, *26* (20), 6106. https://doi.org/10.3390/molecules26206106.

(23) Shima, D.; Sugimoto, H.; Assadillayev, A.; Raza, S.; Fujii, M. Gallium Phosphide Nanoparticles for Low-Loss Nanoantennas in Visible Range. *Adv. Opt. Mater.* **2023**, *11* (12), 2203107. https://doi.org/10.1002/adom.202203107.

(24) O'Connor, K. M.; Rubletz, A.; Ni, C.; He, Y.; Butler, C.; Veinot, J. G. C. High-Temperature Anomaly in the Synthesis of Large ( $d$ > 100 Nm) Silicon Nanoparticles from Hydrogen Silsesquioxane. *Chem. Mater.* **2023**, *35* (19), 7967–7973. https://doi.org/10.1021/acs.chemmater.3c01200.

(25) Parker, M. A.; De Marco, M. L.; Castro-Grijalba, A.; Ghoridi, A.; Portehault, D.; Pechev, S.; Hillard, E. A.; Lacomme, S.; Bessière, A.; Cunin, F.; Rosa, P.; Gonidec, M.; Drisko, G. L. Size-Tunable Silicon Nanoparticles Synthesized in Solution *via* a Redox Reaction. *Nanoscale* **2024**, *16* (16), 7958–7964. https://doi.org/10.1039/D3NR05793C.

(26) Parker, M. A.; Khaddad, S.; Fares, N.; Ghoridi, A.; Portehault, D.; Bonhommeau, S.; Amarouchene, Y.; Rosa, P.; Gonidec, M.; Drisko, G. L. Unveiling the Potential of Redox Chemistry to Form Size-Tunable, High-Index Silicon Particles. *Chem. Mater.* **2024**, *36* (22), 10986–10993. https://doi.org/10.1021/acs.chemmater.4c01439.

(27) Chaâbani, W.; Proust, J.; Movsesyan, A.; Béal, J.; Baudrion, A.-L.; Adam, P.-M.; Chehaidar, A.; Plain, J. Large-Scale and Low-Cost Fabrication of Silicon Mie Resonators. *ACS Nano* **2019**, *13* (4), 4199–4208. https://doi.org/10.1021/acsnano.8b09198.

(28) Semaltianos, N. G.; Logothetidis, S.; Perrie, W.; Romani, S.; Potter, R. J.; Edwardson, S. P.; French, P.; Sharp, M.; Dearden, G.; Watkins, K. G. Silicon Nanoparticles Generated

by Femtosecond Laser Ablation in a Liquid Environment. *J. Nanoparticle Res.* **2010**, *12* (2), 573–580. https://doi.org/10.1007/s11051-009-9625-y.

(29) Kerker, M.; Wang, D.-S.; Giles, C. L. Electromagnetic Scattering by Magnetic Spheres. *J. Opt. Soc. Am.* **1983**, *73* (6), 765. https://doi.org/10.1364/JOSA.73.000765.

(30) Krasnok, A. E.; Miroshnichenko, A. E.; Belov, P. A.; Kivshar, Yu. S. Huygens Optical Elements and Yagi—Uda Nanoantennas Based on Dielectric Nanoparticles. *JETP Lett.* **2011**, *94* (8), 593–598. https://doi.org/10.1134/S0021364011200070.

(31) Gómez-Medina, R. Electric and Magnetic Dipolar Response of Germanium Nanospheres: Interference Effects, Scattering Anisotropy, and Optical Forces. *J. Nanophotonics* **2011**, *5* (1), 053512. https://doi.org/10.1117/1.3603941.

(32) Nieto-Vesperinas, M.; Gomez-Medina, R.; Saenz, J. J. Angle-Suppressed Scattering and Optical Forces on Submicrometer Dielectric Particles. *J. Opt. Soc. Am. A* **2011**, *28* (1), 54. https://doi.org/10.1364/JOSAA.28.000054.

(33) Tapar, J.; Kishen, S.; Emani, N. K. Generalized Kerker Effect in PT-Symmetric Nanoantenna Array. *J. Opt.* **2022**, *24* (3), 034003. https://doi.org/10.1088/2040-8986/ac486f.

(34) Powell, A. W.; Hibbins, A. P.; Sambles, J. R. Multiband Superbackscattering via Mode Superposition in a Single Dielectric Particle. *Appl. Phys. Lett.* **2021**, *118* (25), 251107. https://doi.org/10.1063/5.0054725.

(35) Fu, Y. H.; Kuznetsov, A. I.; Miroshnichenko, A. E.; Yu, Y. F.; Luk'yanchuk, B. Directional Visible Light Scattering by Silicon Nanoparticles. *Nat. Commun.* **2013**, *4* (1), 1527. https://doi.org/10.1038/ncomms2538.

(36) Cao, L.; Fan, P.; Barnard, E. S.; Brown, A. M.; Brongersma, M. L. Tuning the Color of Silicon Nanostructures. *Nano Lett.* **2010**, *10* (7), 2649–2654. https://doi.org/10.1021/nl1013794.

(37) Brönstrup, G.; Jahr, N.; Leiterer, C.; Csáki, A.; Fritzsche, W.; Christiansen, S. Optical Properties of Individual Silicon Nanowires for Photonic Devices. *ACS Nano* **2010**, *4* (12), 7113–7122. https://doi.org/10.1021/nn101076t.

(38) Sugimoto, H.; Fujii, M. Broadband Dielectric–Metal Hybrid Nanoantenna: Silicon Nanoparticle on a Mirror. *ACS Photonics* **2018**, *5* (5), 1986–1993. https://doi.org/10.1021/acsphotonics.7b01461.

(39) Sugimoto, H.; Imaizumi, R.; Hinamoto, T.; Kawashima, T.; Fujii, M. Silicon Nanowire on Mirror Nanoantennas: Engineering Hybrid Gap Mode for Light Sources and Sensing Platforms. *ACS Appl. Nano Mater.* **2020**, *3* (7), 7223–7230. https://doi.org/10.1021/acsanm.0c01559.

(40) Negoro, H.; Sugimoto, H.; Hinamoto, T.; Fujii, M. Template-Assisted Self-Assembly of Colloidal Silicon Nanoparticles for All-Dielectric Nanoantenna. *Adv. Opt. Mater.* **2022**, *10* (8), 2102750. https://doi.org/10.1002/adom.202102750.

(41) Hu, Y.; Probst, P. T.; Habil, M. K.; Sugimoto, H.; Fujii, M. Mechanically Tunable Optical Response in Silicon Nanosphere Metasurface Fabricated via Bottom-Up Process. *Adv. Opt. Mater.* **2025**, 01013. https://doi.org/10.1002/adom.202501013.

(42) Parker, M. A.; Barbosa, R.; Cibaka-Ndaya, C.; Castro-Grijalba, A.; De Marco, M. L.; Korgel, B. A.; Montero, D.; Lacomme, S.; Azéma, A.; Kravets, V. G.; Grigorenko, A. N.;

Ponsinet, V.; Barois, P.; Roach, L.; Drisko, G. L. Self-Assembled Silicon@Silica Metasurfaces with High-Quality Resonances in the Infrared. *Small Sci.* **2025**, *5* (7), 2500119. https://doi.org/10.1002/smsc.202500119.

(43) Kruk, S.; Hopkins, B.; Kravchenko, I. I.; Miroshnichenko, A.; Neshev, D. N.; Kivshar, Y. S. Invited Article: Broadband Highly Efficient Dielectric Metadevices for Polarization Control. *APL Photonics* **2016**, *1* (3), 030801. https://doi.org/10.1063/1.4949007.

(44) Dezert, R.; Richetti, P.; Baron, A. Complete Multipolar Description of Reflection and Transmission across a Metasurface for Perfect Absorption of Light. *Opt. Express* **2019**, *27* (19), 26317. https://doi.org/10.1364/OE.27.026317.

(45) Lermusiaux, L.; Many, V.; Barois, P.; Ponsinet, V.; Ravaine, S.; Duguet, E.; Tréguer-Delapierre, M.; Baron, A. Toward Huygens' Sources with Dodecahedral Plasmonic Clusters. *Nano Lett.* **2021**, *21* (5), 2046–2052. https://doi.org/10.1021/acs.nanolett.0c04666.

(46) Elancheliyan, R.; Dezert, R.; Castano, S.; Bentaleb, A.; Nativ-Roth, E.; Regev, O.; Barois, P.; Baron, A.; Mondain-Monval, O.; Ponsinet, V. Tailored Self-Assembled Nanocolloidal Huygens Scatterers in the Visible. *Nanoscale* **2020**, *12* (47), 24177–24187. https://doi.org/10.1039/D0NR05788F.

(47) Dwivedi, R.; Lafitte, M.; Buisson, L.; Mondain-Monval, O.; Ponsinet, V.; Baron, A. Broadband Forward-Scattering of Light by Plasmonic Balls: Role of Multipolar Interferences. *Appl. Phys. Lett.* **2024**, *124* (1), 011703. https://doi.org/10.1063/5.0182709.

(48) Lafitte, M.; Dwivedi, R.; Elancheliyan, R.; Lagugné-Labarthet, F.; Buisson, L.; Ly, I.; Barois, P.; Baron, A.; Mondain-Monval, O.; Ponsinet, V. Colloidal Self-Assembly of Silver Nanoparticle Clusters for Optical Metasurfaces. *Langmuir* **2024**, *40* (5), 2601–2615. https://doi.org/10.1021/acs.langmuir.3c02900.

(49) Soun, D.; Azma, A.; Roach, L.; Drisko, G. L.; Wiecha, P. R. Gradient-Based Optimization of Core-Shell Particles with Discrete Materials for Directional Scattering. *Opt. Express* **2025**, *33* (12), 25945. https://doi.org/10.1364/OE.561657.

(50) Feng, T.; Xiang, J.; Zhang, C.; Liang, Z.; Xu, Y. Ultrathin Conductive Coating Effects on the Magnetic and Electric Resonances of Silicon Nanoparticles. *J. Opt. Soc. Am. B* **2017**, *34* (3), 653. https://doi.org/10.1364/JOSAB.34.000653.

(51) Tsuchimoto, Y.; Yano, T.; Hada, M.; Nakamura, K. G.; Hayashi, T.; Hara, M. Controlling the Visible Electromagnetic Resonances of $Si/SiO_2$ Dielectric Core–Shell Nanoparticles by Thermal Oxidation. *Small* **2015**, *11* (37), 4844–4849. https://doi.org/10.1002/smll.201500884.

(52) Tsuchimoto, Y.; Yano, T.; Hayashi, T.; Hara, M. Fano Resonant All-Dielectric Core/Shell Nanoparticles with Ultrahigh Scattering Directionality in the Visible Region. *Opt. Express* **2016**, *24* (13), 14451. https://doi.org/10.1364/OE.24.014451.

(53) De Marco, M. L.; Jiang, T.; Fang, J.; Lacomme, S.; Zheng, Y.; Baron, A.; Korgel, B. A.; Barois, P.; Drisko, G. L.; Aymonier, C. Broadband Forward Light Scattering by Architectural Design of Core–Shell Silicon Particles. *Adv. Funct. Mater.* **2021**, *31* (26), 2100915. https://doi.org/10.1002/adfm.202100915.

(54) Chaâbani, W.; Proust, J.; Ouellet, S.; Movsesyan, A.; Béal, J.; Bachelot, R.; Xu, T.; Baudrion, A.-L.; Adam, P.-M.; Boudreau, D.; Chehaidar, A.; Plain, J. Si@Au Core–Shell Nanostructures: Toward a New Platform for Controlling Optical Properties at the

Nanoscale. *J. Phys. Chem. C* **2021**, *125* (37), 20606–20616. https://doi.org/10.1021/acs.jpcc.1c06182.

(55) Sugimoto, H.; Hinamoto, T.; Kazuoka, Y.; Assadillayev, A.; Raza, S.; Fujii, M. Mode Hybridization in Silicon Core–Gold Shell Nanosphere. *Small* **2022**, *18* (45), 2204890. https://doi.org/10.1002/smll.202204890.

(56) Bardhan, R.; Grady, N. K.; Ali, T.; Halas, N. J. Metallic Nanoshells with Semiconductor Cores: Optical Characteristics Modified by Core Medium Properties. *ACS Nano* **2010**, *4* (10), 6169–6179. https://doi.org/10.1021/nn102035q.

(57) Sancho-Parramon, J.; Jelovina, D. Boosting Fano Resonances in Single Layered Concentric Core–Shell Particles. *Nanoscale* **2014**, *6* (22), 13555–13564. https://doi.org/10.1039/C4NR03879G.

(58) Lepeshov, S. I.; Krasnok, A. E.; Belov, P. A.; Miroshnichenko, A. E. Hybrid Nanophotonics. *Phys.-Uspekhi* **2019**, *61* (11), 1035–1050. https://doi.org/10.3367/UFNe.2017.12.038275.

(59) Basu, T. S.; Ray, M. Charge Transfer Induced Encapsulation of Si Quantum Dots by Atomically Larger and Highly Lattice-Mismatched Au Nanoparticles. *J. Phys. Chem. C* **2014**, *118* (9), 5041–5050. https://doi.org/10.1021/jp500576k.

(60) Liu, P.; Chen, H.; Wang, H.; Yan, J.; Lin, Z.; Yang, G. Fabrication of Si/Au Core/Shell Nanoplasmonic Structures with Ultrasensitive Surface-Enhanced Raman Scattering for Monolayer Molecule Detection. *J. Phys. Chem. C* **2015**, *119* (2), 1234–1246. https://doi.org/10.1021/jp5111482.

(61) Saraeva, I. N.; Luong, N. V.; Kudryashov, S. I.; Rudenko, A. A.; Khmelnitskiy, R. A.; Shakhmin, A. L.; Kharin, A. Y.; Ionin, A. A.; Zayarny, D. A.; Tung, D. H.; Duong, P. V.; Minh, P. H. Laser Synthesis of Colloidal Si@Au and Si@Ag Nanoparticles in Water via Plasma-Assisted Reduction. *J. Photochem. Photobiol. Chem.* **2018**, *360*, 125–131. https://doi.org/10.1016/j.jphotochem.2018.04.004.

(62) Gerasimova, E. N.; Uvarov, E.; Yaroshenko, V. V.; Epifanovskaya, O.; Shakirova, A.; Logunov, L. S.; Vlasova, O.; Parodi, A.; Zamyatnin, A. A.; Timin, A. S.; Makarov, S. V.; Zyuzin, M. V. Single-Step Fabrication of Resonant Silicon–Gold Hybrid Nanoparticles for Efficient Optical Heating and Nanothermometry in Cells. *ACS Appl. Nano Mater.* **2023**, *6* (20), 18848–18857. https://doi.org/10.1021/acsanm.3c03189.

(63) Gurbatov, S. O.; Puzikov, V.; Storozhenko, D.; Modin, E.; Mitsai, E.; Cherepakhin, A.; Shevlyagin, A.; Gerasimenko, A. V.; Kulinich, S. A.; Kuchmizhak, A. A. Multigram-Scale Production of Hybrid Au-Si Nanomaterial by Laser Ablation in Liquid (LAL) for Temperature-Feedback Optical Nanosensing, Light-to-Heat Conversion, and Anticounterfeit Labeling. *ACS Appl. Mater. Interfaces* **2023**, *15* (2), 3336–3347. https://doi.org/10.1021/acsami.2c18999.

(64) Gurbatov, S. O.; Zhizhchenko, A. Yu.; Nesterov, V. Yu.; Modin, E. B.; Zabotnov, S. V.; Kuchmizhak, A. A. Au–Si Nanocomposites with High Near-IR Light-to-Heat Conversion Efficiency via Single-Step Reactive Laser Ablation of Porous Silicon for Theranostic Applications. *ACS Appl. Nano Mater.* **2024**, *7* (9), 10779–10786. https://doi.org/10.1021/acsanm.4c01289.

(65) Kutrovskaya, S.; Arakelian, S.; Kucherik, A.; Osipov, A.; Evlyukhin, A.; Kavokin, A. V. The Synthesis of Hybrid Gold-Silicon Nano Particles in a Liquid. *Sci. Rep.* **2017**, *7* (1), 10284. https://doi.org/10.1038/s41598-017-09634-y.

(66) Koromyslov, S.; Ageev, E.; Ponkratova, E.; Larin, A.; Shishkin, I.; Danilov, D.; Mukhin, I.; Makarov, S.; Zuev, D. Femtosecond Laser-Assisted Formation of Hybrid Nanoparticles from Bi-Layer Gold–Silicon Films for Microscale White-Light Source. *Nanomaterials* **2022**, *12* (10), 1756. https://doi.org/10.3390/nano12101756.

(67) Liu, W.; Miroshnichenko, A. E.; Neshev, D. N.; Kivshar, Y. S. Broadband Unidirectional Scattering by Magneto-Electric Core–Shell Nanoparticles. *ACS Nano* **2012**, *6* (6), 5489–5497. https://doi.org/10.1021/nn301398a.

(68) Liu, W.; Zhang, J.; Lei, B.; Ma, H.; Xie, W.; Hu, H. Ultra-Directional Forward Scattering by Individual Core-Shell Nanoparticles. *Opt. Express* **2014**, *22* (13), 16178. https://doi.org/10.1364/OE.22.016178.

(69) Rong, H.; Jones, R.; Liu, A.; Cohen, O.; Hak, D.; Fang, A.; Paniccia, M. A Continuous-Wave Raman Silicon Laser. *Nature* **2005**, *433* (7027), 725–728. https://doi.org/10.1038/nature03346.

(70) Sönnichsen, C.; Reinhard, B. M.; Liphardt, J.; Alivisatos, A. P. A Molecular Ruler Based on Plasmon Coupling of Single Gold and Silver Nanoparticles. *Nat. Biotechnol.* **2005**, *23* (6), 741–745. https://doi.org/10.1038/nbt1100.

(71) Parker, A. R.; McPhedran, R. C.; McKenzie, D. R.; Botten, L. C.; Nicorovici, N.-A. P. Aphrodite's Iridescence. *Nature* **2001**, *409* (6816), 36–37. https://doi.org/10.1038/35051168.

(72) Wiecha, P. R.; Cuche, A.; Arbouet, A.; Girard, C.; Colas Des Francs, G.; Lecestre, A.; Larrieu, G.; Fournel, F.; Larrey, V.; Baron, T.; Paillard, V. Strongly Directional Scattering from Dielectric Nanowires. *ACS Photonics* **2017**, *4* (8), 2036–2046. https://doi.org/10.1021/acsphotonics.7b00423.

(73) Wagner, R. S.; Ellis, W. C. VAPOR-LIQUID-SOLID MECHANISM OF SINGLE CRYSTAL GROWTH. *Appl. Phys. Lett.* **1964**, *4* (5), 89–90. https://doi.org/10.1063/1.1753975.

(74) Lu, W.; Lieber, C. M. Semiconductor Nanowires. *J. Phys. Appl. Phys.* **2006**, *39* (21), R387–R406. https://doi.org/10.1088/0022-3727/39/21/R01.

(75) Wu, Y.; Cui, Y.; Huynh, L.; Barrelet, C. J.; Bell, D. C.; Lieber, C. M. Controlled Growth and Structures of Molecular-Scale Silicon Nanowires. *Nano Lett.* **2004**, *4* (3), 433–436. https://doi.org/10.1021/nl035162i.

(76) Schmidt, V.; Senz, S.; Gösele, U. Diameter-Dependent Growth Direction of Epitaxial Silicon Nanowires. *Nano Lett.* **2005**, *5* (5), 931–935. https://doi.org/10.1021/nl050462g.

(77) Li, W.-N.; Ding, Y.-S.; Yuan, J.; Gomez, S.; Suib, S. L.; Galasso, F. S.; DiCarlo, J. F. Synthesis and Characterization of Silicon Nanowires on Mesophase Carbon Microbead Substrates by Chemical Vapor Deposition. *J. Phys. Chem. B* **2005**, *109* (8), 3291–3297. https://doi.org/10.1021/jp0449298.

(78) Nebol'sin, V. A.; Shchetinin, A. A.; Dolgachev, A. A.; Korneeva, V. V. Effect of the Nature of the Metal Solvent on the Vapor-Liquid-Solid Growth Rate of Silicon Whiskers. *Inorg. Mater.* **2005**, *41* (12), 1256–1259. https://doi.org/10.1007/s10789-005-0296-5.

(79) Wang, F.; Dong, A.; Buhro, W. E. Solution–Liquid–Solid Synthesis, Properties, and Applications of One-Dimensional Colloidal Semiconductor Nanorods and Nanowires. *Chem. Rev.* **2016**, *116* (18), 10888–10933. https://doi.org/10.1021/acs.chemrev.5b00701.

(80) Yu, L.; Alet, P.-J.; Picardi, G.; Roca I Cabarrocas, P. An In-Plane Solid-Liquid-Solid Growth Mode for Self-Avoiding Lateral Silicon Nanowires. *Phys. Rev. Lett.* **2009**, *102* (12), 125501. https://doi.org/10.1103/PhysRevLett.102.125501.

(81) Cosckun, A. U.; Yener, Y.; Arinc, F. Simulation of Dissolution of Silicon in an Indium Solution by Spectral Methods. *Model. Simul. Mater. Sci. Eng.* **2002**, *10* (5), 539–550. https://doi.org/10.1088/0965-0393/10/5/305.

(82) Pereira, L.; Barquinha, P.; Fortunato, E.; Martins, R. Influence of Metal Induced Crystallization Parameters on the Performance of Polycrystalline Silicon Thin Film Transistors. *Thin Solid Films* **2005**, *487* (1–2), 102–106. https://doi.org/10.1016/j.tsf.2005.01.045.

(83) Edy Edward Azrak. Growth and Characterization of In-Plane Solid-Liquid-Solid GeSn and SiSn Nanowires, Normandie Université, 2018. https://theses.hal.science/tel-02422227v1.

(84) Lensch-Falk, J. L.; Hemesath, E. R.; Perea, D. E.; Lauhon, L. J. Alternative Catalysts for VSS Growth of Silicon and Germanium Nanowires. *J. Mater. Chem.* **2009**, *19* (7), 849. https://doi.org/10.1039/b817391e.

(85) Kamins, T. I.; Stanley Williams, R.; Basile, D. P.; Hesjedal, T.; Harris, J. S. Ti-Catalyzed Si Nanowires by Chemical Vapor Deposition: Microscopy and Growth Mechanisms. *J. Appl. Phys.* **2001**, *89* (2), 1008–1016. https://doi.org/10.1063/1.1335640.

(86) Kuo, C. Y.; Gau, C. Vapor–Solid–Solid Growth of Crystalline Silicon Nanowires Using Anodic Aluminum Oxide Template. *Thin Solid Films* **2011**, *519* (11), 3603–3607. https://doi.org/10.1016/j.tsf.2011.01.280.

(87) Barth, S.; Seifner, M. S.; Maldonado, S. Metastable Group IV Allotropes and Solid Solutions: Nanoparticles and Nanowires. *Chem. Mater.* **2020**, *32* (7), 2703–2741. https://doi.org/10.1021/acs.chemmater.9b04471.

(88) Li, X.; Bohn, P. W. Metal-Assisted Chemical Etching in HF/H2O2 Produces Porous Silicon. *Appl. Phys. Lett.* **2000**, *77* (16), 2572–2574. https://doi.org/10.1063/1.1319191.

(89) Huang, Z.; Geyer, N.; Werner, P.; De Boor, J.; Gösele, U. Metal-Assisted Chemical Etching of Silicon: A Review: In Memory of Prof. Ulrich Gösele. *Adv. Mater.* **2011**, *23* (2), 285–308. https://doi.org/10.1002/adma.201001784.

(90) Peng, K. Q.; Hu, J. J.; Yan, Y. J.; Wu, Y.; Fang, H.; Xu, Y.; Lee, S. T.; Zhu, J. Fabrication of Single-Crystalline Silicon Nanowires by Scratching a Silicon Surface with Catalytic Metal Particles. *Adv. Funct. Mater.* **2006**, *16* (3), 387–394. https://doi.org/10.1002/adfm.200500392.

(91) Peng, K. Q.; Yan, Y. J.; Gao, S. P.; Zhu, J. Synthesis of Large-Area Silicon Nanowire Arrays via Self-Assembling Nanoelectrochemis-Try. *Adv. Mater.* **2002**, *14* (16), 1164. https://doi.org/10.1002/1521-4095(20020816)14:16.

(92) Asoh, H.; Arai, F.; Uchibori, K.; Ono, S. Pt–Pd-Embedded Silicon Microwell Arrays. *Appl. Phys. Express* **2008**, *1*, 067003. https://doi.org/10.1143/APEX.1.067003.

(93) Lee, J.-P.; Choi, S.; Park, S. Extremely Superhydrophobic Surfaces with Micro- and Nanostructures Fabricated by Copper Catalytic Etching. *Langmuir* **2011**, *27* (2), 809–814. https://doi.org/10.1021/la1045354.

(94) Asoh, H.; Arai, F.; Ono, S. Effect of Noble Metal Catalyst Species on the Morphology of Macroporous Silicon Formed by Metal-Assisted Chemical Etching. *Electrochimica Acta* **2009**, *54* (22), 5142–5148. https://doi.org/10.1016/j.electacta.2009.01.050.

(95) Kapaklis, V.; Georgiopoulos, A.; Poulopoulos, P.; Politis, C. Patterning of Porous Silicon by Metal-Assisted Chemical Etching under Open Circuit Potential Conditions. *Phys. E Low-Dimens. Syst. Nanostructures* **2007**, *38* (1–2), 44–49. https://doi.org/10.1016/j.physe.2006.12.055.

(96) Chattopadhyay, S.; Bohn, P. W. Surfactant-Induced Modulation of Light Emission in Porous Silicon Produced by Metal-Assisted Electroless Etching. *Anal. Chem.* **2006**, *78* (17), 6058–6064. https://doi.org/10.1021/ac060411j.

(97) Wendisch, F. J.; Abazari, M.; Mahdavi, H.; Rey, M.; Vogel, N.; Musso, M.; Diwald, O.; Bourret, G. R. Morphology-Graded Silicon Nanowire Arrays via Chemical Etching: Engineering Optical Properties at the Nanoscale and Macroscale. *ACS Appl. Mater. Interfaces* **2020**, *12* (11), 13140–13147. https://doi.org/10.1021/acsami.9b21466.

(98) Wendisch, F. J.; Rey, M.; Vogel, N.; Bourret, G. R. Large-Scale Synthesis of Highly Uniform Silicon Nanowire Arrays Using Metal-Assisted Chemical Etching. *Chem. Mater.* **2020**, *32* (21), 9425–9434. https://doi.org/10.1021/acs.chemmater.0c03593.

(99) Chartier, C.; Bastide, S.; Lévy-Clément, C. Metal-Assisted Chemical Etching of Silicon in HF–H2O2. *Electrochimica Acta* **2008**, *53* (17), 5509–5516. https://doi.org/10.1016/j.electacta.2008.03.009.

(100) Walch, S. P.; Dateo, C. E. Thermal Decomposition Pathways and Rates for Silane, Chlorosilane, Dichlorosilane, and Trichlorosilane. *J. Phys. Chem. A* **2001**, *105* (10), 2015–2022. https://doi.org/10.1021/jp003559u.

(101) Hogness, T. R.; Wilson, T. L.; Johnson, W. C. The Thermal Decomposition of Silane. *J. Am. Chem. Soc.* **1936**, *58* (1), 108–112. https://doi.org/10.1021/ja01292a036.

(102) Wang, I.-T.; Liu, T.-R.; Liu, Y.-L.; Chen, C.-Y.; Chang, C.; Cheng, C.-T.; Wen, C.-Y. Investigation of the Cross-Sectional Morphology of Epitaxial Si Nanowires Grown by Chemical Vapor Deposition for the Fabrication of Vertical Devices. *Mater. Sci. Eng. B* **2022**, *281*, 115748. https://doi.org/10.1016/j.mseb.2022.115748.

(103) Harris, B. Whisker Technology. *Nat. Phys. Sci.* **1971**, *232* (28), 47–47. https://doi.org/10.1038/physci232047b0.

(104) Chan, C. K.; Peng, H.; Liu, G.; McIlwrath, K.; Zhang, X. F.; Huggins, R. A.; Cui, Y. High-Performance Lithium Battery Anodes Using Silicon Nanowires. *Nat. Nanotechnol.* **2008**, *3* (1), 31–35. https://doi.org/10.1038/nnano.2007.411.

(105) Hainey, M.; Eichfeld, S. M.; Shen, H.; Yim, J.; Black, M. R.; Redwing, J. M. Aluminum-Catalyzed Growth of ‹110› Silicon Nanowires. *J. Electron. Mater.* **2015**, *44* (5), 1332–1337. https://doi.org/10.1007/s11664-014-3565-8.

(106) Ly, L. Q.; Cordoba, C.; Blackburn, A.; Shi, Y. Platinum-Catalyzed Silicon Nanowire Growth─Evidence for a Switch from Vapor–Liquid–Solid to Vapor–Solid–Solid Mechanism with Platinum Nanoparticle Size. *J. Phys. Chem. C* **2024**, *128* (35), 14811–14823. https://doi.org/10.1021/acs.jpcc.4c03659.

(107) Cerruti, M.; Doerk, G.; Hernandez, G.; Carraro, C.; Maboudian, R. Galvanic Deposition of Pt Clusters on Silicon: Effect of HF Concentration and Application as Catalyst for

Silicon Nanowire Growth. *Langmuir* **2010**, *26* (1), 432–437. https://doi.org/10.1021/la902032x.

(108) Garnett, E. C.; Liang, W.; Yang, P. Growth and Electrical Characteristics of Platinum-Nanoparticle-Catalyzed Silicon Nanowires. *Adv. Mater.* **2007**, *19* (19), 2946–2950. https://doi.org/10.1002/adma.200700288.

(109) Bootsma, G. A.; Gassen, H. J. A Quantitative Study on the Growth of Silicon Whiskers from Silane and Germanium Whiskers from Germane. *J. Cryst. Growth* **1971**, *10* (3), 223–234. https://doi.org/10.1016/0022-0248(71)90188-6.

(110) Iacopi, F.; Vereecken, P. M.; Schaekers, M.; Caymax, M.; Moelans, N.; Blanpain, B.; Richard, O.; Detavernier, C.; Griffiths, H. Plasma-Enhanced Chemical Vapour Deposition Growth of Si Nanowires with Low Melting Point Metal Catalysts: An Effective Alternative to Au-Mediated Growth. *Nanotechnology* **2007**, *18* (50), 505307. https://doi.org/10.1088/0957-4484/18/50/505307.

(111) Shah, P. S.; Holmes, J. D.; Johnston, K. P.; Korgel, B. A. Size-Selective Dispersion of Dodecanethiol-Coated Nanocrystals in Liquid and Supercritical Ethane by Density Tuning. *J. Phys. Chem. B* **2002**, *106* (10), 2545–2551. https://doi.org/10.1021/jp013931l.

(112) Lu, X.; Hanrath, T.; Johnston, K. P.; Korgel, B. A. Growth of Single Crystal Silicon Nanowires in Supercritical Solution from Tethered Gold Particles on a Silicon Substrate. *Nano Lett.* **2003**, *3* (1), 93–99. https://doi.org/10.1021/nl0202307.

(113) Lee, D. C.; Hanrath, T.; Korgel, B. A. The Role of Precursor-Decomposition Kinetics in Silicon-Nanowire Synthesis in Organic Solvents. *Angew. Chem. Int. Ed.* **2005**, *44* (23), 3573–3577. https://doi.org/10.1002/anie.200463001.

(114) Pell, L. E.; Schricker, A. D.; Mikulec, F. V.; Korgel, B. A. Synthesis of Amorphous Silicon Colloids by Trisilane Thermolysis in High Temperature Supercritical Solvents. *Langmuir* **2004**, *20* (16), 6546–6548. https://doi.org/10.1021/la048671o.

(115) Tuan, H.-Y.; Korgel, B. A. Importance of Solvent-Mediated Phenylsilane Decompositon Kinetics for High-Yield Solution-Phase Silicon Nanowire Synthesis. *Chem. Mater.* **2008**, *20* (4), 1239–1241. https://doi.org/10.1021/cm7033068.

(116) Chockla, A. M.; Harris, J. T.; Akhavan, V. A.; Bogart, T. D.; Holmberg, V. C.; Steinhagen, C.; Mullins, C. B.; Stevenson, K. J.; Korgel, B. A. Silicon Nanowire Fabric as a Lithium Ion Battery Electrode Material. *J. Am. Chem. Soc.* **2011**, *133* (51), 20914–20921. https://doi.org/10.1021/ja208232h.

(117) Heitsch, A. T.; Fanfair, D. D.; Tuan, H.-Y.; Korgel, B. A. Solution−Liquid−Solid (SLS) Growth of Silicon Nanowires. *J. Am. Chem. Soc.* **2008**, *130* (16), 5436–5437. https://doi.org/10.1021/ja8011353.

(118) Heitsch, A. T.; Hessel, C. M.; Akhavan, V. A.; Korgel, B. A. Colloidal Silicon Nanorod Synthesis. *Nano Lett.* **2009**, *9* (8), 3042–3047. https://doi.org/10.1021/nl901520t.

(119) Lu, X.; Anderson, K. J.; Boudjouk, P.; Korgel, B. A. Low Temperature Colloidal Synthesis of Silicon Nanorods from Isotetrasilane, Neopentasilane, and Cyclohexasilane. *Chem. Mater.* **2015**, *27* (17), 6053–6058. https://doi.org/10.1021/acs.chemmater.5b02487.

(120) Pan, Z. W.; Dai, Z. R.; Xu, L.; Lee, S. T.; Wang, Z. L. Temperature-Controlled Growth of Silicon-Based Nanostructures by Thermal Evaporation of SiO Powders. *J. Phys. Chem. B* **2001**, *105* (13), 2507–2514. https://doi.org/10.1021/jp004253q.

(121) Hass, G.; Salzberg, C. D. Optical Properties of Silicon Monoxide in the Wavelength Region from 024 to 140 Microns*. *J. Opt. Soc. Am.* **1954**, *44* (3), 181. https://doi.org/10.1364/JOSA.44.000181.

(122) Lim, K. W.; Lee, J.-I.; Yang, J.; Kim, Y.-K.; Jeong, H. Y.; Park, S.; Shin, H. S. Catalyst-Free Synthesis of Si-$SiO_x$ Core-Shell Nanowire Anodes for High-Rate and High-Capacity Lithium-Ion Batteries. *ACS Appl. Mater. Interfaces* **2014**, *6* (9), 6340–6345. https://doi.org/10.1021/am405618m.

(123) Zhang, Y. F.; Tang, Y. H.; Lam, C.; Wang, N.; Lee, C. S.; Bello, I.; Lee, S. T. Bulk-Quantity Si Nanowires Synthesized by SiO Sublimation. *J. Cryst. Growth* **2000**, *212* (1–2), 115–118. https://doi.org/10.1016/S0022-0248(00)00238-4.

(124) Spence, G. C.; Barbieri, R. C.; Pate, D.; Graves, L. S.; Özgür, Ü.; Arachchige, I. U. Sn-Induced Synthesis of Highly Crystalline and Size-Confined Si Nanorods at Moderately High Temperatures Using Hydrogen Silsesquioxane. *J. Phys. Chem. C* **2023**, *127* (24), 11579–11590. https://doi.org/10.1021/acs.jpcc.3c01308.

(125) Puglisi, R. A.; Bongiorno, C.; Caccamo, S.; Fazio, E.; Mannino, G.; Neri, F.; Scalese, S.; Spucches, D.; La Magna, A. Chemical Vapor Deposition Growth of Silicon Nanowires with Diameter Smaller Than 5 Nm. *ACS Omega* **2019**, *4* (19), 17967–17971. https://doi.org/10.1021/acsomega.9b01488.

(126) Cui, Y.; Lauhon, L. J.; Gudiksen, M. S.; Wang, J.; Lieber, C. M. Diameter-Controlled Synthesis of Single-Crystal Silicon Nanowires. *Appl. Phys. Lett.* **2001**, *78* (15), 2214–2216. https://doi.org/10.1063/1.1363692.

(127) Hochbaum, A. I.; Fan, R.; He, R.; Yang, P. Controlled Growth of Si Nanowire Arrays for Device Integration. *Nano Lett.* **2005**, *5* (3), 457–460. https://doi.org/10.1021/nl047990x.

(128) Kayes, B. M.; Filler, M. A.; Putnam, M. C.; Kelzenberg, M. D.; Lewis, N. S.; Atwater, H. A. Growth of Vertically Aligned Si Wire Arrays over Large Areas (>1cm2) with Au and Cu Catalysts. *Appl. Phys. Lett.* **2007**, *91* (10), 103110. https://doi.org/10.1063/1.2779236.

(129) Tilve-Martinez, D.; Abomailek, N.; Lozano-Steinmetz, F.; Pendashteh, A.; Vilatela, J. J. Silicon Nanowire Aqueous Dispersions for Processing into Macroscopic Network Materials. *Chem. Commun.* **2024**, *60* (76), 10592–10595. https://doi.org/10.1039/D4CC02645D.

(130) Lombardi, I.; Hochbaum, A. I.; Yang, P.; Carraro, C.; Maboudian, R. Synthesis of High Density, Size-Controlled Si Nanowire Arrays via Porous Anodic Alumina Mask. *Chem. Mater.* **2006**, *18* (4), 988–991. https://doi.org/10.1021/cm052435x.

(131) Kendrick, C. E.; Redwing, J. M. The Effect of Pattern Density and Wire Diameter on the Growth Rate of Micron Diameter Silicon Wires. *J. Cryst. Growth* **2011**, *337* (1), 1–6. https://doi.org/10.1016/j.jcrysgro.2011.09.049.

(132) Aella, P.; Ingole, S.; Petuskey, W. T.; Picraux, S. T. Influence of Plasma Stimulation on Si Nanowire Nucleation and Orientation Dependence. *Adv. Mater.* **2007**, *19* (18), 2603–2607. https://doi.org/10.1002/adma.200602944.

(133) Zheng, J.; Yang, R.; Xie, L.; Qu, J.; Liu, Y.; Li, X. Plasma-Assisted Approaches in Inorganic Nanostructure Fabrication. *Adv. Mater.* **2010**, *22* (13), 1451–1473. https://doi.org/10.1002/adma.200903147.

(134) Hofmann, S.; Ducati, C.; Neill, R. J.; Piscanec, S.; Ferrari, A. C.; Geng, J.; Dunin-Borkowski, R. E.; Robertson, J. Gold Catalyzed Growth of Silicon Nanowires by Plasma Enhanced Chemical Vapor Deposition. *J. Appl. Phys.* **2003**, *94* (9), 6005–6012. https://doi.org/10.1063/1.1614432.

(135) Ball, J.; Bowen, L.; Mendis, B. G.; Reehal, H. S. Low Pressure Plasma Assisted Silicon Nanowire Growth from Self Organised Tin Catalyst Particles. *CrystEngComm* **2013**, *15* (19), 3808. https://doi.org/10.1039/c3ce00036b.

(136) Rathi, S. J.; Jariwala, B. N.; Beach, J. D.; Stradins, P.; Taylor, P. C.; Weng, X.; Ke, Y.; Redwing, J. M.; Agarwal, S.; Collins, R. T. Tin-Catalyzed Plasma-Assisted Growth of Silicon Nanowires. *J. Phys. Chem. C* **2011**, *115* (10), 3833–3839. https://doi.org/10.1021/jp1066428.

(137) Adachi, M. M.; Anantram, M. P.; Karim, K. S. Optical Properties of Crystalline−Amorphous Core−Shell Silicon Nanowires. *Nano Lett.* **2010**, *10* (10), 4093–4098. https://doi.org/10.1021/nl102183x.

(138) Geaney, H.; Kennedy, T.; Dickinson, C.; Mullane, E.; Singh, A.; Laffir, F.; Ryan, K. M. High Density Growth of Indium Seeded Silicon Nanowires in the Vapor Phase of a High Boiling Point Solvent. *Chem. Mater.* **2012**, *24* (11), 2204–2210. https://doi.org/10.1021/cm301023j.

(139) Mullane, E.; Kennedy, T.; Geaney, H.; Dickinson, C.; Ryan, K. M. Synthesis of Tin Catalyzed Silicon and Germanium Nanowires in a Solvent–Vapor System and Optimization of the Seed/Nanowire Interface for Dual Lithium Cycling. *Chem. Mater.* **2013**, *25* (9), 1816–1822. https://doi.org/10.1021/cm400367v.

(140) Bogart, T. D.; Lu, X.; Korgel, B. A. Precision Synthesis of Silicon Nanowires with Crystalline Core and Amorphous Shell. *Dalton Trans.* **2013**, *42* (35), 12675. https://doi.org/10.1039/c3dt50875g.

(141) Chan, C. K.; Patel, R. N.; O'Connell, M. J.; Korgel, B. A.; Cui, Y. Solution-Grown Silicon Nanowires for Lithium-Ion Battery Anodes. *ACS Nano* **2010**, *4* (3), 1443–1450. https://doi.org/10.1021/nn901409q.

(142) Hanrath, T.; Korgel, B. A. Supercritical Fluid–Liquid–Solid (SFLS) Synthesis of Si and Ge Nanowires Seeded by Colloidal Metal Nanocrystals. *Adv. Mater.* **2003**, *15* (5), 437–440. https://doi.org/10.1002/adma.200390101.

(143) Holmes, J. D.; Johnston, K. P.; Doty, R. C.; Korgel, B. A. Control of Thickness and Orientation of Solution-Grown Silicon Nanowires. *Science* **2000**, *287* (5457), 1471–1473. https://doi.org/10.1126/science.287.5457.1471.

(144) Tuan, H.-Y.; Lee, D. C.; Hanrath, T.; Korgel, B. A. Catalytic Solid-Phase Seeding of Silicon Nanowires by Nickel Nanocrystals in Organic Solvents. *Nano Lett.* **2005**, *5* (4), 681–684. https://doi.org/10.1021/nl050099d.

(145) Chockla, A. M.; Harris, J. T.; Akhavan, V. A.; Bogart, T. D.; Holmberg, V. C.; Steinhagen, C.; Mullins, C. B.; Stevenson, K. J.; Korgel, B. A. Silicon Nanowire Fabric as a Lithium Ion Battery Electrode Material. *J. Am. Chem. Soc.* **2011**, *133* (51), 20914–20921. https://doi.org/10.1021/ja208232h.

(146) Jifa Qi, J. Q.; Takahiro Matsumoto, T. M.; Yasuaki Masumoto, Y. M. Characterizations of Simultaneously Fabricated Silicon and Silicon Monoxide Nanowires. *Jpn. J. Appl. Phys.* **2001**, *40* (2B), L134. https://doi.org/10.1143/JJAP.40.L134.

(147) Zhang, M.-L.; Fan, X.; Jie, J.-S.; Hsu, J.-P.; Wong, N.-B. Millimeter-Long and Uniform Silicon Nanocables. *J. Phys. Chem. C* **2008**, *112* (41), 15943–15947. https://doi.org/10.1021/jp802110y.

(148) Wang, Z.; An, N.; Shen, F.; Zhou, H.; Sun, Y.; Jiang, Z.; Han, Y.; Li, Y.; Guo, Z. Enhanced Forward Scattering of Ellipsoidal Dielectric Nanoparticles. *Nanoscale Res. Lett.* **2017**, *12* (1), 58. https://doi.org/10.1186/s11671-016-1794-x.

(149) Luk'yanchuk, B. S.; Voshchinnikov, N. V.; Paniagua-Domínguez, R.; Kuznetsov, A. I. Optimum Forward Light Scattering by Spherical and Spheroidal Dielectric Nanoparticles with High Refractive Index. *ACS Photonics* **2015**, *2* (7), 993–999. https://doi.org/10.1021/acsphotonics.5b00261.

(150) Zywietz, U.; Schmidt, M. K.; Evlyukhin, A. B.; Reinhardt, C.; Aizpurua, J.; Chichkov, B. N. Electromagnetic Resonances of Silicon Nanoparticle Dimers in the Visible. *ACS Photonics* **2015**, *2* (7), 913–920. https://doi.org/10.1021/acsphotonics.5b00105.

(151) Zywietz, U.; Reinhardt, C.; Evlyukhin, A. B.; Birr, T.; Chichkov, B. N. Generation and Patterning of Si Nanoparticles by Femtosecond Laser Pulses. *Appl. Phys. A* **2014**, *114* (1), 45–50. https://doi.org/10.1007/s00339-013-8007-6.

(152) Gulkin, D. N.; Popkova, A. A.; Afinogenov, B. I.; Shilkin, D. A.; Kuršelis, K.; Chichkov, B. N.; Bessonov, V. O.; Fedyanin, A. A. Mie-Driven Directional Nanocoupler for Bloch Surface Wave Photonic Platform. *Nanophotonics* **2021**, *10* (11), 2939–2947. https://doi.org/10.1515/nanoph-2021-0295.

(153) Makarov, S.; Kolotova, L.; Starikov, S.; Zywietz, U.; Chichkov, B. Resonant Silicon Nanoparticles with Controllable Crystalline States and Nonlinear Optical Responses. *Nanoscale* **2018**, *10* (24), 11403–11409. https://doi.org/10.1039/C8NR02057D.

(154) Hao, N.; Li, L.; Tang, F. Roles of Particle Size, Shape and Surface Chemistry of Mesoporous Silica Nanomaterials on Biological Systems. *Int. Mater. Rev.* **2017**, *62* (2), 57–77. https://doi.org/10.1080/09506608.2016.1190118.

(155) Dawi, E. A.; Mustafa, E.; Siahaan, T. Anisotropic Deformation of Colloidal Particles under 4 MeV Cu Ions Irradiation. *Mater. Res. Express* **2022**, *9* (8), 086506. https://doi.org/10.1088/2053-1591/ac87ef.

(156) Penninkhof, J. J.; Van Dillen, T.; Roorda, S.; Graf, C.; Van Blaaderen, A.; Vredenberg, A. M.; Polman, A. Anisotropic Deformation of Metallo-Dielectric Core–Shell Colloids under MeV Ion Irradiation. *Nucl. Instrum. Methods Phys. Res. Sect. B Beam Interact. Mater. At.* **2006**, *242* (1–2), 523–529. https://doi.org/10.1016/j.nimb.2005.08.116.

(157) Deng, T.; Cournoyer, J. R.; Schermerhorn, J. H.; Balch, J.; Du, Y.; Blohm, M. L. Generation and Assembly of Spheroid-like Particles. *J. Am. Chem. Soc.* **2008**, *130* (44), 14396–14397. https://doi.org/10.1021/ja805278x.

(158) Benke, D.; Feller, T.; Krüsmann, M.; Neuhöfer, A. M.; Ganster, F.; Karg, M.; Retsch, M. Prolate Spheroidal Polystyrene Nanoparticles: Matrix Assisted Synthesis, Interface Properties, and Scattering Analysis. *Soft Matter* **2023**, *19* (46), 9006–9016. https://doi.org/10.1039/D3SM01002C.

(159) Champion, J. A.; Katare, Y. K.; Mitragotri, S. Making Polymeric Micro- and Nanoparticles of Complex Shapes. *Proc. Natl. Acad. Sci.* **2007**, *104* (29), 11901–11904. https://doi.org/10.1073/pnas.0705326104.

(160) Xu, S.; Nie, Z.; Seo, M.; Lewis, P.; Kumacheva, E.; Stone, H. A.; Garstecki, P.; Weibel, D. B.; Gitlin, I.; Whitesides, G. M. Generation of Monodisperse Particles by Using Microfluidics: Control over Size, Shape, and Composition. *Angew. Chem. Int. Ed.* **2005**, *44* (5), 724–728. https://doi.org/10.1002/anie.200462226.

(161) Zhang, X.; Niu, Y.; Yang, Y.; Li, Y.; Zhao, J. Preparation and Magnetic Properties of γ-$Fe_2$ $O_3$ @$SiO_2$ Core Shell Ellipsoids with Different Aspect Ratios. *New J. Chem.* **2014**, *38* (9), 4351. https://doi.org/10.1039/C4NJ00389F.

(162) Candreva, A.; Lewandowski, W.; La Deda, M. Thickness Control of the Silica Shell: A Way to Tune the Plasmonic Properties of Isolated and Assembled Gold Nanorods. *J. Nanoparticle Res.* **2022**, *24* (2), 19. https://doi.org/10.1007/s11051-022-05402-w.

(163) Sacanna, S.; Rossi, L.; Kuipers, B. W. M.; Philipse, A. P. Fluorescent Monodisperse Silica Ellipsoids for Optical Rotational Diffusion Studies. *Langmuir* **2006**, *22* (4), 1822–1827. https://doi.org/10.1021/la052484o.

(164) Wu, Z.; Liang, Y.; Guo, Q.; Zhang, K.; Liang, S.; Yang, L.; Xiao, Q.; Wang, D. Study on Selective Oxidations of Gold Nanorod and Mesoporous Silica-Coated Gold Nanorod. *J. Mater. Sci.* **2019**, *54* (11), 8133–8147. https://doi.org/10.1007/s10853-019-03429-4.

(165) Deng, T.-S.; Van Der Hoeven, J. E. S.; Yalcin, A. O.; Zandbergen, H. W.; Van Huis, M. A.; Van Blaaderen, A. Oxidative Etching and Metal Overgrowth of Gold Nanorods within Mesoporous Silica Shells. *Chem. Mater.* **2015**, *27* (20), 7196–7203. https://doi.org/10.1021/acs.chemmater.5b03749.

(166) Choi, E.; Kwak, M.; Jang, B.; Piao, Y. Highly Monodisperse Rattle-Structured Nanomaterials with Gold Nanorod Core–Mesoporous Silica Shell as Drug Delivery Vehicles and Nanoreactors. *Nanoscale* **2013**, *5* (1), 151–154. https://doi.org/10.1039/C2NR32885B.

(167) Wang, K.; Deng, T.; Zhang, E.; Gao, J.; Liu, J. Controlled Etching of Gold Nanorods Within Mesoporous Silica Shells at Mild Conditions. *Part. Part. Syst. Charact.* **2025**, *42* (3), 2400144. https://doi.org/10.1002/ppsc.202400144.

(168) Van Der Hoeven, J. E. S.; Deng, T.-S.; Albrecht, W.; Olthof, L. A.; Van Huis, M. A.; De Jongh, P. E.; Van Blaaderen, A. Structural Control over Bimetallic Core–Shell Nanorods for Surface-Enhanced Raman Spectroscopy. *ACS Omega* **2021**, *6* (10), 7034–7046. https://doi.org/10.1021/acsomega.0c06321.

(169) Peck, K. A.; Lien, J.; Su, M.; Stacy, A. D.; Guo, T. Bottom-Up Then Top-Down Synthesis of Gold Nanostructures Using Mesoporous Silica-Coated Gold Nanorods. *ACS Omega* **2023**, *8* (45), 42667–42677. https://doi.org/10.1021/acsomega.3c05444.

(170) Zhang, H.; Bandosz, T. J.; Akins, D. L. Template-Free Synthesis of Silica Ellipsoids. *Chem. Commun.* **2011**, *47* (27), 7791. https://doi.org/10.1039/c1cc11787d.

(171) Shen, S.; Gu, T.; Mao, D.; Xiao, X.; Yuan, P.; Yu, M.; Xia, L.; Ji, Q.; Meng, L.; Song, W.; Yu, C.; Lu, G. Synthesis of Nonspherical Mesoporous Silica Ellipsoids with Tunable Aspect Ratios for Magnetic Assisted Assembly and Gene Delivery. *Chem. Mater.* **2012**, *24* (1), 230–235. https://doi.org/10.1021/cm203434k.

(172) Han, L.; Zhou, Y.; He, T.; Song, G.; Wu, F.; Jiang, F.; Hu, J. One-Pot Morphology-Controlled Synthesis of Various Shaped Mesoporous Silica Nanoparticles. *J. Mater. Sci.* **2013**, *48* (17), 5718–5726. https://doi.org/10.1007/s10853-013-7501-8.

(173) Hao, N.; Li, L.; Tang, F. Facile Preparation of Ellipsoid-like MCM-41 with Parallel Channels along the Short Axis for Drug Delivery and Assembly of Ag Nanoparticles for Catalysis. *J. Mater. Chem. A* **2014**, *2* (30), 11565. https://doi.org/10.1039/C4TA01820F.

(174) Stöber, W.; Fink, A.; Bohn, E. Controlled Growth of Monodisperse Silica Spheres in the Micron Size Range. *J. Colloid Interface Sci.* **1968**, *26* (1), 62–69. https://doi.org/10.1016/0021-9797(68)90272-5.

(175) Schumacher, K.; Ravikovitch, P. I.; Du Chesne, A.; Neimark, A. V.; Unger, K. K. Characterization of MCM-48 Materials. *Langmuir* **2000**, *16* (10), 4648–4654. https://doi.org/10.1021/la991595i.

(176) Teng, Z.; Han, Y.; Li, J.; Yan, F.; Yang, W. Preparation of Hollow Mesoporous Silica Spheres by a Sol–Gel/Emulsion Approach. *Microporous Mesoporous Mater.* **2010**, *127* (1–2), 67–72. https://doi.org/10.1016/j.micromeso.2009.06.028.

(177) Hao, N.; Nie, Y.; Tadimety, A.; Closson, A. B.; Zhang, J. X. J. Microfluidics-Mediated Self-Template Synthesis of Anisotropic Hollow Ellipsoidal Mesoporous Silica Nanomaterials. *Mater. Res. Lett.* **2017**, *5* (8), 584–590. https://doi.org/10.1080/21663831.2017.1376720.

(178) Travaglini, L.; De Cola, L. Morphology Control of Mesoporous Silica Particles Using Bile Acids as Cosurfactants. *Chem. Mater.* **2018**, *30* (12), 4168–4175. https://doi.org/10.1021/acs.chemmater.8b01873.

(179) Bao, Z.; Weatherspoon, M. R.; Shian, S.; Cai, Y.; Graham, P. D.; Allan, S. M.; Ahmad, G.; Dickerson, M. B.; Church, B. C.; Kang, Z.; Abernathy Iii, H. W.; Summers, C. J.; Liu, M.; Sandhage, K. H. Chemical Reduction of Three-Dimensional Silica Micro-Assemblies into Microporous Silicon Replicas. *Nature* **2007**, *446* (7132), 172–175. https://doi.org/10.1038/nature05570.

(180) Deqing, W.; Ziyuan, S. Aluminothermic Reduction of Silica for the Synthesis of Alumina-Aluminum-Silicon Composite. *J. Mater. Synth. Process.* **2001**, *9* (5), 241–246. https://doi.org/10.1023/A:1015295200586.

(181) Nguyen, T.-D.; Hamad, W. Y.; MacLachlan, M. J. Hard Photonic Glasses and Corundum Nanostructured Films from Aluminothermic Reduction of Helicoidal Mesoporous Silicas. *Chem. Mater.* **2016**, *28* (8), 2581–2588. https://doi.org/10.1021/acs.chemmater.5b04700.

(182) Wang, J.-F.; Wang, K.-X.; Du, F.-H.; Guo, X.-X.; Jiang, Y.-M.; Chen, J.-S. Amorphous Silicon with High Specific Surface Area Prepared by a Sodiothermic Reduction Method for Supercapacitors. *Chem. Commun.* **2013**, *49* (44), 5007. https://doi.org/10.1039/c3cc41967c.

(183) Yoo, J.; Kim, J.; Choi, M.; Park, Y.; Hong, J.; Baek, K. M.; Kang, K.; Jung, Y. S. Extremely High Yield Conversion from Low-Cost Sand to High-Capacity Si Electrodes for Li-Ion Batteries. *Adv. Energy Mater.* **2014**, *4* (16), 1400622. https://doi.org/10.1002/aenm.201400622.

(184) Ibisate, M.; Golmayo, D.; López, C. Silicon Direct Opals. *Adv. Mater.* **2009**, *21* (28), 2899–2902. https://doi.org/10.1002/adma.200900188.

(185) Qiu, D.; Bu, G.; Zhao, B.; Lin, Z. Mesoporous Silicon Microspheres Fabricated via in Situ Magnesiothermic Reduction of Silicon Oxide as a High-Performance Anode Material

for Lithium–Ion Batteries. *J. Solid State Electrochem.* **2015**, *19* (3), 935–939. https://doi.org/10.1007/s10008-014-2693-7.

(186) Xie, J.; Wang, G.; Huo, Y.; Zhang, S.; Cao, G.; Zhao, X. Nanostructured Silicon Spheres Prepared by a Controllable Magnesiothermic Reduction as Anode for Lithium Ion Batteries. *Electrochimica Acta* **2014**, *135*, 94–100. https://doi.org/10.1016/j.electacta.2014.05.012.

(187) Chen, K.; Bao, Z.; Shen, J.; Wu, G.; Zhou, B.; Sandhage, K. H. Freestanding Monolithic Silicon Aerogels. *J. Mater. Chem.* **2012**, *22* (32), 16196. https://doi.org/10.1039/c2jm31662e.

(188) Bao, Z.; Ernst, E. M.; Yoo, S.; Sandhage, K. H. Syntheses of Porous Self-Supporting Metal-Nanoparticle Assemblies with 3D Morphologies Inherited from Biosilica Templates (Diatom Frustules). *Adv. Mater.* **2009**, *21* (4), 474–478. https://doi.org/10.1002/adma.200801499.

# CHAPTER 2. Experimental methods

2.1 Introduction ..... 97
2.2 Dark-field optical microscopy and scattering spectroscopy ..... 97
2.3 Electron energy loss spectroscopy (EELS) ..... 99
2.4 Optical absorption (UV-vis-IR) ..... 102
2.5 Raman spectroscopy ..... 102
2.6 Dynamic Light Scattering (DLS) ..... 104
2.7 Small-Angle X-ray Scattering (SAXS) ..... 107
2.8 X-ray powder diffraction (XRD) ..... 109
2.9 Fourier transform infrared spectroscopy (FTIR) ..... 110
2.10 Solid-state Nuclear Magnetic Resonance (NMR) Spectroscopy ..... 112
2.11 Optical levitodynamics ..... 113
2.12 Transmission Electron Microscopy (TEM) ..... 115
2.13 Scanning Transmission Electron Microscopy (STEM) ..... 118
2.14 Energy-dispersive X-ray spectroscopy (EDS) ..... 120
2.15 In-situ Transmission Electron Microscopy (TEM) ..... 121
2.16 Scanning Electron Microscopy (SEM) ..... 124
2.17 Thermogravimetric analysis (TGA) ..... 126
2.18 Brunauer–Emmett–Teller (BET) ..... 126
2.19 Mie theory, T-matrix simulations, and simulated EELS spectra ..... 126
References ..... 127

## 2.1 Introduction

The optical properties of the fabricated nanostructures are studied by single nano-object scattering spectroscopy and electron energy loss spectroscopy (EELS). In the following two sections, the instrumentation of these techniques and the post-processing analysis performed on the EELS raw data to extract plasmonic information are discussed. Figure 2.1 shows the basic principles of optical and electron excitation for these two methods[1].

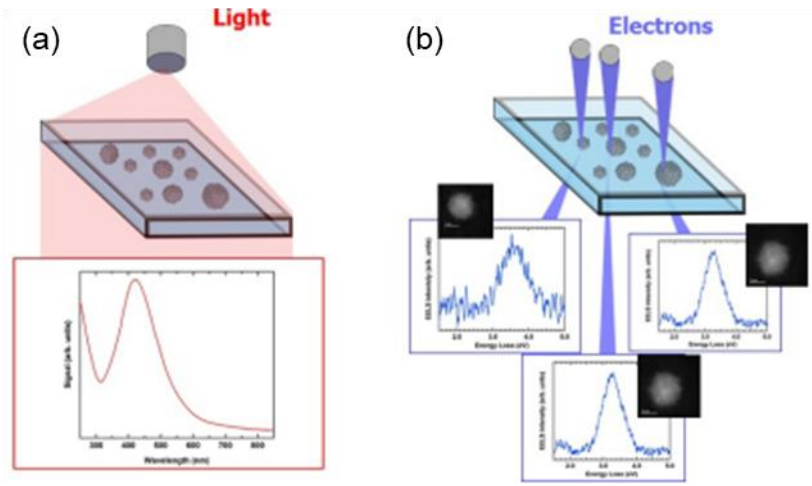



*Figure 2.1 Schematic illustration of the basic principle of the optical scattering and EELS spectroscopy. Reproduced from ref.*[1]

## 2.2 Dark-field optical microscopy and scattering spectroscopy

Dark-field microscopy is a technique based on indirect sample illumination. The light-focusing condenser is equipped with a circular opaque light-stopper preventing the direct illumination of the sample. Unlike in bright-field illumination, where the specimen is illuminated by a directly-focused light producing dark images on a white background, in dark-field microscopy, only peripheral light illuminates the specimen. At the same time, the light-stopper cuts off the direct light. This results in bright images on a dark background. Dark-field sample illumination produces a hollow light cone focused onto the glass slides on which the sample is deposited[2]. The illuminating light rays are being reflected and scattered by the sample particles. Hence, only the light that is scattered by the particles reaches the objective lens (Figure 2.2a). Based on the Tyndall effect, particles that are much smaller than the limit of optical microscope resolution can be visualized (inset: Figure 2.2a). The imaging of plasmon-resonant nanoparticles (such as Ag or Au) results in intense Rayleigh light scattering due to enhanced light absorption and scattering by surfaces conducting electrons. The darkfield images of the sample were observed using the Nikon Eclipse LV100ND microscope (Figure 2.2b).

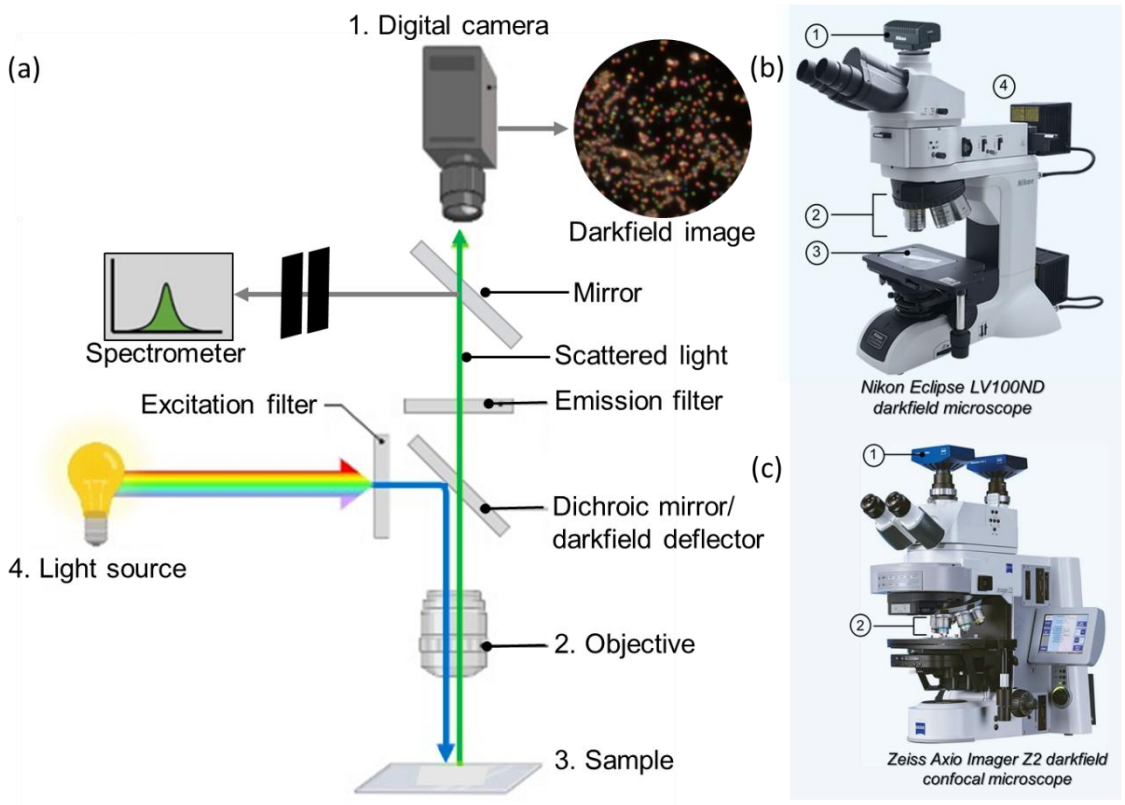



*Figure 2.2 (a) Schematic illustration of the single particle scattering microscopy/spectroscopy in a reflective-mode configuration. (b) Image of the microscope used for the darkfield imaging (c) Image of the microscope used for the spectra analysis. Reproduced from ref.*[3–5]

The single particle scattering spectra were obtained using a Zeiss Axio Imager Z2 darkfield confocal microscope in a reflective-mode configuration. Light from a halogen lamp (Halogen 4100 K, Philips) with a broadband spectrum in the visible and infrared was focused onto the sample using a 50× Zeiss darkfield objective (numerical aperture, $0.8 \geq NA \geq 0.95$; angle of incidence $53° \geq \theta_{inc} \geq 72°$). The reflected light was collected from a region approximately 3 µm in diameter on the substrate by the same objective and passed through a 50 µm optical fiber ($NA$ = 0.8) to an Ocean Optics QE65000 spectrometer[6]. The collected spectrum, $I_{SIG}$ was corrected for backscattered light from the substrate by subtracting the background spectrum of a region without particles, $I_{BKGD}$. Finally, the background-corrected spectrum was corrected for the non-uniform spectral intensity of the light source by dividing the lamp spectrum, $I_0$ recorded using a flat reference (polytetrafluoroethylene). The final single particle scattering spectrum, $I_{SCA}$, was obtained by:

$$I_{SCA} = (I_{SIG} - I_{BKGD}) / I_0 \qquad (2.1)$$

The diameter of the collection area can be calculated by:

$$D_{collect} = \frac{D_{fiber} \times f_{tube}}{M \times f_{lens}} \qquad (2.2)$$

Where, $D_{fiber}$ is the diameter of the fiber core; $f_{tube}$ is the focal length of the tube lens of the microscope; $M$ is the magnification of the objective; and $f_{lens}$ is the focal length of the lens which focuses the light to the fiber. The diameter of the collection area on the substrate can be controlled by changing the fiber core size or the coupling lens / focal length[6].

## 2.3 Electron energy loss spectroscopy (EELS)

The EELS measure the energy of the electrons from the transmitted beam. The electron beam is collected at a low angle and dispersed in a magnetic prism, which sorts the electrons by kinetic energy[7]. In Figure 2.3, the various electron inelastic interactions leading to the EELS spectrum are represented. Figure 2.3a represents an EELS spectrum that shows the zero-loss peak, plasmons, and two core-loss spectral features (from atoms A and B). Figure 2.3b shows the band diagram of a semiconductor, indicating the energy level origin of each EELS spectral feature. The excitation of the deep electrons gives rise to inner-shell edges on the EELS spectrum, whereas the excitation from the valence and conduction bands creates low-loss spectral features such as plasmons[8].

At zero energy, an intense peak is observed, corresponding to the electrons that do not lose energy during interaction. This peak is called the zero-loss peak (ZLP), and its full width at half maximum (FWHM) defines the energy resolution of the spectrometer. A decreasing tail expands from the ZLP towards the higher energies as a result of the interaction between incoming electrons and the valence electrons of the sample. Spectral features originating from inter- and intra-band absorption are observed. These can be divided into two energy ranges of 0 – 100 eV for the low-loss, and > 100 eV for the core-loss.

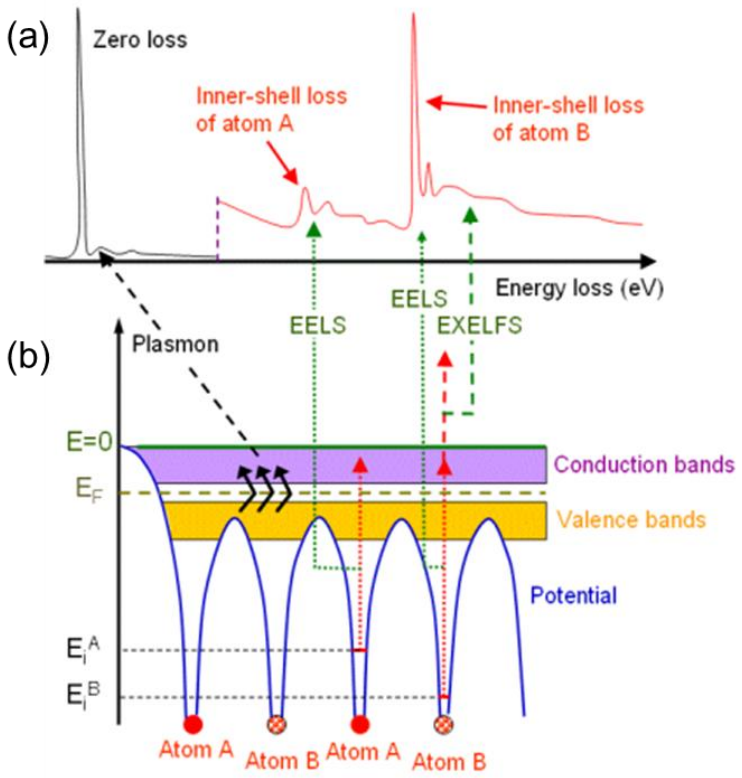



*Figure 2.3 Schematic illustration of the basic principle of EELS. Reproduced from ref.*[9]

In the context of this thesis, the low-loss region is studied. This is related to the excitation of phonons, excitons, interband transitions, or collective oscillations such as volume plasmon or surface plasmons. They all have resonances in the energy range corresponding to the UV-visible-IR. The excitons are electron-hole pairs bound by Coulomb interaction. Their energy is linked to that of the bandgap of a semiconductor[9]. The plasmons are collective oscillations of electrons in the conduction band. Their energy is linked to the plasma frequency that depends on the number of valence electrons per atom[8]. The phonons are crystal lattice oscillations. They have energy in the IR part of the optical spectrum. In the study of signals at very low energies, the ZLP tail can mask the peaks. Therefore, deconvolution techniques or monochromation solutions have to be employed[1].

Therefore, EELS were performed with an aberration-corrected, monochromated NION HERMES-200S microscope (CHROMATEM) fitted with a NION-IRIS spectrometer and a CMOS camera. The acceleration voltage was set to 60 keV, with a condenser semi-angle of 10 mrad and a typical energy resolution of around 15 meV. All EELS spectra images were aligned by the maximum of the zero-loss peak (ZLP) in each spectrum. The EELS spectra in this thesis were extracted as the sum of spectra in a region of interest, a few nanometers inside the bulk dielectric particle, and surrounding the particles for the surface plasmon. The ZLP was

subtracted by a power-law using the Gatan DigitalMicrograph (Version 3.60.4441.0). The samples were prepared by drop casting a diluted water dispersion of the particles onto a lacey carbon grid (Agar, 300 mesh Cu grid).

### The EELS data acquisition (spectrum-image):

The EELS spectrometer is coupled to a scanning transmission electron microscope (STEM), which makes it possible to acquire a high-angle annular dark-field (HAADF) signal and EELS spectrum in each electron position during scanning. Once the electrons pass through the sample, they are simultaneously collected by the HAADF detector and the EELS spectrometer. At the end of the scan, both a HAADF image and a spectrum-image are generated, which can be compared. In Figure 2.4, the spectrum-image is represented by a cube in which the *x* and *y* axes correspond to the coordinates of the electron beam scanning on the sample, and the *z* axis corresponds to the EELS spectra recorded in each point of the scan[1].

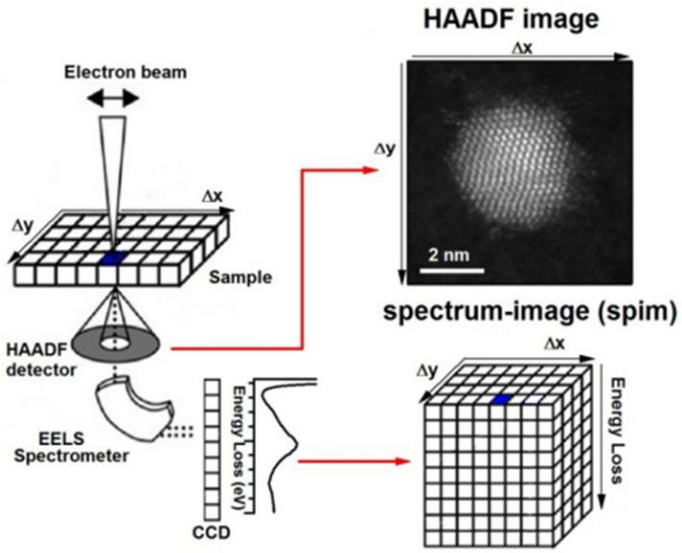



*Figure 2.4 Schematic diagram of the operating principle of a STEM microscope with an EELS spectrometer. Reproduced from ref.*[1]

### Filtered maps:

The filtered maps are created from the acquired spectrum-image. A filtered map is generated by plotting the EELS signal intensity of each pixel in a specific energy range. Figure 2.5 shows an example of the way to understand the formation of a filtered map. Here, two specific energy intervals and their corresponding filtered maps are generated. The energy ranges corresponding to plasmon resonance energies display maps with spatial symmetry.

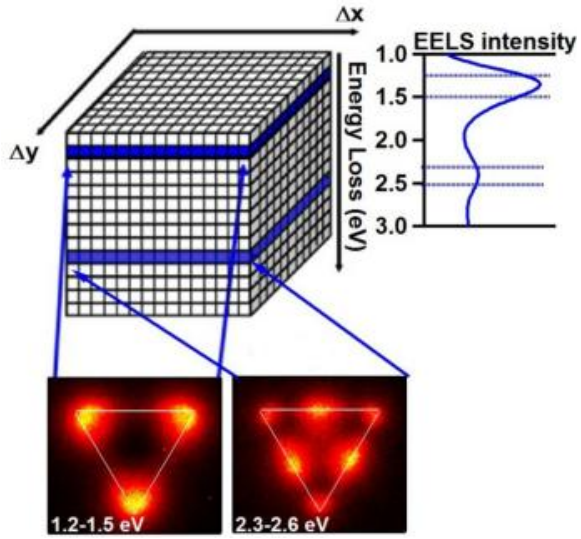



*Figure 2.5 Schematic illustration of the formation of filtered maps from the EELS spectra intensity. Reproduced from ref.*[1]

## 2.4 Optical absorption (UV-vis-IR)

The optical absorption characterization of the colloidal solution of the fabricated nanostructures was recorded using a Shimadzu UV-3600 extinction spectrometer. The absorption of radiation by a sample can be studied using a transmitted light beam. The transmission measures how much of a known light intensity incident on a sample passes through it, as a function of the wavelength of the light. The transmission can be described by the Beer-Lambert law:

$$T = I/I_0 = e^{-AK_{abs}} \qquad (2.3)$$

Where, $I_0$ is the incident signal intensity, $I$ the transmitted intensity, $K_{abs}$ the absorption coefficient, and $A$ the path length. The product $AK_{abs}$ is known as absorbance, and it is often called the optical density of the object. The absorption cross-section can be expressed as:

$$\sigma_{abs} = K_{abs}/N \qquad (2.4)$$

Where $N$ is the atomic number density.

## 2.5 Raman spectroscopy

Raman scattering is an inelastic scattering phenomenon. This means that light does not conserve its energy through the scattering process. When a laser radiation with a wavelength, $\lambda_0$ impinges on a sample, light may be scattered with the same wavelength (Rayleigh scattering), or with a shorter wavelength, $\lambda_0 - \lambda_1$ (anti-Stokes Raman scattering), or with a longer wavelength, $\lambda_0 + \lambda_1$ (Stokes Raman scattering). The Stokes and anti-Stokes scattering peaks are

shifted by a quantity $\lambda_1$ with respect to the exciting wavelength, $\lambda_0$. The Stokes scattering is at the lower energy side of the excitation beam, and the anti-Stokes is at the higher energy side. The Stokes and anti-Stokes Raman shifts correspond to the excitation of vibrational states within the sample. Typically, only Stokes Raman is considered when analyzing a Raman spectrum, since Stokes scattering is more intense than anti-Stokes scattering[10].

This technique is used to characterize the chemical composition and the structure of a variety of samples. In particular, the structure of silicon has been widely described. Silicon has a characteristic scattering with a Raman peak corresponding to the first-order optical vibration mode. This is called the transverse optical (TO) mode. This technique can be used to characterize the degree of crystallinity and bond order of silicon (Figure 2.6)[11]. The width and Raman shift of the TO mode are sensitive to the bond order, strain, and crystallinity of the sample[12–14]. It is well known that monocrystalline silicon exhibits a sharp Raman shift at 522 $cm^{-1}$, with a FWHM of 3.5 $cm^{-1}$, while amorphous silicon exhibits a broad and weak Raman shift at about 480 $cm^{-1}$ [15,16]. The TO peak gradually red-shifts and becomes broader as crystallite size decreases [13,14,16]. This trend is found in porous crystalline silicon, as the crystallite size decrease with increasing porosity[16]. For amorphous silicon, broadening is due to the relaxation of the selection rule for this mode, due to the loss in long-range order or disorder of finite dimensions effects[16].

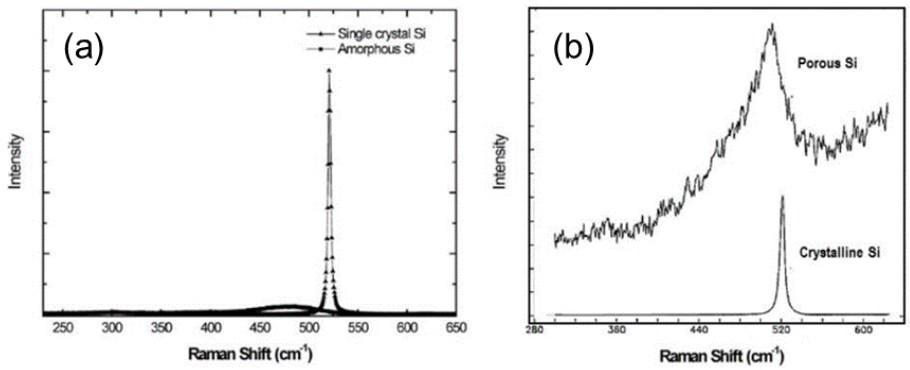



*Figure 2.6 Comparison between the Raman shift of a (a) single crystal Si and amorphous Si (b) single crystal Si and porous Si. Reproduced from ref.*[11,17]

In this thesis, the Raman scattering spectra were collected using an Xplora spectrometer by Horiba, equipped with a confocal microscope. The samples were prepared by drop casting a droplet of the suspension/powder onto a glass microscope slide. An objective lens with a magnification of 50× was used to observe the sample and choose the measurement area. A 100×

objective lens was employed to focus the laser beam on the measurement area. Five measurements in five different zones were collected for each sample to assess its homogeneity in terms of composition and structure. The spectra were run using a 532 nm excitation wavelength, with the laser power reduced to 50% of the total power by a filter. A 1800T grating was used to analyse the scattered light spectrally. Baseline subtraction was performed on each spectrum, using a linear baseline.

## 2.6 Dynamic Light Scattering (DLS)

DLS is an optical characterization technique that makes it possible to determine the average size and the size distribution of colloidal particles dispersed in a solvent. It is used to determine the average dimensions of individual nanoparticles and clusters in suspension. Unlike results obtained by microscopy or small-angle X-ray scattering, the size measured here corresponds to the hydrodynamic radius of the particles. In the case of nanoparticles that are charged or stabilized by a ligand, this means that it accounts not only for their solid core but also for the thickness of the ionic or polymeric layer that surrounds it (Figure 2.7).

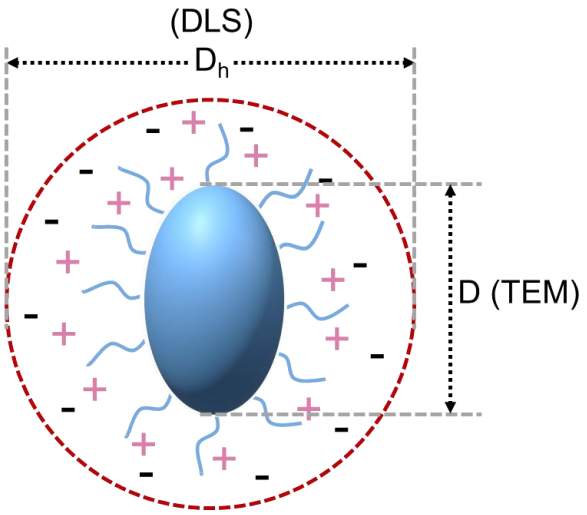



*Figure 2.7 Schematic diagram of the average hydrodynamic radius of a particle, indicating the hydration layer of a charged particle and the surfactant layer of particle stability.*

In a colloidal suspension, there are continuous collisions of the particles with the solvent molecules or with each other. These collisions cause a disordered and random motion of the particles, called Brownian motion. This leads to particle diffusion. The DLS technique measures the characteristic time of motion and determines the diffusion coefficient, *D,* of particles undergoing Brownian motion. This is related to their hydrodynamic radius according to the Stokes–Einstein relation:

$$D = \frac{K_B T}{6\pi\eta R_h} \text{ (m}^2\text{.s}^{-1}\text{)} \qquad (2.5)$$

Where $K_B$ is the Boltzmann constant ($1.38 \times 10^{-23}$ J · $K^{-1}$), T is the temperature (K), η is the viscosity of the liquid medium (Pa·s), and $R_h$ is the average hydrodynamic radius (m).

DLS measurements were carried out on diluted aqueous suspensions of the $SiO_2$ nanoparticles dispersed in ethanol. It was performed using an ALV laser goniometer equipped with a 632.8 nm HeNe laser and a photodiode detector with a movable angle between 45 – 135°. The measurements were carried out at a controlled temperature of 20 ± 2 °C, using low-volume disposable plastic cuvettes (UVette, Eppendorf Austria GmbH, Wien, Austria). The interaction of the incident radiation with the particles induces an oscillating polarization of the particles, which in turn emits electromagnetic radiation in all spatial directions. In a colloidal suspension, the waves scattered by all the particles interfere, forming an interference pattern that contains quantitative information on the spatial position of the scattering sources. Since colloids undergo Brownian motion, their position, and thus the interference pattern of their scattered light evolves. This evolution is measured by the DLS technique in the form of fluctuations in the intensity of light scattered by the particles as a function of time. These scattering intensity fluctuations can then be directly related to the particle size, which determines the speed at which they can move through the liquid. The small particles diffuse faster in a given suspension than larger ones. Therefore, their scattering intensity fluctuates more rapidly over time (Figure 2.8).

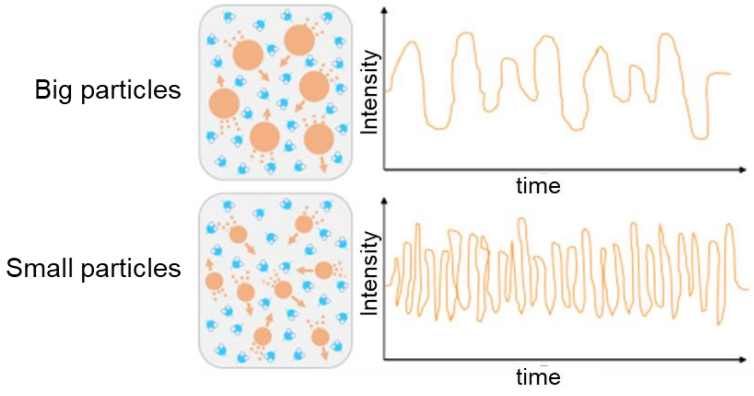



*Figure 2.8 Schematic illustration of the differences in scattered light intensity fluctuations over time between large particles and small particles dispersed in a liquid. Reproduced from ref.*[18,19]

The fluctuations in scattered light intensity from colloidal particles over time were recorded at 20 ± 2 °C using an ALV laser goniometer equipped with a 632.8 nm HeNe laser and a

photodiode detector with a movable angle between 45 – 135°. Measurements at θ = 45, 90, and 135° were carried out for the diluted suspensions. A single measurement of 30s was performed at each angle for the samples. The collected data were then analyzed with a multi-tau digital correlator (ALV 5000/EPP) and Origin software. This enables the analysis of scattered light intensity fluctuations over time by comparing those detected at a time, t and at a slightly later time, t + δt. This allows the generation of an autocorrelation curve (Figure 2.9), which represents the evolution of this correlation over all time intervals, δt. The correlation gradually weakens over time, as the particles move further away from their original positions, and eventually disappear beyond a characteristic time interval, $\tau_c$.

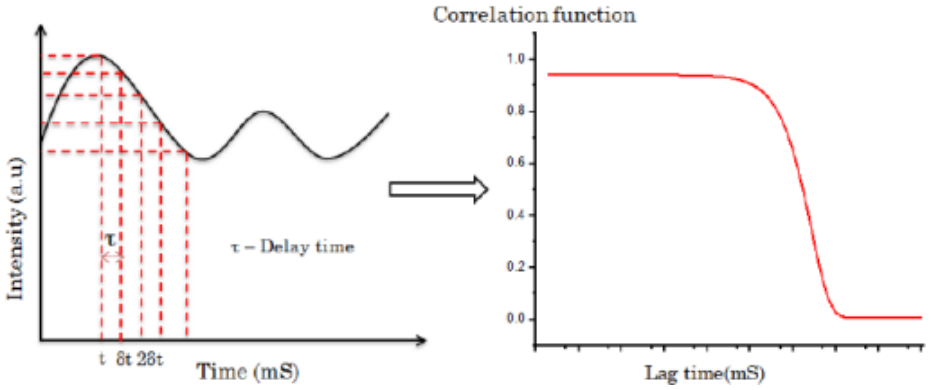



*Figure 2.9 Schematic illustration of fluctuation of light scattering intensity from particles over time. Perfect correlation corresponds to y = 1, and the absence of correlation to y = 0 [1]. Reproduced from ref.*[18,19]

The average autocorrelation curve obtained from the measurement carried out on the colloidal dispersions over the angle range is described by a decaying exponential function. For a monodisperse particle suspension, its equation is:

$$G(\tau) = A + \beta \exp\left(-\frac{\tau}{\tau_c}\right) = A + \beta \exp\left(-2q^2 D\tau\right) \qquad (2.8)$$

Where, A is the baseline, $\beta$ the instrumental factor, τ the time interval, $\tau_c$ the characteristics diffusion time of the particles, D is the diffusion coefficient of the particles, and $q$ is the scattering wave vector.

The correlograms could be nicely fitted using a mono-exponential fit function exp(-$\Gamma\tau$), which indicates a good monodispersity of the objects, from which the decay rate $\Gamma$ is mathematically determined. The decay rate, $\Gamma$ can be related to the hydrodynamic radius, $R_h$ of the objects by:

$$\Gamma = 2Dq^2 \qquad (2.6)$$

$$q = \frac{4\pi\eta}{\lambda} sin\frac{\theta}{2} \qquad (2.7)$$

Where, $D$ is the diffusion coefficient of the objects, $q$ is the scattering wavevector, $\eta$ and $n$ are the viscosity and refractive index of the solvent, respectively, $\lambda$ is the light wavelength ($\lambda$ = 632.8 nm), and $\theta$ is the scattering angle.

## 2.7 Small-Angle X-ray Scattering (SAXS)

This is a non-destructive technique that makes it possible to determine the shape and average size of individual nanoparticles, as well as the positional correlations that exist between them. This is based on the fact that each particle in a sample illuminated by X-rays scatters them elastically. The SAXS method measures these scattered intensities at very small angles, generally below 5°, thus providing access to information about the geometry and structure of objects with dimensions on the order of 5 nm to 100 nm[19,20].

The scattering phenomenon occurs when the electrons of the particles interacting with the X-ray beam oscillate at the same frequency as the incident radiation. They then emit secondary radiation that has the same frequency as the incident waves. Moreover, the set of radiations emitted by neighboring particles interferes and forms an interference pattern on the detector. These interferences may be constructive (i.e., in phase), destructive (out of phase), or intermediate, depending on the scattering angle 2θ and the distance r separating two neighboring particles. When the interferences between the emitted waves are constructive, they produce the formation of a bright spot on the detector. Conversely, when they are destructive and the emitted waves cancel each other out, this causes the formation of a dark spot on the detector. The succession of these bright and dark spots creates a 2D scattering pattern in which the intensity varies from one position to another depending on the scattering angle 2θ[21], as illustrated in Figure 2.10.

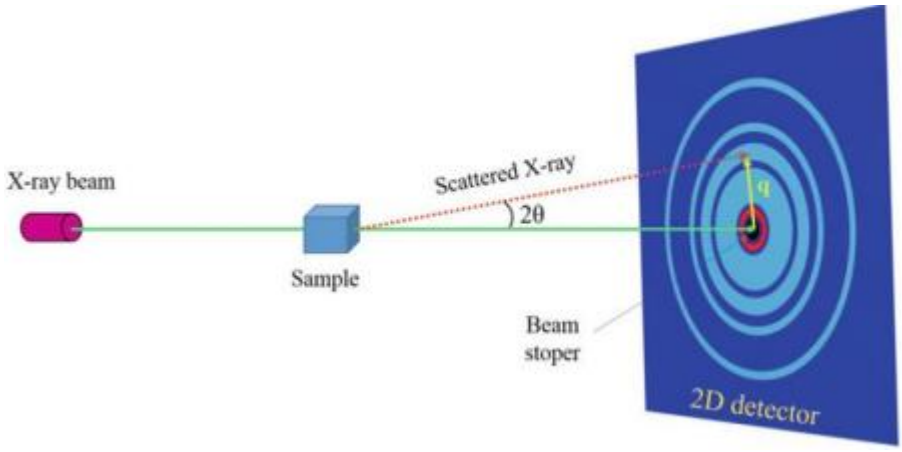



*Figure 2.10 Schematic illustration of the basic operating principle of SAXS*[20]

From this pattern, information about the internal structure of the objects can ultimately be extracted, in particular, the average distance separating the particles. The patterns are thus converted into graphs representing the intensity of the light scattered by the particles as a function of the scattering vector, $\vec{q}$, which is expressed as follows:

$$\vec{q} = \overrightarrow{k_l} - \overrightarrow{k_d} \qquad (2.9)$$

Where, $\overrightarrow{k_l}$ and $\overrightarrow{k_d}$ are the incident and scattered wave vectors, respectively. The magnitude of the scattering vector, $q$ is expressed as:

$$q = \frac{4\pi\sin(\theta)}{\lambda} \qquad (2.10)$$

Where, $2\theta$ is the scattering angle and λ the wavelength of the X-ray beam (0.154 nm). The scattered intensity, $I_q$ from a sample, depends on the number of particles present in the scattering volume and on the electron density contrast between the particle and the solvent: the higher these values, the greater $I_q$ becomes. In the case of a highly diluted sample of spherical colloids (such as individual nanoparticles suspended in water), the scattered intensity can be written as:

$$\mathrm{I}(q) = \mathrm{N} \cdot I_0 \cdot (\Delta\rho)^2 \cdot V^2 \cdot \mathrm{P}(q) \propto \mathrm{N} \cdot \mathrm{P}(q) \qquad (2.11)$$

Where, N is the number of particles in the sample solution, $I_0$ is the intensity of the incident beam, $\Delta\rho$ the difference in electron density between the solvent and the particle, V the volume of the particle, and P($q$) the form factor, which depends on its size and shape. In the case of a higher particle concentration (suspensions of dense clusters in dodecane), the influence of neighboring particles on each other becomes significant. A certain degree of structural

correlations may then exist within the sample, which implies that the scattered intensity is this time expressed as:

$$I(q) = N \cdot I_0 \cdot (\Delta\rho)^2 \cdot V^2 \cdot P(q) \cdot S(q) \propto N \cdot P(q) \qquad (2.12)$$

Where, $S(q)$ is the structure factor of the particles, which accounts for their relative positions with respect to one another and therefore reflects their correlations.

The SAXS signals were acquired in transmission using a XEUSS instrument (Xenocs), equipped with a copper microfocus anode source, a scatterless collimation system, and a 2D PILATUS detector, providing access to scattering vector values, $q$ ranging from 0.08 – 8 $nm^{-1}$. The studied aqueous suspensions of the silica nanoparticles in ethanol were placed in very thin glass capillaries with a thickness of 1.5 nm. The resulting 2D images were isotropic, and the data were therefore azimuthally averaged to obtain the particle scattering curve, representing the intensity, $I_q$ corrected for experimental background noise as a function of $q$.

The data collected from the dried silica particles reveal structure factor peaks arising from the internal micellar order: the first order peak at $q_o$ is followed by higher orders at $\sqrt{3}q_o$, $2q_o$, $\sqrt{7}q_o$, and in some cases $3q_o$, indicating a hexagonal order of cylindrical micelles. The center-to-center distance between neighboring micelles can then be calculated by:

$$d_{c\text{-}c} = \frac{4\pi}{\sqrt{3}\, q_o}$$

For some samples, a shoulder on the left side of the main peak suggests the presence of domains of disordered micelles, resulting in a single correlation peak.

## 2.8 X-ray powder diffraction (XRD)

X-ray diffraction is a non-destructive technique used to identify crystalline compounds. When the parallel monochromatic x-ray beam hit a sample, part of the beam is diffracted by crystal planes of the sample. The diffracted rays will interfere with each other to form diffraction spots and form constructive interferences in certain angles. These constructive diffraction interferences of the sample can be explained by the Bragg's law:

$$2d_{hkl} sin\theta = n\lambda \qquad (2.22)$$

Where $d_{hkl}$ is the inter-planar spacing, θ the angle of diffracted beam, λ the wavelength of the incident x-ray beam, and $n$ the integer that represents the number of diffraction mode.

The angle between the diffracted and transmitted beams will be equivalent to $2\theta$ all the time. Therefore, the results of XRD are expressed interms of 2θ, and this angle can be obtained in the experimenet.

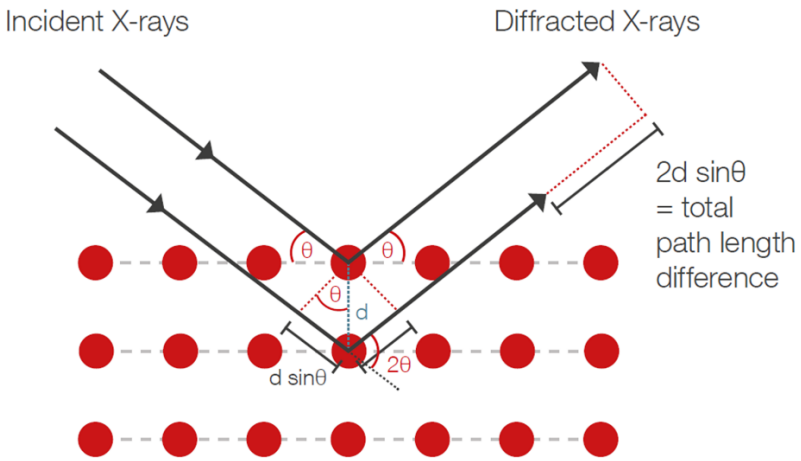



*Figure 2.11 Schematic illustration of the basic principle of X-ray powder diffraction (XRD).*

X-ray diffraction confirmed the presence of crystalline or amorphous Si in our final products throughout this thesis. Additionally, it was used to confirm the presence of metallic particles that induced the growth of Si nanowires. XRD measurements were realized with ground samples spread evenly onto a zero-background sample holder using a PANalytical X'Pert Pro apparatus (Cu radiation source λ = 0.15418 nm) equipped with an X'Celerator detector.

## 2.9 Fourier transform infrared spectroscopy (FTIR)

Infrared spectroscopy deals with molecular vibrations in matter interacting with an incident infrared radiation (IR) as a function of photon frequency. The resulting spectrum demonstrates the transmission and absorption of the sample molecules, creating its molecular fingerprint. The absorption peak frequency determines the vibrational energy gap of sample molecules, and the number of absorption peaks corresponds to the number of molecules' vibrational freedom. The possibility of the transition of energy levels and the change of dipole moment determines the magnitude of the absorption peak.

The measured signal by the detector is digitized and sent to the computer for the Fourier transformation. The final infrared spectrum is then presented for interpretation and further manipulation. The mathematical expression of the Fourier transform can be presented as:

$$F(\omega) = \int_{-\infty}^{+\infty} f(x) e^{i\omega x} dx \qquad (2.18)$$

Where, $\omega$ refers to angular frequency, and $x$ is the optical path difference. $F(\omega)$ is the spectrum, and $f(x)$ is the interferogram. If the interferogram, $f(x)$, is determined experimentally, the spectrum, F(ω), can be obtained by the Fourier transform.

Infrared radiation is electromagnetic radiation that covers the wavenumbers between 13300 – 3.3 $cm^{-1}$. The infrared region is usually divided into three regions: near-infrared (13300 – 4000 $cm^{-1}$), mid-infrared (4000 – 200 $cm^{-1}$), and far-infrared (200 – 3.3 $cm^{-1}$).

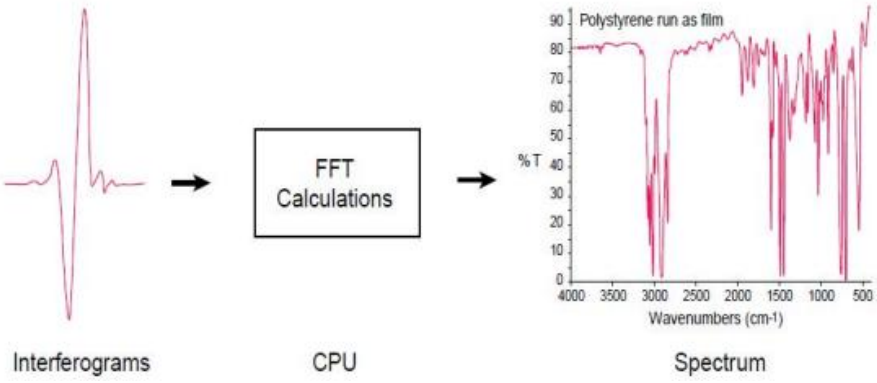



*Figure 2.12 Schematic illustration of FTIR for the analysis process of the sample*

FTIR provides valuable insights into the rotation and vibration of molecular structures, as well as the chemical bonding status of materials. Since each unique composition of atoms makes up different materials, there are no two materials that create the same infrared spectrum. Consequently, infrared spectroscopy can lead to the identification of materials. Besides, with the FTIR, we can determine the quality of a sample, identify unknown materials, and determine the number of components in a mixture. Hence, this method was used to identify the chemical bonding presence in the silicon-rich oxide precursors. Also, it provides information in complement with literature as the component of the precursor in terms of it being a cage-, ladder-, or linear- structure.

In an FTIR system, there are three basic spectrometer parts, which are the radiation source, an interferometer, and a detector. The interferometer creates an optical path difference between the radiant beams by dividing them and then produces repetitive interference signals by recombining the radiant beams. Interference signals are measured as a function of optical path difference by a detector. After passing through a sample, interference signals produced by the interferometer provide infrared spectral information. The Michelson interferometer is one of the most commonly used interferometers. It includes active components: a fixed mirror, a moving mirror, and a beam splitter (Figure 2.13). The moving mirror is perpendicular to another

fixed mirror. The beam splitter is a semi-reflecting device, and it is made by putting a thin film of germanium onto a flat KBr substrate. Broadband IR source generates radiation, which goes into the interferometer in a collimated way, and impinges on the beam splitter.

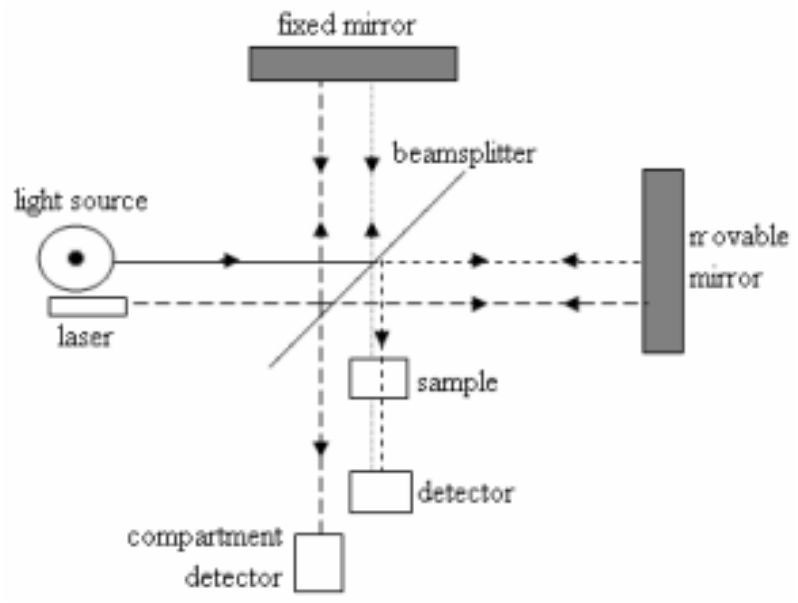



*Figure 2.13 Schematic illustration of the Michelson Interferometer*

## 2.10 Solid-state Nuclear Magnetic Resonance (NMR) Spectroscopy

Nuclear Magnetic Resonance (NMR) spectroscopy examines the frequency of atomic transitions from one nuclear spin state to another when a sample is placed in a large, static magnetic field. The transition or resonance frequency of a given nuclide depends on the total magnetic field at the nucleus. The resonance frequencies of a nuclide rely on the chemical bonding environment of the atom. Thus, NMR spectroscopy is a powerful tool for examining the local structural environment of atoms in both crystalline and amorphous solids. Solid-state NMR spectroscopy provides detailed structural information via the isotropic chemical shift interaction. More specifically, $^{29}$Si solid-state NMR analyzes silicon atoms in a solid-state environment, providing information on the coordination and chemical environment of these atoms.

Crystalline materials are highly ordered with a well-defined structural environment around each NMR-active isotope. The structural order of a crystalline material leads to well-defined, sharp peaks in its NMR spectrum. For example, the spectrum of a highly crystalline quartz is a single narrow signal because every $^{29}$Si nucleus is located in the same structural environment throughout the entire material. Therefore, it is composed of a connected 3D network of corner-

sharing $SiO_4$ tetrahedral units. On the other hand, an amorphous material like silicate glass, although it has a similar structure to the crystalline silicate, differs in lacking the periodic structural order[22].

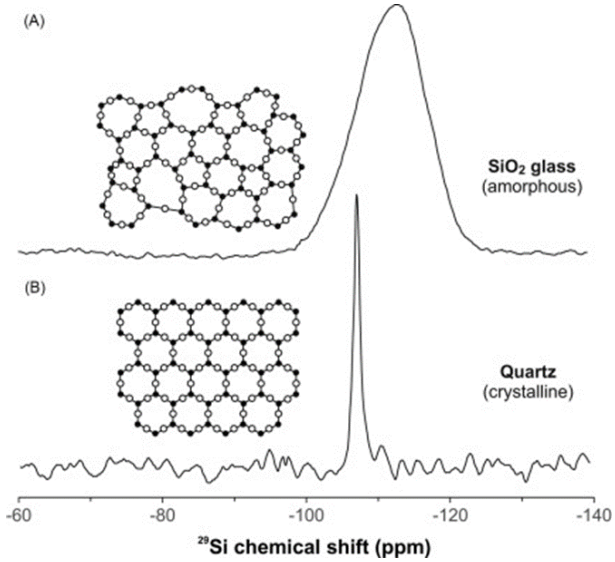



*Figure 2.14 Schematic structures and $^{29}Si$ MAS NMR spectra of (a) silica glass and (b) quartz. Both structures are composed of $SiO_2$. Reproduced from ref.* [23]

The samples were recorded on a Bruker Avance 500MHz spectrometer equipped with a 4 nm HX probe. The samples were analyzed with magic angle spinning (MAS) at a rate of 11 kHz using $ZrO_2$ rotors (100µL):

- CPMAS: Cross Polarization (CP) Magic Angle Spinning (MAS). The observation of rigid sample parts, non-quantitative analysis
- DPMAS: Direct Polarization (DP) Magic Angle Spinning (MAS). The quantitative analysis (subject to certain conditions)

This method was used further to quantify the structural components of the silicon-rich oxide precursor. We were able to define the component of the precursor in terms of it being a cage-, ladder-, or linear- structure.

## 2.11 Optical levitodynamics

Levitodynamics, which is the optical trapping of mesoscopic particles at low pressure, is an emerging field in optomechanics. Optical levitation in vacuum enables isolation of individual nanoparticles from environmental perturbations, allowing precise measurement of their mechanical and geometric properties in 3D. Unlike electron microscopy, this method avoids artifacts from sample support and provides dynamic information on particle orientation and

rotational modes. Levitodynamics provides a highly controlled, sensitive, and non-invasive technique to characterize the size and shape of optically levitated particles[24]. By leveraging precise measurements of motion and damping rates as a function of pressure, it offers detailed insights into the geometric particle properties, making it a valuable tool in both fundamental research and practical applications[25]. The optical trapping experiment was carried out by the collaborator from Laboratoire Ondes et Matière d'Aquitaine (LOMA) – Manon Barrière, Yacine Amarouchene, and Yann Louyer.

The optical tweezer is calibrated at relatively high pressures (T = 300 K), where the power spectral densities are given by:

$$S_{ii}(\omega) = \frac{2k_BT}{m}\frac{\Gamma_i}{(\Omega_i^2 - \omega^2)^2 + (\omega\Gamma_i)^2} \qquad (2.19)$$

Fitting Lorentzian power spectral densities allows the calibration from volts to meters for each axis. This is through the prefactor, $2K_BT/m$. The particle mass, $m$ is determined from the effective radii, $r_i$ and the assumed silica density, $\rho$ = 2200 kg/m$^3$. $\Omega_i$ is the resonance frequency of the oscillator (rad/s), $\Gamma_i$ is the damping rate along the $x$, $y$, and $z$ axes, $\omega$ is the analysis (Fourier) frequency.

The effective radii, $r_i$ (along $x$, $y$, and $z$ axes) are obtained from the damping coefficients in the molecular regime:

$$\Gamma_i = \frac{6\pi\eta r_i^2}{m}\frac{0.619}{l_{mfp}p_0}p \qquad (2.20)$$

Where, $\eta$ is the air viscosity at atmospheric pressure; the air molecular mean free path, $l_{mfp}$ = 68 nm; reference pressure, $p_0$ = 1 bar; and ambient pressure, $p$ the pressure in the vacuum chamber. $m$ is the effective mass of the oscillator.

The 1064 nm laser light is focused in the vacuum chamber through a high numerical aperture microscope objective (N.A.= 0.8). It is then divided into two parts: one is sent to the detection system to measure the motion of the particle, and the other part is analyzed by a polarizer before reaching a balanced photodiode, allowing a measurement of the orientation of the particle (Figure 2.15).

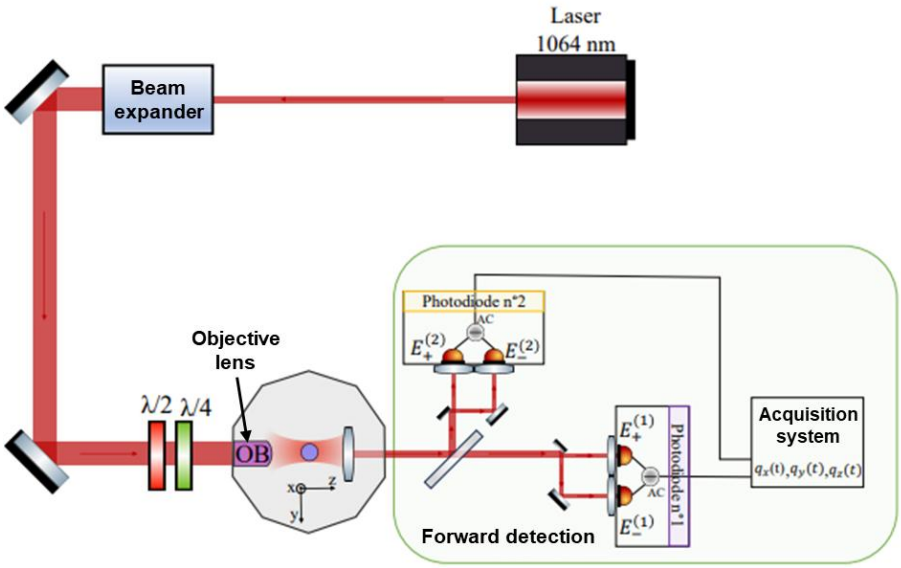



*Figure 2.15 Simplified optical diagram including the elements for forward interferometric detection. Reproduced from ref.*[26]

## 2.12 Transmission Electron Microscopy (TEM)

Transmission electron microscopy is applied to thin samples. It acquires information about the crystallinity of the sample. The electron beam emitted by the electron gun hits the sample, and it is transmitted along the column. The electrons hit a fluorescent screen, designing a two-dimensional image or diffraction pattern of the sample. In the imaging mode, thicker objects (such as nanoparticles) appear darker on the fluorescent green screen. If the diffraction mode is selected, and the sample contains a crystalline object, bright green diffraction spots or rings can be observed on the dark screen. Images or diffraction patterns are captured with a charge-coupled device (CCD) camera (Figure 2.16a).

The electrons are emitted either by the thermionic effect, using a lanthanum hexaboride single crystal ($LaB_6$), or through a field emission gun (FEG). The electrons are accelerated by an applied voltage whose intensity can vary from 60 to 300 kV. The electron beam is focused using magnetic lenses, typically coiled metallic wires. The electric current flowing through these solenoids induces strong magnetic fields that deflect the trajectory of the electrons. The focusing power of the magnetic lenses can be adjusted by varying the electric current. They are very versatile and can focus, defocus, and collimate the electron beam. The resolution of TEM at the angstrom scale is derived from the capability of magnetic lenses to focus the beam to a spot the size of an atom.

The diffraction mode provides an image of the sample in reciprocal space, while the conventional imaging mode provides an image in real space. By adjusting the electron lenses, the microscope can switch from real to reciprocal space. A reciprocal space image of the sample consists of the diffraction pattern. The diffraction pattern is composed of a central spot and concentric haloes (if the sample is amorphous) or concentric rings or spots (if the sample is crystalline). The spots or rings correspond to families of planes in real space. The central spot corresponds to transmitted light, while the rings correspond to diffuse/diffracted light.

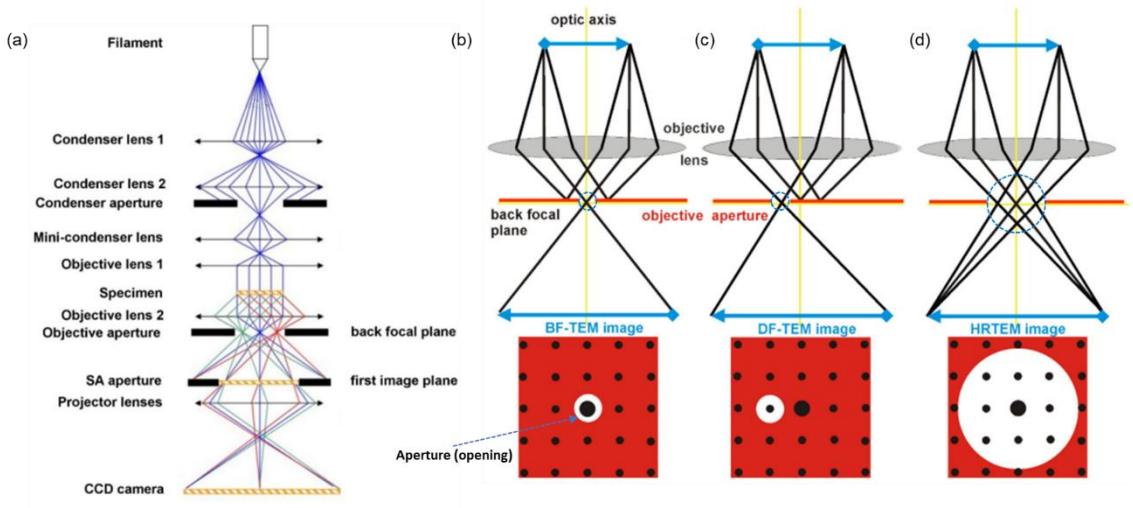



*Figure 2.16 (a) Schematic diagram of a transmission electron microscope in the (b) bright-field mode, (c) dark-field mode, and (d) high-resolution mode*

### Bright-field (BF):

The name bright-field comes from the image contrast obtained with this imaging mode. Bright field (BF) mode selects only the transmitted light from the diffraction pattern, using a small diaphragm to eliminate diffused/diffracted light (Figure 2.16b and 2.17a). The microscope is then set to the imaging mode, and a bright-field image of the sample is obtained, where the particles appear as dark spots on a bright background. In BF mode, the contrast between the particles and the carbon film is enhanced, and small particles or particles composed of atoms with a low atomic number are easily imaged. If the beam is in a vacuum, with no interaction with a sample, the image will appear bright, since all the beam is detected. The detector is a disk located on the optical axis with a contrast known as phase contrast.

### Dark-field (DF):

In dark mode, the image appears dark because no electrons are detected (no interaction with the sample) when the beam is in a vacuum. The electrons diffracted or diffused by the particles are selected with the diaphragm (Figure 2.16c and 2.17b). When the microscope is set to imaging mode, the particles appear as bright spots on a dark background. The image appears to be the negative version of the bright-field image. This is because only diffracted light from a specific family of planes is allowed to reach the fluorescent screen and the CCD camera. Dark field is a method used to verify whether particles are crystalline. Selecting different diffraction rings reveals different families of planes in a real-space dark-field image.

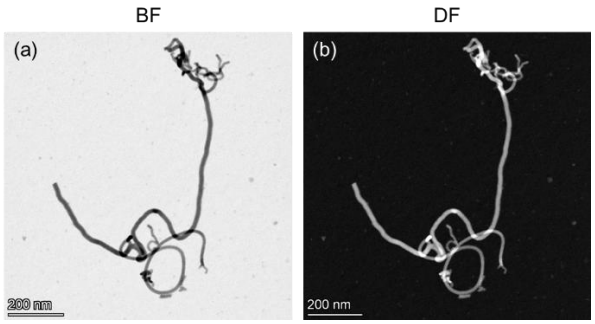



*Figure 2.17 TEM images of fabricated silicon nanowires (a) Bright-field (BF) image. (b) High-angle annular dark-field (HAADF).*

We obtained the micrographs of samples using a Jeol JEM-1400+ transmission electron microscope with an acceleration voltage of 120kV. Drops of the suspension were deposited on grids composed of a carbon film-coated 300 mesh square copper lattice, and ethanol was allowed to evaporate under ambient conditions before analysis. All TEM images were acquired with the Gatan software Digital Micrograph. Particle sizes were manually determined from TEM images using ImageJ.

High-resolution TEM resolves details at the atomic scale. In crystalline samples, different planes can be distinguished. The image of crystalline planes is formed due to the interference between the transmitted and diffracted electrons as they hit the sample (Figure 2.16d). The inter-lattice distances, $d_{hkl}$, can be easily measured and used to identify the crystalline phase of the sample. In this thesis, high-resolution imaging of crystalline particles was carried out using the electron microscope Talos F200S G2 at the Bordeaux Imaging Center, in collaboration with Sabrina Lacomme.

## 2.13 Scanning Transmission Electron Microscopy (STEM)

In the basic operating principle of a STEM microscope, the electron gun is a tip from which the electrons are extracted. In the setup used in this study (Figure 2.18), the electron source is a cold field emission gun (FEG). The electron optics and apertures shape the electron beam in the microscope column. This include the condenser lenses for the demagnification of the probe, the aberration corrector that allows for atomically-resolved imaging, the objective lens for the formation of the probe on the sample, the scanning coils that would enable the focused beam to move on the sample to create the sample images, and the projector lenses for the coupling between the transmitted beam and the detectors at the end of the column[1,9].

The mechanical stability of the sample holder is crucial for high-resolution imaging of the sample. The monochromator allows access to low-energy phenomena with high spectral resolution. The principle is to narrow the primary electron beam in energy, so that the ZLP is narrower, and low-energy features become accessible. At the voltage used in this work (60 – 100 keV), the electron mean free path is about 50 – 150 nm, depending on the sample. This means that for measuring the transmitted electron beam, such as what is done in STEM, the samples need to be of this thickness, or thinner. This makes the STEM microscopes particularly fitted for the study of nano-objects[1,9].

The chromatic aberration is from the fact that the magnetic field acts on an electron depending on its kinetic energy. The name chromatic comes from the analogy with optics, where the lenses are dispersive and each wavelength is not focused at the same position, blurring the image. The use of a cold FEG reduces the effects of chromatic aberrations. It can also be further reduced by using a monochromator[1,9]. The EELS spectrometer includes a magnetic prism (deflection of the electrons depending on their speed, which depends on the kinetic energy lost during inelastic interaction with the sample) with Lorentz force, $\vec{F} = \vec{v} \times \vec{B}$. The EELS spectrometer has to be aberration corrected to improve the spectral resolution.

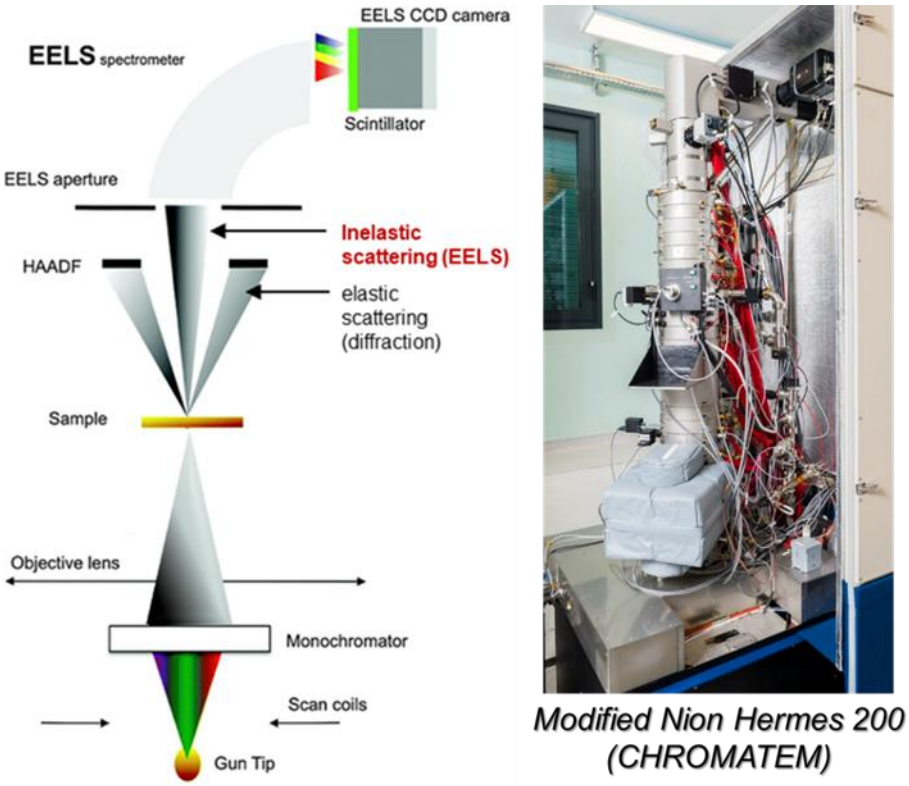



*Figure 2.18 Schematic illustration of a STEM microscope equipped with a monochromator.*

The detectors include the bright-field (BF) and dark-field (DF) for imaging (Figure 2.19). It can be annular darkfield (ADF) or high-angle annular darkfield (HAADF). The HAADF detector measures the electrons deflected at high angles (> 30 mrad). The contrast is proportional to the atomic number of the atoms. The intensity comes from the detected electrons, which have been scattered elastically by the nuclei of the sample atoms. In this case, the intensity detected is proportional to the square of the atomic number of the atom. The HAADF intensity also depends on the sample thickness (projected atomic number). Elastic scattering arises from the Coulomb interaction between electrons and the nuclei of atoms. It is characterized by the Rutherford scattering:[6]

$$\frac{d\sigma(\theta)}{d\Omega} = \frac{\lambda_e^4 Z^2}{64\pi a_0^2 \left(sin^2\left(\frac{\theta}{2}\right) + \frac{\theta_0^2}{2}\right)^2} \alpha\, Z^2 \qquad (2.21)$$

The scattering cross-section, which is related to the number of electrons scattered at a specific angle, is proportional to the square of the atomic number. Hence, high-angle scattering images, such as HAADF, are often referred to as Z-contrast imaging. In Figure 2.19, a typical example of a BF and HAADF image is shown.

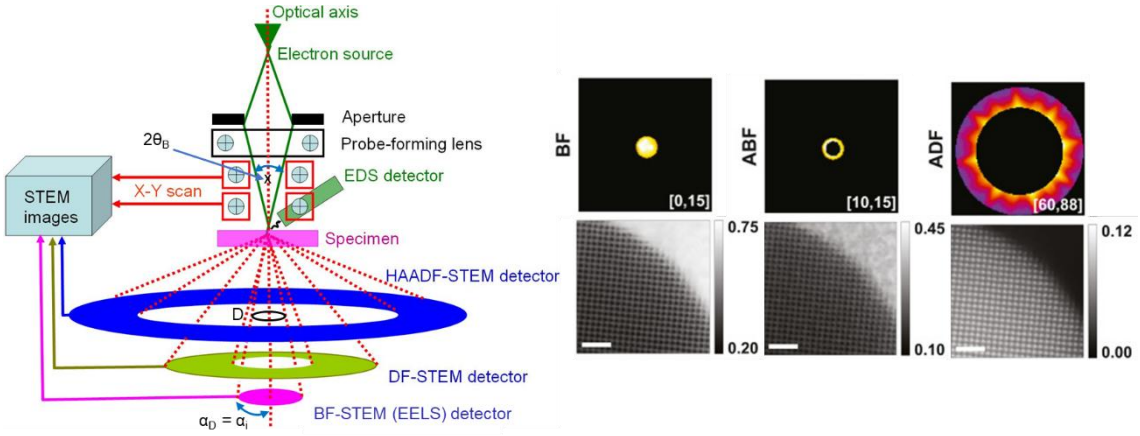



*Figure 2.19 Schematic diagram of the electron beam crossing the sample in STEM imaging modes.*

The convergent electron beam is scanned across the sample. At each beam position, the detectors record an intensity proportional to the number of electrons they measure. Point by point, the images are constructed with these intensities, corresponding to the scanned area. The shape of the active area of the detectors is either a disk, as in bright-field imaging, or annular, such as in annular dark-field imaging (Figure 2.19). The collection of transmitted electrons by detectors spans different areas around the optical axis. The detectors consist of a single pixel and are composed of a scintillator and a photomultiplier. In STEM, the spatial resolution is limited by the size of the probe. The limitation of the probe size is mainly due to three factors:

- the aberration of the lenses. The electron optics are not stigmatic: the image of a point object is not exactly a point.
- the diffraction of the electrons: Rayleigh criterion $d_d = 0.611 \times \frac{\lambda_e}{\alpha}$, where $d_d$ is the smallest probe size, and for $\lambda_e$ = 3.7 pm (100 keV), 30 mrad, $d_d$ = 75 pm.
- The source size: $d = \sqrt{d_a^2 + d_s^2}$, where $d_a$ is the probe size considering the effects of aberrations, and $d_s$ is the source size, which is linked to the probe current, $I$ with $I = \frac{B\pi^2 d_s^2 \alpha^2}{4}$, where $B$ is the brightness of the source.

## 2.14 Energy-dispersive X-ray spectroscopy (EDS)

The technique is commonly paired with STEM to provide correlative spectral maps of elemental composition and electronic structure. The materials prepared for STEM need to be electron-transparent, meaning they allow electrons to transmit through the sample with minimal

scattering. This property enables a high number of transmitted electrons to be collected by the various detectors, thereby improving the signal-to-noise ratio.

The expulsion of an electron from one of the inner orbitals of the element causes a second electron to decay from an outer shell to an inner empty level, with the emission of characteristic X-ray radiation. The EDS analysis was performed to elucidate the composition and structure of silicon particles, nanowires, and shell composition. The samples are prepared by drop-casting a colloidal suspension containing the particles onto a carbon-coated copper grid. Due to the nanometric thickness of the film, along with the low atomic number of carbon, the contrast of the carbon film in transmission mode is very low. Hence, sharp images of heavier nanoparticles deposited onto the carbon film are obtained.

For elemental mapping of the samples, a ThermoFisher (FEI) Talos F200S G2 setup was used. The microscope utilizes a field-emission gun (FEG) as its electron source and operates at an accelerating voltage of 200 kV. This was carried out at the Bordeaux Imaging Center, in collaboration with Sabrina Lacomme. Images were acquired using the software VELOX (Version 2.13.1.1138-af4e0daa7d).

## 2.15 In-situ Transmission Electron Microscopy (TEM)

The growth mechanisms of Si-based nanostructures during thermal annealing of Au particles embedded in a silicon-rich oxide, $(HSiO_{3/2})_n$ were investigated through real-time *in situ* electron microscopy. Experiments were carried out using a JEOL JEM-2100 FEG S/TEM microscope operated at 200 keV and equipped with a spherical aberration probe corrector (Cs from CEOS), high-resolution objective lens pole piece, an UltraScan 1000 CCD array detector (GATAN), and a Centurio EDX detector (JEOL). In this study, we adopted the closed gas cell system (Figure 2.20), manufactured by Protochips, which can be installed in commercially available TEMs, because it does not require special lens systems or alterations to the TEM column.

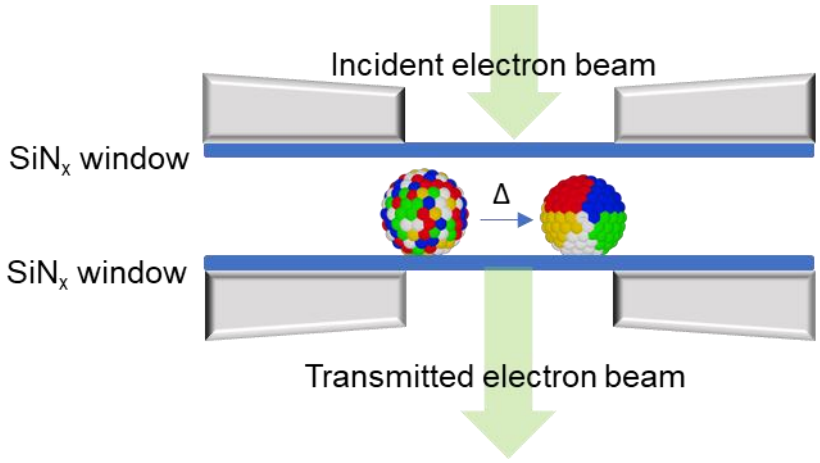



*Figure 2.20 Schematic diagram of the Microelectromechanical system (MEMS)-based closed cell for in-situ observation of the sample.*

In the system shown in Figure 2.21, a closed-cell sample holder (Protochips Atmosphere system) is employed to create a reactive gaseous environment around the sample, while the high vacuum is preserved within the microscope column. The environmental cell (E-cell) is constituted of a MEMS-based device with electronically transparent windows made of amorphous silicon nitride with a SiC heating ceramic, and six micrometric holes covered with a thin, electron-transparent $SiN_x$ film (~30 nm). Another Si chip, also equipped with a $SiN_x$ window, is used to close the "micro-reactor" and insulate the sample from the TEM vacuum. The high elasticity and fracture strength of the $SiN_x$ membranes enable the system to withstand pressures up to 1 bar under both static and dynamic conditions. At the same time, the SiC heating ceramic allows heating up to 1000 °C. The micro-reactor is typically less than 4 μm thick. The gas is supplied to the MEMS micro-reactor through capillary gas channels running through the sample holder. The pressure inside the chamber is controlled by inlet and outlet needle valves, providing precise control over the sample conditions. It is possible to flow different reactive gases to the "micro-reactor", including $H_2$, $O_2$, Ar, $N_2$, $CO_2$, and CO. The temperature, ramp rate, gas flow, and pressure are controlled with the software AXON atmosphere, and up to a temperature of 1000 °C[27,28].

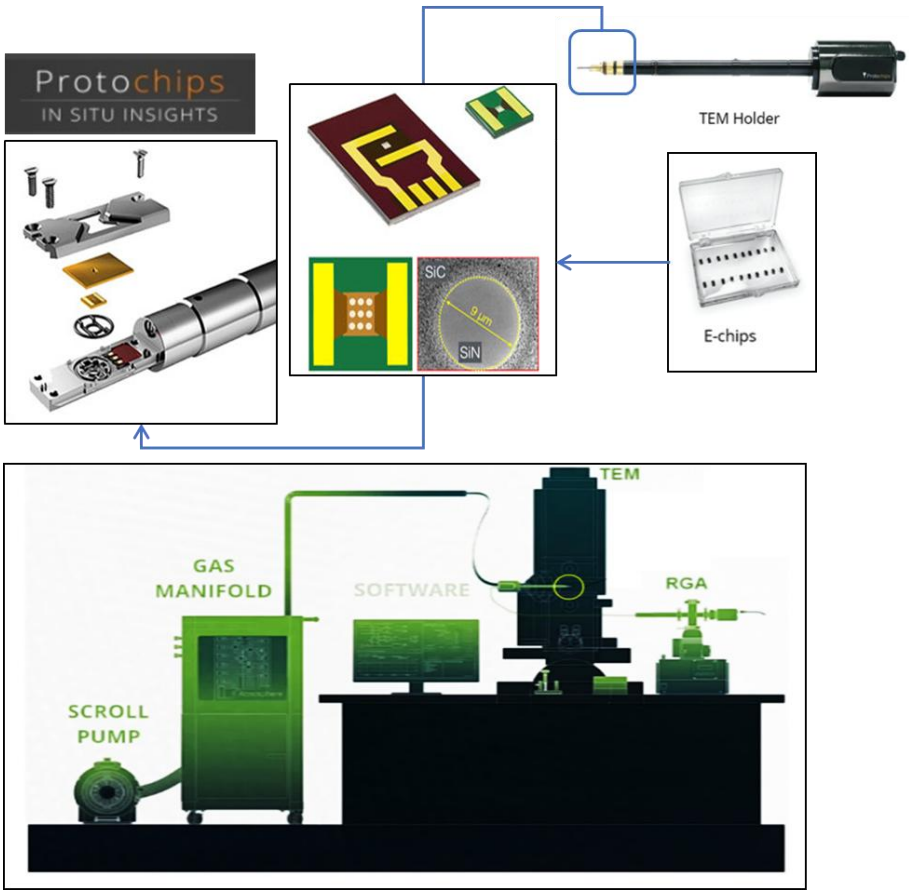



*Figure 2.21 Schematic diagram of the in situ TEM setup used for the thermal annealing of the silicon-rich oxide. Reproduced from ref.* [29]

### Sample preparation:

The heating MEMS chip (bottom chip) was plasma-cleaned with a mixture of Ar and $O_2$ for 30 seconds. The synthesized precursor used for the fabrication of silicon nanowires *ex situ* was ground and dispersed in methanol with sonication. A 10 µL droplet of the slurry was drop-cast on the plasma-cleaned chip and evaporated under air before analysis. Then the bottom chip was sealed with the top chip, and the assembled sample holder was inserted into the microscope. The sample holder was purged with nitrogen gas for 1 h at ~ 150 °C and ~ 3.8 torr to remove any residual solvent and other contaminants.

### *In-situ* TEM experiment:

The pressure was raised to atmospheric pressure (~ 768 torr) with the introduction of pure hydrogen as the reducing gas, at a flow rate of 0.1 sccm. In a typical experiment, the temperature was raised from room temperature to 1000 °C at a rate of 10 °C/s, with ~ 10 min of observation at 800 °C and 900 °C. At 1000 °C, thermal annealing was observed for 1 h, unless otherwise stated. The sample was cooled to room temperature at a rate of –2 °C/s, with a final pressure of

~ 600 torr. Typical TEM images of the chosen zones were recorded at a low temperature (<100 °C), where changes are not expected. To minimize electron beam effects like contamination and sample damage, preliminary observations were conducted to determine the maximum electron beam dose that the sample could withstand under the gaseous environment.

## 2.16 Scanning Electron Microscopy (SEM)

SEM images micro- or nanostructured surfaces in a reflection mode, allowing acquisition of information about the morphology and chemical composition of the sample. The microscope is composed of an electron gun, or cathode, which emits electrons through the thermionic effect, for instance, using a tungsten filament, or by field emission (FEG source, typically a tip-shaped single crystal of tungsten) (Figure 2.22). The images acquired with the FEG source have better resolution than those acquired with a thermionic source. An applied voltage accelerates the electrons, and the electron beam is focused with a condenser lens. The size of the beam spot determines the resolution of the microscope, i.e., the higher the magnification at which two objects can be resolved. The surface of the sample is scanned in a raster fashion with a pair of lenses that tilt the beam in the *x* and *y* directions. The sample region penetrated by incident electrons has the shape of a droplet, and its extent depends on both the energy of the incoming electrons and the atomic number of the sample atoms. The electron beam, interacting with the sample's atoms, produces different signals at varying depths of penetration. Each of these signals carries different information.

When the incoming electrons interact with the electrons of the atoms in the sample, they can be either elastically back-scattered (reflected), conserving all their kinetic energy. The impact can also result in inelastic scattering, in which the energy of the incident electron is used to emit a secondary electron from the sample. The energy of these secondary electrons is lower than the energy of the incident electrons.

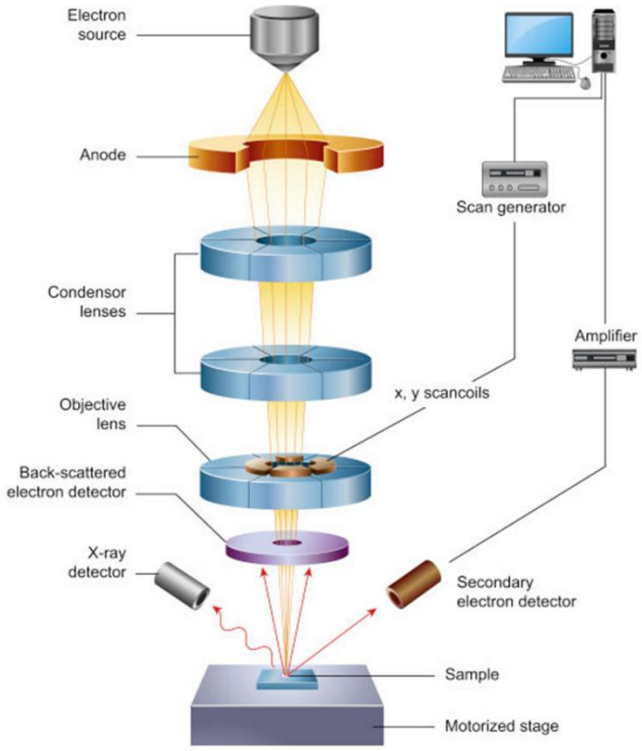



*Figure 2.22 Schematic diagram of the scanning electron microscope. Reproduced from ref.*[30]

When a secondary electron is emitted from one of the inner shells, an electron from an outer shell decays to fill the inner shell, emitting characteristic X-ray radiation that allows for elemental identification. This technique, known as energy-dispersive X-ray spectroscopy (EDX), is used to determine the chemical composition of a specimen. The secondary and back-scattered electrons are used to obtain a three-dimensional image of the sample surface. The secondary electrons provide higher-resolution images of the surface, as they are emitted very close to the sample surface.

In this thesis, SEM analysis of the elliptical silica particles was conducted using a Hitachi S-4500 microscope with an acceleration voltage of 5–10 kV, depending on the desired resolution. This is to visualize the morphology of individual/cluster of particles, verifying their shape, size, and external structure. Drops of the dispersion were deposited on a silicon wafer, and ethanol was allowed to evaporate under ambient conditions before 30 s of sputter coating with a thin layer of Au. Field emission SEM was performed using a field emission gun system (Hitachi SU 8030 N) with an acceleration voltage of 5−10 kV to characterize the particle morphology. For the core-shell particles, the same substrate analyzed with dark field optical microscopy was prepared for SEM characterization by plasma coating the substrate with an Au layer (~ 4 nm). Particle sizes were manually determined from FE-SEM images using ImageJ.

## 2.17 Thermogravimetric analysis (TGA)

The thermal reduction of the HSQ was carried out using a TGA/DSC with a thermal analyser (SETARAM Setsys Evolution 12) and a PFEIFFER Omnistar mass spectrometer. The experimental condition is an atmosphere of 5% $H_2$ in Air with a gas flow rate of 50 cc·min$^{-1}$. The temperature ranges from 25 – 1000 °C at a heating rate of 10 °C/min. The data were processed and analysed using the software Calisto, Setsoft. This experiment was carried out in collaboration with Thibaut Cornier from the Institute for Research on Catalysis and the Environment (Ircelyon).

## 2.18 Brunauer–Emmett–Teller (BET)

The Brunauer-Emmett-Teller (BET) method makes it possible to determine the specific surface area of nanoparticles based on the phenomena of adsorption and desorption of $N_2$ (which makes it possible to deduce the total surface area of the sample) and on the mass of the previously degassed sample. The specific surface area is the accessible surface developed by the material per unit mass. In the case where the assumption of spherical particles can be applied, their equivalent diameter, Ø can be estimated by:

$$\emptyset = \frac{6000}{S_{BET} \cdot \rho} \qquad (2.23)$$

Where, $S_{BET}$ is the specific surface area ($m^2/g$), and $\rho$ the density (g/$cm^3$).

The measurement was carried out using a Micrometritics 3Flex analyser at the ICMCB. The samples were degassed at 300 °C for 24 h before analysis under the flow of nitrogen.

## 2.19 Mie theory, T-matrix simulations, and simulated EELS spectra

The optical scattering spectra of spherical particles were simulated using the T-matrix method and implemented using the SMUTHI Python toolkit[31] by Peter Weicha from the Laboratory for Analysis and Architecture of Systems (LAAS-CNRS) in Toulouse. Optical spectra for homogeneous spherical and core-shell particles were calculated using Mie theory, as implemented in the PyMieScatt Python package[32]. Simulated EELS spectra were calculated using Green's dyadic method implemented using the PyGDM Python toolkit[33,34]. Refractive index data for Au and Si were taken from the literature[35,36]. Under plane wave excitation, the forward and backward scattering were evaluated over either the entire forward or backward hemisphere for both the Si@Au and bare Si particles.

## References


(1) Alfredo Campos Otero. Optics and Structure of Metal Clusters at the Atomic Scale, Université Paris Saclay, 2018. https://theses.hal.science/tel-02342598/.

(2) Fakhrullin, R.; Nigamatzyanova, L.; Fakhrullina, G. Dark-Field/Hyperspectral Microscopy for Detecting Nanoscale Particles in Environmental Nanotoxicology Research. *Sci. Total Environ.* **2021**, *772*, 145478. https://doi.org/10.1016/j.scitotenv.2021.145478.

(3) *Zeiss Axio Imager Z2 Upright Microscope Manual. Light Microscopy Core Facility*. https://microscopy.duke.edu/manuals/zeiss-axio-imager-z2-upright-microscope-manual.

(4) MMK Mikroskope Shop. *Nikon reflected/transmitted light microscope LV100ND.* https://mmk-mikroskope.de/en/produkt/nikon-reflected-light-transmitted-light-microscope-lv100nd-led/.

(5) S., P. *Fluorescence Microscopy - Principle, parts, uses - Biology Notes online. Biology Notes Online.* https://biologynotesonline.com/fluorescence-microscopy-principle-parts-uses/.

(6) Movsesyan, A. Plasmonic Properties of Metallic Nanoparticles: Beyond the Dipolar Resonance., Université de Technologie de Troyes, 2018. https://theses.hal.science/tel-03610410/.

(7) Reimer, H. K. L. *Transmission Electron Microscopy. Springer, fifth edition*.

(8) Egerton, R. F. *Electron Energy-Loss Spectroscopy in the Electron Microscope. Plenum Publishing Corporation, second edition*.

(9) Bonnet, N. Electron and Optical Spectroscopy of 2D Semiconductors and Defects in the Electron Microscope., Université Paris-Saclay, 2022. https://inria.hal.science/tel-03712021/.

(10) Kauffmann, T. H.; Kokanyan, N.; Fontana, M. D. Use of Stokes and anti-Stokes Raman Scattering for New Applications. *J. Raman Spectrosc.* **2019**, *50* (3), 418–424. https://doi.org/10.1002/jrs.5523.

(11) Parker, J. H.; Feldman, D. W.; Ashkin, M. Raman Scattering by Optical Modes of Metals. In *Light Scattering Spectra of Solids*; Wright, G. B., Ed.; Springer Berlin Heidelberg: Berlin, Heidelberg, 1969; pp 389–397. https://doi.org/10.1007/978-3-642-87357-7_42.

(12) Harris, J. T.; Hueso, J. L.; Korgel, B. A. Hydrogenated Amorphous Silicon (a-Si:H) Colloids. *Chem. Mater.* **2010**, *22* (23), 6378–6383. https://doi.org/10.1021/cm102486w.

(13) Tsu, D. V.; Chao, B. S.; Jones, S. J. Intermediate Order in Tetrahedrally Coordinated Silicon: Evidence for Chainlike Objects. *Sol. Energy Mater. Sol. Cells* **2003**, *78* (1–4), 115–141. https://doi.org/10.1016/S0927-0248(02)00435-X.

(14) Viera, G.; Huet, S.; Boufendi, L. Crystal Size and Temperature Measurements in Nanostructured Silicon Using Raman Spectroscopy. *J. Appl. Phys.* **2001**, *90* (8), 4175–4183. https://doi.org/10.1063/1.1398601.

(15) Richter, H.; Wang, Z. P.; Ley, L. The One Phonon Raman Spectrum in Microcrystalline Silicon. *Solid State Commun.* **1981**, *39* (5), 625–629. https://doi.org/10.1016/0038-1098(81)90337-9.

(16) Sui, Z.; Leong, P. P.; Herman, I. P.; Higashi, G. S.; Temkin, H. Raman Analysis of Light-Emitting Porous Silicon. *Appl. Phys. Lett.* **1992**, *60* (17), 2086–2088. https://doi.org/10.1063/1.107097.

(17) Hong, W.-E.; Ro, J.-S. Kinetics of Solid Phase Crystallization of Amorphous Silicon Analyzed by Raman Spectroscopy. *J. Appl. Phys.* **2013**, *114* (7), 073511. https://doi.org/10.1063/1.4818949.

(18) Rajam Elancheliyan. Directed Assembly of Hybrid Colloids for Optics, 2021. https://theses.hal.science/tel-03116369/.

(19) Maeva Lafitte. Fabrication and Optimization of Optical Resonators by Self-Assembly in Emulsion for the Development of Metasurfaces, 2023. https://theses.fr/2023BORD0330.

(20) Londoño, O. M.; Tancredi, P.; Rivas, P.; Muraca, D.; Socolovsky, L. M.; Knobel, M. Small-Angle X-Ray Scattering to Analyze the Morphological Properties of Nanoparticulated Systems. In *Handbook of Materials Characterization*; Sharma, S. K., Ed.; Springer International Publishing: Cham, 2018; pp 37–75. https://doi.org/10.1007/978-3-319-92955-2_2.

(21) Schnablegger, H., Singh, Y.,. *The SAXS guide. Getting Acquainted with the Principles, 3rd Edition, Anton Paar GmbH*.

(22) Mabboux, P.-Y.; Gleason, K. K. Chemical Bonding Structure of Low Dielectric Constant Si:O:C:H Films Characterized by Solid-State NMR. *J. Electrochem. Soc.* **2005**, *152* (1), F7. https://doi.org/10.1149/1.1830353.

(23) Brouwer, D. H. Applications of Silicon-29 NMR Spectroscopy. In *Comprehensive Inorganic Chemistry III*; Elsevier, 2023; pp 107–137. https://doi.org/10.1016/B978-0-12-823144-9.00032-7.

(24) Bellando, L.; Kleine, M.; Amarouchene, Y.; Perrin, M.; Louyer, Y. Giant Diffusion of Nanomechanical Rotors in a Tilted Washboard Potential. *Phys. Rev. Lett.* **2022**, *129* (2), 023602. https://doi.org/10.1103/PhysRevLett.129.023602.

(25) Gonzalez-Ballestero, C.; Aspelmeyer, M.; Novotny, L.; Quidant, R.; Romero-Isart, O. Levitodynamics: Levitation and Control of Microscopic Objects in Vacuum. *Science* **2021**, *374* (6564), eabg3027. https://doi.org/10.1126/science.abg3027.

(26) Manon Barrière. Study of Nanomaterials in Levitodynamics, 2025. https://theses.hal.science/tel-05281164v1.

(27) De Alwis Goonatilleke, M.; Thomas, M. P.; Ullah, A.; Pham, R. H.; Guiton, B. S. Direct Observation of Sample Dynamics in the Gaseous Environment: A Perspective on Current Trends and Future Directions of *In Situ* Gas Cell Transmission Electron Microscopy. *J. Phys. Chem. C* **2023**, *127* (38), 18791–18808. https://doi.org/10.1021/acs.jpcc.3c03759.

(28) Institut de Physique et Chimie des Matériaux de Strasbourg. Institut De Physique Et Chimie Des Matériaux De Strasbourg. *Institut de Physique et de Chimie des Matériaux de Strasbourg. Environmental TEM in gas atmosphere*. https://www.ipcms.fr/equipe/nanomateriaux/environmental-tem-in-gas-atmosphere/.

(29) Protochips. *TEM Environmental Gas Cell: Atmosphere AX | Protochips. Protochips*. https://www.protochips.com/solutions/in-situ-tem-solutions/in-situ-gas-cell/.

(30) AIRG. *Scanning Electron Microscope - AIRG. AIRG - APPLIED ISOTOPE RESEARCH GROUP.* https://www.air.app.br/scanning-electron-microscope/.

(31) Egel, A.; Czajkowski, K. M.; Theobald, D.; Ladutenko, K.; Kuznetsov, A. S.; Pattelli, L. SMUTHI: A Python Package for the Simulation of Light Scattering by Multiple Particles near or between Planar Interfaces. *J. Quant. Spectrosc. Radiat. Transf.* **2021**, *273*, 107846. https://doi.org/10.1016/j.jqsrt.2021.107846.

(32) Sumlin, B. J.; Heinson, W. R.; Chakrabarty, R. K. Retrieving the Aerosol Complex Refractive Index Using PyMieScatt: A Mie Computational Package with Visualization Capabilities. *J. Quant. Spectrosc. Radiat. Transf.* **2018**, *205*, 127–134. https://doi.org/10.1016/j.jqsrt.2017.10.012.

(33) Wiecha, P. R. pyGDM—A Python Toolkit for Full-Field Electro-Dynamical Simulations and Evolutionary Optimization of Nanostructures. *Comput. Phys. Commun.* **2018**, *233*, 167–192. https://doi.org/10.1016/j.cpc.2018.06.017.

(34) Wiecha, P. R.; Majorel, C.; Arbouet, A.; Patoux, A.; Brûlé, Y.; Colas Des Francs, G.; Girard, C. "pyGDM" - New Functionalities and Major Improvements to the Python Toolkit for Nano-Optics Full-Field Simulations. *Comput. Phys. Commun.* **2022**, *270*, 108142. https://doi.org/10.1016/j.cpc.2021.108142.

(35) Johnson, P. B.; Christy, R. W. Optical Constants of the Noble Metals. *Phys. Rev. B* **1972**, *6* (12), 4370–4379. https://doi.org/10.1103/PhysRevB.6.4370.

(36) *Handbook of Optical Constants of Solids*; Palik, E. D., Ed.; Academic Press: San Diego, 1998.

# CHAPTER 3. Directional light scattering in Mie-resonant Si particles with Au shells


3.1 Review of the colloidal Si@Au core-shell particles ..... 131
3.2 Experimental section ..... 132
3.2.1 Materials ..... 132
3.2.2 Synthesis of silica particles ..... 132
3.2.3 Synthesis of silicon particles ..... 135
3.2.4 Synthesis of the Au-decorated silicon particles ..... 136
3.3 Results ..... 138
3.3.1 Morphological analysis ..... 138
3.3.2 Electron energy loss spectroscopy (EELS) ..... 140
3.3.3 Single particle darkfield spectroscopy ..... 143
3.3.4 T-matrix/Mie-theory calculations of scattering spectra ..... 148
3.4 Conclusions and Perspective ..... 152
References ..... 153

## 3.1 Review of the colloidal Si@Au core-shell particles

There have been reported approaches to synthesize Si particles coated with (non-) particulate Au shells. However, we identified the need to realize a more continuous plasmonic Au shell based on the results in the literature, which we have summarized in a section of Chapter 1. The non-continuous nature of the fabricated nanostructures made it impossible to achieve optimum directional light scattering. The reported approaches discussed involve the surface chemical modification of pre-synthesized Si particles by functionalizing with an amine functional group. These particles are then decorated with pre-synthesized colloidal Au particles of a specific size. The particles realized by Chaâbani *et al*.[1] have non-uniform Au islands/shells that are composed of Au particles with diameters between 10 and 25 nm. Also, the Si core is not perfectly spherical. This offers another complexity in the study of the optical properties. Sugimoto *et al*.[2] adopted the same approach to fabricate an Au shell with particles around 25 nm. But while the Si cores are highly spherical, the shells are rough. The effect of these particle inhomogeneities is that neither report could accurately fit the experimental optical properties with the simulations. Other studies have attempted the laser ablation in liquid technique to fabricate the continuous shell. The gold particles are produced either by reducing in situ the solution of chloroauric acid ($HAuCl_4$)[3–7], laser ablation of Au film[8], or electrostatically attracting pre-synthesized Au particles[9]. However, none of these approaches has been able to produce ultrathin, homogeneous shells around a silicon core.

To benefit from the resonant properties of the dielectric core, the plasmonic shell must be thin enough that it does not strongly attenuate light entering the core. However, continuous thin plasmonic shells are challenging to realize due to the difficulty in depositing noble metals such as gold or silver onto Si particle surfaces. Therefore, this chapter aims to optimize the colloidal synthesis approach to improve the continuity of the Au plasmonic shell.

In this chapter, we present a two-step aqueous approach to prepare Si@Au core-shell particles with controllable shell thickness below 10 nm. The Au nanoparticle (AuNP) density around the Si particles can be increased by performing a second functionalization and deposition step.

The electromagnetic response of the particles was then studied using single-particle scattering spectroscopy and electron energy loss spectroscopy (EELS). Our results were compared with reference Si spheres and $SiO_2$@Au core-shell particles. This allows us to establish the contribution of the Au decoration to the optical response of the silicon particles. To further

elucidate the nature of the electromagnetic response of the particles, we performed T-matrix simulations, which replicated our experimental findings. We showed the importance of controlling the shell/core dimensions and the need for a continuous shell to maximize forward scattering.

## 3.2 Experimental section

### 3.2.1 Materials

Fuming sulfuric acid (reagent grade, 20% free $SO_3$ bases), trichlorosilane (99%), and toluene (HPLC grade) were purchased from Millipore Sigma. Hydrofluoric acid (electronic grade, 48–50 %), sulfuric acid (reagent grade, 95–98 %), and absolute ethanol (2350323, 99 %) were purchased from Fisher Scientific. Sodium chloride (0278, ≥ 99 %) was purchased from J.T. Baker. Tetrakis (hydroxymethyl) phosphonium chloride (THPC, A0412467, 75–85 %) was purchased from ThermoScientific. Sodium hydroxide (S5881, 98 %), (*3*-aminopropyl) trimethoxysilane, (APTMS, 281778, 97 %), Au (III) chloride trihydrate, (520918, 99.9 %), tetraethyl orthosilicate, (TEOS, ≥ 99 %, 86578), ammonium hydroxide solution (28 %, 221228), and L-arginine (≥ 99.5 %, 11009) were purchased from Sigma-Aldrich. Hydrochloric acid (AC07411000, 37 %) was purchased from Scharlau and used as received. For silica particle synthesis, absolute ethanol (99.9 %, PC80101.9200) was supplied by Atlantic Labo. Aqueous solutions were prepared using deionized water, produced using a Type 1 Milli-Q water purification system (18.2 MΩ cm). All chemicals were used without further purification. For the silver shell formation, Tin(II)chloride dehydrate ($SnCl_2 \cdot 2H_2O$, 98%), poly(vinylpyrrolidone) (PVP, 44,000 g/mol, 98%), silver nitrate ($AgNO_3$, 99.0%), and formaldehyde (HCHO, 37 wt% in water, containing 10-15 wt% methanol as a stabilizer) were supplied by Sigma-Aldrich.

### 3.2.2 Synthesis of silica particles

The synthesis of silica particles was carried out using a two-step regrowth strategy. The small silica particles were first obtained according to a previously published protocol where tetraethyl orthosilicate (TEOS) was slowly hydrolyzed in an aqueous layer using L-arginine as a base catalyst (Protocol 3.1). The latter is suitable for obtaining small monodisperse particles. The size distribution of the silica particles was assessed by statistical analysis of the transmission electron microscopy (TEM) images, as shown in Figure 3.1a. At the same time, the concentration of the batch was determined by the dry extract method. The average size of the particles was measured to be 34 ± 3 nm, and the particle concentration was determined to be ~

$4.7 \times 10^{14}$ particles/mL. Figure 3.1b shows the TEM image and size distribution of the regrowth particles (Protocol 3.2), whose average diameter was estimated to be 197 ± 4 nm.

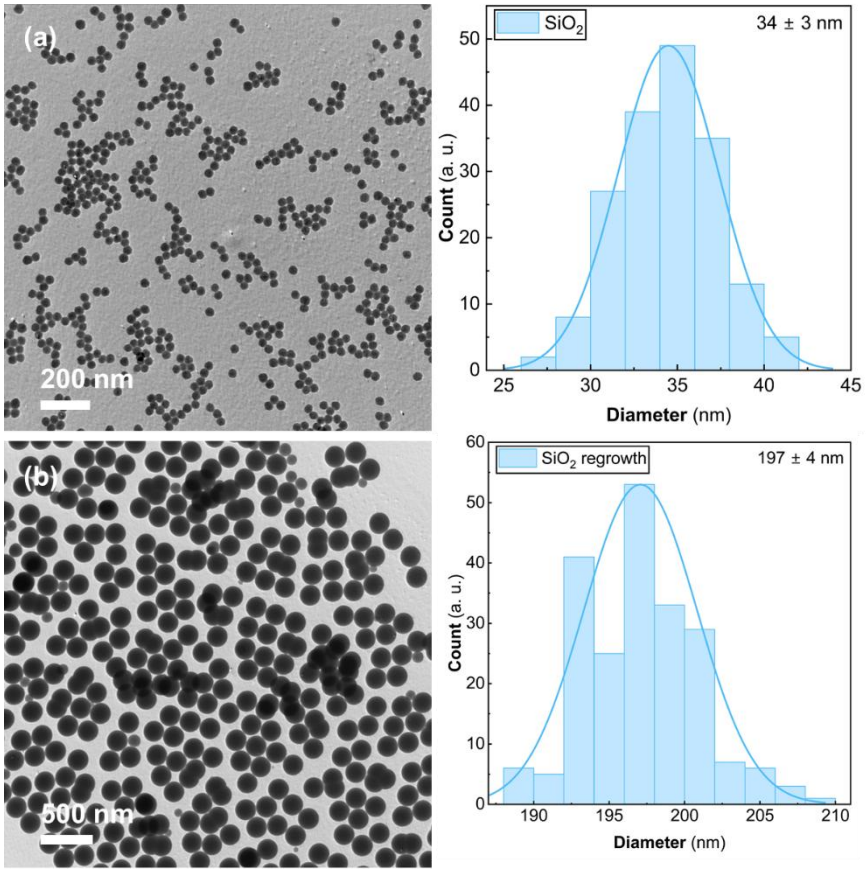



*Figure 3.1 TEM images of the (a) small silica particles and (b) big silica particles after regrowth*

**Protocol 3.1 Growth of 30 nm $SiO_2$ particles**

100 mL of an aqueous L-arginine solution (6 mM) was added to a 150 mL flat-bottomed, cylindrical, jacketed reaction vessel with hot water circulation at 60°C, equipped with a reflux condenser. The solution was stirred at 150 rpm using a 30 × 8 $mm^2$ Teflon-coated stir bar. To this was then added gently 10 mL tetraethylorthosilicate (TEOS), which remained in a separate phase from the aqueous solution. The mixture was left until the upper TEOS phase completely vanished (~ 3 days). The particle size was checked by TEM before use and confirmed to be (34 ± 3) nm. The sample concentration was determined by dry extraction to be ~ 14.5 g $L^{-1}$ (~ $4.7 \times 10^{14}$ particles/mL). This synthesis approach is based on the protocol first published by Hartlen et al.[10] and optimized by Désert et al.,[11,12]

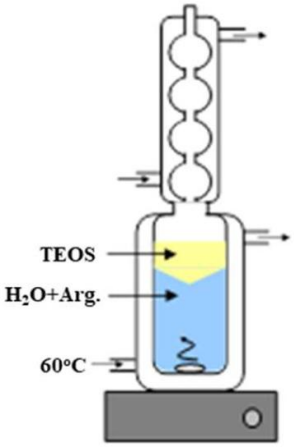



*Figure 3.2 Schematic diagram of the setup for the synthesis of silica seeds*

The silica mass concentration was measured by weighing the solid residue obtained from drying 5 mL of the dispersion in an oven at 70°C overnight. Then the concentration of particles was calculated from the equation, where $\rho_{SiO_2}$ and $D_{SiO_2}$ are the silica density (2.2 × $10^{-21}$ g/$nm^3$) average diameter of the particles (nm) as measured by TEM, respectively.

$$C_{SiO_2} = \frac{6 \times C_m(SiO_2)}{\pi \times D^3{}_{SiO_2} \times \rho_{SiO_2}} \qquad (3.1)$$

The 30 nm silica seed particles were regrown to a larger size following a Stöber approach. The amount of TEOS to be added for the regrowth of the particles is critical to control the final size of the silica particles. This can be determined using the formula below:

$$V_{TEOS} = \frac{M_{TEOS} \times \rho_{SiO_2}}{M_{SiO_2} \times \rho_{TEOS}} N_{SiO_2} \times \frac{\pi}{6} \times (D_f^3 - D_i^3) \qquad (3.2)$$

Where $D_f$, $D_i$, and $N_{SiO_2}$ are the targeted diameter, the initial diameter, and the number of the silica particles contained in the regrowth volume dispersion. $M_{TEOS}$ is the molecular weight of TEOS (208.32 g/mol); $\rho_{TEOS}$ the TEOS density (0.94 g/$cm^3$) and $M_{SiO_2}$ is the molecular weight of silica (60.08 g/mol).

**Protocol 3.2 Regrowth of silica particles to 200 nm**

Absolute ethanol (910 mL) and ammonium hydroxide solution (29 %, 70 mL) were mixed in a 2 L round-bottomed flask to which 1.6 mL of the 30 nm $SiO_2$ particle suspension was added under stirring. TEOS (100 mL) was then added by a syringe pump (KD Scientific, 78-9100F) at a rate of 1.4 mL $h^{-1}$ through a cannula (Braun, Venofix A). The solution was left for ~24 h after the TEOS addition had been completed. The ammonia was removed, and the volume of the particle solution was reduced by rotary evaporation (ice-cooled condenser, 60 °C, 0.2 atm,

240 rpm). Once a suitable volume had been reached, the particles were cleaned by centrifugation (3000 × g, 5 min) before resuspension in ethanol. The size of the particles was determined to be (197 ± 4) nm by TEM. The concentration of the particles was determined by dry extraction to be 26.9 g $L^{-1}$ ($1.5 \times 10^{12}$ particles/mL).

### 3.2.3 Synthesis of silicon particles

The synthesis of the silicon particles was carried out in a two-step protocol. This was carried out by the research group of pur collaborator, Professor Jonathan G. C. Veinot, at the University of Alberta, Canada[13]. First, the silicon-rich oxide precursor known as hydrogen silsesquioxane was synthesized according to protocol 3.3[14]. The white, solid sample obtained was transferred into a crucible and loaded into a furnace. The solid precursor was heated to 1700 °C for 1h under the flow of Ar gas to obtain silicon particles with an average size of 160 nm, as shown in Figure 3.3a and b. The silicon particles have a native oxide shell of silica, as shown in the high-resolution TEM in Figure 3.3c.

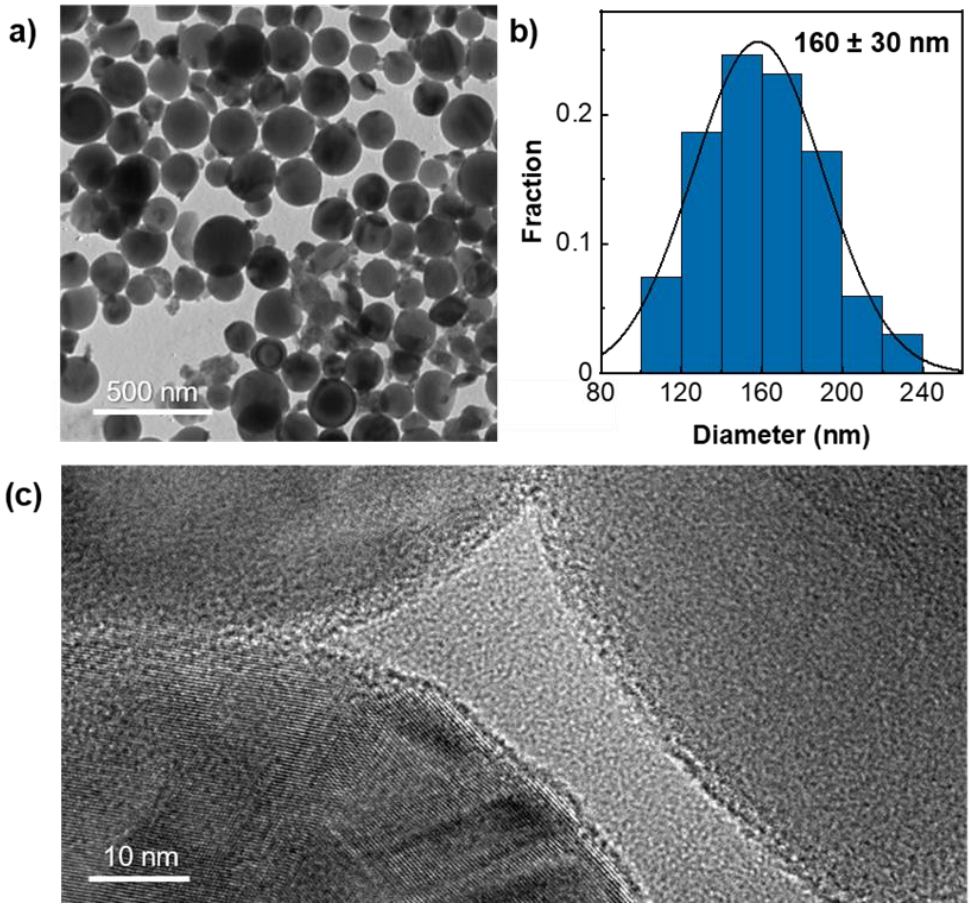



*Figure 3.3 (a) Transmission electron microscopy (TEM) of a batch of bare silicon cores and (b) their size distribution, (c) HRTEM image where the native oxide shell is visible.*

**Protocol 3.3 Preparation of hydrogen silsesquioxane (HSQ)**

The synthesis of HSQ was based on a published literature protocol[14]. On an Ar-filled Schlenk line, concentrated sulfuric acid (15 mL) and fuming sulfuric acid (7 mL) were mixed in a 2 L round-bottom flask. Dry toluene (45 mL) was added dropwise, followed by a solution of trichlorosilane (16 mL) in dry toluene (110 mL), added dropwise overnight. Both additions were performed under vigorous stirring using a Teflon-coated stir bar. The mixture was decanted into a separatory funnel, where the toluene layer was isolated and then washed three times with a solution of aqueous sulfuric acid (1.2 L of $H_2O$, 0.4 L of $H_2SO_4$). The washed organic layer was dried and neutralized over $MgSO_4$ and $CaCO_3$ overnight. The volume of solvent was reduced using a rotary evaporator, followed by drying under a high vacuum, yielding a white solid that was stored under vacuum until use.

**Protocol 3.4 Preparation of Si core particles**[13]

HSQ (2 g) was transferred to a yttria-stabilized zirconia crucible and loaded into a Carbolite CTF 18/300 tube furnace equipped with an alumina tube. The furnace was programmed to heat at a ramp rate of 5 °C $min^{-1}$ to 1700 °C under the flow of Ar gas, held at this temperature for 2h, and then cooled at 10 °C $min^{-1}$. This thermal treatment yielded an oxide composite containing Si nanodomains within a $SiO_x$ matrix. The resulting composite was ground using an agate mortar and pestle before shaking in a solution of ethanol and glass beads for 12 h to achieve a powder with an approximate grain size of 1 μm. The powder was collected via vacuum filtration and dried overnight. To create a colloidal dispersion of Si particles, the powdered composite (300 mg) was etched using a solution of ethanol : $H_2O$ : HF (3 mL : 3 mL : 3 mL) in a plastic beaker, under stirring with a Teflon-coated stir bar. After 90 min, toluene was added to the aqueous solution, and the Si particles were extracted using a plastic pipette. The colloidal solution of Si particles was isolated by centrifugation (1200 × g for 5 min) before redispersing in 15 mL of toluene. This process was repeated twice to remove residual etchant.

### 3.2.4 Synthesis of the Au-decorated silicon particles

The Au seed solution was prepared according to the Duff synthesis detailed in protocol 3.6 (Figure 3.4). The functionalization of the silicon particles with (3-aminopropyl) trimethoxysilane changes the surface chemistry from hydroxyl to an amine group. The APTMS acts as a sol-gel linker for the adsorption of the Au seeds, which are sparsely distributed around the Si core. After the first deposition, a second APTMS functionalization was used as a linker to reactivate the first Au-seeded silicon particles. The hydrolysis of the APTMS forms an

amine-rich solution, which enables the second deposition of the Au seeds. The addition of a salt solution during the coating is to increase the deposition density of the Au seeds. The increase in the Au seed density between the first and second deposition can be shown in the TEM images in Figure 3.6.

**Protocol 3.5 Surface amination of the Si particles**[15]

The Si particle dispersion (50 mg) was diluted in 200 mL of ethanol. APTMS (5 mL) was added to the mixture and stirred overnight. The dispersion was then heated at 60 °C under reflux overnight. The aminated Si particles were purified by three cycles of centrifugation/redispersion in ethanol (8000 × g, 10 min). The particles were dispersed in 40 mL of ethanol upon the final cycle.

**Protocol 3.6 Synthesis of Au seeds using the Duff protocol**[16]

To 228 mL of deionized $H_2O$ in a 500 mL round-bottom flask under stirring at 800 rpm, 7.5 mL NaOH (0.2 M), and 5 mL diluted THPC (0.01 % vol.) were sequentially added and stirred for 15 min. Then, 5 mL $HAuCl_4$ (25 mM) was quickly added in a single portion, and the solution immediately changed from colorless to brown, indicating the formation of Au seeds. The prepared Au seed solution was aged at 4 °C for 14 days before use. This is based on a previous study establishing that aged Au seeds for 7 days produced a relatively monodisperse deposition onto the $SiO_2$ particles, while 1 day-aged Au seeds produced a heterogeneous deposition[15].

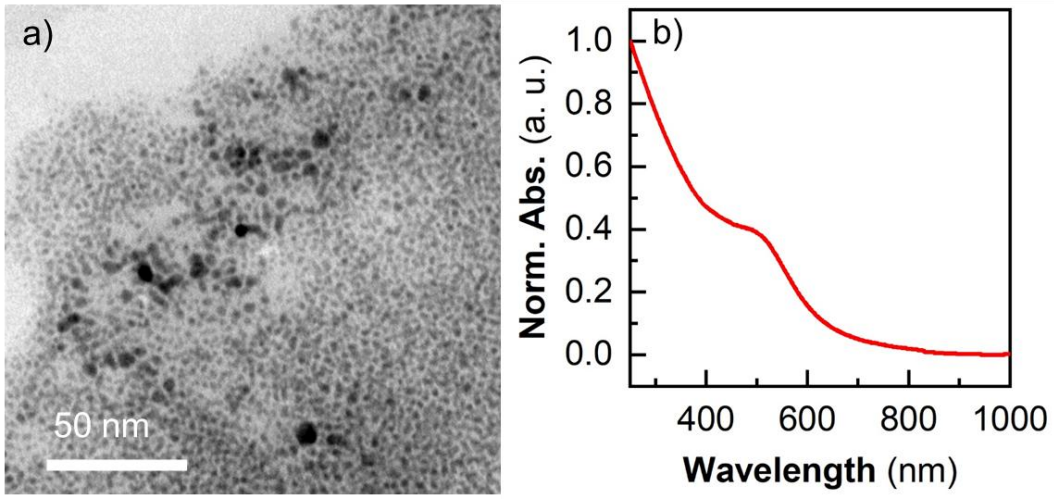



*Figure 3.4 (a) TEM image of the gold seeds. (b) The absorption spectrum of the Au particles (average size, 3 – 5 nm) shows a small plasmon resonance peak at ~ 505 nm.*

**Protocol 3.7 First deposition of the Au seeds onto the Si core**[15]

APTMS-functionalized Si particles (5 mL) were added to 38 mL of Au seed solution with an additional 3.50 mL of NaCl (1 M). The dispersions were slowly agitated overnight at 250 rpm on a roller-mixer. Excess Au seeds were removed by two cycles of centrifugation/redispersion in water (8000 × g, 10 min). After the final cycles, the particles were redispersed in water (10 mL).

**Protocol 3.8 Preparation of pre-polymerized APTMS solution**

This synthesis was adapted from a published protocol[17]. $H_2O$ (33 mL) was mixed with 1.10 mL of HCl (0.1 M) and 1.30 mL of APTMS (stock solution) and vigorously stirred (800 rpm) for 1 h.

**Protocol 3.9 Second deposition of the Au seeds onto the Si core**[15]

Single-coated Si@Au suspension (5 mL) was mixed with 35.4 mL of pre-polymerized APTMS solution and stirred for 20 min. Then, the excess pre-polymerized APTMS was removed by three cycles of centrifugation/redispersion in water (8000 × g, 10 min). After the final washing cycle, the particles were redispersed in 20 mL of Au seed solution with an additional 1.70 mL of 1 M NaCl. The dispersions were slowly stirred overnight at 250 rpm. The excess Au seeds were removed by two cycles of centrifugation/redispersion in water (8000 × g, 10 min). After the final cycle, the particles were redispersed in water (5 mL).

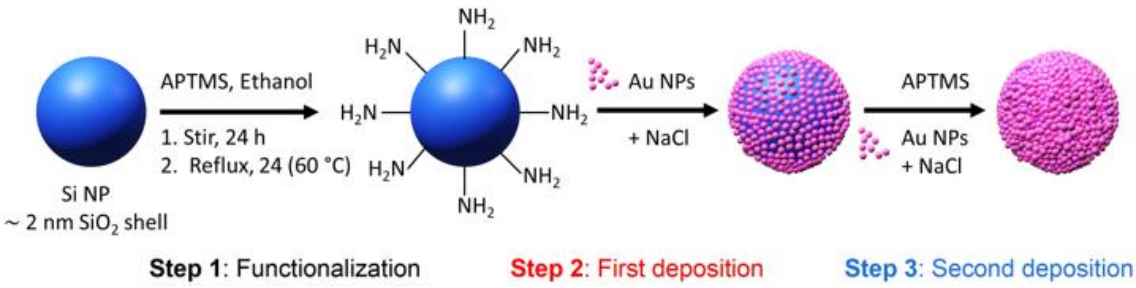



*Figure 3.5 Schematic illustration of the protocol for the synthesis of the Au-decorated silicon particles.*

## 3.3 Results

### 3.3.1 Morphological analysis

The produced Si particles are crystalline, size polydisperse, and spherical within the size range required to scatter visible light (100 – 200 nm) in a single batch (Figure 3.3), allowing us to study the effect of core size on the optical properties. Upon exposure to air, the

polycrystalline silicon forms a passivating $SiO_2$ layer of ~ 2 nm, which can be visualized as a lower contrast material in a high-resolution TEM image shown in Figure 3.3c.[18] We then functionalized the native $SiO_2$ layer using an aminosilane according to the protocol in Figure 3.5.[15] Following this, we mixed the aminated Si particles with negatively charged AuNPs (Figure 3.4) in a NaCl buffer. Particles produced at this point are hereafter referred to as "*single coating"* (Figure 3.5). The $Na^+$ and $Cl^-$ ions in solution screen the electrostatic repulsions between AuNPs, enabling a higher deposition density. Following the same protocol, we also fabricated $SiO_2$@Au core-particulate shell particles as a low-index (non-Mie resonant) reference with only plasmonic contributions. On a fraction of the single coating Si samples, we deposited a second layer of AuNPs by functionalizing the AuNP-decorated Si particles with polymerized aminosilane, followed by re-mixing with the colloidal AuNPs. Samples prepared this way are hereafter referred to as "*double coating"* (Figure 3.5). We estimate the Au shell thickness to be ~4 nm after the single coating protocol and ~7 nm after the double coating protocol based on energy-dispersive X-ray mapping (Figure 3.6).

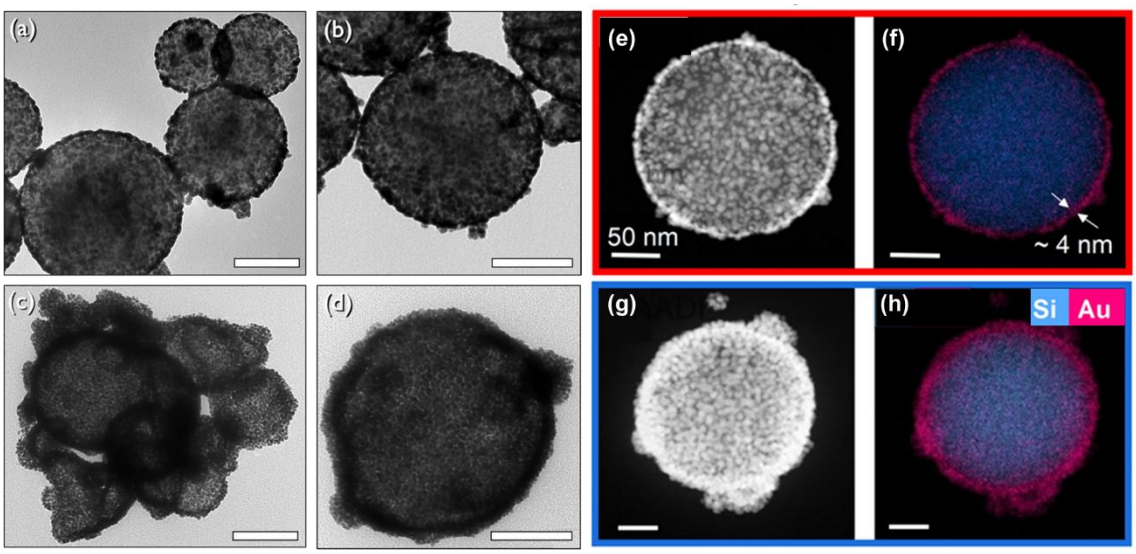



*Figure 3.6 TEM images allowing the comparison of the surface density of the single (a & b) and double (c & d) Au-decorated silicon particles. All scale bars are 100 nm. High-angle annular darkfield, and TEM/EDS elemental mapping of the core Si (dark-blue) and decorated Au particles (pink). The scale bar represents 50 nm.*

The ultraviolet (UV)-Vis-NIR extinction spectroscopy shows the optical properties of the two batches of Si@Au and the bare Si particles (Figure 3.7a). The UV-vis-NIR extinction spectrum of the colloidal Si particles (black curve) has a maximum at $\lambda$ ~ 603 nm. The spectra of the Si particles after the first AuNP deposition have a slightly blueshifted maximum at

$\lambda \sim 581$ nm, and after the second AuNP deposition, the maximum was similar at $\lambda \sim 581$ nm. This is similar to the simulated scattering cross-sections of hollow Au particulate shell with diameter of 186 nm made of Au particles with diameter of 5 nm. The intensity of the scattering increase and the electric dipole red-shift with increased surface coverage (Figure 3.7b). We can thus conclude that both the Au shell and the Si core contribute to the particle's optical behavior.

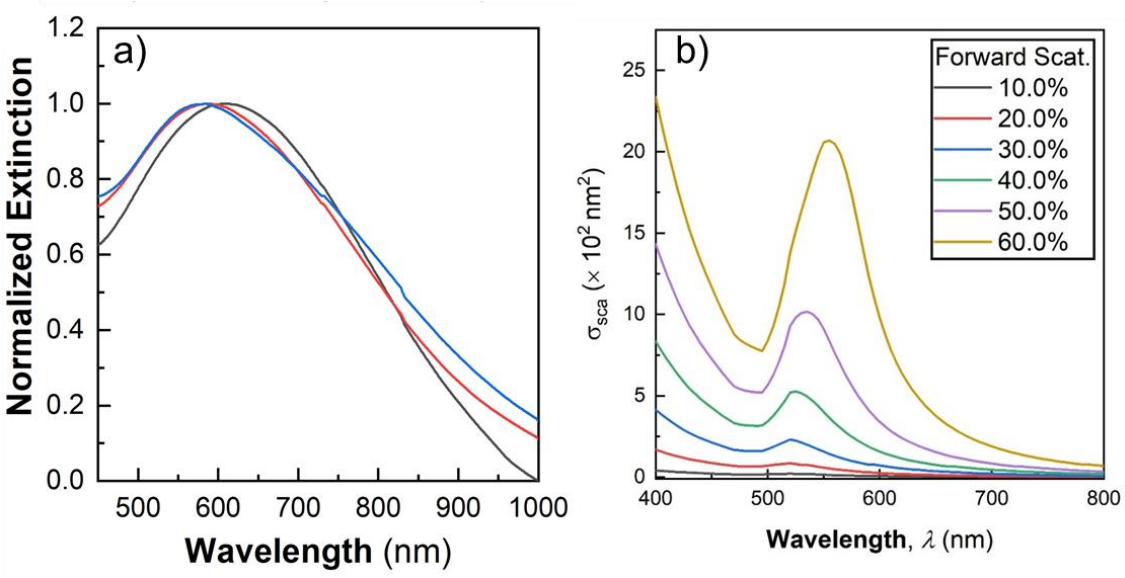



*Figure 3.7 a) UV-Vis-NIR extinction spectra of the Au-decorated 160 nm Si particles with single coating (red), double coating (blue), and bare Si particles (black). (b) T-matrix simulated optical scattering cross-sections of hollow 186 nm shells comprised of a single layer of 5 nm Au particles with increasing density. As the number of Au particles increased, we observed not only a redshift in the electric dipole (ED) but also an increase in intensity.*

### 3.3.2 Electron energy loss spectroscopy (EELS)

To better understand the contributions to the optical spectra arising from the Si core and the Au particles, we performed single-particle spectroscopy experiments. In a first step, we compared the electron energy loss spectra (EELS) of $SiO_2$@Au (single coating), bare Si, and Si@Au (single coating). These EELS results are shown in Figure 3.8a-c for particles of comparable size ($d \sim 180$ nm), showing the spatial distribution of electron energy losses, $\Delta E$, associated with the electromagnetic resonances of the particles. The spectra are obtained from the average sum signal around the particle surface in the suspended zone, unsupported by the lacy carbon substrate. For the $SiO_2$@Au particles (Figure 3.8a), we observe a single peak at ~2.25 eV, attributed to the LSPR of the Au particles, which can also be seen in simulated optical spectra (Figure 3.7b).

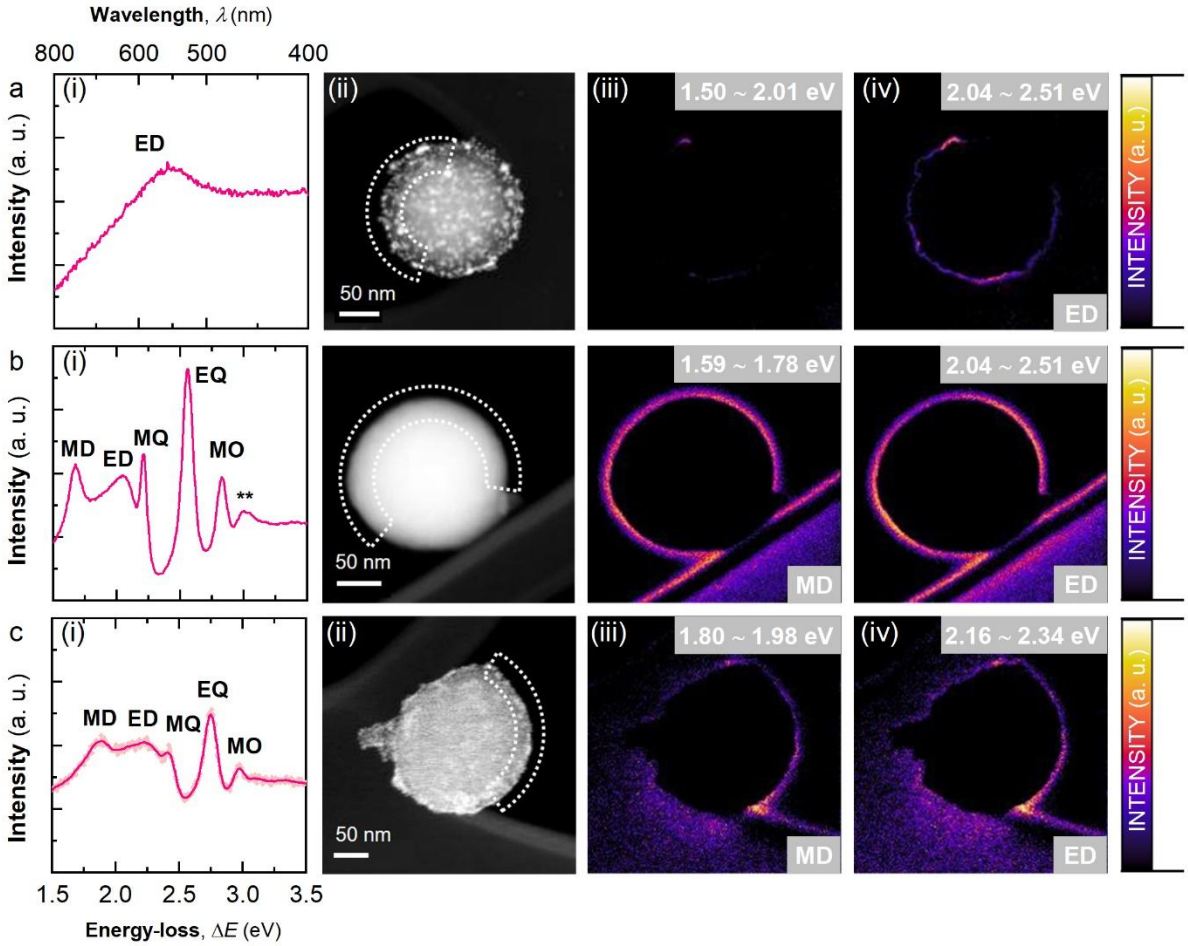



*Figure 3.8 EELS analysis of particles with a core diameter of ~ 180 nm: (a) $SiO_2$@Au (single coating), (b) bare Si, and (c) Si@Au (single coating). (i) Experimental EELS for single particles taken from areas with particles unsupported by lacy carbon. (ii) High-angle annular darkfield Scanning TEM images, and (iii, iv) EELS intensity maps for the (iii) magnetic dipole (MD), and (iv) electric dipole (ED) of each particle. Higher energy resonances are also identified in the spectra resulting from the electric quadrupole (EQ), magnetic quadrupole (MQ), magnetic octopole (MO), and superpositions of higher-order Mie resonances (**).*

For the bare Si particle (Figure 3.8b), we observe several peaks arising from Mie resonance. From the multipolar decomposition of the EELS simulations shown in Figure 3.9a, the low-energy peak at ~1.70 eV results from the MD resonance of the particle, while the high-energy peak at ~2.10 eV results from the ED resonance, very well within the accuracy range of Figure 3.8b and 3.8c. For the Si@Au particle, a first observation is that there seems to be no systematic shift in the peak energies of the different order Mie resonances after Au coating (Figure 3.8b/3.8c) with any differences largely consistent with expected shifts due to slight variations in particle size and geometry between measurements. Comparing the EELS intensity

of the Si and Si@Au particles, the decorated particles show noisier peaks, which are attributed to the core resonances being damped by the plasmonic particles located at the Si surface (Figure 3.8).

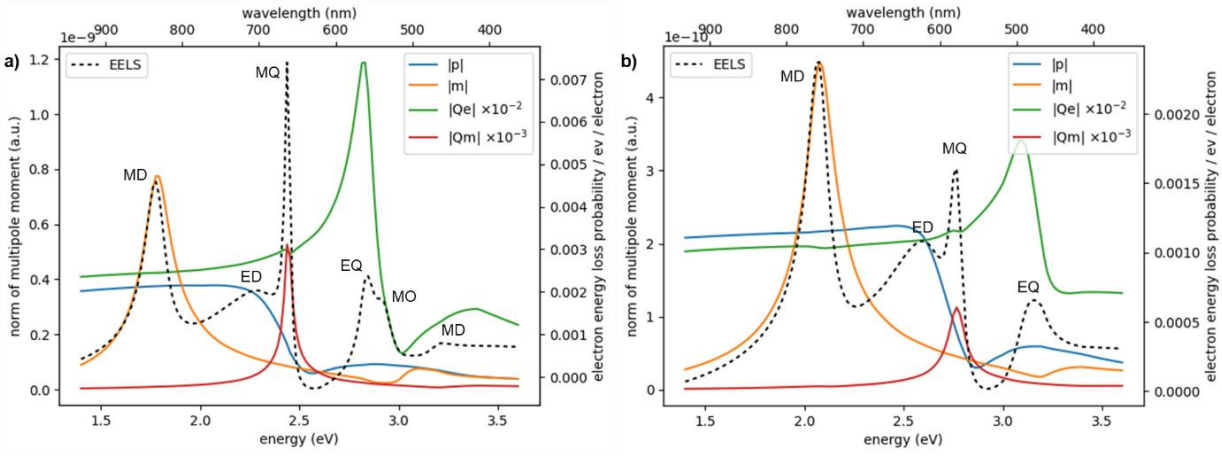



*Figure 3.9. Simulated Experimental electron energy loss spectra (EELS) and their multipolar decomposition for Si particles with diameters of a) 180 nm, and b) 150 nm, respectively. The EELS simulations were calculated using the fast electron module of pyGDM on a full silicon sphere. The multipole decomposition of electron-beam-induced responses for different diameter Si particles was calculated using Green's dyadic method. (2, 3)*

In Figure 3.10, similar observations were made for a bare Si particle with a diameter of ~ 150 nm. The low-energy peak at ~1.98 eV results from the MD resonance, while the high-energy peak at ~2.41 eV results from the ED resonance of the particle. These correspond to the position of the peaks in the simulated spectra in Figure 3.9b. Comparing the EELS intensity of the Si and Si@Au particles, the same damping effect of the core resonances was observed, which could be attributed to the plasmonic particles located at the Si surface (Figure 3.10).

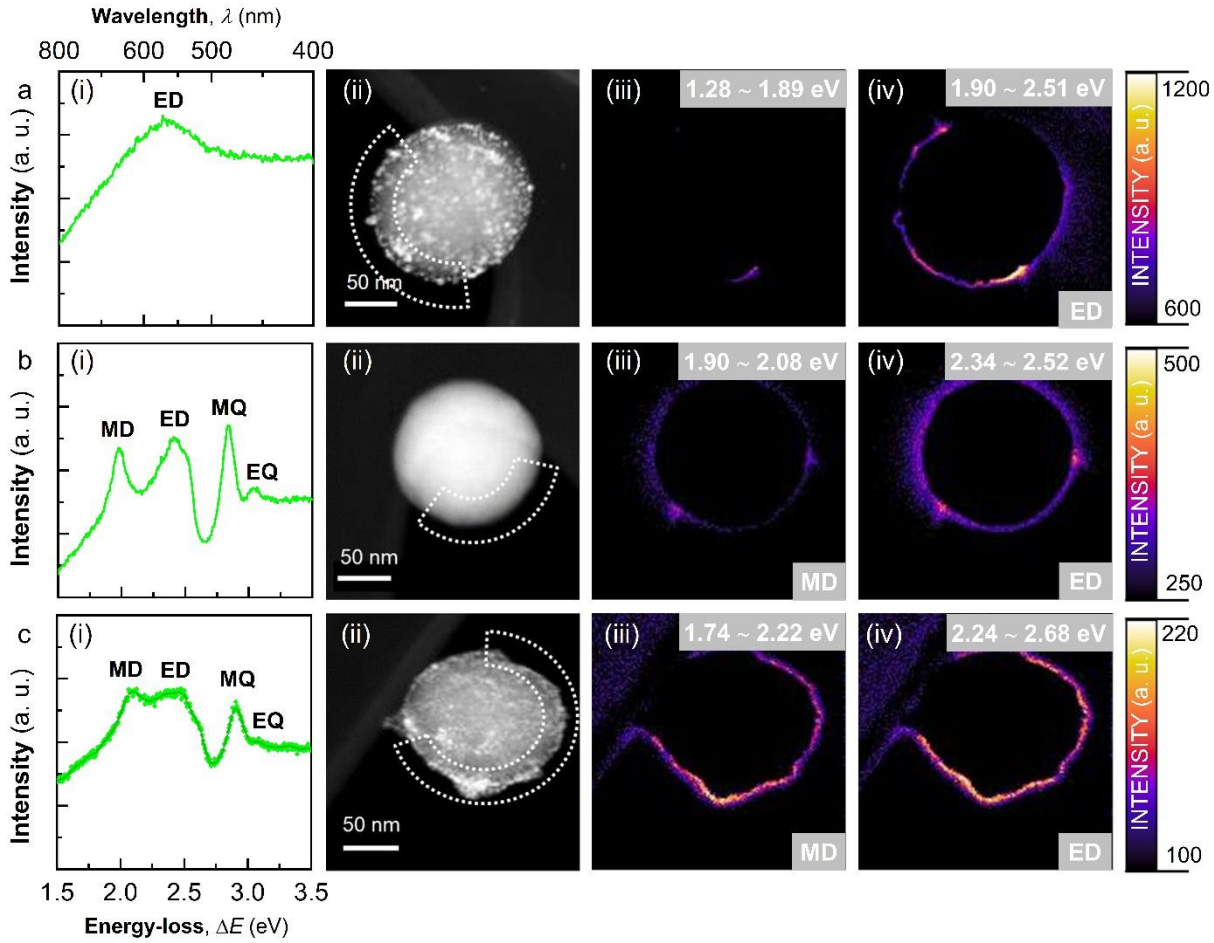



*Figure 3.10. EELS analysis of particles with a core diameter of ~ 140 nm: (a) $SiO_2$@Au (single coating), (b) bare Si, and (c) Si@Au (single coating). (i) Experimental EELS spectra for single particles taken from areas of the particles unsupported by the lacy carbon substrate. (ii) Scanning TEM – high angle annular darkfield images, and (iii, iv) EELS intensity maps for the (iii) ED, and (iv) magnetic dipole (MD) of each particle. Higher energy resonances are also identified in the spectra resulting from the electric quadrupole (EQ), magnetic quadrupole (MQ), magnetic octopole (MO), and superpositions of higher order Mie resonances.*

### 3.3.3 Single particle darkfield spectroscopy

Figure 3.11 shows the optical darkfield microscopy, single particle backscattering spectroscopy, and the corresponding scanning electron microscopy (SEM) images of the Si@Au nanostructures with a range of core sizes from 110 – 190 nm. The observed particle color in the darkfield optical microscopy images shifted from blue to red and increased in scattering intensity with increasing Si core diameter (100 – 200 nm).

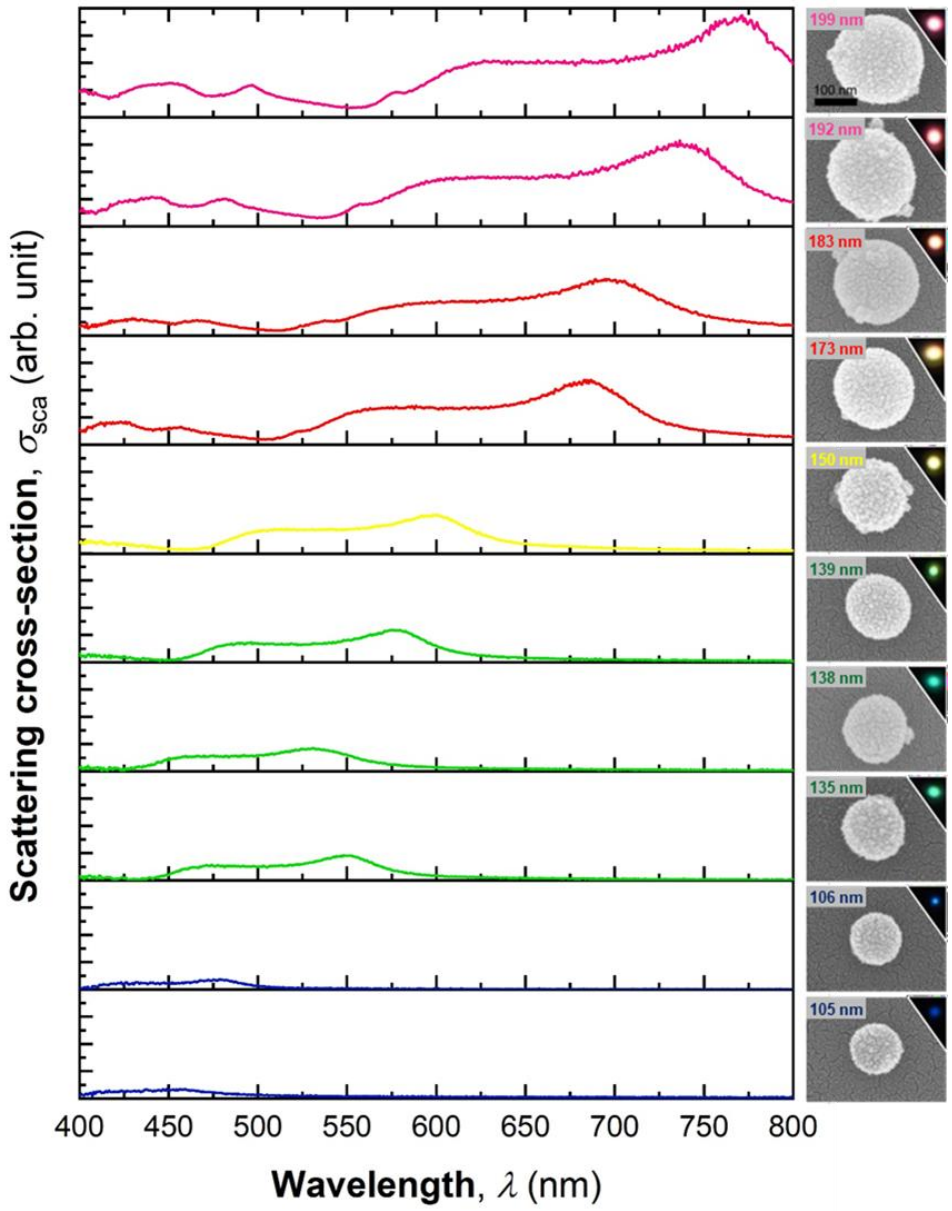



*Figure 3.11 Single particle scattering spectroscopy/microscopy of different diameters single coating Au-decorated Si particles. Darkfield scattering spectra and images, and the corresponding Field-emission scanning electron microscope of various sizes (105 – 200 nm in core diameter), single Si@Au heterostructures placed on a glass substrate. The lowest-order ED and MD resonances are observed. These peaks shift to longer wavelengths, and the scattering color changes from bluish to reddish with increasing core size.*

Due to the core being highly spherical and the shells being homogeneous, the results are highly consistent between similarly sized particles. In Figure 3.12, the measurements on twenty particles showed a strong linear correlation between the core diameter and the peak (ED and MD modes) scattering wavelength. We confirmed the red-shift in both the ED and MD modes

due to the increase in the diameter of the core Si particle. Also, we confirmed that the distance between the ED and MD is less in the Si@Au particles compared to the bare Si particles.

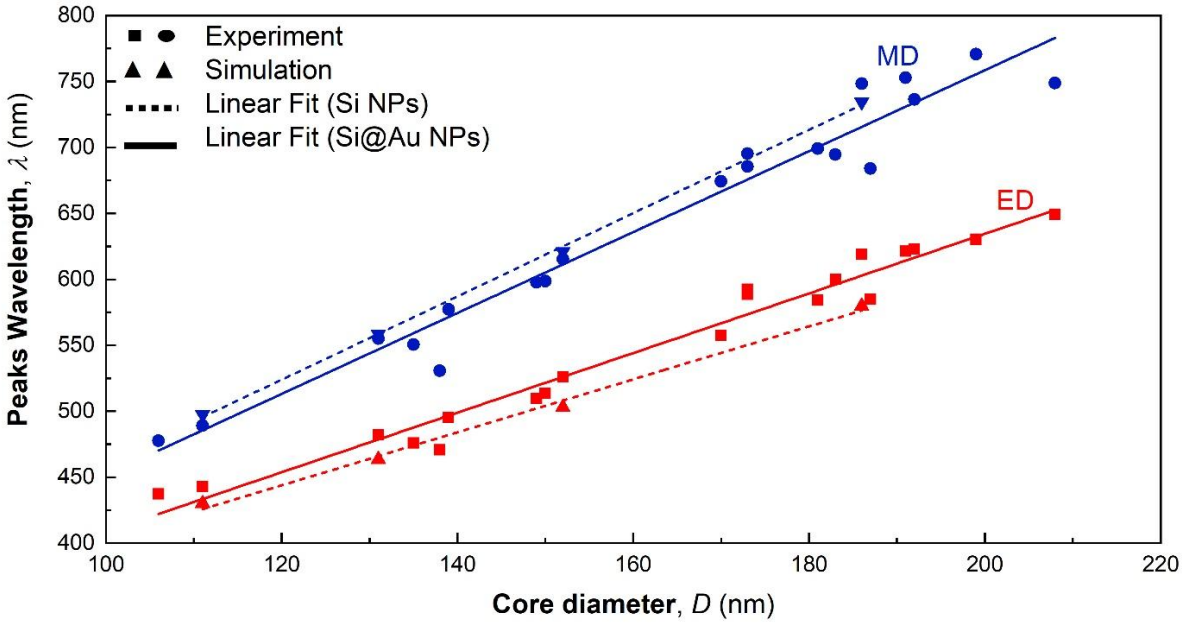



*Figure 3.12 Peak of scattering wavelength of the ED and MD resonances of the single coating Au-decorated Si particles as a function of the silicon core diameter. The experimental data are linearly fitted (solid lines) for the ED and MD resonances. The core diameter ranges between 100 and 200 nm.*

To interpret the resonant features of the experimental scattering spectra, we compare the experimental spectra (blue lines) to T-matrix simulated backscattering spectra of single coating Si@Au particles, using Au spheres of ~ 4 nm diameter for the coating with 50 % surface coverage (red lines). First, different surface coverages were tested to best fit the experimental spectra, as shown in Figure 3.13a. The best fit of the experimental data is the surface coverage of 50%. From Figures 3.13b and 3.13c, we can see a slight red-shift in the scattering wavelength and a dampening of the intensity with increasing surface coverage of the Si core with Au particles of 4 nm.

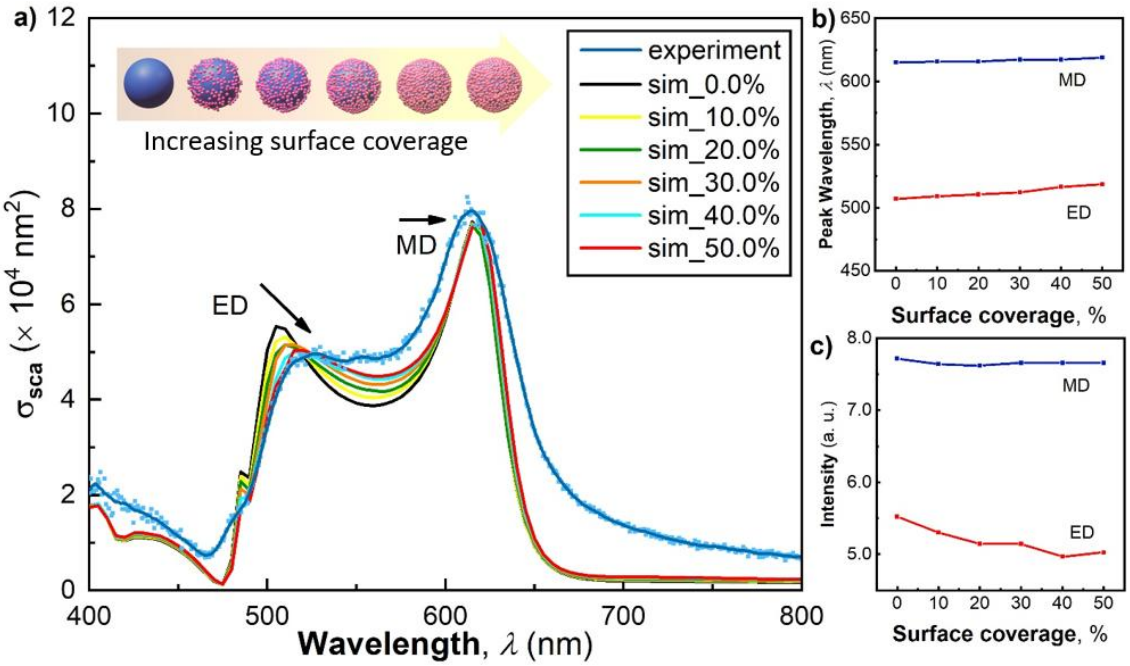



*Figure 3.13 (a) Simulated optical scattering spectra for a 152 nm silicon core decorated with different surface coverage of 4 nm diameter Au particles. Scattering wavelength (b) and intensity (c) as a function of the percentage surface coverage of Au nanoparticles. The peak wavelength redshifts roughly linearly with increased surface coverage. Scattering intensity decreases approximately linearly with increased surface coverage.*

We determined the particle sizes using scanning electron microscopy images of the prepared substrates after scattering spectra collection (Figure 3.14a). In Figure 3.14b, the T-matrix simulations of the Si@Au nanostructures fit very well the experimental measurements, with slight deviations that can be explained by factors such as substrate, broad-angle and non-plane wave illumination, non-perfect spherical shape, and the darkfield detection configuration. As a reference, we also show calculated backscattering spectra of Si spheres without coating (green lines). In the case of the 186 nm particle, systematic relative shifts of the full spectra can be attributed to potential size mismatches with our estimations from SEM images. In comparison with the bare Si core (green), the main impact of the Au sphere shell is a small redshift as well as a slight broadening of the electric dipole mode, whereas the magnetic dipole is almost unchanged for all sphere sizes. We also observe that, if a mode falls within the spectral region of the LSPR of the AuNP-decorated spheres between 500 nm and 600 nm, its intensity is weakened relative to the rest of the spectrum. This is the case for Si core diameter between 100 – 130 nm, where the MD is affected. Also, for a Si core diameter of 150 nm, the ED mode is affected.

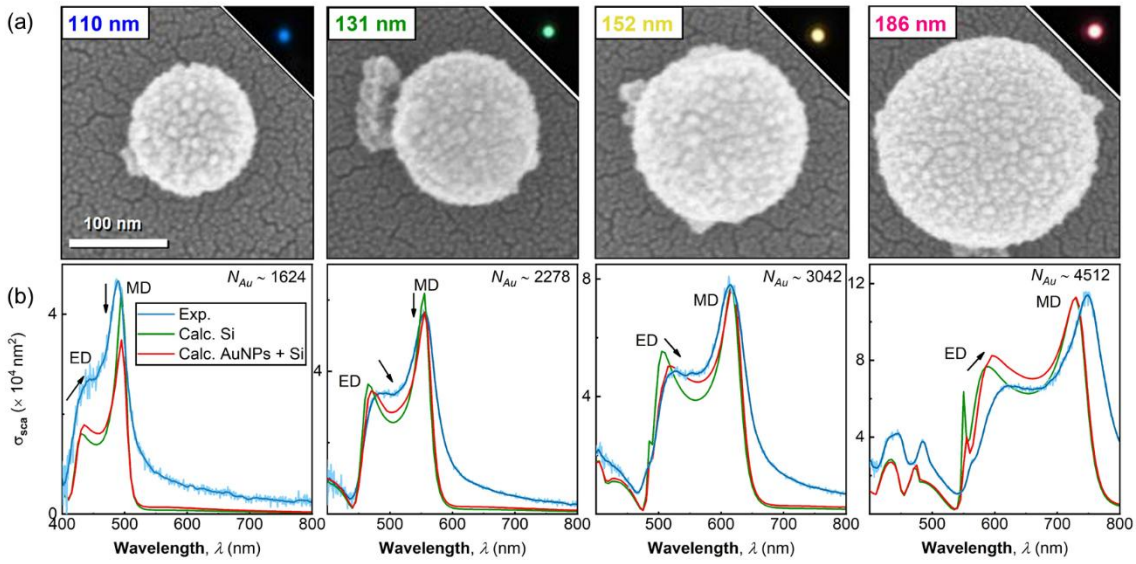



*Figure 3.14 (a) Field-emission SEM and (Inset, top-right) darkfield optical images of single coating Si@Au particles with core diameters of (left to right) 110, 131, 152, and 186 nm. (b) Experimental single particle scattering spectra of a Si@Au particle with corresponding Si core diameters (blue). T-matrix–simulated scattering spectra for bare Si (green) and single-coated Si@Au using Au satellites of 4 nm diameter and 50 % surface coverage (red). The instrumental noise of the measured scattering spectra has been smoothed using a Savitzky-Golay filter.*

The double-coating Si@Au particles gave similar results to the single coating, apart from a notably greater ED redshift and significantly stronger damping, mainly of the ED (Figure 3.15). However, achieving a good fit between the experimental and simulated spectra is more complicated. We hypothesized that the reasons for this are the overlapping nature of the Au particles, the bumpy nature of the coating, and the increased non-spherical and inhomogeneous nature of the particles.

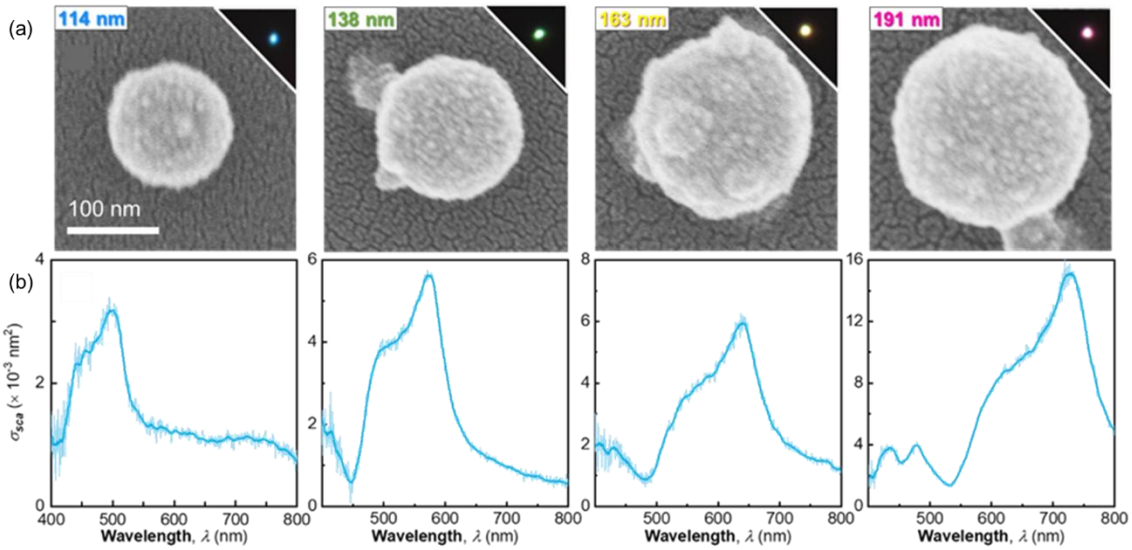



*Figure 3.15 (a) Field-emission scanning electron microscope and darkfield optical images of double coating Si@Au nanospheres with different core sizes (Inset, top-right). (b) Experimental scattering spectra of different diameter silicon cores decorated with Au nanoparticles. The instrumental noise of the measured scattering spectra is smoothed using a Savitzky-Golay filter. The scale is the same for all SEM images.*

### 3.3.4 T-matrix/Mie-theory calculations of scattering spectra

Next, the forward scattering fraction was elucidated using T-matrix calculations for the single coating Si@Au particles and using analytical Mie-theory calculations for bare Si particles (Figure 3.16). The forward and backward scattering were integrated over the full hemisphere. We found that the Mie resonances that are spectrally overlapping the LSPR of the Au shell (500 – 600 nm) were damped compared with the bare Si sphere. For all particle sizes studied, there was a redshift of the ED, up to $\Delta\lambda \sim 15$ nm for the 186 nm Si core (Figure 3.14b) after decoration with Au particles. This leads to better mode overlap and, correspondingly, an increased proportion of forward scattered light. In terms of the scattering intensity for smaller particles, such as a 110 nm particle, the scattering spectra for the core-particulate shell particle show decreased MD intensity (~ 500 nm) and increased ED intensity (~ 430 nm) for both forward and backward scattering, compared to the bare Si particle (Figure 3.14b). By comparison, a larger 186 nm decorated particle shows enhanced scattering at both the ED and MD compared to a bare Si particle of the same size.

To better compare the impact of these differences, we plotted the fraction of light scattered in the forward direction (Figure 3.16e-h). The forward scattering ratio does not dramatically change upon decoration with the AuNPs compared to bare Si, irrespective of the core Si

diameter. On the other hand, more light is scattered in the case of the larger decorated Si spheres.

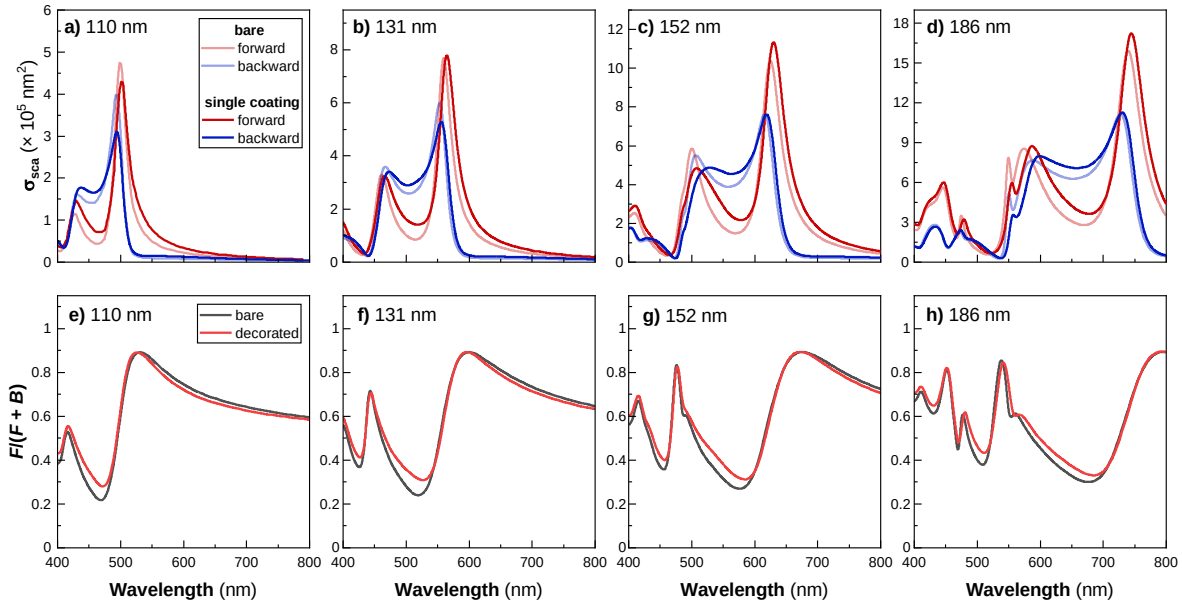



*Figure 3.16 T-matrix simulated scattering spectra of particles having a diameter of (a, e) 110, (b, f) 131, (c, g) 152, and (d, h) 186 nm; the (a-d) (red) forward and (blue) backward scattering cross-sections of (dark) single-coating Si@Au and (light) bare Si particles. (e-h) The forward scattering fraction (F/(F+B)) of the (red) single-coating Si@Au and (black) bare Si particles.*

In both the EELS and optical single-particle spectra, there is no evidence of peaks resulting from a hybridized mode between the plasmonic shell resonance and Mie resonance of the core, in contrast to what has been previously reported[2,19]. We believe that this is because the Au coatings are composed of individual, electrically isolated, small particles. In Figure 3.17a, the T-matrix simulations of a particulate shell with the same core diameter, the hybridized mode known from continuous shells, does not appear for any size of Au satellite particle up to surface coverage of 50% as experimentally realized. In contrast, the theoretical spectra for continuous shells feature a hybridized mode in the infrared region, as illustrated by the example of a 186 nm Si sphere (Figure 3.17b).

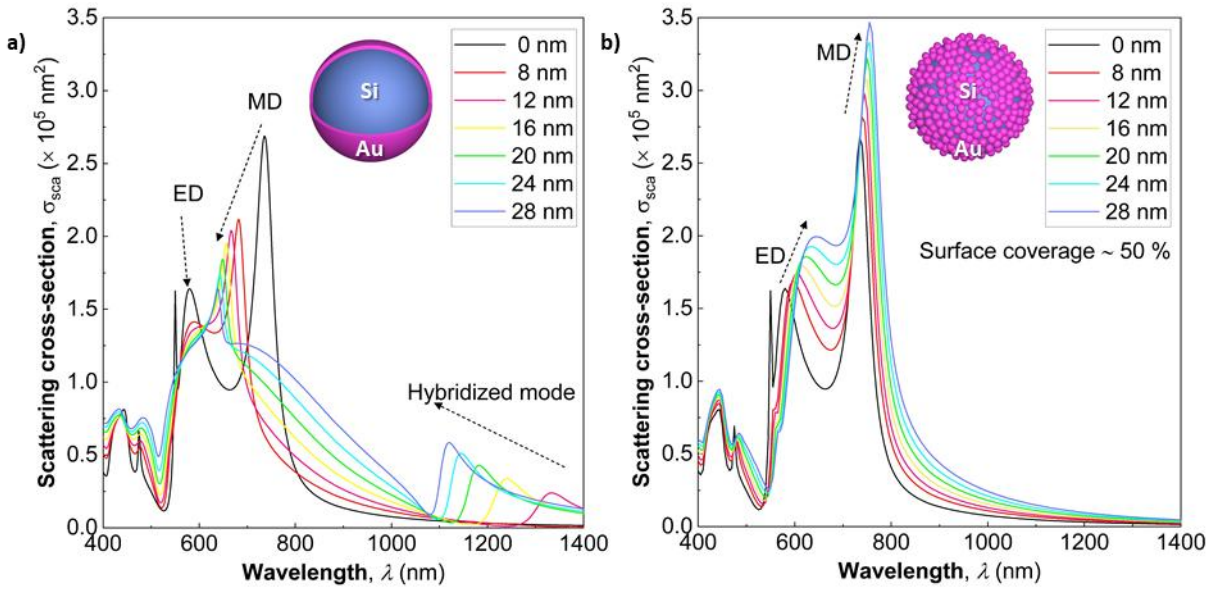



*Figure 3.17 T-matrix simulated scattering spectra for Si@Au particles with a 186 nm diameter Si core with (a) an Au particle shell composed of particles between 0 and 30 nm in diameter, $d_{Au}$, with a surface coverage of 50 % or (b) a continuous Au shell between 0 and 30 nm in thickness, $t_s$.*

In Figure 3.17a, to blueshift the hybridized mode from the near-infrared towards the visible region for Si core sizes (120 – 220 nm) and produce an exact spectral overlap of ED and MD, the shell thickness must be increased to more than 40 nm (Figure 3.18). However, such a thick shell would attenuate the MD to such an extent that the ED would dominate and the particle would not act as a forward scatterer. Experimentally, it would be difficult to observe any mode hybridization, both because of the thin nature of the shells produced and because any hybridized mode will be too far into the infrared.

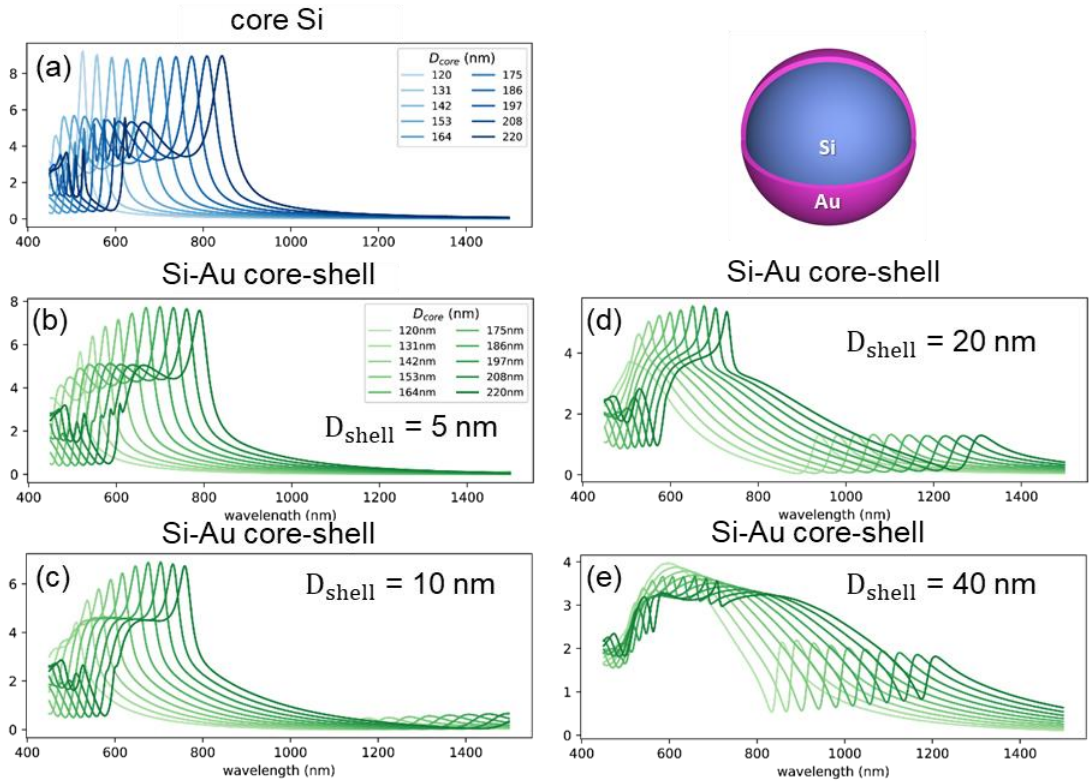



*Figure 3.18 Mie-theory calculated optical scattering spectra for different sizes of silicon cores with a continuous gold shell of varying thickness. The hybridized mode in the infrared region blueshifts towards the visible region with increasing shell thickness.*

The forward scattering behavior is improved by using a continuous gold shell. The ED intensity reduces with increasing shell thickness, with a slight redshift in peak wavelength. The MD intensity decreases by a much larger amount than the ED with the same increase in shell thickness. It also blueshifts by ~ 100 nm, which likely results from stronger mode confinement to the Si core[3]. The MD then has a smaller effective resonator size, leading to the observed blueshift. Thus, both the intensity and the spectral overlap of the ED and MD modes are more similar in the continuous shell. Even so, the increase in the F/B scattering ratio is modest in these Si@Au core-shell particles compared to Si@$SiO_2$[20], even with a high quality of both the core and shell.

Further routes towards improving the overlap of ED and MD in Si particles include working towards very thin, yet electrically connected shells, as well as the exploration of other shell materials. For example, silver (Ag) may be a promising alternative to gold (Au), as it is a better plasmonic material with less dissipation and therefore produces more intense effects for the same shell thickness. Additionally, dielectric materials such as silicon dioxide ($SiO_2$), titanium dioxide ($TiO_2$), and zirconium dioxide ($ZrO_2$) with a thick shell are a suitable choice for

enhancing the overlap of the ED and MD of core spherical silicon particles. However, a batch colloidal synthesis approach needs to be developed.

## 3.4 Conclusions and Perspective

We report the synthesis of high-index dielectric@metal Si@Au colloidal nanostructures. The cores are produced through thermal disproportionation of HSQ, a Si-rich oxide precursor. We created the shell by chemically attaching Au seeds to the Si core particles in solution. The optical spectra of individual core-shell particles were highly consistent between similarly-sized particles, because of the highly spherical shape of the Si core and the very thin, homogeneous Au coating. We produced both single and double coatings of AuNPs around Si spheres, finding a homogeneous thickness of ~4 and ~7 nm, respectively. We estimate that the surface coverage was ~ 50 %, based on comparison with simulated scattering spectra. These core-shell particles were optically characterized with dark-field optical microscopy, single particle backscattering spectroscopy, and EELS to understand the scattering behavior and the interactions between plasmonic and Mie resonances. These experimental spectra could be accurately reproduced by the T-matrix simulation due to the high quality of the experimental objects.

From simulations, we found that the forward scattering of the core-shell particles is slightly improved for all particle diameters within the range of 100 – 200 nm. We also found that the formerly reported hybridization between the ED of the Si core and decorated Au particles does not occur for shells composed of electrically isolated satellite particles[2]. Thus, to further investigate if the MD and ED overlap could be optimized, we calculated the theoretical spectra of Si cores decorated with either particulate or continuous shells. When decorated with a particulate shell (surface coverage of 50 %), both the ED and MD redshift progressively with increasing Au particle diameter. The ED broadens and redshifts at a higher rate than the MD, resulting in a marginal improvement of the dipolar spectral overlap and an increase in the directionality of optical scattering. By comparison, particles decorated with continuous Au shells show a different trend. The continuous shells move the ED and MD closer to each other more efficiently, mainly due to a strong blueshift effect on the MD, which is not observed for particulate shells. The ideal Au shell would need to be both thin ($\lesssim$ 12 nm) and continuous for optimal forward scattering. However, even in the case of a potential continuous Au shell, the gains in dipole overlap are associated with strongly decreased resonance amplitude. In addition to the efforts of fabricating electrically continuous shells, other materials such as Ag, $SiO_2$, $TiO_2$, $Si_3N_4$, and $ZrO_2$ should be explored as meta-atoms for directional light scattering.

## References


(1) Chaâbani, W.; Proust, J.; Ouellet, S.; Movsesyan, A.; Béal, J.; Bachelot, R.; Xu, T.; Baudrion, A.-L.; Adam, P.-M.; Boudreau, D.; Chehaidar, A.; Plain, J. Si@Au Core–Shell Nanostructures: Toward a New Platform for Controlling Optical Properties at the Nanoscale. *J. Phys. Chem. C* **2021**, *125* (37), 20606–20616. https://doi.org/10.1021/acs.jpcc.1c06182.

(2) Sugimoto, H.; Hinamoto, T.; Kazuoka, Y.; Assadillayev, A.; Raza, S.; Fujii, M. Mode Hybridization in Silicon Core–Gold Shell Nanosphere. *Small* **2022**, *18*, 2204890. https://doi.org/10.1002/smll.202204890.

(3) Liu, P.; Chen, H.; Wang, H.; Yan, J.; Lin, Z.; Yang, G. Fabrication of Si/Au Core/Shell Nanoplasmonic Structures with Ultrasensitive Surface-Enhanced Raman Scattering for Monolayer Molecule Detection. *J Phys Chem C* **2015**, *119*, 1234. https://doi.org/10.1021/jp5111482.

(4) Saraeva, I. N.; Luong, N. V.; Kudryashov, S. I.; Rudenko, A. A.; Khmelnitskiy, R. A.; Shakhmin, A. L.; Kharin, A. Y.; Ionin, A. A.; Zayarny, D. A.; Tung, D. H.; Duong, P. V.; Minh, P. H. Laser Synthesis of Colloidal Si@Au and Si@Ag Nanoparticles in Water via Plasma-Assisted Reduction. *J Photochem Photobiol A* **2018**, *360*, 125. https://doi.org/10.1016/j.jphotochem.2018.04.004.

(5) Gerasimova, E. N.; Uvarov, E.; Yaroshenko, V. V.; Epifanovskaya, O.; Shakirova, A.; Logunov, L. S.; Vlasova, O.; Parodi, A.; Zamyatnin, A. A.; Timin, A. S.; Makarov, S. V.; Zyuzin, M. V. Single-Step Fabrication of Resonant Silicon–Gold Hybrid Nanoparticles for Efficient Optical Heating and Nanothermometry in Cells. *ACS Appl Nano Mater* **2023**, *6*, 18848. https://doi.org/10.1021/acsanm.3c03189.

(6) Gurbatov, S. O.; Puzikov, V.; Storozhenko, D.; Modin, E.; Mitsai, E.; Cherepakhin, A.; Shevlyagin, A.; Gerasimenko, A. V.; Kulinich, S. A.; Kuchmizhak, A. A. Multigram-Scale Production of Hybrid Au-Si Nanomaterial by Laser Ablation in Liquid (LAL) for Temperature-Feedback Optical Nanosensing, Light-to-Heat Conversion, and Anticounterfeit Labeling. *ACS Appl Mater Interfaces* **2023**, *15*, 3336. https://doi.org/10.1021/acsami.2c18999.

(7) Gurbatov, S. O.; Zhizhchenko, A. Y.; Nesterov, V. Y.; Modin, E. B.; Zabotnov, S. V.; Kuchmizhak, A. A. Au–Si Nanocomposites with High near-IR Light-to-Heat Conversion Efficiency via Single-Step Reactive Laser Ablation of Porous Silicon for Theranostic Applications. *ACS Appl Nano Mater* **2024**, *7*, 10779. https://doi.org/10.1021/acsanm.4c01289.

(8) Koromyslov, S.; Ageev, E.; Ponkratova, E.; Larin, A.; Shishkin, I.; Danilov, D.; Mukhin, I.; Makarov, S.; Zuev, D. Femtosecond Laser-Assisted Formation of Hybrid Nanoparticles from Bi-Layer Gold–Silicon Films for Microscale White-Light Source. *Nanomaterials* **2022**, *12*, 1756. https://doi.org/10.3390/nano12101756.

(9) Kutrovskaya, S.; Arakelian, S.; Kucherik, A.; Osipov, A.; Evlyukhin, A.; Kavokin, A. V. The Synthesis of Hybrid Gold-Silicon Nano Particles in a Liquid. *Sci Rep* **2017**, *7*, 10284. https://doi.org/10.1038/s41598-017-09634-y.

(10) Hartlen, K. D.; Athanasopoulos, A. P. T.; Kitaev, V. Facile Preparation of Highly Monodisperse Small Silica Spheres (15 to >200 Nm) Suitable for Colloidal Templating and Formation of Ordered Arrays. *Langmuir* **2008**, *24*, 1714. https://doi.org/10.1021/la7025285.

(11) Désert, A. Colloïdes Hybrides Silice/Polystyrène de Morphologie Contrôlée. PhD Thesis, 2011. https://tel.archives-ouvertes.fr/tel-00949569.

(12) Désert, A.; Chaduc, I.; Fouilloux, S.; Taveau, J.-C.; Lambert, O.; Lansalot, M.; Bourgeat-Lami, E.; Thill, A.; Spalla, O.; Ravaine, S.; Duguet, E. High-Yield Preparation of Polystyrene/Silica Clusters of Controlled Morphology. *Polym Chem* **2012**, *3*, 1130. https://doi.org/10.1039/C2PY20058A.

(13) O'Connor, K. M.; Rubletz, A.; Ni, C.; He, Y.; Butler, C.; Veinot, J. G. C. High-Temperature Anomaly in the Synthesis of Large ($d$ > 100 Nm) Silicon Nanoparticles from Hydrogen Silsesquioxane. *Chem Mater* **2023**, *35*, 7967. https://doi.org/10.1021/acs.chemmater.3c01200.

(14) Frye, C. L.; Collins, W. T. Oligomeric Silsesquioxanes, $(HSiO_{3/2})_n$. *J Am Chem Soc* **1970**, *92*, 5586. https://doi.org/10.1021/ja00722a009.

(15) Lermusiaux, L.; Plissonneau, M.; Bertry, L.; Drisko, G. L.; Buissette, V.; Le Mercier, T.; Duguet, E.; Tréguer-Delapierre, M. Seeded Growth of Ultrathin Gold Nanoshells Using Polymer Additives and Microwave Radiation. *Sci Rep* **2021**, *11*, 17831. https://doi.org/10.1038/s41598-021-97171-0.

(16) Duff, D. G.; Baiker, A.; Edwards, P. P. A New Hydrosol of Gold Clusters. 1. Formation and Particle Size Variation. *Langmuir* **1993**, *9* (9), 2301. https://doi.org/10.1021/la00033a010.

(17) Zhang, X.; Guo, L.; Luo, J.; Zhao, X.; Wang, T.; Li, Y.; Fu, Y. Metallic Nanoshells with Sub-10 Nm Thickness and Their Performance as Surface-Enhanced Spectroscopy Substrate. *ACS Appl Mater Interfaces* **2016**, *8*, 9889. https://doi.org/10.1021/acsami.6b01658.

(18) Bohling, C.; Sigmund, W. Self-Limitation of Native Oxides Explained. *Silicon* **2016**, *8*, 339. https://doi.org/10.1007/s12633-015-9366-8.

(19) Chaâbani, W.; Proust, J.; Ouellet, S.; Movsesyan, A.; Béal, J.; Bachelot, R.; Xu, T.; Baudrion, A.-L.; Adam, P.-A.; Boudreau, D.; Chehaidar, A.; Plain, J. Si@Au Core–Shell Nanostructures: Toward a New Platform for Controlling Optical Properties at the Nanoscale. *J Phys Chem C* **2021**, *125*, 20606. https://doi.org/10.1021/acs.jpcc.1c06182.

(20) Soun, D.; Azma, A.; Roach, L.; Drisko, G. L.; Wiecha, P. R. Gradient-Based Optimization of Core-Shell Particles with Discrete Materials for Directional Scattering. *Opt. Express* **2025**, *33* (12), 25945. https://doi.org/10.1364/OE.561657.

# CHAPTER 4. Synthesis of silicon nanowires by thermal annealing of Si-rich oxide precursor containing metal nanoparticles


4.1 Introduction ..... 157
4.2 Experimental section ..... 158
4.2.1 Materials ..... 158
4.3 Synthesis of silicon nanowires ..... 158
4.4 Results ..... 159
4.4.1 Formation of the silicon nanowires ..... 159
4.4.2 Formation mechanism of the silicon nanowires ..... 164
4.4.3 In-situ study of the thermal annealing ..... 166
4.4.4 Tailoring the morphology of the silicon nanowires ..... 171
4.4.5 Generalization of nanowire growth to other catalysts ..... 178
4.5 Conclusion and Perspectives ..... 181
References ..... 183

## 4.1 Introduction

Silicon nanowires with a cylindrical cross-section morphology with a diameter ranging between 70 – 200 nm have been shown in Chapter 1 to control the direction of light scattering in visible light (400–800 nm) wavelengths. Wiecha, P. R., *et al.*[1] showed that for an infinitely long silicon nanowire with a diameter of ~100 nm, an optimum forward/backward scattering ratio is achieved for a broad spectral range of 550 – 700 nm when the incident light is TM-polarized. In terms of the directional light scattering properties, the choice of gold and silver particles could be interesting. Instead of the core-shell system discussed in Chapter 3, a design composed of a metal particle at the tip of the silicon nanowire could possibly increase the directional light scattering of the silicon nanowire. The goal is thus to synthesize both silicon nanowires and silicon-plasmonic composite nanowires for directional light scattering.

Common bottom-up synthesis routes for silicon nanowires involve the decomposition of molecular precursors in the presence of a metal catalyst to form silicon nanowires. Silicon tetrachloride, silicon tetrahydride, disilicon hexahydride, diphenylsilane, trisilane, diethylsilane, teraethylsilane, phenylsilane, and octylsilane are some of the widely explored precursors in common bottom-up strategies, such as chemical vapor deposition, molecular beam epitaxy, supercritical fluid system, and high boiling point solvents approach[2–8]. However, the limitations associated with these techniques include the need for specialty equipment because of the self-igniting precursors (silicon tetrahydride used in chemical vapor deposition), sophisticated setups and high pressure (supercritical fluid system), and toxic high boiling point organic solvents (squalene, octacosane).

More recently, trichlorosilane has been used to synthesize a silicon-rich oxide (hydrogen silsesquioxane) that was incorporated with a tin precursor and later thermally decomposed to fabricate silicon nanorods[9]. This bottom-up approach is straightforward and less dangerous in terms of the molecular precursor. Their experimental route is simple to implement and yields crystalline silicon nanowires at much lower temperatures than those usually needed when using HSQ for silicon nanoparticles (> 1000°C). This approach could be a potential alternative if it can be extended to other metal catalysts and if the nanowire length could be increased. Therefore, we explored the incorporation of size-controlled gold (Au), silver (Ag), and iron(III) oxide ($Fe_2O_3$) particles in the silicon-rich oxide, followed by attempts to fabricate silicon nanowires through this thermal annealing method. We additionally aim to understand the growth mechanism of the silicon nanowires within the context of the known growth mechanisms (VLS, SLS, and VSS) that have been discussed in Chapter 1.

## 4.2 Experimental section

### 4.2.1 Materials

Trichlorosilane (99 %), methanol (HPLC grade), and Au (III) chloride trihydrate (520918, 99.9 %) were purchased from Sigma Aldrich. Aqueous solutions were prepared using deionized water, prepared using a Type 1 Milli-Q water purification system (18.2 MΩ cm). All chemicals were used without further purification.

## 4.3 Synthesis of silicon nanowires

The synthesis of silicon nanowires was carried out in a two-step approach. A colloidal synthesis approach was first established for the synthesis of the silicon-rich oxide precursor, incorporated with different metal particles (Au, Ag, $Fe_2O_3$) with a size range of 30 – 100 nm. The synthesized precursor was then thermally annealed under optimized reaction parameters of temperature, choice of metal catalysts, and size, annealing time, precursor surface area, and gas flow rates.

**Protocol 4.1 Synthesis of the silicon-rich precursor**

To a 250 mL round-bottom flask immersed in a water/ice bath and equipped with a magnetic stirrer, 80 mL of methanol ($CH_3OH$) was added and left under continuous argon gas flow for 30 min. Thereafter, trichlorosilane ($HSiCl_3$, 4.5 mL) was slowly added and allowed to stir for 15 min. As a next step, the metal nanoparticle dispersion (18 mL) was rapidly added to the well-stirred $HSiCl_3$/methanol mixture. It was stirred for 2 h to complete the hydrolysis-condensation reaction to synthesize the silicon-rich oxide. After the dehydration-condensation reaction, a precipitate of the metal-incorporated silicon-rich oxide was collected by vacuum filtration. The obtained silicon-rich oxide was rinsed several times with methanol and dried at 70 °C for 24h in an oven.

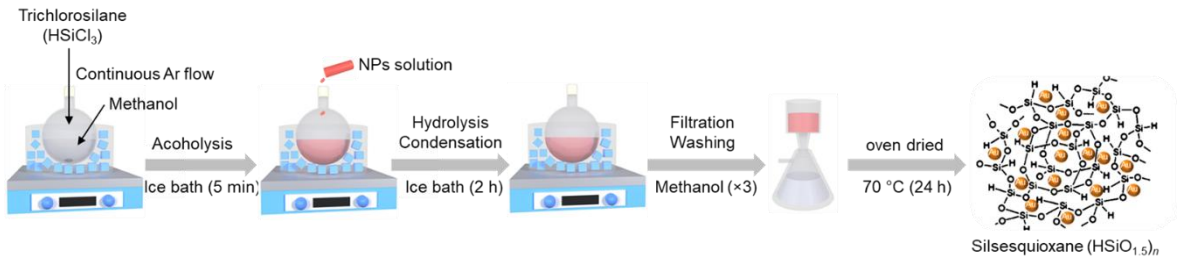



*Figure 4.1 Schematic diagram of the synthesis of silicon nanowires using silicon-rich oxide in the presence of different metal particles.*

**Protocol 4.2 Thermal annealing of the silicon-rich precursor**

For the thermal annealing of the Au nanoparticles incorporated into the silicon-rich oxide, 0.2g of the oven-dried and ground powder was placed in an alumina boat and put into an alumina tube furnace. The furnace was purged under a gas flow (5%$H_2$–95%Ar) with a flux rate of 200 mL/min for 30 min. Thereafter, the temperature was increased to a set value (700 - 1200 °C) at a ramp rate of 7 °C/min, and held at this temperature for 2 h at ambient pressure. After the annealing, the furnace was cooled by 2 °C/min.

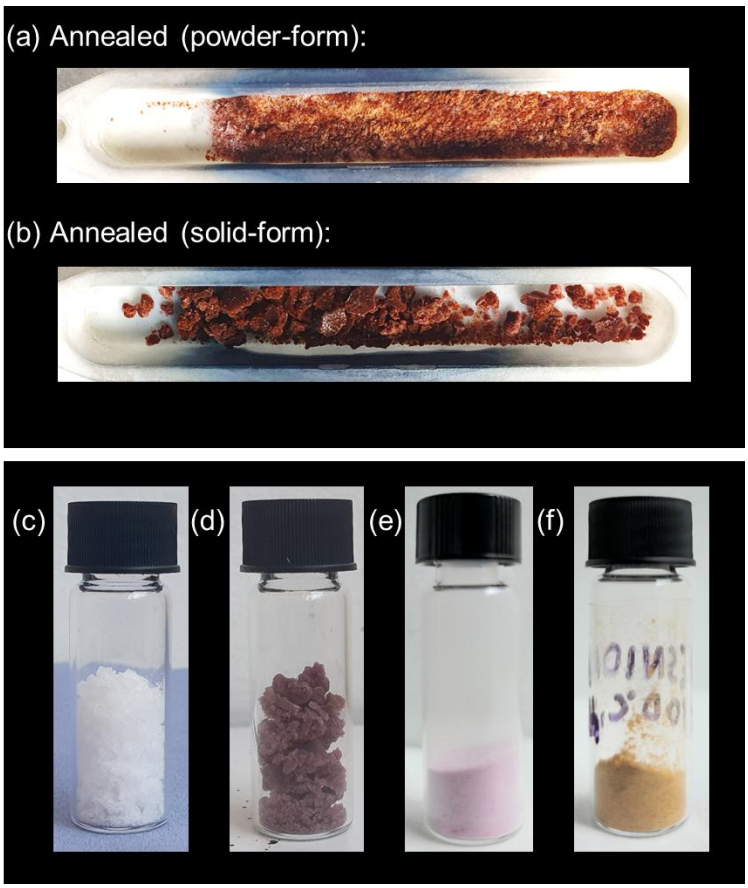



*Figure 4.2 Thermal annealing of the Au nanoparticles incorporated into the silicon-rich oxide in (a) powder form, and (b) solid form in an alumina boat at 800 °C for 2 h. Images of the silicon-rich oxide (c) without Au nanoparticles, (d) with Au nanoparticles, (e) with Au nanoparticles after grinding, and (f) after grinding and thermal annealing.*

## 4.4 Results

### 4.4.1 Formation of the silicon nanowires

To make silicon nanowires, we added pre-formed nanoparticles to the sol-gel synthesis of a silicon-rich oxide. We studied three nanoparticles: gold (Au), silver (Ag), and iron oxide ($Fe_2O_3$). The silicon-rich oxide containing the nanoparticles was synthesized in one-pot via

multiple steps (Figure 4.1). First, an alcoholysis reaction of trichlorosilane, $HSiCl_3$ (4.5 ml) occurred by dropwise addition of this precursor into methanol, $CH_3OH$ (80 ml) in an ice-water bath and under the flow of argon. Then, the metallic nanoparticles suspended in water (18 ml), were rapidly added to the reaction flask, initiating the hydrolysis and condensation of the silicon-rich oxide around the nanoparticles. The reaction mixture was allowed to stir for 2 h for the complete condensation of the mixture. The obtained product was collected by vacuum filtration.

Figure 4.3a shows the Fourier transform infrared spectroscopy (FTIR) absorption spectra of the silicon-rich oxide with and without the Au nanoparticle dispersion. The spectra without Au nanoparticles is composed of two major bands, namely the band for the Si–O–Si stretching mode at approximately 1060 $cm^{-1}$ and the band for the Si–H stretching mode at 2250 $cm^{-1}$. This is in good agreement with the previously reported FTIR spectra of $(HSiO_{1.5})_n$ polymers[10,11]. The broad band at 3500–3700 $cm^{-1}$ in the spectra with Au nanoparticles is related to the C–OH stretching vibration. The peaks around 1524 and 1695 $cm^{-1}$ are for the symmetric and asymmetric C–O–O stretching bands in citrate–Au nanoparticles. This established the successful incorporation of the Au particles into the silicon rich oxide. We then studied where the nanoparticles were found with respect to the silicon-rich oxide matrix. From the TEM image (Figure 4.3b), Au nanoparticles with sizes between 55 – 70 nm can be seen in the center of the matrix. However, as this is a 2D image, it is not clear how the nanoparticles are positioned relative to the matrix in the z-axis. We next acquired SEM images at 20 kV with a secondary electron detector (Figure 4.3c), which allows for a deep penetration depth. We observe the presence of Au nanoparticles with a low intensity, that appear partially or fully embedded in the matrix. Using the back-scattering detector (Figure 4.3d), it is clear that these embedded nano-objects are of higher atomic number due to their brighter signal, and thus must be Au nanoparticles.

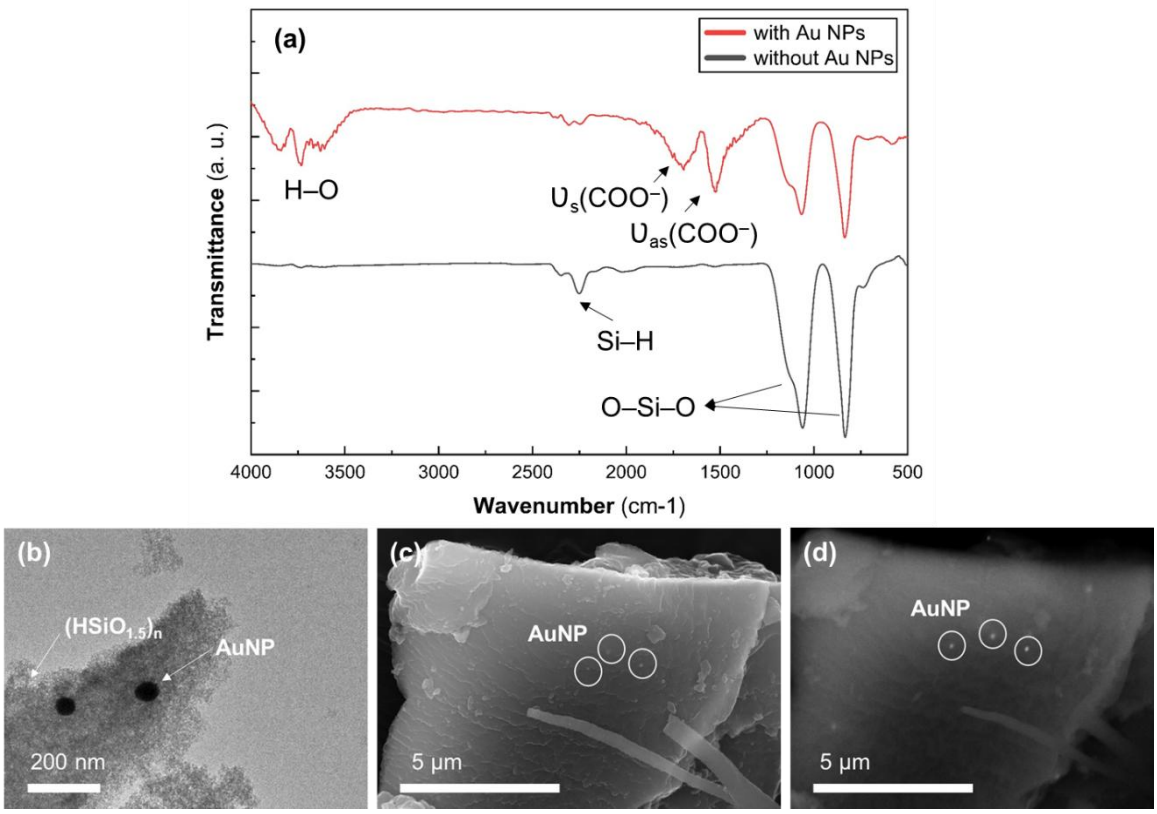



*Figure 4.3 (a) FTIR absorption spectra of the synthesized silicon-rich oxide with and without the incorporation of Au nanoparticle solution. (b) TEM image, (c) SEM image in secondary electron mode, (d) SEM image in back-scattering mode of the silicon-rich oxide with Au nanoparticles.*

It was found that the processing steps prior to thermal annealing were critical to forming silicon nanowires. Two processes were performed: gentle heating at 70 °C for 24 h, and grinding in a mortar and pestle. Before grinding, the silicon-rich oxides have a bulky texture. The thermal annealing of the unground precursor (incorporated with ~30 nm diameter Au nanoparticles) in this state at 800 °C for 2 h does not produce any nanowires, as shown in Figure 4.4a. However, grinding the silicon-rich oxide with a mortar and pestle before thermal annealing led to the formation of nanowires (Figure 4.4b). The corresponding SEM image of the product is shown in Figure 4.4c. From the SEM image, it seems the nanowires extend from the surface of the oxide matrix. Therefore, the grinding step appears to be important for the formation of the nanowires, but it is not immediately evident why this should be the case.

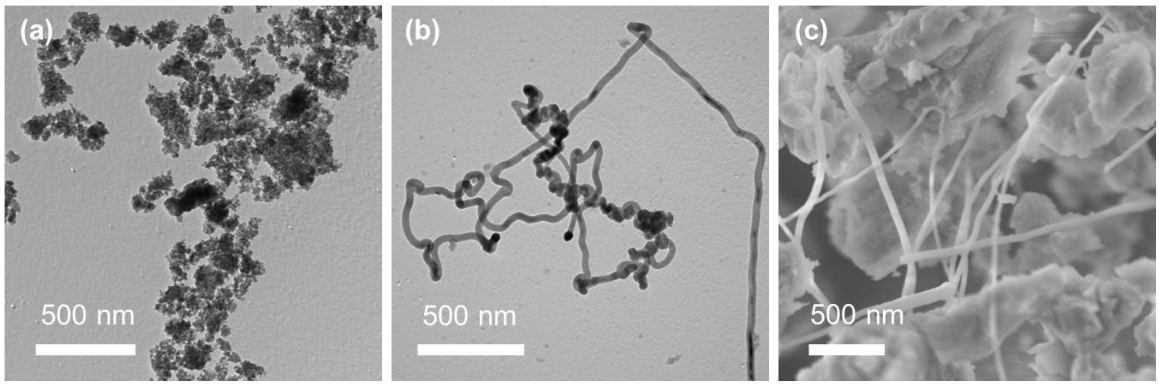



*Figure 4.4 TEM image of the thermally annealed product from (a) not ground precursor, and (b) ground precursor. (c) SEM image of the product from the ground precursor.*

The effects of the drying and grinding steps on the chemical composition of the precursor were investigated through nuclear magnetic resonance (NMR) spectroscopy using the direct polarization (DP) magic angle spinning (MAS) – quantitative analysis of the air-dried (25 °C) and oven-dried (70 °C) silicon-rich oxide incorporated with Au nanoparticles. Therefore, we want to investigate the structures and substituent groups of the silicon-rich oxide as a function of the grinding (Figure 4.5b and 4.5c) and drying (Figure 4.5c and 4.5d) steps. The chemical shift signal observed at -86 ppm was assigned to the $T_{10}^{H}$ which has a cage-like structure of silsesquioxane[12]. The other chemical shift signals at -76, -101, and -111 ppm were assigned to the $Q^0$ $(OCl_3)Si(OH)$, $Q^3$ $(SiO)_3Si(OH)$, and $Q^4$ $(SiO)_4Si$ substituent groups, respectively[12,13]. For the air-dried plus unground sample, the quantitative yield for the $T_{10}^{H}$, $Q^4$, $Q^3$, and $Q^0$ corresponds to 76, 10, 7, and 7%, respectively (Figure 4.5a). For the air-dried plus ground sample, the $T_{10}^{H}$, $Q^4$, $Q^3$, and $Q^0$ correspond to 84, 6, 6, and 3%, respectively. From these results, the slight difference is the increase in the cage-like component ($T_{10}^{H}$) by ~6% upon gentle thermal treatment. Compared to the oven-dried plus ground sample (Figure 4.5d), the $T_{10}^{H}$, $Q^4$, $Q^3$, and $Q^0$ correspond to 80, 7, 8, 5%, respectively. From these results, there is no significant chemical difference between the ground and unground samples. Generally, the cage-like structure ($T_{10}^{H}$) constitutes 80 – 84% of the product yield, while the other < 20% could be attributed to the residual groups ($Q^4$, $Q^3$, and $Q^0$). Therefore, the change in mass could be attributed to the volatile fraction of the precursor, as well as to water and methanol still present in the samples. The chemical composition of the silicon-rich oxide containing the Au nanoparticles is unchanged by the drying and grinding pre-treatments.

(a)

| samples | $Q^0$ (%) | $T^H_{10}$ (%) | $Q^3$ (%) | $Q^4$ (%) |
|---|---|---|---|---|
| Air-dried (25 °C) | 7 | 76 | 7 | 10 |
| Air-dried + Ground | 3 | 84 | 6 | 6 |
| Oven-dried (70 °C) + Ground | 5 | 80 | 8 | 7 |

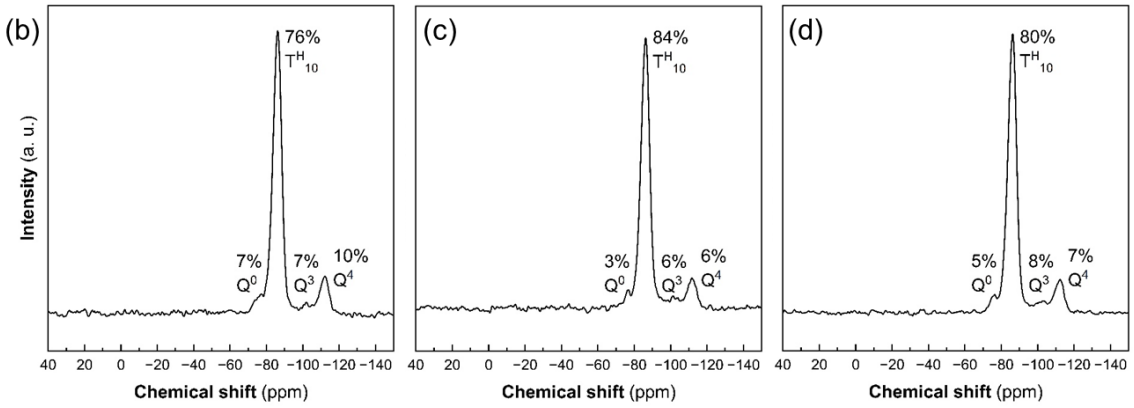



*Figure 4.5 The $^{29}Si$ solid state nuclear magnetic resonance (NMR) spectra of the silicon-rich oxide incorporated with Au nanoparticles (a) air-dried (25 °C), (b) air-dried and ground (c) oven-dried (70 °C) and ground.*

We thus studied the materials during *in situ* thermal treatment using thermal gravimetric analysis mass spectroscopy (TGA/DTA–MS). Others have previously discussed the generation of silane gas ($SiH_4$) through the decomposition of the silicon-rich oxide in the presence of hydrogen ($H_2$), which then is reduced to silicon on the gold surface[14]. The analysis we performed here was carried out under similar conditions to those used for the nanowire formation in the furnace. Thermogravimetric analyses of the bulk and ground samples of the oven-dried precursor exhibit identical profiles from temperature > 200 °C. Figure 4.6a shows a weight loss of 1.67% at temperatures between 200 – 800 °C for the ground sample, while Figure 4.6b shows a weight loss of 1.94% for the unground sample at the same temperatures. This gives rise to a well-defined peak in the DTA data at around 498 – 510 °C. In both samples, the mass-to-charge ratio (m/z) of the released gas in this temperature range is 30–31, predominantly corresponding to $SiH_4$ degradation products $^{28}SiH_2^{+2\alpha}$ and $^{28}SiH_3^{+\alpha}$.[15] Hence, the thermal degradation at 200 – 800 °C could be attributed to the thermal dissociation of the Si–H bond, accompanied by the release of $SiH_4$ and other by-product gases as previously reported[10]. In the ground sample, a second weight loss of 1.26% was observed at temperatures between 24 – 108 °C, with a mass-to-charge ratio (m/z) of 15–16. We associated this with a methyl group that could be from the volatile organic compound from the citrate of the Au nanoparticles. Thus,

there are only marginal differences in the quantity and the temperature of formation of the silane released by the ground and unground samples.

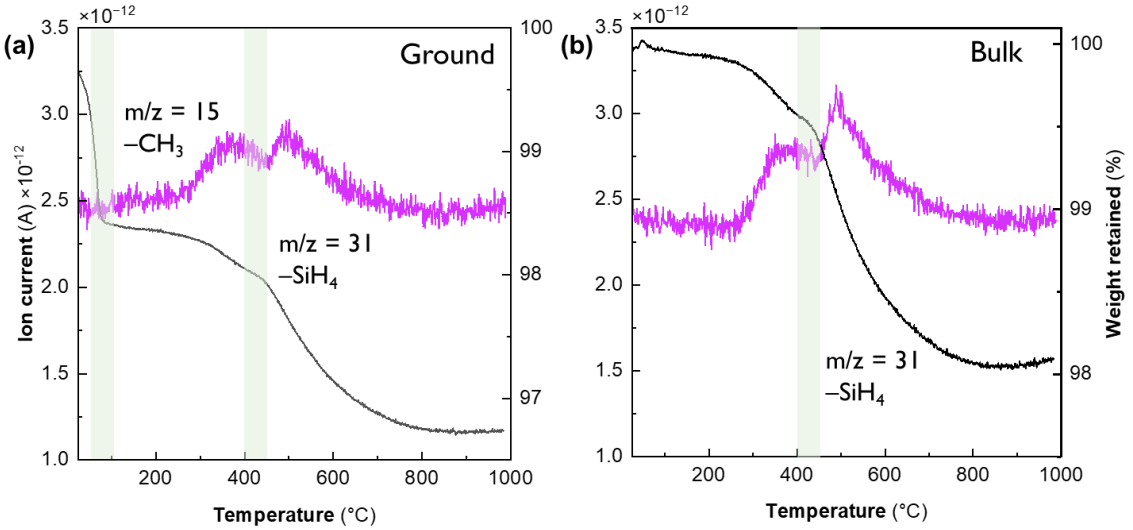



*Figure 4.6 The thermogravimetric analysis (TGA) of the oven-dried precursor (a) ground (b) not ground into powder. Thermal annealing at 1000 °C for 2h under flow of 5%$H_2$–95%Ar.*

We thus hypothesize that the difference in the ability to form wires must result from a surface area effect. Using nitrogen adsorption-desorption analysis, the surface areas of the two materials were measured to be 163 $m^2/g$ for the unground and 250 $m^2/g$ for the ground. It seems that prior to thermal treatment, the samples are chemically identical, but because of surface area differences, silane gas is more apt to encounter the Au nanoparticles during thermal annealing.

### 4.4.2 Formation mechanism of the silicon nanowires

After exploring the importance of grinding for the formation of nanowires, it is necessary to analyze the annealed product further to characterize the obtained nanowires. The chemical composition of the ground silicon-rich oxide before and after annealing was explored using FTIR. From the FTIR spectra in Figure 4.7, multiple peaks are observable. The peaks at ~832 and 1060 $cm^{-1}$ are attributed to the Si–O–Si stretching mode of the cage and network silsesquioxane. The two peaks at ~1524 and 1695 $cm^{-1}$ are attributed to the symmetric and asymmetric stretching mode of $COO^-$ in trisodium citrate on the surface of the gold nanoparticles. The peak at ~2250 $cm^{-1}$ is assigned to the Si–H stretching mode, while the broad peak at ~ 3500 – 3700 $cm^{-1}$ is attributed to the O–H stretching mode from water, silanol species, and C–OH group on gold nanoparticles. The main difference in the spectra of the precursor and that of the annealed product is the disappearance of the vibrational band at ~832 $cm^{-1}$ and the reduction in the transmittance intensity of the band at ~1060 $cm^{-1}$, both peaks related to the

cage structure. It should be noted that Si–Si bonds are not IR active; thus, these peaks are not expected.

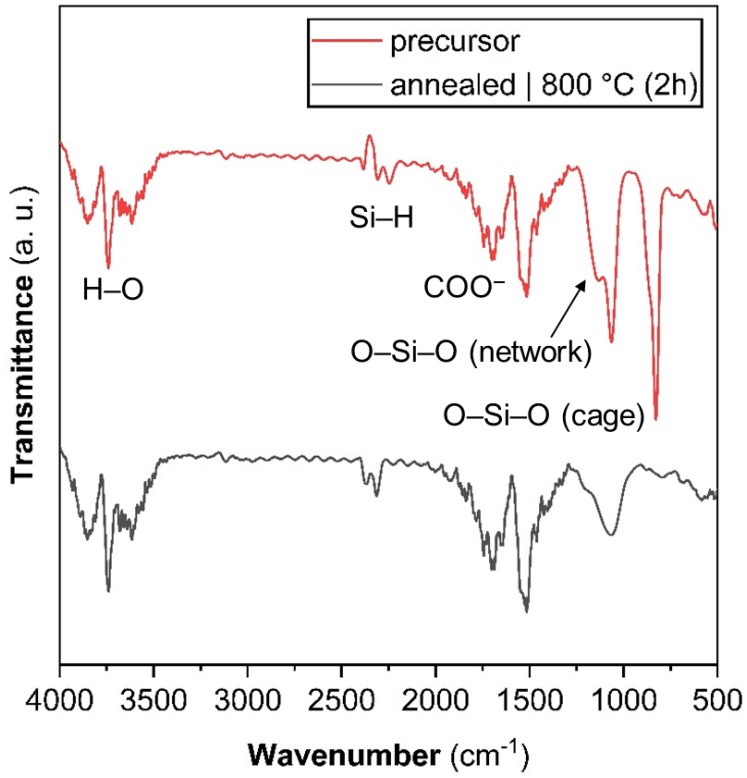



*Figure 4.7 FTIR spectra of the precursor and the thermally annealed ground precursor at 800 °C for 2h.*

STEM-EDS was used to study the elemental composition of the wires (Figure 4.8a and 4.8b). Surprisingly, the wires were composed of a silicon core and an oxide shell. The core diameter varied from wire to wire, but the oxide layer was consistently 9 nm for the nanowires treated at 800 °C. In Figure 4.8c, electron diffraction was used to obtain the d-spacing of the silicon core. Typically, the d-spacing for cubic Si (111) is 0.3135 nm, whereas we observed a d-spacing of 0.3203 nm. The possible reasons for this expanded lattice will be discussed later. There is no detectable amount of gold in the nanowire.

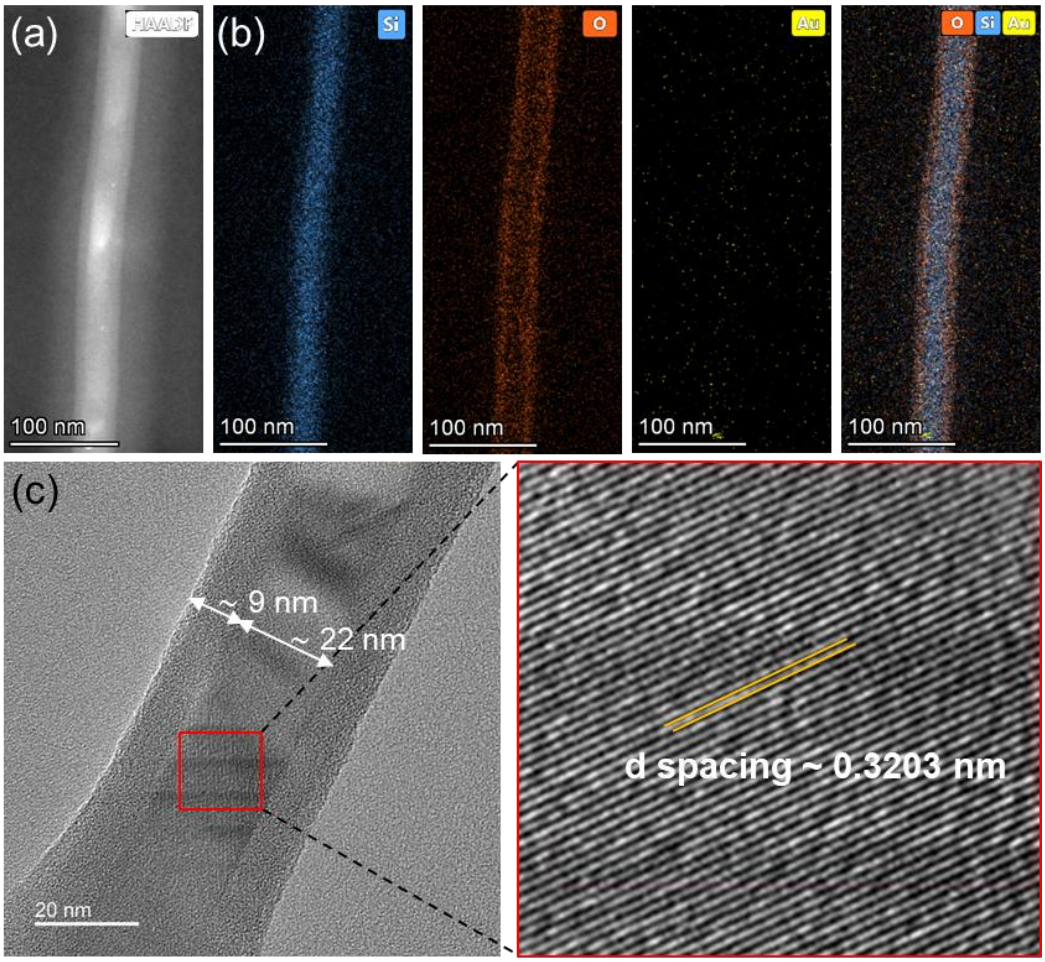



*Figure 4.8 (a) STEM/HAADF image of Si nanowires synthesized by thermal annealing of silicon-rich oxide embedded with gold particles at 800 °C for 2 h under the flow of 5% $H_2$–Ar at ambient pressure (b) STEM-EDS analysis of the fabricated Si nanowires (c) HRTEM image and calculated d-spacing of the Si core.*

### 4.4.3 In-situ study of the thermal annealing

*In-situ* TEM studies are pivotal to understanding the evolution of materials at the nanoscale under reactive conditions, providing information about the process that cannot be obtained with traditional *ex-situ* characterization. They can help identify intermediate species in material synthesis and degradation that could not be identified post-reaction. Additionally, they may provide new insights into predicting the performance of similar systems. We established the *in-situ* release of $SiH_4$ gas through the reduction of the silicon-rich oxide in a reducing gas atmosphere by TGA-MS (Figure 4.6). Also, we observed that the Au particle is at the tips of most of the nanowires. This is common in metal-catalyzed vapor-liquid-solid (VLS) growth mechanism[14]. The hypothesized role of the metal catalyst is to form a liquid solution for a vapor-phase absorption of the Si atoms. This becomes supersaturated under the constant supply

of the Si vapor atoms and nucleates the growth of the Si nanowire[14]. Therefore, it might be interesting to study the thermal annealing of the silicon-rich oxide under *in-situ* transmission electron microscopy.

From the real-time observations of the thermal annealing of the silicon-rich oxide between room temperature (RT) and 1000 °C under the reducing conditions, the main phenomena observed are: growth of an amorphous shell around the Au particles, formation of filaments, degradation of the silicon oxide matrix, sintering of the Au particles, and loss of facetting of the Au particle shape. Figure 4.9 illustrates several of these phenomena, presenting a representative sequence of TEM images taken at various temperatures, ranging from RT to 1000 °C and then during cooling. The large gold particle is not in contact with the silicon-rich oxide. The bulk of the matrix is displayed in the bottom right corner. The matrix continuously loses shape, appearing smoother and decreasing in volume as it undergoes heating and cooling. We attribute this to the degradation of the matrix, as observed in the TGA-MS data (Figure 4.6). The ~145 nm Au particle is facetted before heating. This faceting progressively disappears through heating to and holding at 1000 °C. Bulk gold has a melting point of 1064 °C, and the silicon-gold eutectic point is at 363 °C. There is evidently not enough silicon to completely alloy and thus melt the gold particle. However, it is possible that the softening of the faceting, which starts at 800 °C, is due to alloying at the surface. Most interestingly is the formation of a shell around the Au particle. As the temperature increases under a reducing atmosphere ($H_2$), the growth of a shell was observed. However, shell growth is most substantial when cooling under $H_2$ to RT, with a final shell thickness of 13 nm. It is possible that as the temperature decreases and the silicon becomes less miscible with the gold, it is ejected from the particle, forming an amorphous shell.

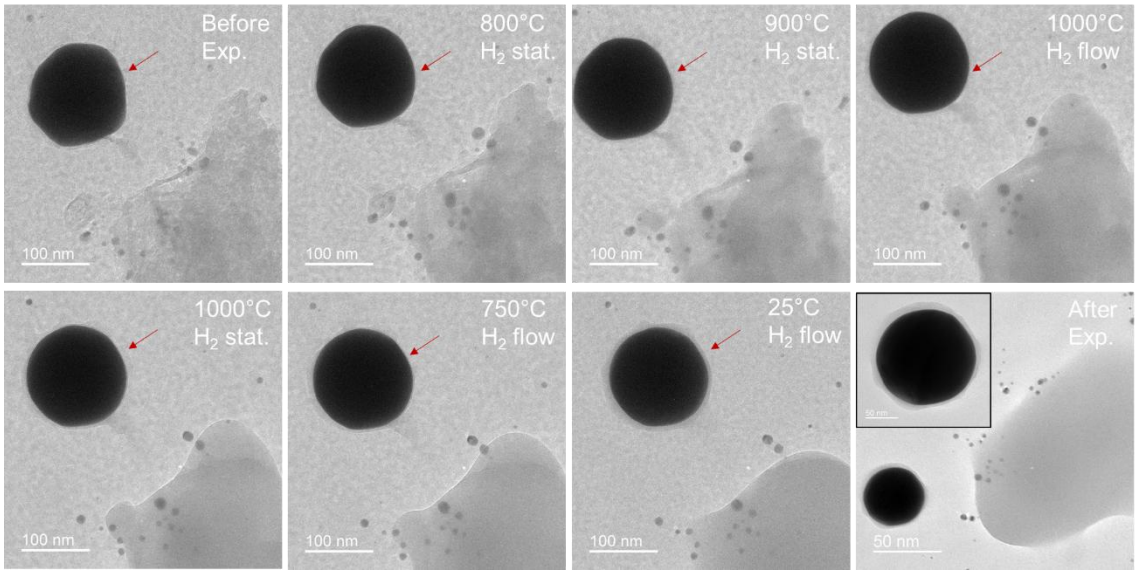



*Figure 4.9. A sequence of in situ TEM images of the thermal annealed silicon-rich oxide showing the growth of a shell around an Au particle and silicon-rich oxide degradation.*

The gold particle from Figure 4.9 was analyzed for its elemental composition post-cooling. Figure 4.10b-e shows the STEM/EDS images of the single particle to obtain detailed information about its composition. The elemental mapping clearly showed a core-shell structure, in which the Au sphere is fully covered on its surface by Si and O atoms. In fact, the O atoms are dispersed in a semi-spherical region of the Au sphere due to a shadow effect (the detector is oriented towards the bottom of the image). Surprisingly, it is also revealed that Si atoms are homogeneously dispersed throughout the volume of the Au sphere after heating. This supports the hypothesis that there is contamination of the Au particle with Si atoms, though the concentration of Si is too low to significantly decrease the melting point of gold. A similar result was observed in Figure 4.10g-j, which shows elongated, node-like amorphous SiOx, indicating the presence of Si and O atoms. This confirmed the growth of an amorphous $SiO_x$ from the surface of the Au particle. The short nature of the observed $SiO_x$ could be attributed to the insufficient quantity of silicon-rich oxide precursor in the system to supply enough Si atoms for the growth of the nanowire. Additionally, the amorphous nature of the observed growth aligns with the *ex-situ* results at this temperature.

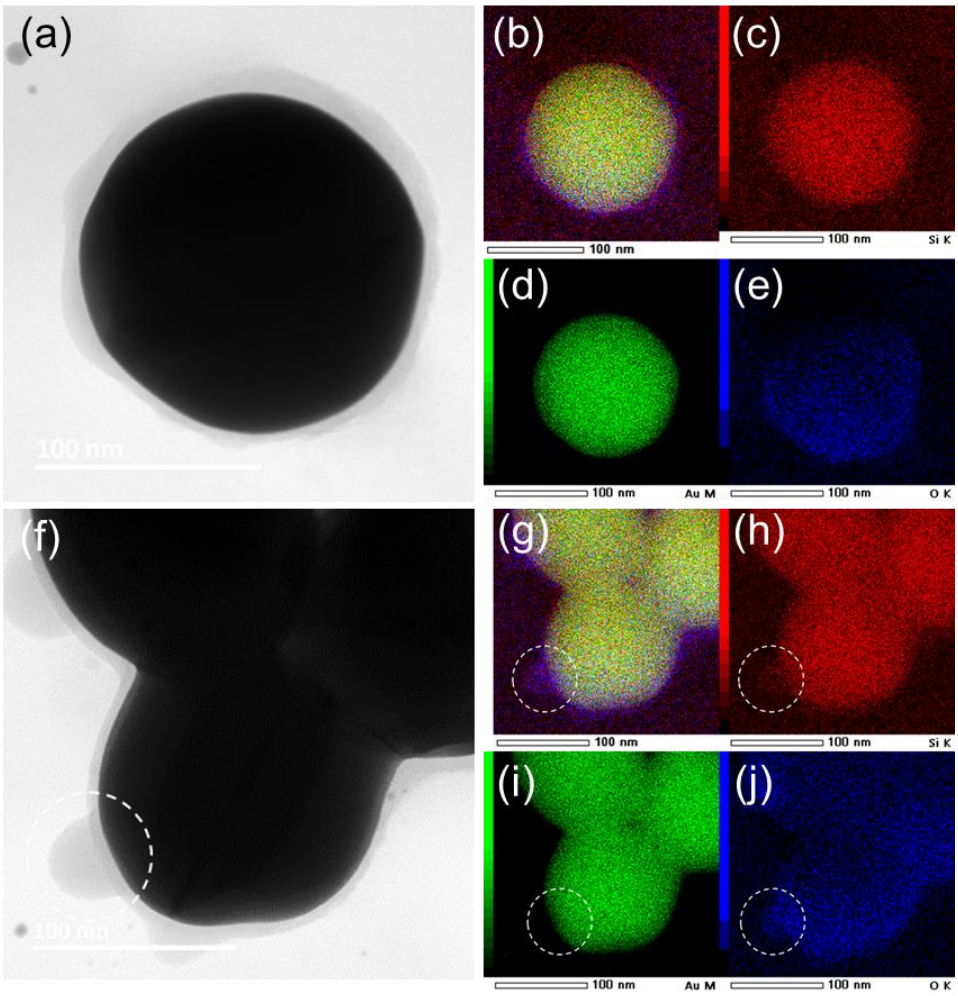



*Figure 4.10 (a, f) The (S)TEM images and EDS elemental mapping images of the (b-e) Au/$SiO_2$ particle, (g-j) sintered Au particles with the growth of amorphous SiOx shell/nodes.*

The partial melting of Au particles can be seen when a cluster of particles is observed together, as they partially fuse during heating. Five gold particles with a mean diameter of 130 nm were found, arranged in the form of an airplane (Figure 4.11a). Figure 4.11b shows TEM images taken at 1000 °C, which show that although faceting is not completely lost, the Au particles have partially sintered. The silicon-rich oxide matrix present before heating has nearly completely disappeared by 1000 °C. As before, upon cooling, a shell of amorphous $SiO_x$ grows around the Au particles. The sintering of the Au particles, while the original facet structure remains visible, indicates that melting is confined to the surface of the Au particles.

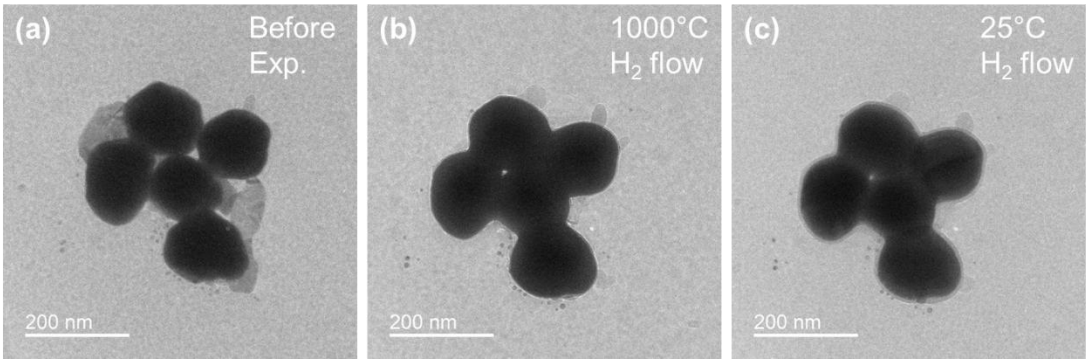



*Figure 4.11. A sequence of in situ TEM images showing sintering of multiple Au particles at 1000 °C and growth of $SiO_x$ shell/nodes. The arrow and circle in the first frame indicate the silicon-rich oxide near to the Au particles.*

We investigated the effect of the proximity of the Au nanoparticles to the silicon-rich oxide matrix. A zone was identified with a large piece of silicon-rich oxide attached to an aggregate of gold nanoparticles with a median diameter of 30 – 150 nm (Figure 4.12). The sample is heated to 1000 °C for over 180 min. After 90 min at 1000 °C, the gold nanoparticles had undergone significant fusing (d ≈ 191 – 354 nm) and loss of faceting, indicating melting. Moreover, after 90 min at 1000 °C, filaments of amorphous $SiO_x$ appear around the sintered Au particles (Frame 6). This was not present at the initial stage of the experiment (Frame 1). Therefore, the proximity of the Au particles to the silicon-rich oxide might not necessarily be important for the growth of the nanowire. This might further complement the TGA-MS experiment, where we observed the release of $SiH_4$ gas from the precursor, which could then be reduced to Si atoms far from the matrix for the growth of the nanowire.

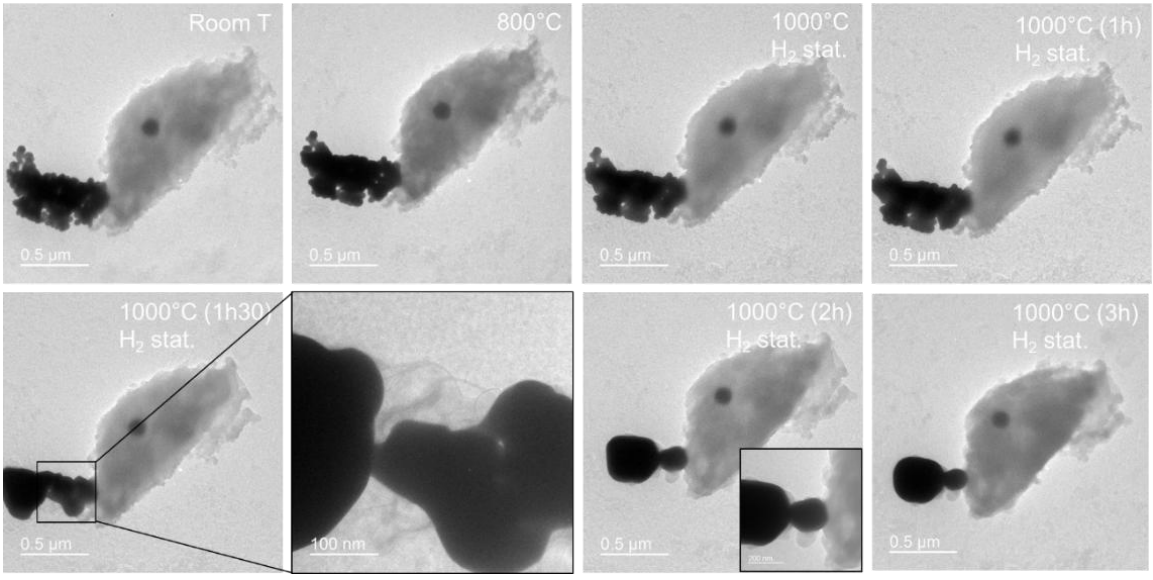


*Figure 4.12. A sequence of in situ TEM images of the thermally annealed silicon-rich oxide showing the growth of a shell around an Au particle and elongated $SiO_x$ material.*

The growth of filaments has also been observed during cooling. A well-facetted Au particle of 130 nm in diameter was found with two filaments extending out like arms (Figure 4.13). As this particle cooled, its form changed, becoming smaller on the side where the filaments extended. Figure 4.13a-c shows that the observed filament becomes thicker during the cooling, which could be due to oxidation. Figure 4.13d shows the SAED pattern spots indexed to a value of 0.324 nm, which is close to the d-spacing of 0.3203 nm defined from the *ex-situ* Si nanowire for Si (111) (Figure 4.8). Also, spots indexed to a value of ~ 0.244 are slightly larger than the d-spacing of ~ 0.233 defined for Au (111) from the *ex-situ* experiment.

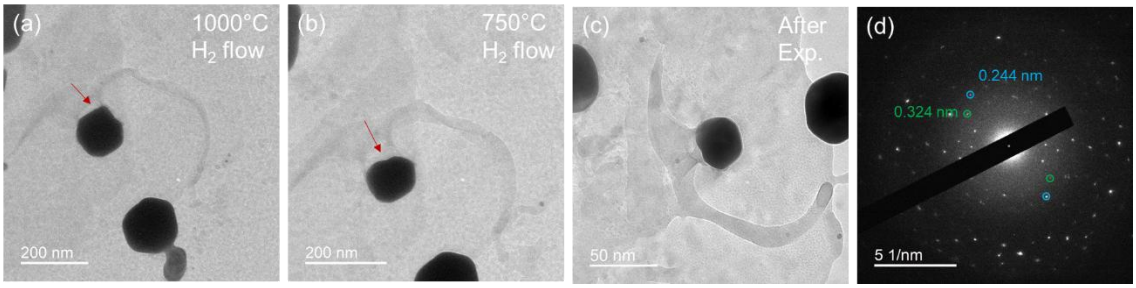



*Figure 4.13. (a-c) A sequence of in situ TEM images of the thermal annealed silicon-rich oxide showing the growth of a filament from the surface of an Au particle. (d) Selected area of electron diffraction (SAED) pattern of the Au particle.*

### 4.4.4 Tailoring the morphology of the silicon nanowires

We examined the impact of multiple synthetic parameters on nanowire formation, including thermal annealing temperature, annealing time, and gold nanoparticle diameter. The effect of the temperature on the thermal annealing of the silicon-rich oxide was studied between 700 – 1100 °C. No nanowires were observed at temperatures lower than 800 °C (Figure 4.14). The diameters of the nanowires become smaller with increased temperature.

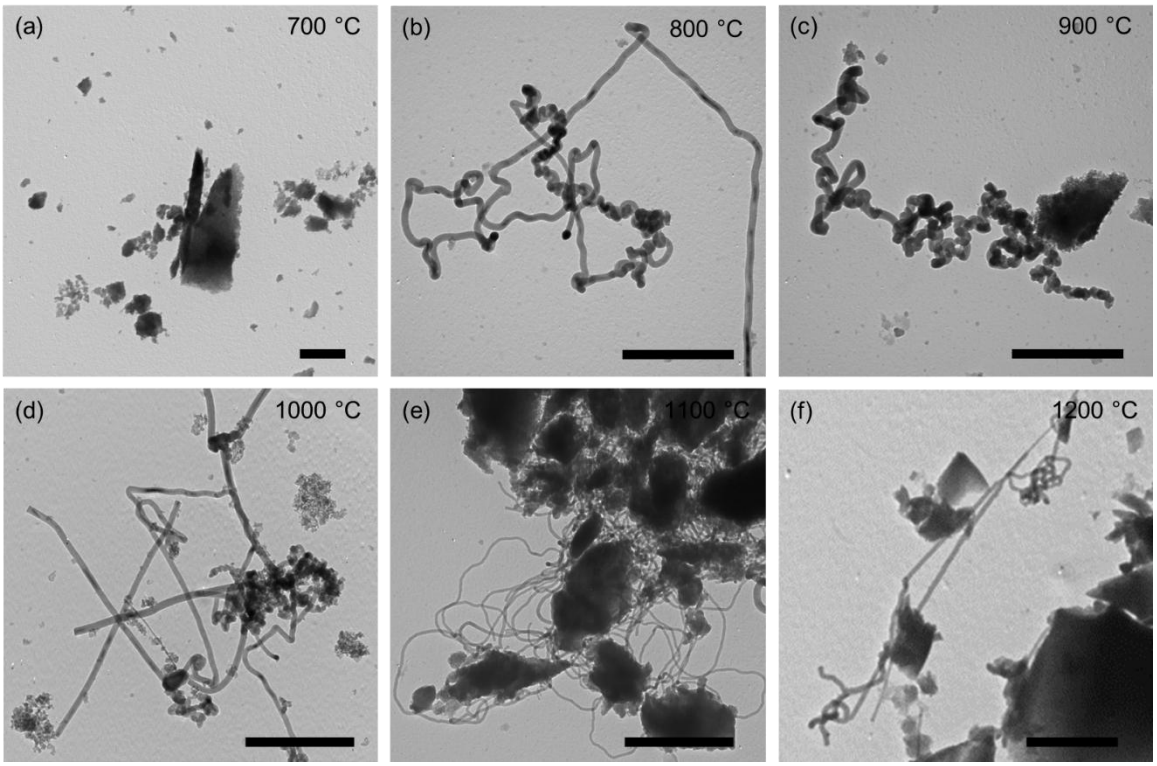
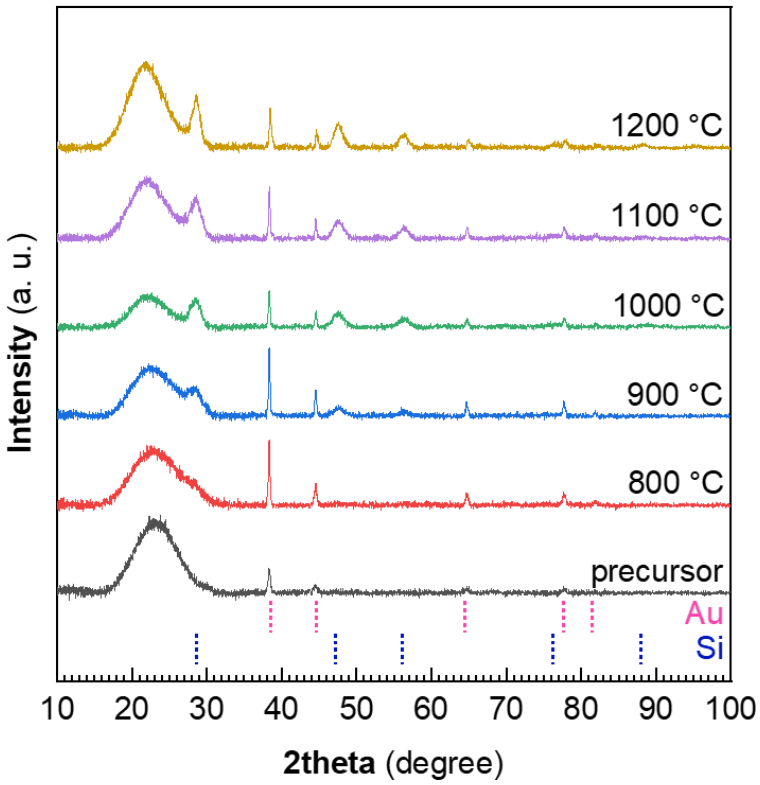



*Figure 4.14 TEM images of the Si nanowires obtained at different annealed temperatures of 700 – 1200 °C for 2h. The scale bar in all the images represents 500 nm.*

Figure 4.15 shows the XRD patterns of the nanowires grown at different temperatures. At 700 °C, no crystalline Si peaks were observed due to no formation of Si nanowires. At 800 °C, the lack of Si peaks could be attributed to the poor yield of Si nanowires and the dominant nature of the Au diffraction peaks. However, the Si peaks are apparent in the XRD patterns of the nanowires produced at the other temperatures (800 – 1200 °C). A semi-quantitative phase analysis (see experimental section for details) of the products within the temperature range of 800, 900, 1100, and 1200 °C gives an increasing Si composition of 4.3, 5.0, 7.5, and 7.8%, respectively. The amorphous silica composition decreases from 51.5 to 39.5 % for temperatures ranging from 800 to 900 °C.




| Pattern | Compound Name | Formula | System | 800 °C | 900 °C | 1100 °C | 1200 °C |
|---|---|---|---|---|---|---|---|
| PDF 27-1402 | Silicon, syn | Si | Cubic | 4.3% | 5.0% | 7.5% | 7.8% |
| PDF 04-0784 | Gold, syn | Au | Cubic | 44.2% | 55.5% | 44.1% | 28.8% |
| PDF 29-0085 | Silicon oxide | $SiO_2$ | Amorphous | 51.5% | 39.5% | 48.5% | 63.4% |

*Figure 4.15 XRD patterns obtained from the Si nanowires at different temperatures. The diffraction peaks index to diamond cubic Si. The indexes in blue correspond to diamond Si peaks while those in pink are for cubic Au. The pattern in black at 1100* °C is for pure silicon-rich oxide without Au particles. *The table shows the semi-quantitative analysis of the product yield at different annealing temperature.*

After studying the materials with XRD, we studied them by electron diffraction. The HRTEM of the product thermally annealed at 1100 °C showed no Si crystalline domains (Figure 4.16a). The FFT analysis of the product showed crystalline planes around the Au particle (Figure 4.16b and 4.16c), which has a d-spacing value of ~ 0.233 nm, corresponding to Au (111) with a d-spacing of 0.236 nm. The FFT analysis of the nanowire showed no crystalline diffraction spots, which confirms the amorphous nature of the nanowire. However, by XRD, the product showed Si crystalline domains for materials prepared at 1100 – 1200 °C. Therefore, the crystalline Si peaks from the XRD could be attributed to quasi-spherical Si nanoparticle byproducts[16]. This result makes it difficult to quantify the yield of the silicon nanowires.

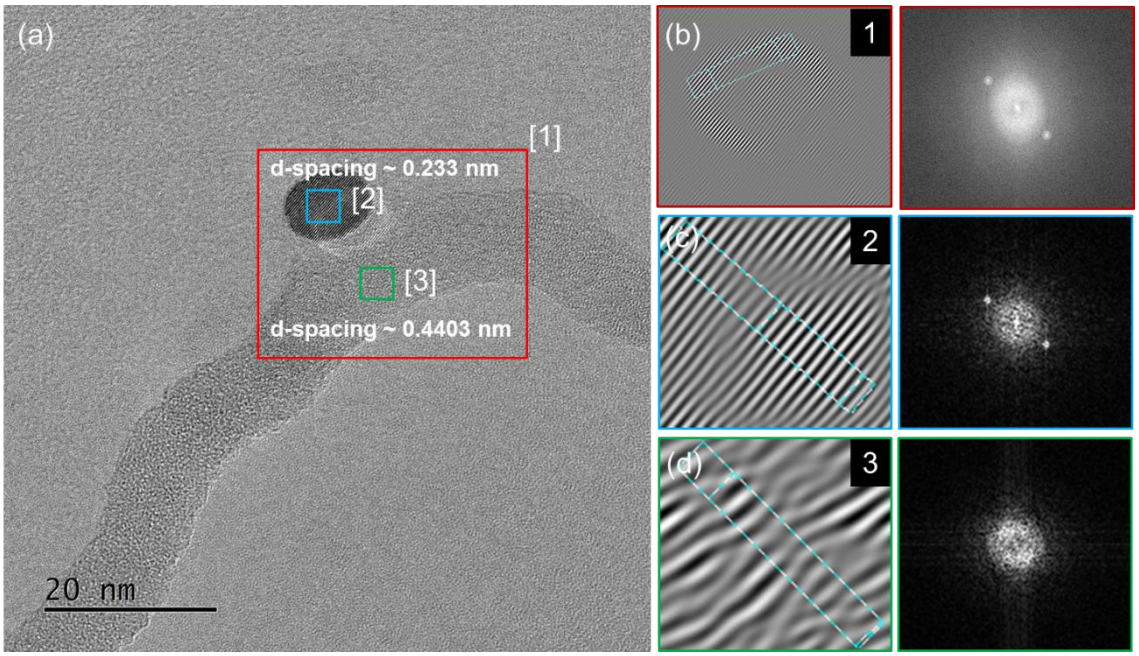



*Figure 4.16 (a) HRTEM image of Si/$SiO_x$ nanowire synthesized by thermal annealing of silicon-rich oxide embedded with gold nanoparticles at 1100 °C for 2 h under the flow of 5% $H_2$–Ar at ambient pressure. FFT analysis of (b) region-of-interest from the product, (c) Au nanoparticle, (d) fabricated nanowire.*

Raman spectroscopy (Horiba micro-Raman spectroscopy with a 532 nm wavelength laser) was used to evaluate the effect of the annealing temperatures and times on the nanowires. Figure 4.17a shows the typical Raman spectra of the Si nanowires after it was annealed at different temperatures from 700 – 1200 °C for 2 h. The Raman scattering peak of the Si-Si vibration modes for the crystalline Si nanowires (800 – 900 °C) appears at 501 – 507 $cm^{-1}$ (Figure 4.17a). The Raman peak of the annealed Si nanowires was shifted to a lower wavenumber by 13 – 19 $cm^{-1}$ (Figure 4.17b) when compared to the Raman peak of bulk Si at 520 $cm^{-1}$. This indicates the presence of a strain effect, which could be induced by the metal catalyst or the oxide shell in the nanowire structure[17]. At higher temperatures (1100 – 1200 °C), the Raman scattering peaks were at 488 – 494 $cm^{-1}$, which is a shift of 8 – 14 $cm^{-1}$ from the peak of amorphous Si (480 $cm^{-1}$)[18].

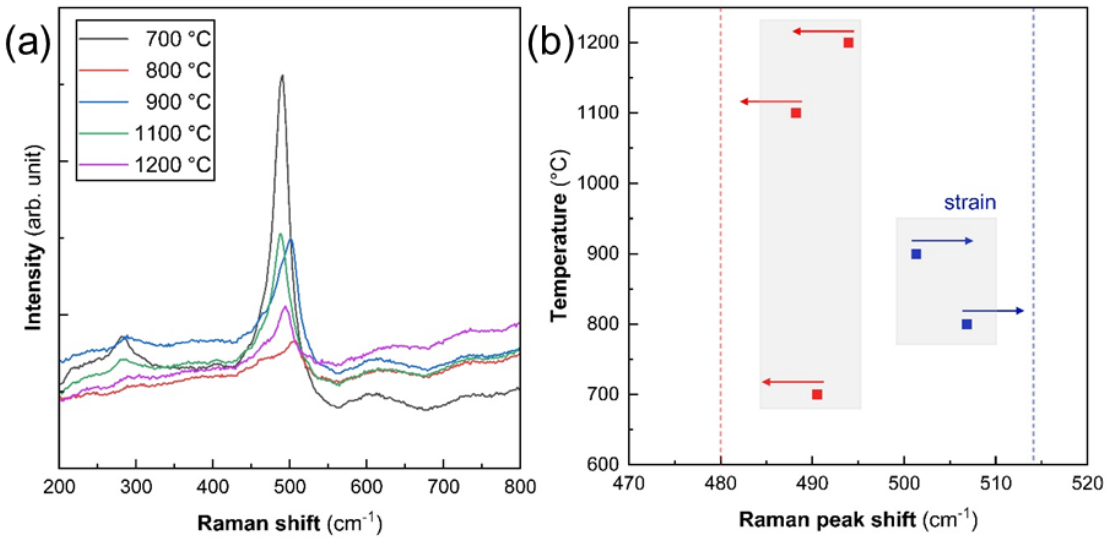



*Figure 4.17 (a) Raman spectra of the Si nanowires obtained at different annealing temperatures for 2 h. (b) Raman peak shift ($cm^{-1}$) in the Si nanowires with respect to the annealing temperature. The dotted red and blue lines represent the reference Raman peak shift for amorphous and crystalline silicon nanowires, respectively.*

Figure 4.18a and 4.18b show the effect of annealing time at a fixed temperature of 800 °C. The Raman scattering peak appears at 505 and 501 $cm^{-1}$ for an annealing time of 60 and 120 min, respectively. The Si-Si peak was much more intense for the material treated for 2 h with respect to 1 h annealing. No nanowires were observed by electron microscopy at an annealing time of 1 h (Figure 4.18c), perhaps due to very low yield. Some nanowires were observable for the materials annealed for 2 h; thus, this annealing time was conserved.

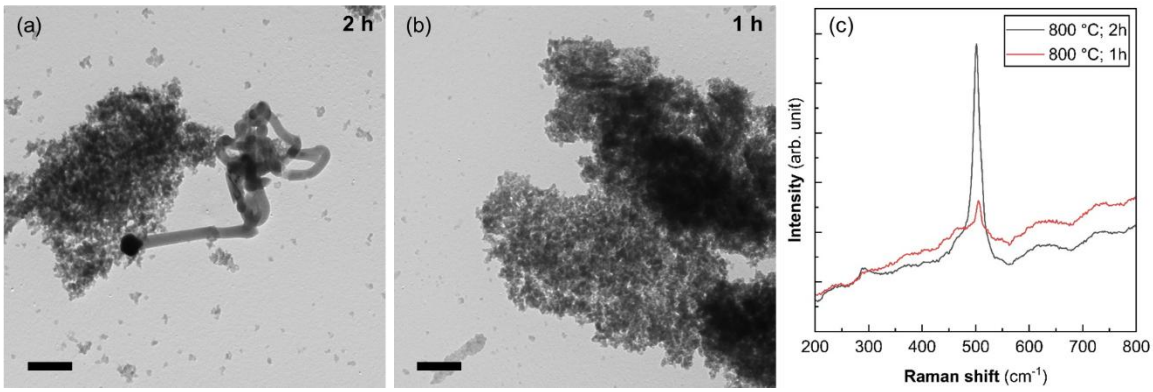



*Figure 4.18 TEM images of the products obtained at an annealing temperature of 800 °C for (a) 1 h and (b) 2 h dwell time at the maximum temperature. (c) Raman spectra of the Si nanowires annealed at 800 °C for different annealing times. The scale bar represents 200 nm in all images.*

The size of the Au nanoparticles affects the diameter of the nanowires. Figure 4.19a shows Si nanowires grown with ~ 30 nm Au nanoparticles. The nanowires have a diameter of ~ 20 nm with an oxide shell of ~ 9 nm. An increase in Au nanoparticle size to ~ 95 nm changed the Si wire diameter to ~ 40 nm (Figure 4.19c) with an oxide layer of 10 – 17 nm (Figure 4.19c). In all cases, the nanowires are several microns (1–6 μm) long, rendering them highly anisotropic.

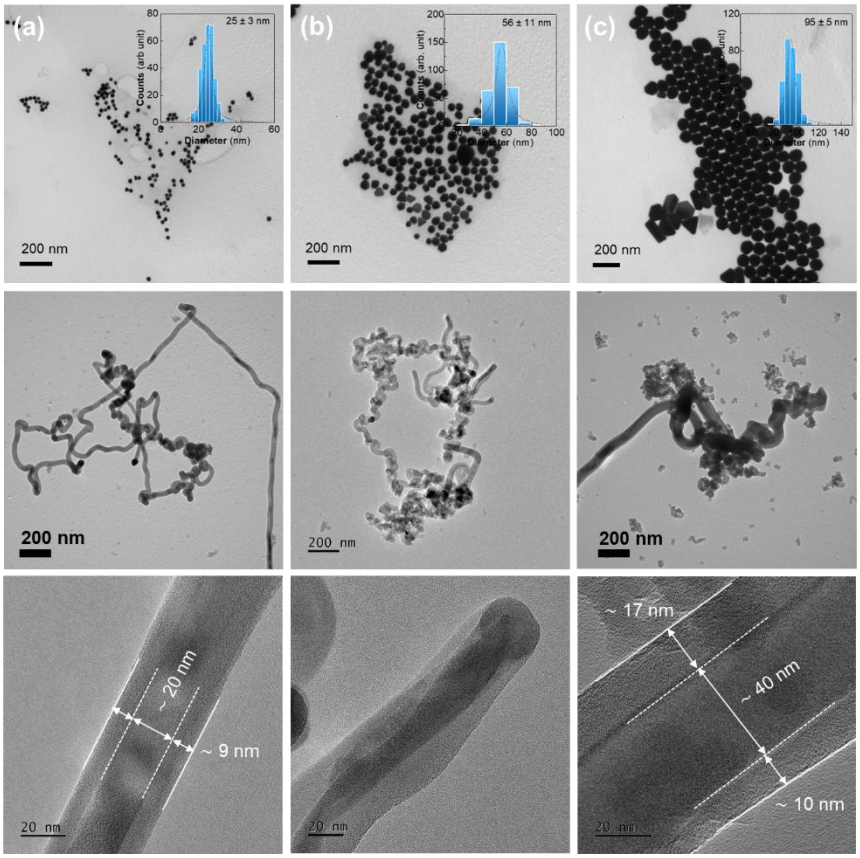



*Figure 4.19 TEM image of Si nanowires synthesized at 800 °C for 2 h with different Au nanoparticle sizes, namely a mean size of (a) 25, (b) 56, and (c) 95 nm.*

In Figure 4.20, we hypothesize the mechanism for the oxidation effect observed in the nanowires. After the nucleation and growth of the crystalline Si nanowire, simultaneously inward oxidation by oxygen occurs to form the $SiO_x$ layer. It is not clear if this is residual oxygen in the furnace or oxygen released during the thermal degradation of the silicon-rich oxide. As thermal annealing continues, the crystalline Si core is completely consumed, transitioning from crystalline Si to amorphous $SiO_x$ nanowire. The $SiO_x$ layer could also cover the Au particle (Figure 4.20b), rendering it inactive and ending the growth of the nanowire[19], as observed in some samples.

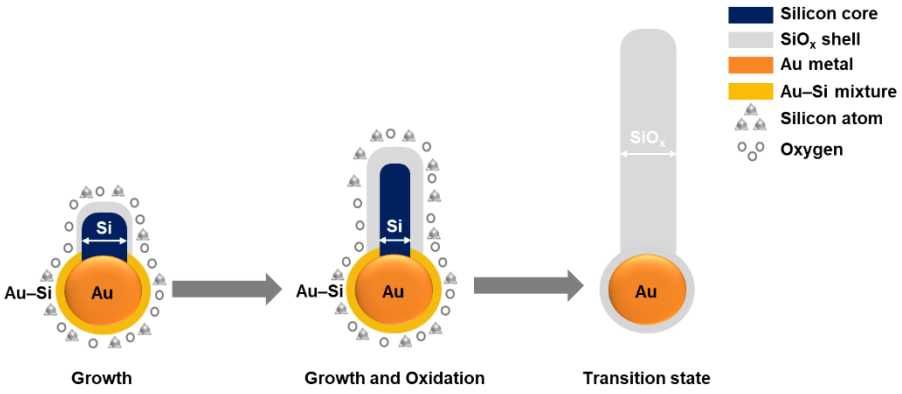



*Figure 4.20 Schematic illustration of the growth and oxidation of crystalline Si nanowire.*

Common defects in the growth of metal-catalyzed silicon nanowires include kinking (sudden change in growth direction), twinning, and stacking faults which are associated with variations in pressure, temperature, and composition of metal particles[20–22]. Kinking was observed in the grown Si nanowires (Figure 4.19). The bending and tangling of the nanowires observed could be due to possible stress during growth or annealing. We hypothesized the source of the stress could be from the silicidation of gold particles which act as catalyst for the growth of the Si nanowires. These metal particles are usually located at the tip of the nanowires and can provide a flux that diffuse to the Si/$SiO_x$ interface and induce the silicidation of gold. The lattice mismatch between Si – Au – Si and Si – Si bonds would induce the stress. This is further proven by the observation of Au particles in the core Si as will be shown later. Another hypothesis for the stress could be the molar volume mismatch between Si and $SiO_x$. A coil-like appearance of some silicon nanowires was observed (Figures 4.21). Madras, P., *et al.*[22] has reported a similar growth phenomenum which was attributed to the erratic change in the axial growth direction in an apparent random fashion causing the coil-like growth trajectory.

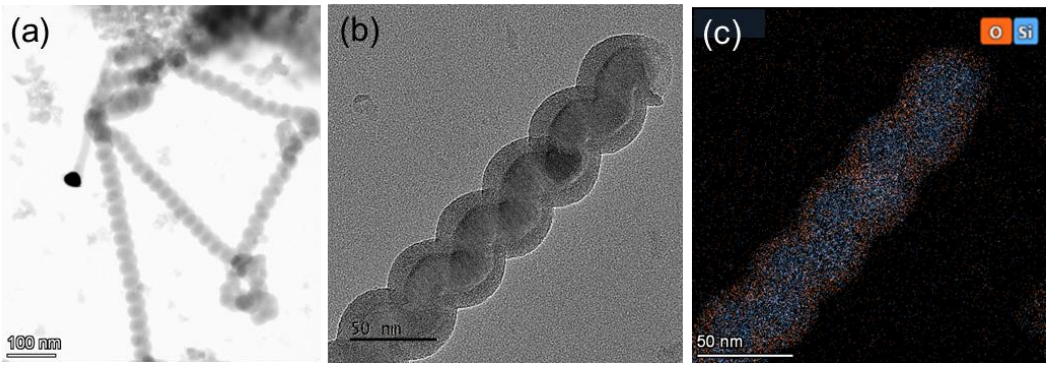



*Figure 4.21 (a) Bright-field TEM image, (b) HRTEM, (c) elemental mapping of Si nanowires synthesized at 800 °C for 2 h, showing coil-like and core-shell morphology. The elemental mapping of the nanowire shows Si, and $SiO_x$.*

Figure 4.22a shows an elongated Au nanoparticle directing the growth of the amorphous $SiO_x$ nanowire. The Au nanoparticle has a diameter of ~60 nm and length of ~112 nm, with the nanowire diameter ~44 nm. In Figure 4.22b, the Au particle (~48 nm) is surrounded by a $SiO_x$ layer of 3 – 5 nm. The EDS elemental mapping in Figure 4.22c confirms the presence of the Au particle at the tip of the nanowire. These observations further confirm that the Au nanoparticles contribute to the growth of the nanowires. Possibly trapped Au nanoparticles at arbitrary intervals within the nanowire was observed (Figure 4.22d).

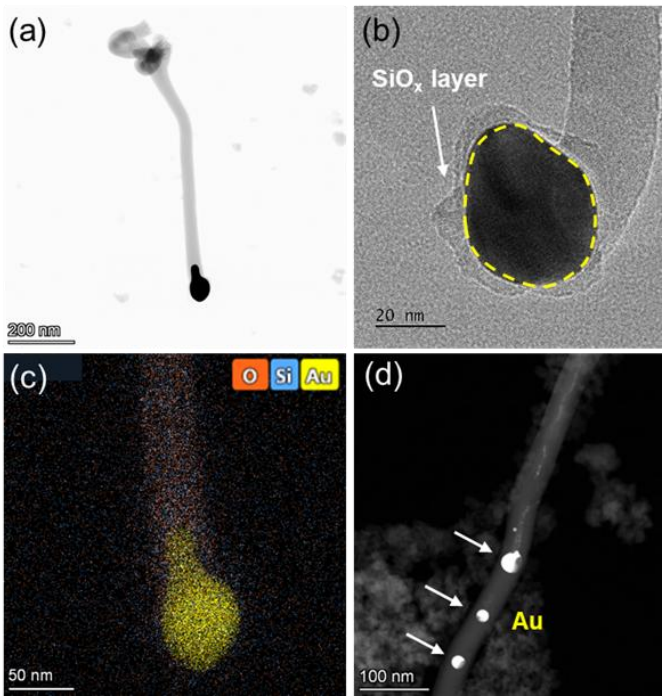



*Figure 4.22 (a) Bright-field STEM image, (b) HRTEM, (c) elemental mapping (d) dark-field STEM of Si nanowires synthesized at 800 °C for 2 h, showing oxidation effect and trapping of Au particles by oxide layer. The elemental mapping of the nanowire shows Si, $SiO_x$, and Au particle.*

### 4.4.5 Generalization of nanowire growth to other catalysts

To test the generalizability of this technique, the choice of metal particles used for the growth of Si nanowires was changed to silver (Ag) particles of ~30 nm and thermal annealing was carried out at 800 – 1200 °C. However, nanowires were not observed until 1200 °C (Figure 4.23c). The higher necessary annealing temperature could possibly be explained by the thermal decomposition temperature of the silicon-rich oxide and the eutectic point of Si–Ag ($T_{EP}$ = 837.1 °C). Despite the observation of nanowires when Ag nanoparticles are added to the silicon-rich oxide (Figure 4.23d), no crystalline silicon domain was observed in the nanowires at any

of the annealed temperatures. The brighter zones observed in Figure 4.23e are where two wires cross, and thus the electron pathway through the material is longer. Elemental mapping shows that the nanowires are $SiO_x$ (Figure 4.23f). As no Ag nanoparticles were observed in the STEM-EDX analysis, we cannot be certain that they were at the tips of the wires.

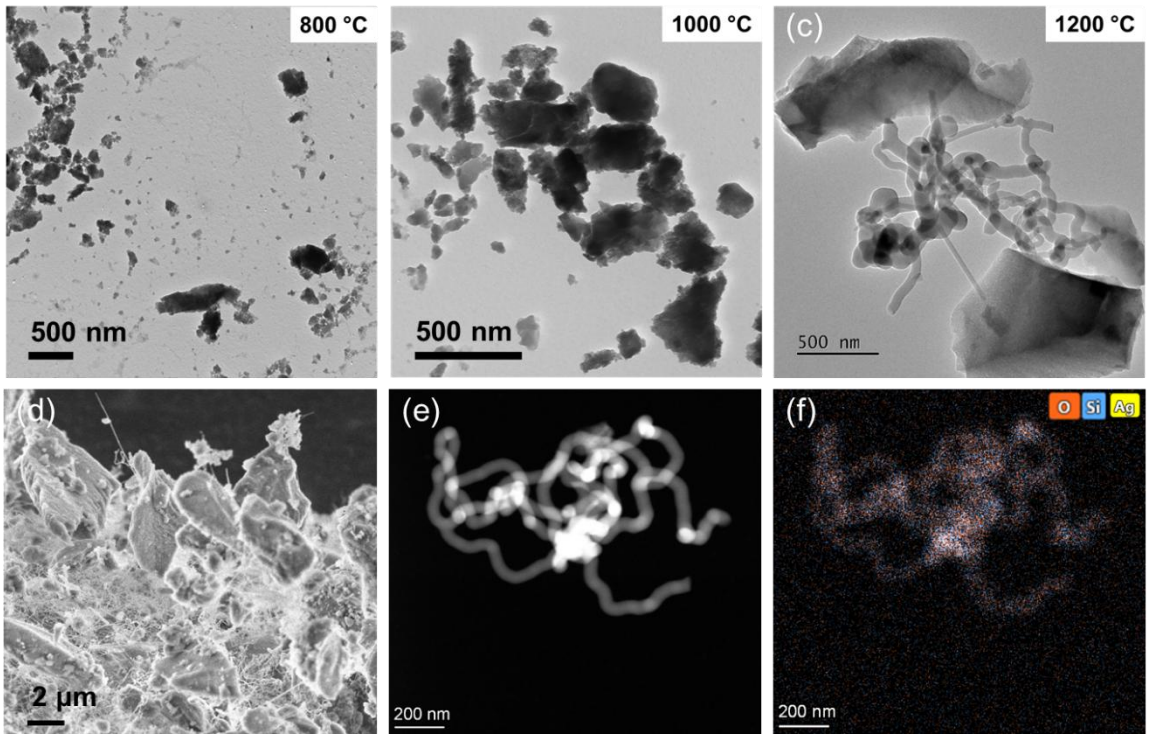



*Figure 4.23 (a-c) TEM image of the products synthesized at different temperatures for 2h with Ag particles. (d) SEM (e) Bright-field STEM, and (c) elemental mapping image of nanowires synthesized at 1200 °C for 2h. The elemental mapping of the nanowire shows Si, $SiO_x$ and Ag particle.*

From the XRD patterns of the products annealed at 1000 and 1200 °C, the peaks at 2θ values of 28.4°, 47.3°, and 56.1° correspond to the (111), (220), and (311) crystalline planes of cubic Si (PDF 05-0565). This is evidence in the annealing of pure silicon-rich oxide at 1100 °C which show the peaks corresponding to the cubic silicon peaks. The peak at 2θ value of 38.1° correspond to the (111) of cubic Ag. This peak disappeared with increasing temperature, but wire growth becomes more evident. This observation could possibly be explained by the sublimation temperature of Ag which has been investigated to be ~720 °C for ~30 nm particles under an *in-situ* TEM conditions[23].

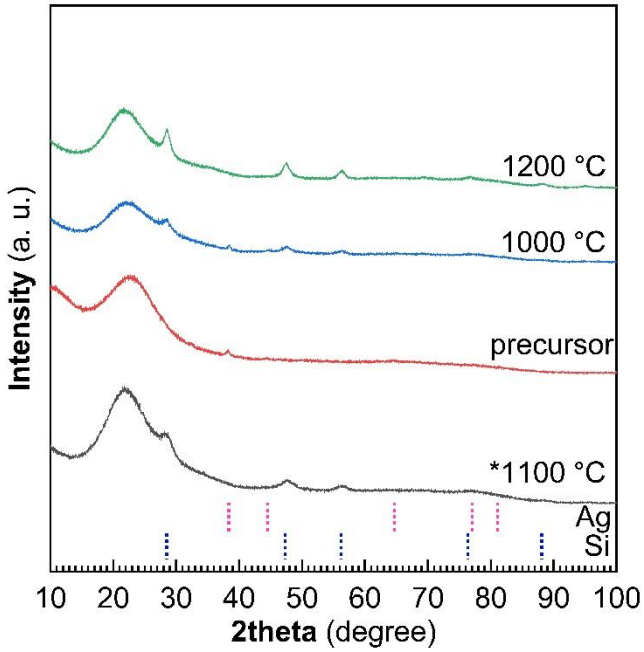



*Figure 4.24 XRD patterns obtained from the products at different temperatures. The indexes in blue correspond to diamond cubic Si peaks while those in pink are for cubic Ag.*

The change in the metal particle to iron(III)oxide ($Fe_2O_3$) with size ~30 nm also has a high nanowires density especially at 1100 °*C*. However, no Si crystalline domain was observed in the nanowires at any of the annealed temperatures.

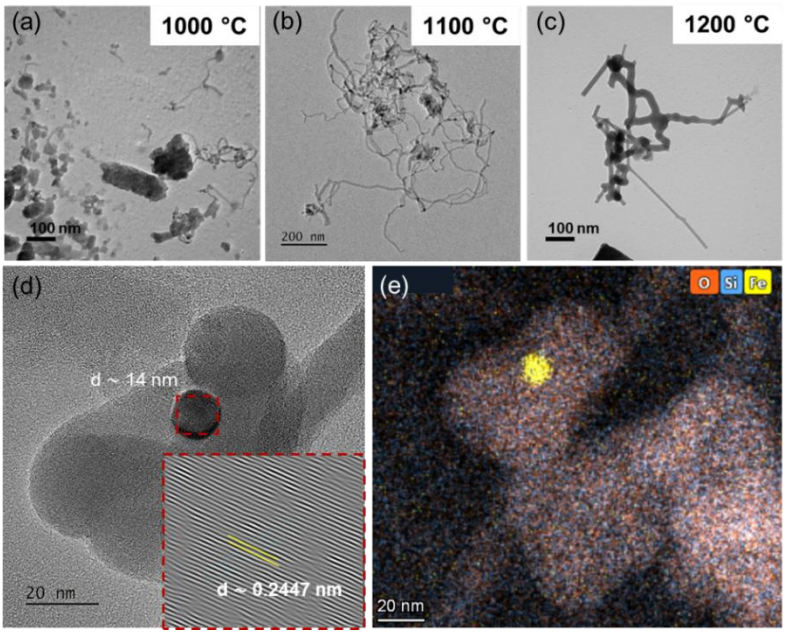



*Figure 4.25 (a-c) TEM images of nanowires obtained by thermal annealing of silicon-rich oxide incorporated with iron oxide ($Fe_2O_3$) particles at different temperature for 2h. (d) HRTEM with an inset of the FFT analysis, (e) Elemental mapping of nanowire annealed at 1100 °C for 2h with $Fe_2O_3$ nanoparticles.*

The XRD patterns of the products annealed at 1100 and 1200 °C show intense peaks at 2θ values of 28.4°, 47.3°, and 56.1° corresponding to the (111), (220), and (311) crystalline planes of cubic Si (PDF 05-0565).

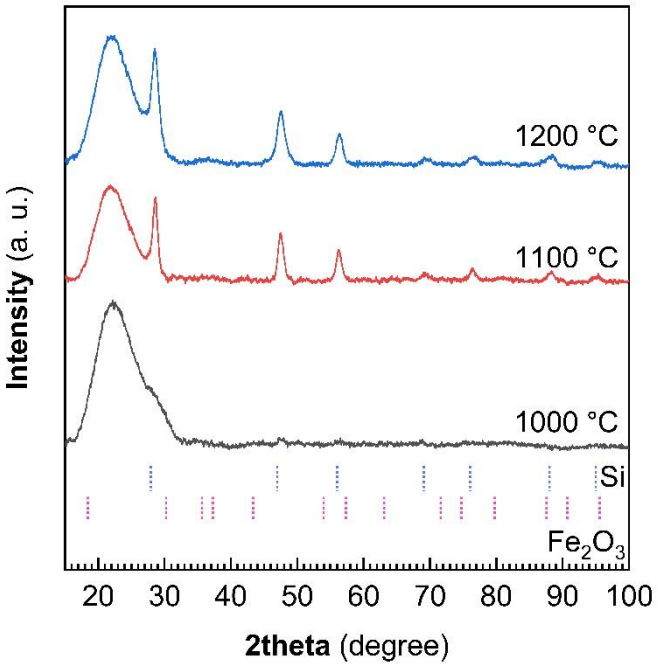



*Figure 4.26 XRD patterns obtained from the products at different temperatures. The indexes in blue correspond to diamond cubic Si peaks while those in pink are for maghemite $Fe_2O_3$.*

## 4.5 Conclusion and Perspectives

Silicon nanowires have been fabricated by the thermal annealing of a silicon-rich oxide over the temperature range of 800 – 1200 °C using different metal catalysts (Au, Ag, $Fe_2O_3$) at ambient pressure. The nanowires grown under some conditions have a crystalline core with a diameter between 15 – 80 nm, sheathed with an amorphous $SiO_x$ layer between 10 – 20 nm. They are micrometers in length (0.5 – 3 μm). The effect of the growth parameters (temperature, choice of metal catalysts and size, annealing time, precursor surface area, and gas flow rates) on the morphology and microstructures of the nanowires was systematically studied. There are no nanowires formed without increasing the surface area of the silicon-rich oxide precursors through grinding. For precursors incorporated with Au nanoparticles, crystalline Si nanowire growth occurs from 800 – 1000 °C. Beyond this temperature (1100 – 1200 °C), the nanowires are amorphous $SiO_x$ and of smaller diameter. However, the increase in temperature resulted in a higher nanowire density. The change in the choice of metal catalyst affects the temperature at which nanowires are formed and their degree of oxidation. The choice of silver nanoparticles increased the growth temperature to 1200 °C. In the case of $Fe_2O_3$ nanoparticles, a minimum

growth temperature of 1000 °C is required, and high nanowire density is achieved at 1100 °C. In both cases, the obtained nanowires are amorphous $SiO_x$. The high thermal annealing temperature of the Ag and $Fe_2O_3$ samples was attributed to the high eutectic point of Si/Ag (~837 °C), and Si/Fe (~1197 °C), compared to Si/Au (~363 °C). Therefore, other metals with a low eutectic temperature of metal/Si, such as Sn (~232 °C) and Ga (~30 °C), could be a better choice of metal catalysts.

From the real-time observations of the thermal annealing of the silicon-rich oxide between room temperature (RT) and 1000 °C under the reducing conditions, the main phenomena observed are: growth of an amorphous shell around the Au particles, formation of filaments, degradation of the silicon oxide matrix, sintering of the Au particles, and loss of facetting of the Au particle shape. We observed the formation of a shell around the Au particle, which is more substantial when cooling under $H_2$ to RT, with a final shell thickness of 13 nm. We hypothesized that as the temperature decreases, the silicon becomes less miscible with the gold and gets ejected from the Au particle, forming an amorphous shell. The elemental mapping clearly showed a core-shell structure, in which the Au sphere is fully covered on its surface by Si and O atoms. It was also revealed that Si atoms are homogeneously dispersed throughout the volume of the Au sphere after heating. This supports the hypothesis that there is contamination of the Au particle with Si atoms. The SAED pattern spots are indexed to a value of 0.324 nm, which is close to the d-spacing of 0.3203 nm defined from the *ex-situ* Si nanowire for Si (111) (Figure 4.8). Also, spots indexed to a value of ~ 0.244 nm are slightly larger than the d-spacing of ~ 0.233 nm defined for Au (111) from the *ex-situ* experiment. The observed softening of the gold particle facets starts at 800 °C. This was attributed to the contamination of the Au particle with Si atoms, which was not sufficient for the complete melting of the Au particle. The monodispersity of size and shape is a crucial parameter for studying the optical properties of single or assembled particles. This was not achievable in the bottom-up approach developed in this thesis. This is the same as other bottom-up approaches discussed in the literature in Chapter 1, except for the chemical vapor deposition approach.

## References


(1) Wiecha, P. R.; Cuche, A.; Arbouet, A.; Girard, C.; Colas Des Francs, G.; Lecestre, A.; Larrieu, G.; Fournel, F.; Larrey, V.; Baron, T.; Paillard, V. Strongly Directional Scattering from Dielectric Nanowires. *ACS Photonics* **2017**, *4* (8), 2036–2046. https://doi.org/10.1021/acsphotonics.7b00423.

(2) Chan, C. K.; Peng, H.; Liu, G.; McIlwrath, K.; Zhang, X. F.; Huggins, R. A.; Cui, Y. High-Performance Lithium Battery Anodes Using Silicon Nanowires. *Nat. Nanotechnol.* **2008**, *3* (1), 31–35. https://doi.org/10.1038/nnano.2007.411.

(3) Holmes, J. D.; Johnston, K. P.; Doty, R. C.; Korgel, B. A. Control of Thickness and Orientation of Solution-Grown Silicon Nanowires. *Science* **2000**, *287* (5457), 1471–1473. https://doi.org/10.1126/science.287.5457.1471.

(4) Lu, X.; Hanrath, T.; Johnston, K. P.; Korgel, B. A. Growth of Single Crystal Silicon Nanowires in Supercritical Solution from Tethered Gold Particles on a Silicon Substrate. *Nano Lett.* **2003**, *3* (1), 93–99. https://doi.org/10.1021/nl0202307.

(5) Hanrath, T.; Korgel, B. A. Supercritical Fluid–Liquid–Solid (SFLS) Synthesis of Si and Ge Nanowires Seeded by Colloidal Metal Nanocrystals. *Adv. Mater.* **2003**, *15* (5), 437–440. https://doi.org/10.1002/adma.200390101.

(6) Lee, D. C.; Hanrath, T.; Korgel, B. A. The Role of Precursor-Decomposition Kinetics in Silicon-Nanowire Synthesis in Organic Solvents. *Angew. Chem. Int. Ed.* **2005**, *44* (23), 3573–3577. https://doi.org/10.1002/anie.200463001.

(7) Geaney, H.; Kennedy, T.; Dickinson, C.; Mullane, E.; Singh, A.; Laffir, F.; Ryan, K. M. High Density Growth of Indium Seeded Silicon Nanowires in the Vapor Phase of a High Boiling Point Solvent. *Chem. Mater.* **2012**, *24* (11), 2204–2210. https://doi.org/10.1021/cm301023j.

(8) Mullane, E.; Kennedy, T.; Geaney, H.; Dickinson, C.; Ryan, K. M. Synthesis of Tin Catalyzed Silicon and Germanium Nanowires in a Solvent–Vapor System and Optimization of the Seed/Nanowire Interface for Dual Lithium Cycling. *Chem. Mater.* **2013**, *25* (9), 1816–1822. https://doi.org/10.1021/cm400367v.

(9) Spence, G. C.; Barbieri, R. C.; Pate, D.; Graves, L. S.; Özgür, Ü.; Arachchige, I. U. Sn-Induced Synthesis of Highly Crystalline and Size-Confined Si Nanorods at Moderately High Temperatures Using Hydrogen Silsesquioxane. *J. Phys. Chem. C* **2023**, *127* (24), 11579–11590. https://doi.org/10.1021/acs.jpcc.3c01308.

(10) Terada, S.; Xin, Y.; Saitow, K. Cost-Effective Synthesis of Silicon Quantum Dots. *Chem. Mater.* **2020**, *32* (19), 8382–8392. https://doi.org/10.1021/acs.chemmater.0c02320.

(11) Yin, G. The effect of $CH_4$ plasma treatment on low dielectric HSQ films. *Ceram. - Silik.* **2018**, 293–297. https://doi.org/10.13168/cs.2018.0024.

(12) Sato, Y.; Hayami, R.; Gunji, T. Characterization of NMR, IR, and Raman Spectra for Siloxanes and Silsesquioxanes: A Mini Review. *J. Sol-Gel Sci. Technol.* **2022**, *104* (1), 36–52. https://doi.org/10.1007/s10971-022-05920-y.

(13) Mabboux, P.-Y.; Gleason, K. K. Chemical Bonding Structure of Low Dielectric Constant Si:O:C:H Films Characterized by Solid-State NMR. *J. Electrochem. Soc.* **2005**, *152* (1), F7. https://doi.org/10.1149/1.1830353.

(14) Lu, W.; Lieber, C. M. Semiconductor Nanowires. *J. Phys. Appl. Phys.* **2006**, *39* (21), R387–R406. https://doi.org/10.1088/0022-3727/39/21/R01.

(15) Tarczay, G.; Förstel, M.; Maksyutenko, P.; Kaiser, R. I. Formation of Higher Silanes in Low-Temperature Silane ($SiH_4$ ) Ices. *Inorg. Chem.* **2016**, *55* (17), 8776–8785. https://doi.org/10.1021/acs.inorgchem.6b01327.

(16) Schäufele, R. S.; Vazquez-Pufleau, M.; Pendashteh, A.; Vilatela, J. J. Controlling Reaction Paths for Ultra-Fast Growth of Inorganic Nanowires Floating in the Gas Phase. *Nanoscale* **2022**, *14* (1), 55–64. https://doi.org/10.1039/D1NR07261G.

(17) Dupré, L.; Buttard, D.; Leclere, C.; Renevier, H.; Gentile, P. Gold Contamination in VLS-Grown Si Nanowires: Multiwavelength Anomalous Diffraction Investigations. *Chem. Mater.* **2012**, *24* (23), 4511–4516. https://doi.org/10.1021/cm301739n.

(18) Mohammed, M. S. G.; Cazzanelli, E.; Fasanella, A.; Castriota, M. Silicon Nanocrystals on the Surface of Standard Si Wafers: A Micro-Raman Investigation. *J. Mater. Sci. Chem. Eng.* **2018**, *06* (07), 104–116. https://doi.org/10.4236/msce.2018.67012.

(19) Li, F. J.; Zhang, S.; Kong, J. H.; Guo, J.; Cao, X. B.; Li, B. Growth of Crystalline Silicon Nanowires on Nickel-Coated Silicon Wafer beneath Sputtered Amorphous Carbon. *Thin Solid Films* **2013**, *534*, 90–99. https://doi.org/10.1016/j.tsf.2013.02.007.

(20) Su, Z.; Dickinson, C.; Wan, Y.; Wang, Z.; Wang, Y.; Sha, J.; Zhou, W. Crystal Growth of Si Nanowires and Formation of Longitudinal Planar Defects. *CrystEngComm* **2010**, *12* (10), 2793. https://doi.org/10.1039/b925198g.

(21) Razaghi, Z.; Zhu, G. Microscopic Characteristics of Kinking Phenomenon in Vertically Free-Standing Nanowires. *Crystals* **2023**, *13* (10), 1459. https://doi.org/10.3390/cryst13101459.

(22) Madras, P.; Dailey, E.; Drucker, J. Kinetically Induced Kinking of Vapor−Liquid−Solid Grown Epitaxial Si Nanowires. *Nano Lett.* **2009**, *9* (11), 3826–3830. https://doi.org/10.1021/nl902013g.

(23) Asoro, M. A.; Kovar, D.; Ferreira, P. J. *In Situ* Transmission Electron Microscopy Observations of Sublimation in Silver Nanoparticles. *ACS Nano* **2013**, *7* (9), 7844–7852. https://doi.org/10.1021/nn402771j.

# CHAPTER 5. L-tyrosine-directed synthesis and 3D characterization of ellipsoidal silica particles via optical levitation

5.1 Interest in the colloidal fabrication of ellipse-shaped silicon particles ..... 187
5.2 Experimental section ..... 189
5.2.1 Materials ..... 189
5.3 Synthesis of the ellipsoidal silica particles ..... 189
5.4 Results ..... 190
5.4.1 Formation of ellipsoidal particle suspensions ..... 190
5.4.2 Optical levitation of the ellipsoidal particle ..... 193
5.4.3 Effect of experimental conditions on morphology ..... 194
5.4.4 Formation mechanism of the ellipsoidal silica particles ..... 201
5.4.5 Magnesiothermic reduction of the particles ..... 205
5.5 Conclusions and perspectives ..... 207
Annexe 1. Tumbling time calculation from Perrin's formula ..... 209
References ..... 210

## 5.1 Interest in the colloidal fabrication of ellipse-shaped silicon particles

Ellipsoidal Si particles are of particular interest because their optical properties can be tuned systematically by changing their aspect ratio[1,2]. This has already been discussed in Chapter 1 of this thesis. However, the synthesis of ellipsoidal particles is a big challenge because of the minimization of surface free energy that favors simple spherical shapes[3]. Most of the approaches to fabricate ellipsoidal particles rely on deformation strategies such as ionic irradiation[4,5], chemical ion etching[6], mechanical stretching[7,8], and microfluidics processing[9]. The limitations of these approaches include low yield of deformed particles, the need for sophisticated equipment, and multi-step preparation procedures.

The sol-gel strategy provides an alternative method to produce ellipsoidal silica particles by carefully controlling the nucleation and growth processes. If these $SiO_2$ particles are successfully fabricated, they can be reduced to elemental Si by magnesiothermic reduction, as discussed in Chapter 1. However, only a few known methods are available to generate ellipsoidal particles through a surfactant templating approach without the use of a hard-templating agent. However, the available methods are not without the challenges of experimental reproducibility, control over particle size, aspect ratio, and degree of aggregation. These approaches have been discussed in Chapter 1. The synthetic methods reported propose three different hypothesized formation mechanisms to explain the generation of anisotropic silica particles. The first approach is attributed to shear forces, where strong stirring is considered responsible for the shape[10]. The second hypothesis proposes an emulsion approach in that the particles' shapes are formed in an equilibrium process between the particle's free surface energy and mesostructure formation free energy[11]. Specifically, through controlling the surface tension force via the water/oil emulsion volume ratio, the silica morphology changes from spherical to anisotropic[12]. The third hypothesis is related to the presence of micelles, i.e., self-assembled surfactant structure complexed within the growing silica particles. The micelle structure was attributed to the formation of elliptically shaped particles[13]. These can be summarized in Figure 5.1 below:

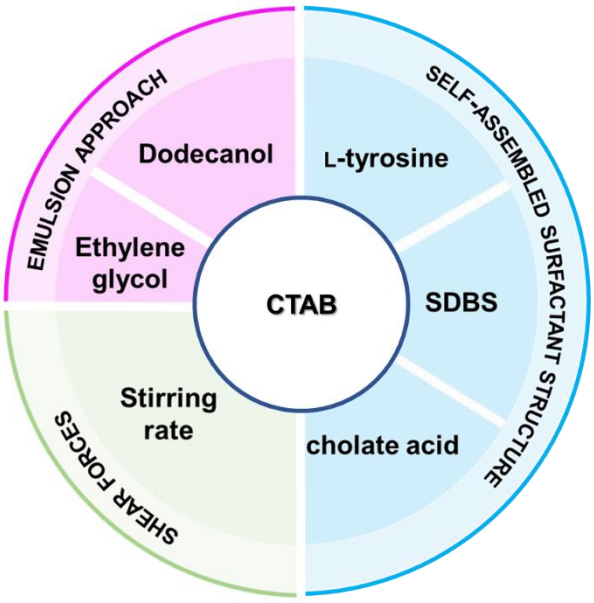



*Figure 5.1 Schematic diagram of the different proposed mechanisms for the synthesis of ellipsoidal silica particles via shear forces*[10]*, the emulsion approach*[12]*, and the self-assembled surfactant structure*[13–15].

To better understand the origins of anisotropy in amorphous silica, we studied in detail the protocol of Hao, N., *et al*.[15] Our first aim is to elucidate how silica particle morphology, size, and aggregation depend upon the surfactants (CTAB and L-tyrosine) and the different reaction parameters (such as the surfactant ratio, pH, TEOS concentration and addition rate, and temperature). It has been reported that the molar ratio of cationic surfactants to the number of Si atoms in the alkoxysilanes can affect the phase of mesostructure formation, the particle diameter, and the particle dispersibility.[16] Our second aim is to understand which of the formation mechanisms discussed is responsible for the anisotropic shape.

Finally, we introduce an experimental platform for straightforward characterization of the shape and size of an optically levitated particle. Optical levitation in vacuum enables isolation of individual nanoparticles from environmental perturbations, allowing precise measurement of their mechanical and geometric properties in 3D. Unlike electron microscopy, this method avoids artifacts from sample support and provides dynamic information on particle orientation and rotational modes. Levitodynamics provides a highly controlled, sensitive, and non-invasive technique to characterize the size and shape of optically levitated particles[17]. By leveraging precise measurements of motion and damping rates, it offers detailed insights into the geometric particle properties, making it a valuable tool in both fundamental research and practical applications[18]. Among the objects that can be used in Levitodynamics, silica nanoparticles are

specifically suitable for optical trapping. The main drawback of optical trapping is the heating of nanoparticles due to their light absorption. Thus, thanks to low absorption of silica particles, they are among the most commonly used nanoparticles. Additionally, it is the only nanoparticle for which the fundamental quantum state has been reached. Therefore, the behavior of the ellipsoidal form could be interesting to study.

## 5.2 Experimental section

### 5.2.1 Materials

Tetraethyl orthosilicate, TEOS (86578, ≥99.0%), cetyltrimethylammonium bromide, CTAB (H5882, ≥98%), and L-tyrosine (T3754, ≥98%), were purchased from Sigma-Aldrich. The ethanol (99.9 %, PC80101.9200) was supplied by Atlantic Labo. The ammonia solution (AM02561000, 28% w/w) was supplied by Scharlab S.L. Aqueous solutions were prepared using deionized water, prepared using a Type 1 Milli-Q water purification system (18.2 MΩ cm). Carbon/copper grids were obtained from Delta Microscopies. All chemicals were used without further purification.

## 5.3 Synthesis of the ellipsoidal silica particles

The protocol of Hao, N., *et al.*[15] was adopted to synthesize the ellipsoidal silica particles (42). In a typical synthesis, the molar ratio of reactants was 3.6 : 3.6 : 87.5 : 53930 : 55.7 mM for CTAB:L-Tyr:TEOS:$H_2O$:$NH_4OH$, respectively. First, CTAB (3.6 mM) and L-tyrosine (3.6 mM) were ultrasonically dissolved, separately, in 56 mL of milli-Q water (~10 min) and then mixed in a 250 mL round-bottom flask placed in an oil bath and equipped with a reflux condenser. The mixture was stirred with a 3 cm cylindrical magnetic stirrer for 20 min to ensure a homogeneous solution before adding 25 wt.% Aq. $NH_4OH$ (1 mL, pH = 10 - 11) and further stirred for another 20 min before the addition of TEOS (87.5 mM) dropwise using a syringe pump. The mixture was then stirred for 1 h. The solid material was recovered by centrifugation, and the precipitate was washed with deionized $H_2O$ (×3) and EtOH (×2) to remove the remaining CTAB and L-tyrosine from the product. The effect of the addition rate of TEOS (2.25 – 27 mL/h), stirring speed (250 – 1000 rpm), ammonia concentration (0.069 – 0.228 M), the molar ratio of CTAB/L-tyrosine (1:1 – 1:3), and increased L-tyrosine concentration (0 – 14 mM) on the particle size, morphology, and aggregation was investigated.

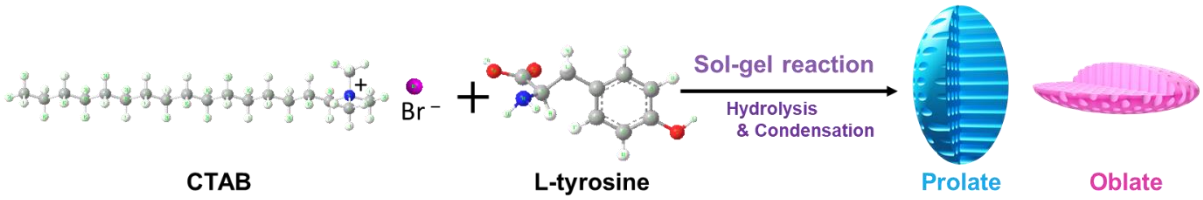



*Figure 5.2 Schematic diagram of the synthesis approach for ellipsoidal silica particles. The chemical structures elements are carbon (grey), hydrogen (white), oxygen (red), nitrogen (blue), and bromine (purple).*

## 5.4 Results

### 5.4.1 Formation of ellipsoidal particle suspensions

The protocol reported by Hao, N., *et al*.[15] was successfully reproduced to form mesoporous ellipsoidal silica particles. As shown in Figure 5.3 below, it is hard to determine the exact ratio as prolate and oblate particles cannot be differentiated when the oblate particles are resting on their minor axis. The typical hexagonal cylindrical mesoporous channels are observed in the micrographs[15]. For a typical sample, the mesostructure observed in the ellipsoidal particles revealed pore channels parallel to the particle minor axis and perpendicular to the major axes (Figure 5.3).

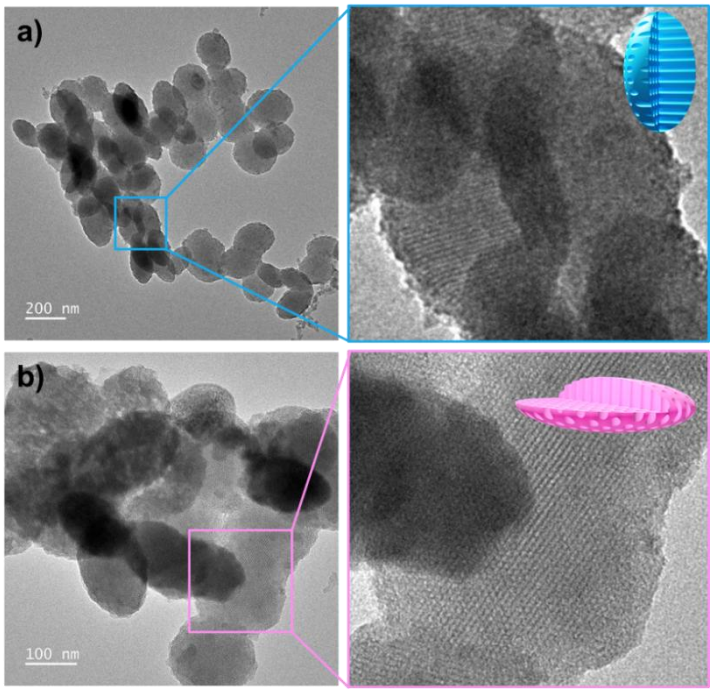



*Figure 5.3 The TEM images of the synthesized particles showing the mesostructures formed by the CTAB/L-tyrosine surfactants in solution*

Particle aggregation is observed in the micrographs, both as observed in reference[15], and as shown in the TEM and SEM images in Figure 5.4a and 5.4b. It has been demonstrated that mesoporous silica particles are prone to aggregation during post-synthetic treatments such as template removal, surface modification, and drying[19–21]. Therefore, as a first step, dynamic light scattering (DLS) measurements were used to analyze the state of particle aggregation in the as-synthesized dispersion. The autocorrelation function, measured at scattering angles of 45, 90, and 135° (Figure 5.4c), cannot be well adjusted by a single exponential function due to the high polydispersity of the particles. For the as-synthesized particles without any post-synthetic treatment, the mean hydrodynamic diameter was estimated to be approximately 2054 nm. This was determined from the plot of decay constant, extracted from the short times domain of the curves, against the square of scattering vector (Figure 5.4f), using data at 45 and 90°. Both of these observations indicate a certain degree of particle aggregation in the suspension. However, the autocorrelation curves for particles upon centrifugation/redispersion, and from sedimentation after centrifugation/redispersion, shown respectively in Figure 5.4d and 5.4e, present a neat monoexponential shape, corresponding to a more monodisperse population of suspended objects. The hydrodynamic diameters were calculated to be approximately 337 and 363 nm for centrifuged and sedimented samples, respectively (Figure 5.4f). This suggests a significant reduction in aggregation after the post-synthesis treatments.

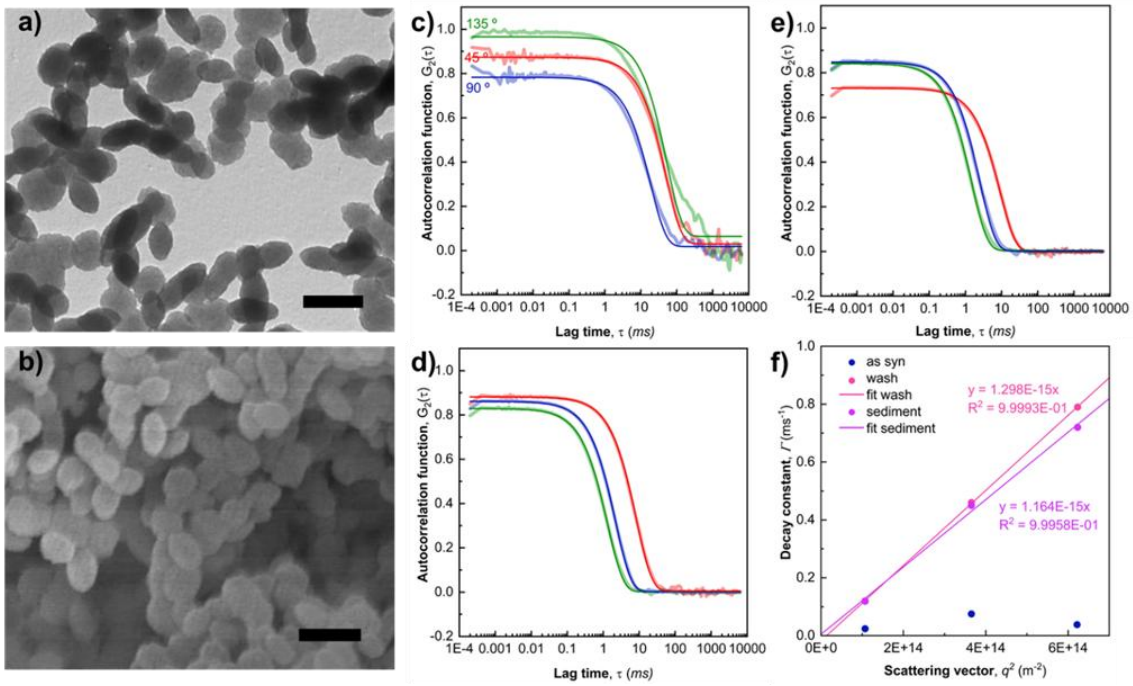



*Figure 5.4 (a) TEM and (b) SEM images of the synthesized ellipsoidal silica particles under a TEOS addition rate ($R_{TEOS}$) of 27 mL $h^{-1}$ (5 min) for $V_{TEOS}$ = 2.25 mL. [CTAB] = 3.6 mM,*

*[L-tyrosine] = 3.8 mM, [TEOS] = 0.088 M, [$H_2O$] = 54.0 M, [$NH_4OH$] = 0.056 M; pH = 11 – 12, reaction time = 1 h, T = (25 ± 2) ˚C, and stirring rate = 250 rpm. The scale bar represents 250 nm in both micrographs. The light scattering autocorrelation curves for the ellipsoidal silica particles (c) before centrifugation, (d) after three cycles of centrifugation at 8000 g, and (e) after redispersion in 40 mL of ethanol and overnight sedimentation of the centrifuged sample. (f) The plot of decay constant against scattering vector to calculate the hydrodynamic diameter of the particles before centrifugation (blue), after three cycles of centrifugation at 8000 g (pink), and after redispersion in 40 mL of ethanol and overnight sedimentation of the centrifuged sample (purple). Three different scattering angles were measured, 135˚ (green), 90˚ (blue), and 45˚ (red). The experimental data are represented in light colors, while the fitted curve is represented in dark colors.*

Nevertheless, these dimensions are larger than the values of 156 ± 19 nm × 105 ± 14 nm measured for single particles counted from the TEM images (Figure 5.5). Thus, using this protocol leads to some degree of aggregation, with particles occurring in small clusters of 1-3 particles that are not separated during the post-synthesis treatment.

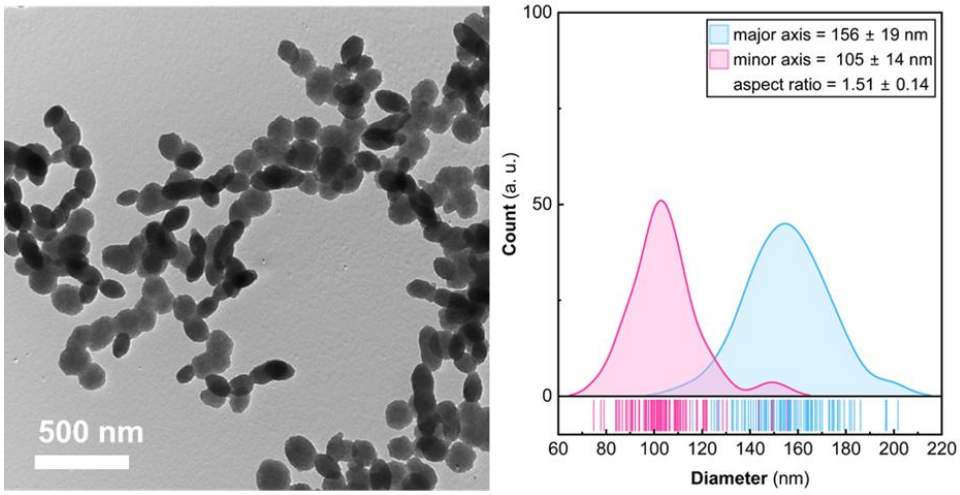



*Figure 5.5 TEM image and its size distribution for the synthesized ellipsoidal silica particles under a TEOS addition rate ($R_{TEOS}$) of 27 mL h−1 (5 min) for $V_{TEOS}$ = 2.25 mL. [CTAB] = 3.59 mM, [L-tyrosine] = 3.77 mM, [TEOS] = 0.088 M, [$H_2O$] = 53.93 M, [$NH_4OH$] = 0.0557 M; pH = 11 – 12, reaction time = 1 h, T = (25 ± 2) ˚C, and stirring rate = 250 rpm. The scale bar represents 500 nm in the micrograph. The histogram is based on 100 particle counts.*

### 5.4.2 Optical levitation of the ellipsoidal particle

Having determined a satisfactory dispersion of colloidal particles, individual particles were studied using optical levitation. The optical trapping experiment was carried out by our collaborator from Laboratoire Ondes et Matière d'Aquitaine (LOMA) – Manon Barrière, Yacine Amarouchene, and Yann Louyer. An extensive discussion of the experimental study is in a different thesis by Manon Barrière[22]. The experimental platform used optical levitation to measure the size and 3D shape of the silica particle trapped in a moderate vacuum. After trapping a particle at ambient pressure, the vacuum chamber is cleared of other particles to determine the trapped particle size and shape.

The tightly focused trapping beam is linearly polarized, requiring analysis beyond the paraxial approximation[23]. This leads to distinct resonance frequencies for the nanomechanical oscillator, as evidenced by the power spectral densities in Figure 5.6a. The lower radial frequency, associated with the *x*-axis, indicates that the trapping beam's polarization aligns along the *x*-axis. Consequently, the major axis of the ellipsoidal particle, which has the highest polarizability, aligns with the *x*-axis. This alignment allows qualitative analysis of how damping rates, $\Gamma_i$ along the *x*, *y*, and *z*-axes vary with pressure. In the free molecular regime, where the gas molecule's mean free path greatly exceeds the particle size, the damping coefficient, $\Gamma_i \sim r_j^2 p$, with $r_j$ being the effective radius perpendicular to $r_i$, and $p$ the gas pressure. As shown in Figure 5.6b, the $\Gamma_i$ values scale linearly with $p$, and as anticipated, motion along the *x*-axis experiences less drag than along the *y*-axis ($\Gamma_x < \Gamma_y$).

By quantitatively fitting the widths of the power spectral densities to the damping rate equation (equations 2.19 and 2.20 in the experimental section), the diameter along each axis was determined: $d_x$ = 172 ± 11 nm, $d_y$ = 106 ± 6 nm, and $d_z$ = 117 ± 5 nm. For a single particle, the aspect ratio is 1.62, and the average aspect ratio for multiple particles trapped is 1.5. This corresponds to the aspect ratio determined from the TEM images (Figure 5.5).

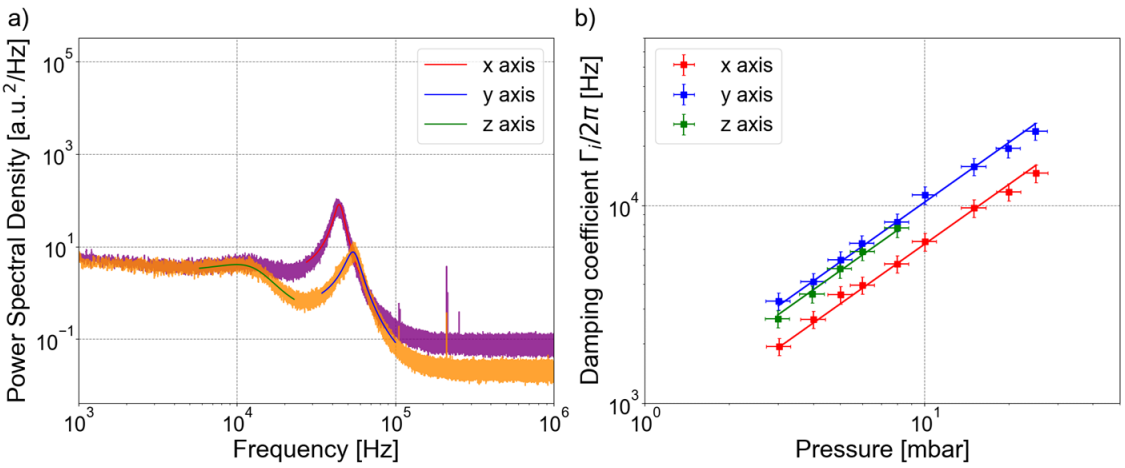



*Figure 5.6 (a) Power spectral densities along the x- and y-axis, obtained by doing the Fourier transform of the autocorrelation function of position. The peaks correspond to translational modes (x and y), not rotational. (b) Pressure evolution of the damping rates along each axis, calculated by fitting with equation 2.19 the widths of the Lorentzian form seen in the power spectral densities.*

### 5.4.3 Effect of experimental conditions on morphology

To better understand the reaction mechanism leading to ellipsoidal particles, we tried to optimize the synthesis parameters. Non-spherical shape could be due to an anisotropic growth caused by heterogeneities in the surface chemistry. To investigate this point, we have modified the surface-active components of the reaction mixture. First, we varied the CTAB/ L-tyrosine molar ratio from 1:1 to 1:3 by varying the CTAB concentration between 1.19 and 3.60 mM. From the result shown in Figure 5.7a, minimal changes were observed in both particle size and aspect ratio. The particle size changed from 140 ± 16 nm (major axis) × 89 ± 15 nm (minor axis) to 136 ± 17 nm (major axis) × 86 ± 12 nm, and the aspect ratio from 1.59 ± 0.2 to 1.63 ± 0.2 (Figure 5.7b). Thus, CTAB is not the principal reagent impacting morphology.

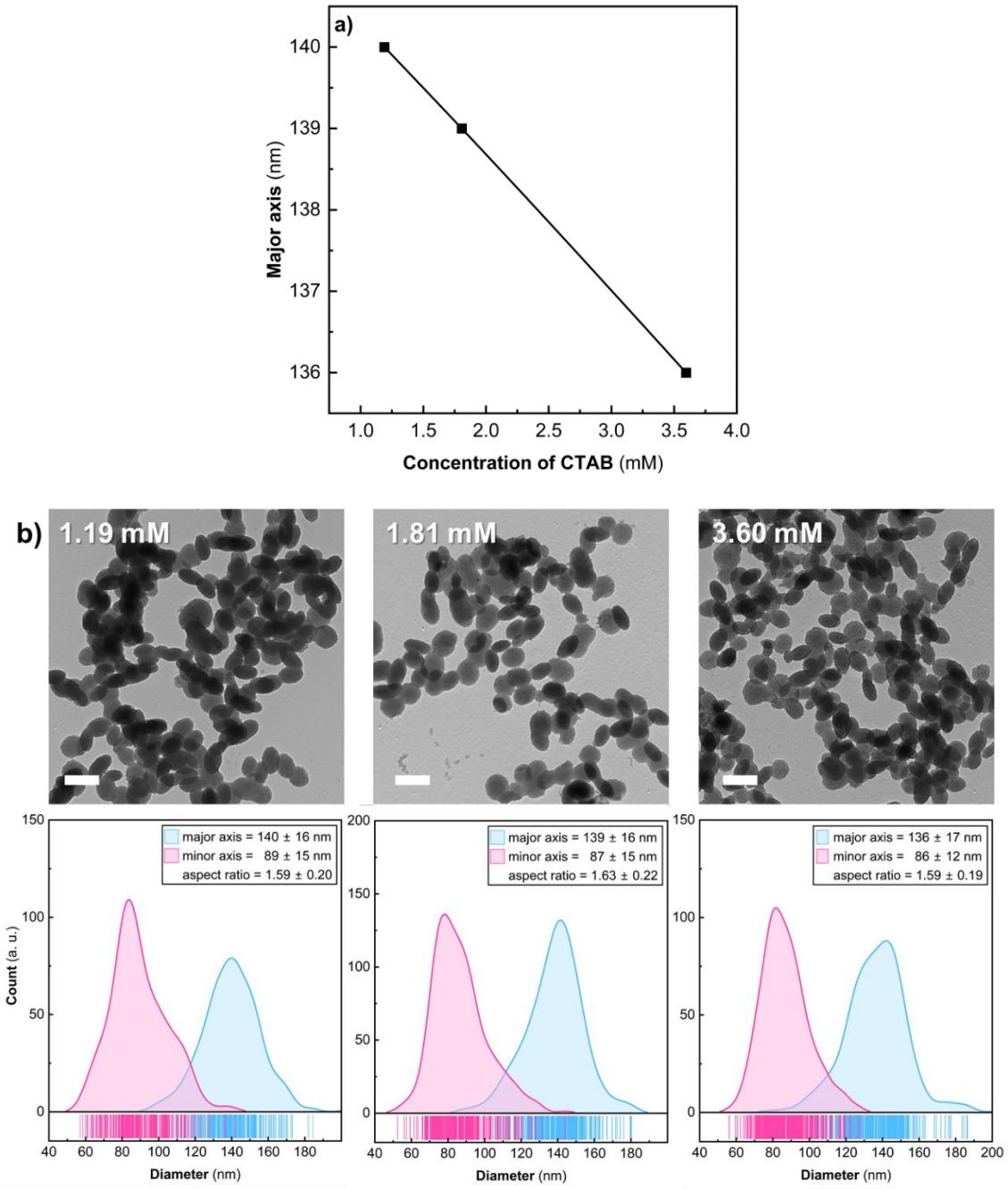



*Figure 5.7 (a) Plot of the dependence of the particle dimension on the molar concentration ratio of surfactants. (b) TEM images and size distribution of silica particles synthesized using [CTAB] = 1.2, 1.8, 3.6 mM corresponding to [CTAB]/[L-tyrosine] ratio of 1:1, 1:1.5, and 1:3, respectively. [L-tyrosine] = 3.7 ± 0.02 mM. The scale bar represents 500 nm. [CTAB] = 1.2, 1.8, 3.6 mM corresponding to [CTAB]/[L-tyrosine] ratios of 1:3, 1:2, and 1:1, respectively. [L-tyrosine] = 3.66 ± 0.02 mM. The scale bar represents 200 nm in the micrographs. The histogram is based on 300 particle counts.*

Second, we studied the effect of adding poly(vinylpyrrolidone) (PVP), known to stabilize silica particle surfaces[24]. The effect of adding 0.5 - 1% (w/v) PVP concentration at the start of the synthesis was investigated. From Figure 5.8, it can be observed that the PVP has a very minor effect on the size and anisotropy of the ellipsoids with the particle size changing from 137 ± 17 nm (major axis) × 87 ± 13 nm (minor axis) to 129 ± 17 nm (major axis) × 94 ± 14 nm, and the aspect ratio from 1.6 ± 0.2 – 1.4 ± 0.1.

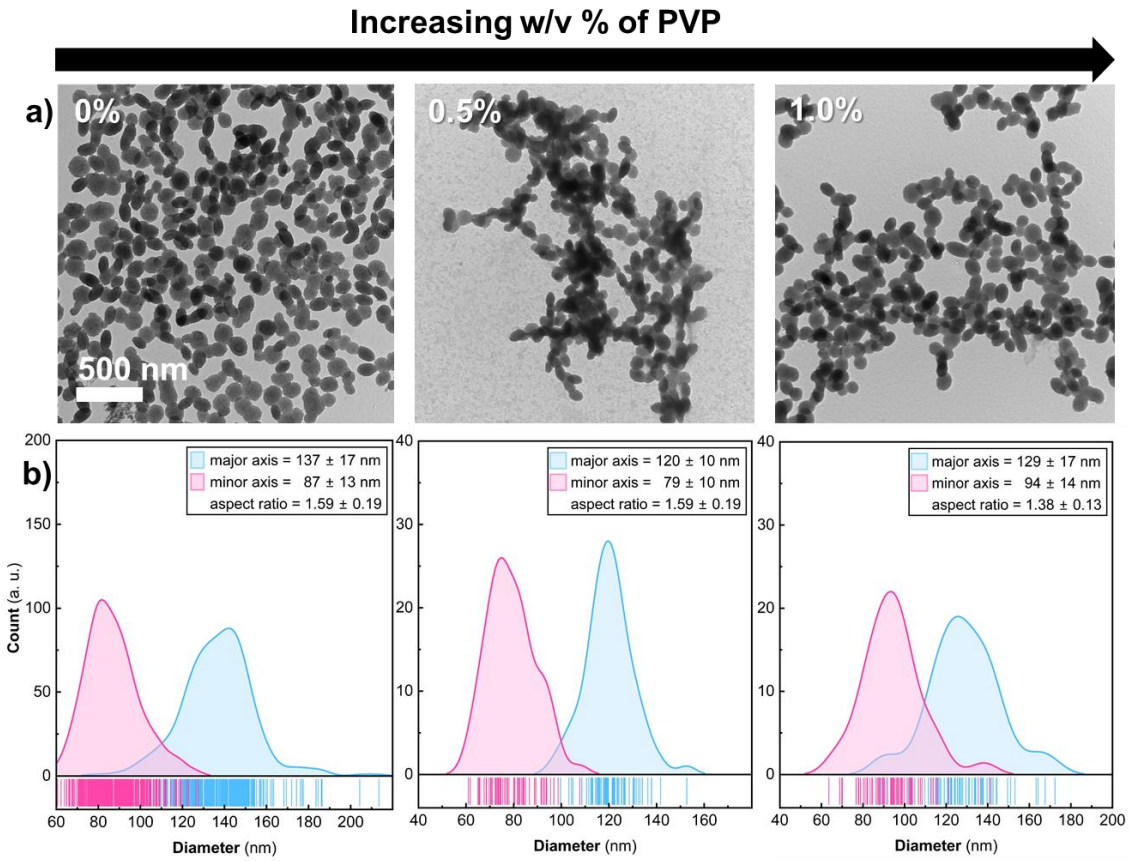



*Figure 5.8 TEM images of silica particles synthesized using 0 - 1% (w/v) PVP, and [CTAB] = 3.5 mM, [L-tyrosine] = 3.4 mM, [$H_2O$] = 54.0 M, [TEOS] = 0.088 M, [$NH_4OH$] = 0.056 M, pH = 9 – 10, a reaction time of 1 h, T = 25 ± 2 ˚C, a stirring rate of 250 rpm. The scale bar represents 500 nm.*

Condensation rate is related to temperature and pH. The increase in reaction temperature has been shown to increase the amount of silicic acid available to form new nuclei. This means that soluble silica species are consumed, forming more nuclei, rendering them unavailable for particle growth[25,26]. Thus, to explore the possible relationship between particle growth rate and aspect ratio, we synthesized the particles at three different temperatures of 25, 30, and 60 °C. Figure 5.9a show a decrease in particle size as temperature increases, with a change in the

particle morphology from elliptical to spherical. It should be noted that L-tyrosine solubility also increases with increased temperature. From Figure 5.9b, the TEM images shows that the particles sizes are 136 ± 13 nm (major axis) × 86 ± 12 nm (minor axis) at 25 °C, 110 ± 15 nm (major axis) × 75 ± 12 nm (minor axis) at 30 °C, and 63 ± 9 nm (major axis) × 53 ± 8 nm (minor axis) at 60 °C; where aspect ratio decreases from 1.6 ± 0.2 at 25 °C to 1.2 ± 0.1. Hence, ambient temperature leads to the formation of more elliptical structures.

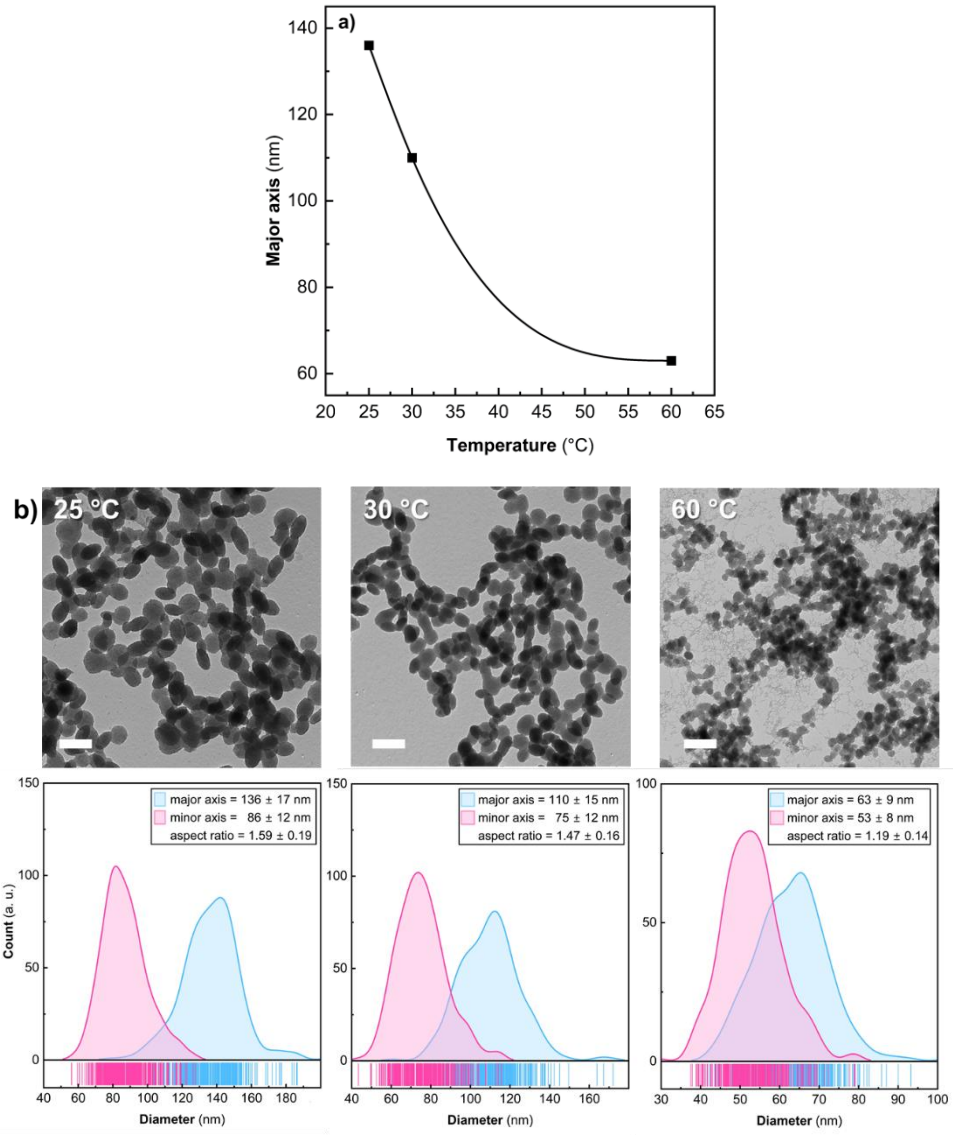



*Figure 5.9 (a) Plot of the dependence of the particle dimension on the reaction temperature. The line is a guide for the eye. (b) The TEM images and size distribution of silica particles under different temperatures of 25 ˚C, 30 ˚C, and 60 ˚C, [$NH_4OH$] is 0.056 M; pH = 9 – 10. [CTAB] = 3.6 mM, [L-tyrosine] = 3.8 mM, [$H_2O$] = 54.0 M, [TEOS] = 0.088 M, reaction time = 1 h, T = (20 ± 4) ˚C, and stirring rate = 250 rpm. The scale bar represents 500 nm. The histogram is based on 300 particle counts.*

An increase in the concentration of the base catalyst during the reaction has been found to lead to an increase in condensation rate, particle size, surface smoothness, sphericity, and can avoid aggregation[20]. In our system, the particle size increased with an increase in the ammonia concentration, as shown in Figure 5.10a. From Figure 5.10b, the TEM images show that the particle sizes are 99 ± 12 nm (major axis) × 68 ± 9 nm (minor axis) at 0.034 M, 136 ± 17 nm (major axis) × 86 ± 12 nm (minor axis) at 0.056 M, and 202 ± 25 nm (major axis) × 125 ± 19 nm (minor axis) at 0.084 M; where aspect ratio increases from 1.47 ± 0.13 at 0.034 M to 1.63 ± 0.18 at 0.084 M.

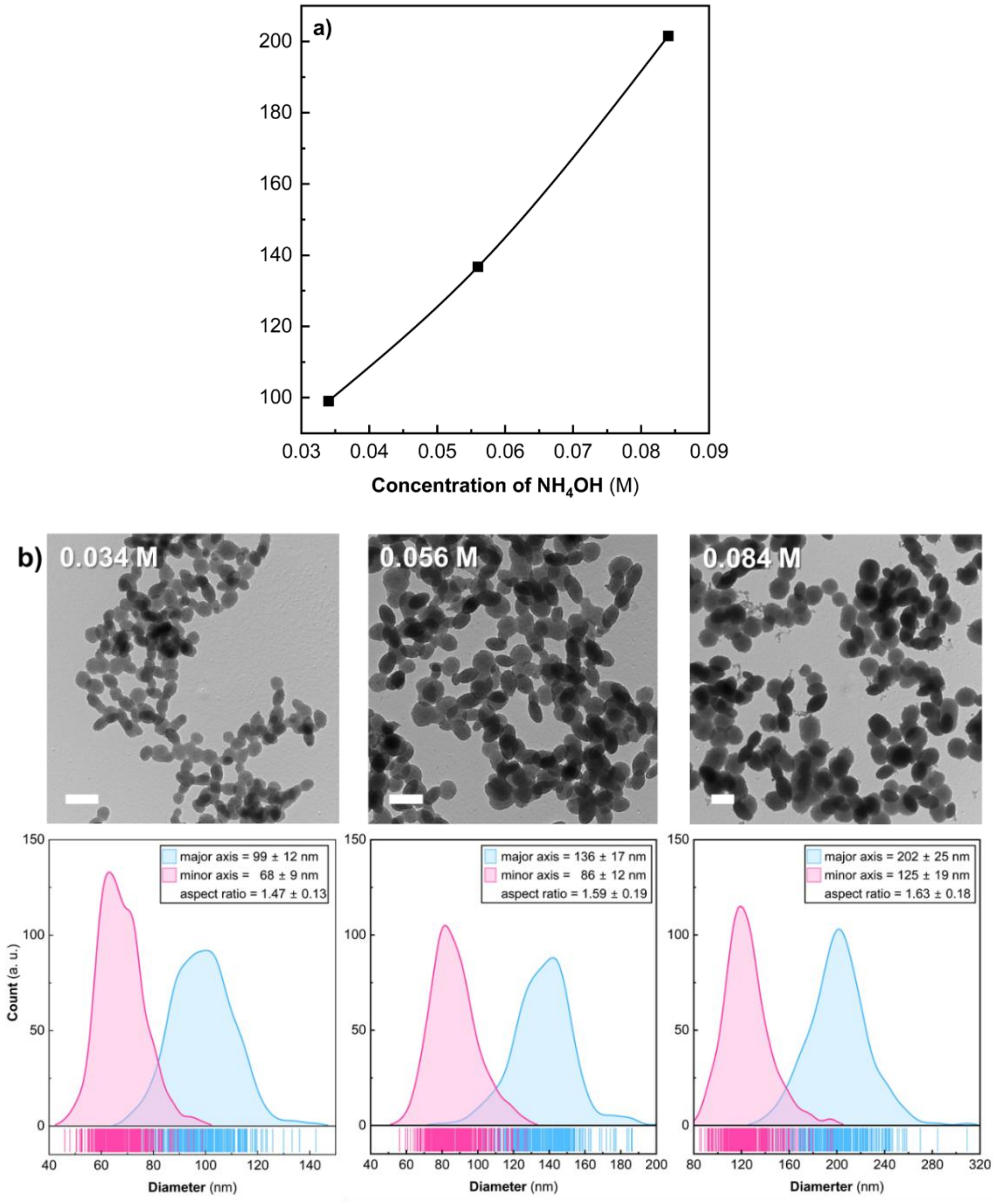
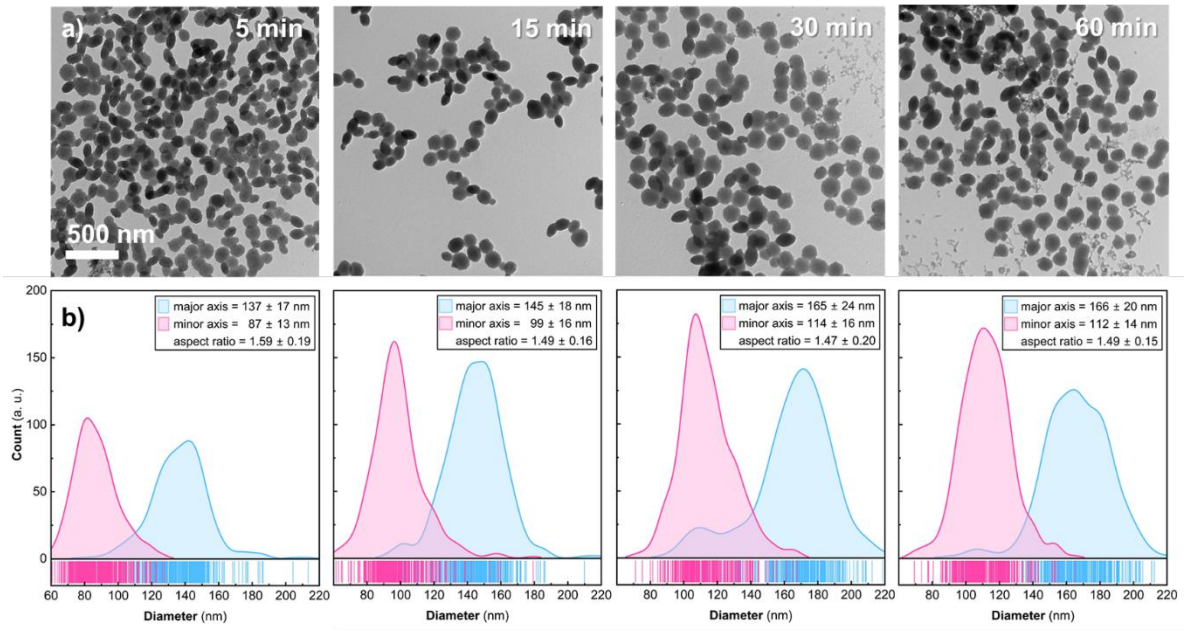


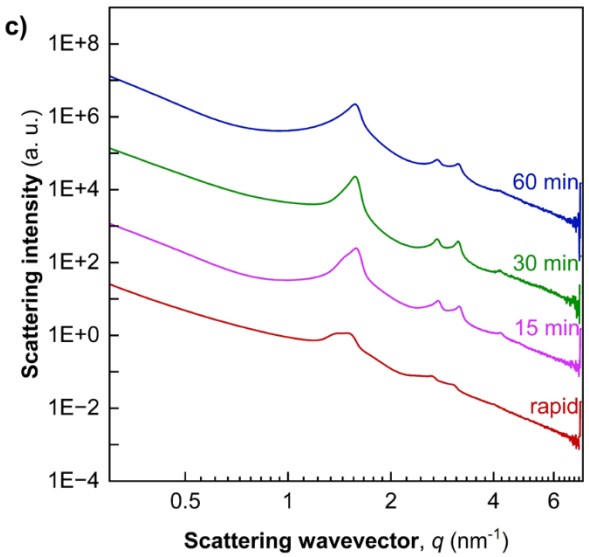

*Figure 5.10 The TEM images of silica particles under different experimental conditions (a) at different temperatures of 25 ˚C, 30 ˚C, and 60 ˚C, [$NH_4OH$] is 0.056 M; pH = 9 – 10, (the line is a guide for the eye) and (b) at different ammonia concentrations, [$NH_4OH$] of 0.034, 0.056,*

*and 0.084M, respectively. [CTAB] = 3.6 mM, [L-tyrosine] = 3.8 mM, [$H_2O$] = 54.0 M, [TEOS] = 0.088 M, reaction time = 1 h, T = (20 ± 4) ˚C, and stirring rate = 250 rpm. The scale bar represents 500 nm in both figure panels. The histogram is based on 300 particle counts.*

In summary, the increase in temperature triggered the acceleration of the hydrolysis and condensation, and the particle size decreased. Also, the increase in pH triggered the acceleration of the condensation, and the particle size increased. Thus, it is not the TEOS hydrolysis and condensation rate that impacts primary seed aggregation into an elliptical particle.

The effect of TEOS addition rate on the aspect ratio of the silica particles has been investigated, varying between 5 and 60 min. The slow addition rate is meant to favor particle growth over particle nucleation[21,25]. We observe that the aspect ratio varies little between the addition rates, with 1.6 for a fast addition rate and 1.5 for a slow addition rate. Figure 5.11a shows that particles that appear spherical in the 2D projection display lighter contrast probably because they are lying flat and are oblate ellipsoids, while particles that appears in darker contrast are prolate ellipsoids because they are lying on the edge.






d)

| TEOS addition rate (min) | $d_{c\text{-}c}$ of the hexagonal array (center-to-center distance, nm) |
|---|---|
| Rapid | 4.73 |
| 15 | 4.54 |
| 30 | 4.58 |
| 60 | 4.58 |

*Figure 5.11 (a) The TEM images of silica particles synthesized at different TEOS addition rates ($R_{TEOS}$). The $R_{TEOS}$ (addition time) are 27 mL $h^{-1}$ (5 min), 9 mL $h^{-1}$ (15 min), 4.5 mL $h^{-1}$ (30 min), and 2.25 mL $h^{-1}$ (60 min), respectively, for $V_{TEOS}$ = 2.25 mL. (b) The corresponding size distribution of the synthesized particles at different addition rates. [CTAB] = 3.6 mM, [L-tyrosine] = 3.7 mM, [TEOS] = 0.088 M, [$H_2O$] = 54.0 M, [$NH_4OH$] = 0.056 M; pH = 11 – 12, reaction time = 1 h, T = (25 ± 2) ˚C, and stirring rate = 250 rpm. Histograms are based on 300 particle counts. (c) The Small angle X-ray scattering (SAXS) of particles synthesized at different TEOS addition rates ($R_{TEOS}$). The $R_{TEOS}$ (addition time) are 27 mL $h^{-1}$ (5 min), 9 mL $h^{-1}$ (15 min), 4.5 mL $h^{-1}$ (30 min), and 2.25 mL $h^{-1}$ (60 min), respectively, for $V_{TEOS}$ = 2.25 mL. [CTAB] = 3.59 mM, [L-tyrosine] = 3.68 mM, [TEOS] = 0.088 M, [$H_2O$] = 53.93 M, [$NH_4OH$] = 0.0557 M; pH = 11 – 12, reaction time = 1 h, T = (25 ± 2) ˚C, and stirring rate = 250 rpm. c) corresponding center-to-center distance. The data have been rescaled for better visibility.*

To verify that the augmentation in particle size/aspect ratio is due to slow addition rather than longer particle aging, we observed particles aged for 24 h. We found that the aspect ratio had not changed (Figure 5.12). Particle size increases significantly with a slower TEOS addition, increasing from 137 ± 17 nm (major axis) × 87 ± 13 nm (minor axis) to 166 ± 20 nm (major axis) × 112 ± 14 nm (minor axis), and the aspect ratio from 1.6 ± 0.2 – 1.5 ± 0.2.

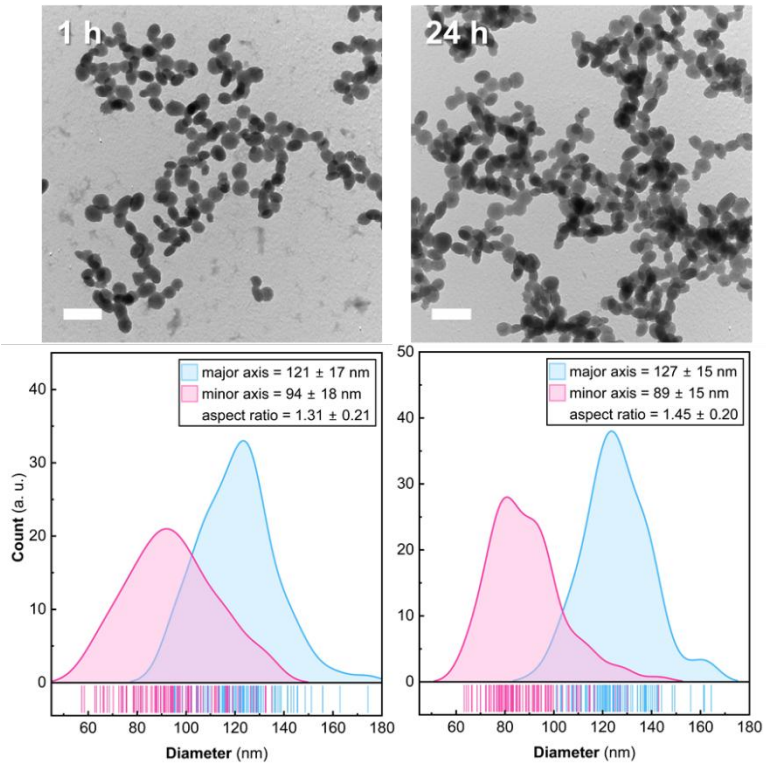



*Figure 5.12 The TEM images of silica particles aged for 24 h. [CTAB] = 3.59 mM, [L-tyrosine] = 3.77 mM, [$H_2O$] = 53.93 M, [TEOS] = 0.088 M, [$NH_4OH$] = 0.056 m, reaction time = 1 h, T = (20 ± 4) ˚ C, and stirring rate = 250 rpm. The scale bar represents 200 nm in all micrographs.*

### 5.4.4 Formation mechanism of the ellipsoidal silica particles

We have found three proposed synthesis mechanisms for the formation of the ellipsoidal shape in the literature. First, we examine the hypothesis put forward by Meoto, S., *et al.*[10], i.e., that shear from stirring is responsible for the elliptical structure. We calculate the tumbling time (i.e., the time taken to reorient the particle by a certain angle) using Perrin's formula approach (see details in annexe 5.1)[27–30]. The tumbling times along the major and minor axes were calculated to be 18.6 and 37 ms, respectively. Intuitively, it seems like the particles are tumbling moderately fast compared to the stirring rate, so shear should have an isotropic effect on the particles.

However, to experimentally test this mechanism, we have varied the stirring rate between 250 – 1000 rpm as shown in Figure 5.13. The resulting changes to aspect ratio are insignificant, from 1.5 ± 0.1 to 1.6 ± 0.2. Thus, shear is not responsible for the anisotropic form. However, we do see a change in the particle size as a function of stir rate. The particle size decreased from 156 ± 19 nm (major axis) × 105 ± 14 nm (minor axis) to 133 ± 18 nm (major axis) × 87 ± 15 nm (minor axis) with stirring rate from 250 to 1000 rpm (Figure 5.12b). Similar observations

have been found in other studies, showing that a higher stirring rate can produce smaller silica sizes,[26] due to the increased TEOS hydrolysis rate.

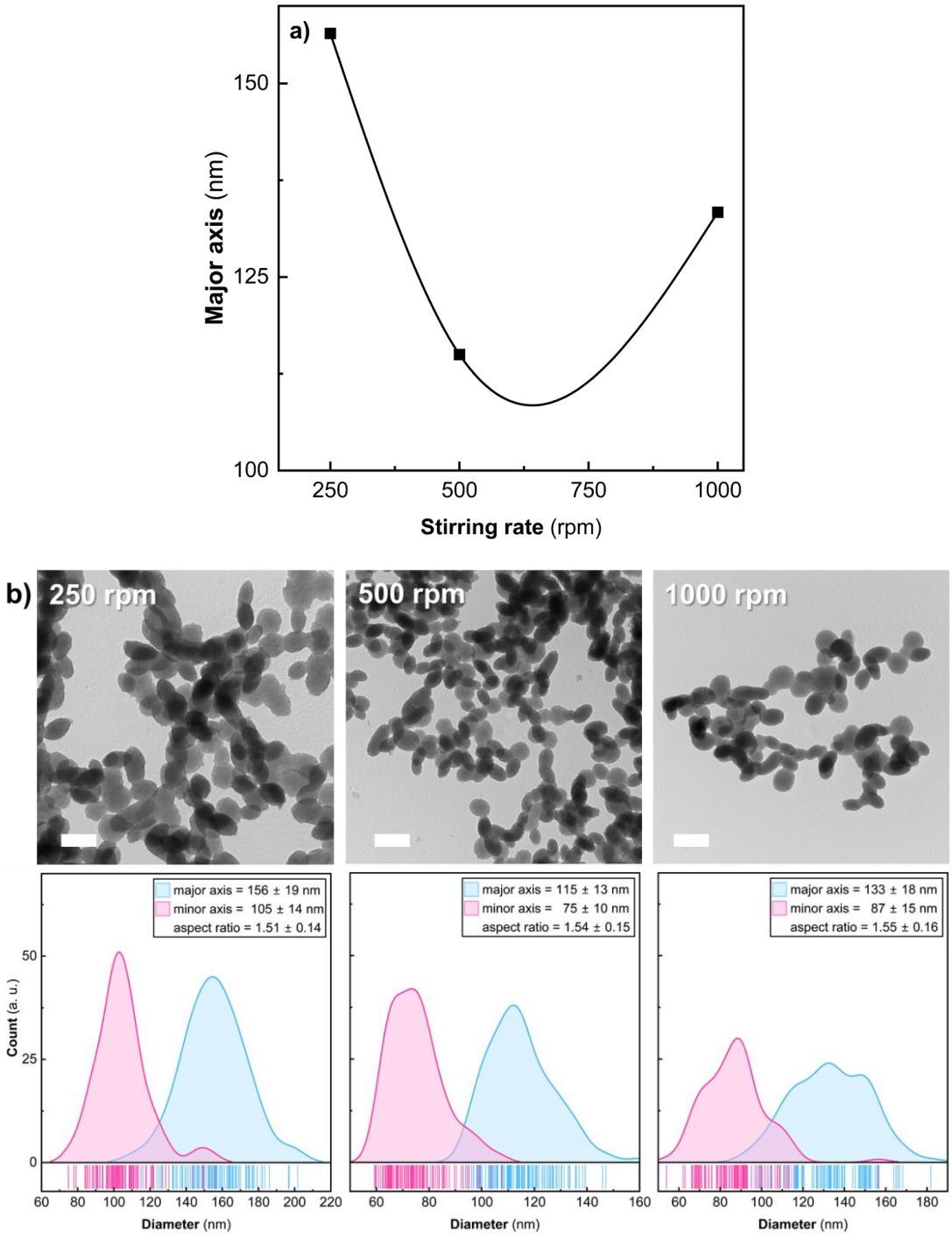



*Figure 5.13 (a) The plot of the dependence of particle dimension on the stirring rate. The line is a guide for the eye. (b) The TEM images of silica particles synthesized at different stirring rates. The stirring rates are 250, 500, and 1000 rpm. [CTAB] = 3.6 mM, [L-tyrosine] = 3.7 mM, [TEOS] = 0.088 M, [$H_2O$] = 54.0 M, [$NH_4OH$] = 0.056 M; pH = 9 – 10, reaction time = 1 h, and T = (25 ± 2) ˚C. This is based on 100 particle counts.*

The second hypothesis found in the literature proposes differences in the surface tension forces on the forming silica particle[12]. However, by adding surfactants, no observable difference in aspect ratio was observed. The aspect ratio remained steady at 1.6 while varying the CTAB concentration from 1.2 to 3.6 mM (Figure 5.7), and adding PVP changed the aspect ratio from 1.6 ± 0.2 to 1.4 ± 0.1 (Figure 5.8). Thus, surface tension forces do not seem to be the most significant contributing factor.

Travaglini, L., *et al.*[13] found a relationship between micelle nanostructure and silica particle formation.[13] We found no variation in aspect ratio, particle size, or form by varying CTAB concentration (Figure 5.7). From Figure 5.3, we see that the cylindrical alignment of the mesostructure is parallel to the minor axis of the ellipsoids, which is counterintuitive if the hexagonal mesostructure is responsible for an elongated axis. To test the relationship between CTAB concentration, mesostructure, and particle shape, silica particles with different CTAB concentrations of 1.75, 3.59, and 7.00 mM without L-tyrosine were produced. The results in Figure 5.14 showed that, without L-tyrosine, spherical to short rod-like particles are formed.

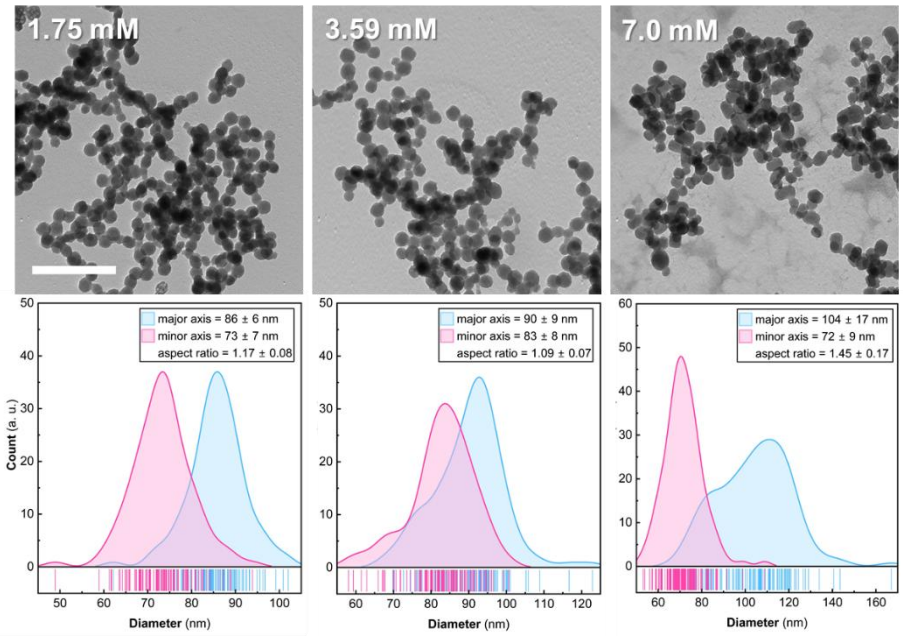
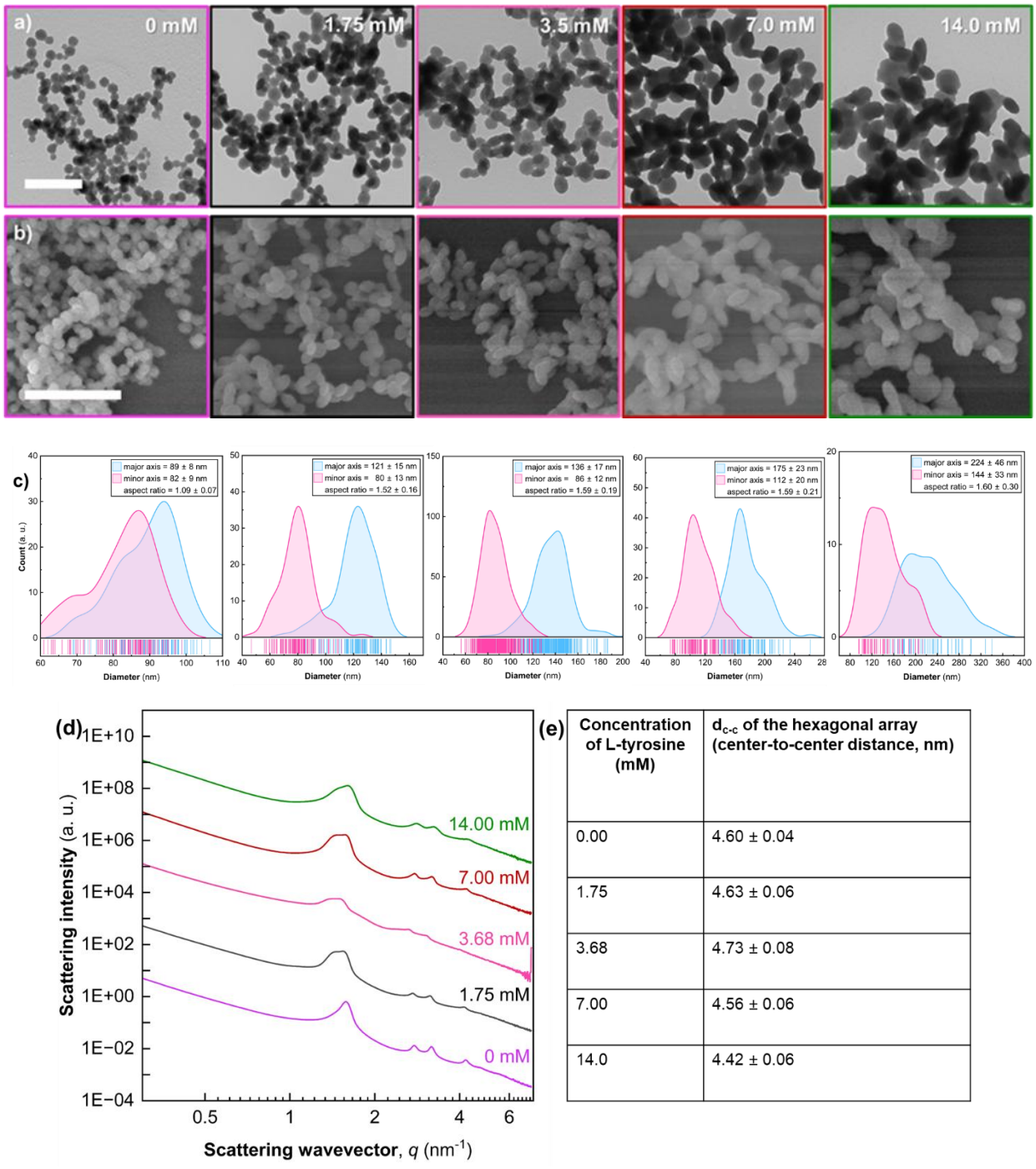



*Figure 5.14 The TEM images of silica particles synthesized at different CTAB concentrations, [CTAB]. The [CTAB] are 1.75, 3.59, and 7.0 mM, respectively. [TEOS] = 0.088 M, [$H_2O$] = 53.93 M, [$NH_4OH$] = 0.056 M; pH = 10 – 11, reaction time = 1 h, T = (25 ± 2) ˚C, and stirring rate = 250 rpm. The scale bars represent 500 nm in all micrographs.*

The other possible influence on mesostructure is the quantity of L-tyrosine. Thus, we altered the L-tyrosine concentration between 0 – 14 mM. This co-surfactant heavily impacts the size and shape of the particles (Figure 5.15a–c), with the d-spacing of the mesostructure varying

between 4.4 – 4.7 nm (Figure 5.15d–e), with the micellar organization corresponding to hexagonal packing and a mixture of hexagonal and wormhole mesopores. Thus, in the case of the elliptical structures presented here, micelle structure cannot be readily accredited with particle anisotropy.




(e)

| Concentration of L-tyrosine (mM) | $d_{c-c}$ of the hexagonal array (center-to-center distance, nm) |
|---|---|
| 0.00 | 4.60 ± 0.04 |
| 1.75 | 4.63 ± 0.06 |
| 3.68 | 4.73 ± 0.08 |
| 7.00 | 4.56 ± 0.06 |
| 14.0 | 4.42 ± 0.06 |

*Figure 5.15 (a) TEM images (b) SEM images (c) size distributions of silica particles synthesized at different L-tyrosine concentrations: 0, 1.75, 3.68, 7.0, and 14.0 mM and [CTAB] = 3.7 mM, [TEOS] = 0.088 M, [$H_2O$] = 54.0 M, [$NH_4OH$] = 0.056 M; pH = 10 – 11, reaction time = 1*

*h, T = (25 ± 2) ˚C, and stirring rate = 250 rpm. The scale bars represent 500 nm (TEM) and 750 nm (SEM) in the micrographs. (d) Small-angle X-ray scattering (SAXS) of particles at different concentrations of L-tyrosine and (e) corresponding center-to-center distance between cylindrical pores. The data have been vertically rescaled for better visibility.*

The only parameter among those we have studied that significantly impacts particle shape and size is the quantity of L-tyrosine. In the TEM and SEM images, we see that in the absence of L-tyrosine, the silica particles are spherical. With the addition of a small amount of L-tyrosine (1.75 mM), elliptical particles are formed. The quantity of prolate ellipsoids seems to increase as the quantity of L-tyrosine increases, but it is hard to determine the exact ratio as prolate and oblate particles cannot be differentiated when the oblate particles are resting on their minor axis. The particle size changed from 89 ± 8 nm (major axis) × 82 ± 9 nm (minor axis) at 0 mM of L-tyrosine to 224 ± 46 nm (major axis) × 144 ± 33 nm (minor axis) at 14 mM of L-tyrosine, with aspect ratio changing from 1.1 ± 0.1 to 1.6 ± 0.3 (Figure 5.14c). It is, however, still unclear exactly how L-tyrosine encourages anisotropic growth, and computational studies should be applied to explore possible silica particle surface-L-tyrosine interactions.

### 5.4.5 Magnesiothermic reduction of the particles

Having investigated the effect of the reaction parameters on the formation of the ellipsoidal silica particles, we then attempted to reduce the particles to elemental Si through the magnesiothermic reduction using flakes of magnesium homogeneously grounded with the dried silica particle powder. Figure 5.16 shows the powder XRD patterns of the resulting product. Comparing the two reduction conditions of 500 °C for 12h and 650 °C for 2h, the amount of Si increases with increasing reaction temperature, as evidenced by the increased intensities of peaks at 28.5°, 47.4°, 56.1°, 69.1°, 76.5°, 88.3°, and 95.1° corresponding to the (111), (220), (311), (400), (331), (422), and (511) crystal planes of diamond structured Si, respectively[31]. At the melting point of Mg (650 °C), the reaction appears to proceed at a faster rate, as evidenced by the significantly higher XRD intensity after 2h compared to the intensity at 500 °C after 12h. Under these two reaction conditions, the amount of silica seems to have significantly reduced, as the broad amorphous silica peak at $2\theta = 22°$ is not present. The removal of byproducts was also confirmed from the XRD patterns, as no peaks could be assigned to either a Mg residue, MgSi, or MgO.

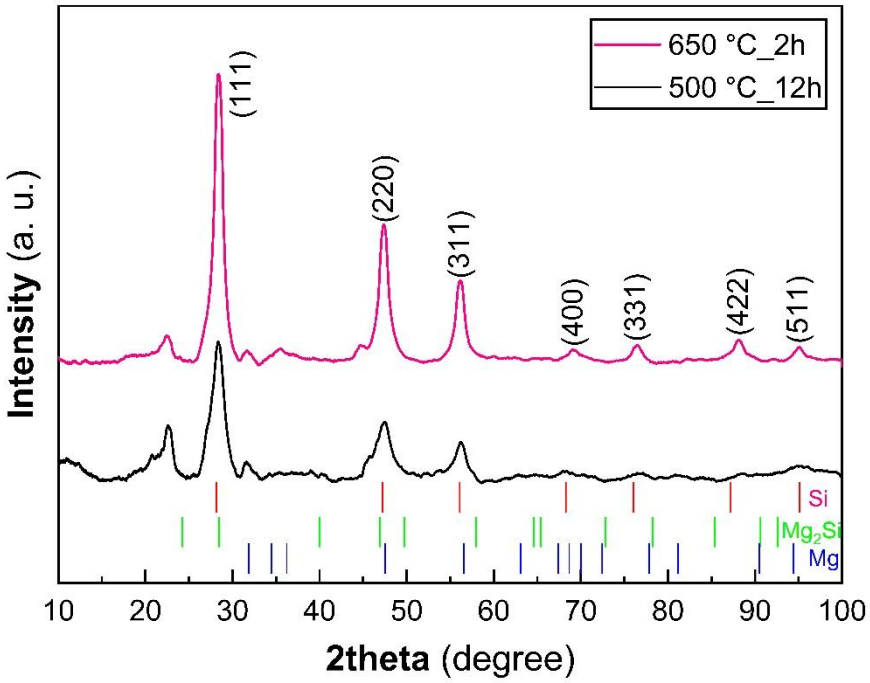



*Figure 5.16 Powder XRD patterns of the products obtained from magnesiothermic reduction of the ellipsoidal silica particles at different temperatures and times.*

Figure 5.17 shows the TEM images of the Mg-reduced ellipsoidal silica particles. There is a significant loss of structural morphology and a large increase in porosity for the annealing products processed at 650 °C for 2h compared to those at 500 °C for 12h. There is a significant quantity of unreduced particles at 500 °C for 12h. It is well known that Mg reduction can lead to a 70 vol% increase in porosity, which can explain the fractured appearance of these particles. The loss of morphological integrity, combined with the high degree of porosity, means that these anisotropic silicon particles make poor meta-atoms. Optical characterization of the reduced materials was not attempted, they are not dense enough to be promising candidates for Mie resonant building-blocks.

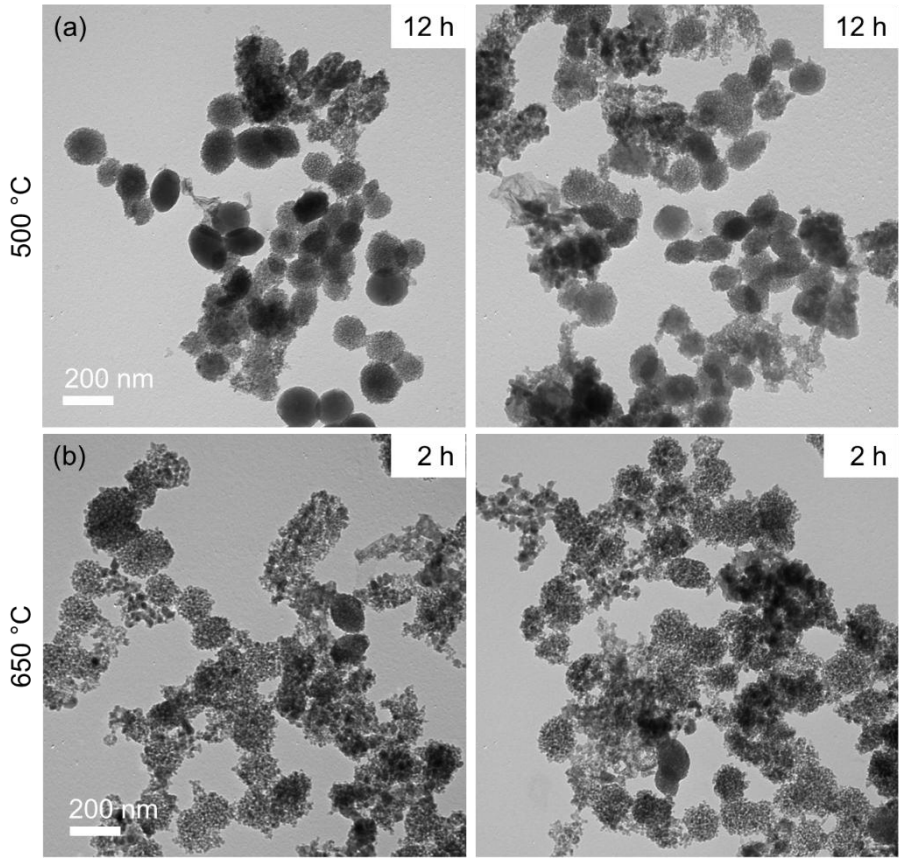



*Figure 5.17 TEM images of the ellipsoidal silica particles reduced with Mg at (a) 500 °C for 12h, and (b) 650 °C for 2h*

## 5.5 Conclusions and perspectives

Our study of the sol-gel synthesis of anisotropic silica particles demonstrates that L-tyrosine acts as a critical morphology-directing agent for ellipsoidal silica particles, with minimal influence from shear or micellar structure. A typical synthesis of ellipsoidal particles has a major axis of 137 ± 17 nm and a minor axis of 87 ± 13 nm, and an average aspect ratio of 1.6. The aspect ratio could be varied between 1.0 and 1.6. The reactions carried out under varying CTAB concentration, with no L-tyrosine, only formed spherical to rod-like particles. With increased concentrations of L-tyrosine, the particles transitioned from isotropic spherical particles to anisotropic prolate and oblate ellipsoidal particles with increased dimensions.

Furthermore, we show that optical levitation offers a method for precise 3D particle characterization. By examining the drag coefficient of optically trapped anisotropic particles, the 3D physical dimensions of a particle can be ascertained, a difficult task with TEM/SEM images without resorting to tomography. Thus, levitodynamics offers an alternative approach to determining particle morphology and a complementary method to traditional microscopy and

physical characterization. The dimensions of individual ellipsoidal silica particles were measured using optical trapping. A typical particle dimensions were measured to be: $d_x$ = 172 ± 11 nm, $d_y$ = 106 ± 6 nm, and $d_z$ = 117 ± 5 nm; with an aspect ratio of 1.62.

Previously proposed formation mechanisms cannot be used to explain the anisotropy observed in this system. The L-tyrosine is likely interacting with the surface of the silica, but not impacting the mesostructure organization. We characterized the mesostructure of the particles using small-angle x-ray scattering, which showed that the distance between centers of adjacent cylinders ($d_{c\text{-}c}$) is on average 4.6 nm, with a main peak at q = 1.63 $nm^{-1}$, indicating a mixture of hexagonal and wormhole structures. Dynamic light scattering analysis revealed that the colloidal particles have a low degree of aggregation in suspension. The magnesiothermic reduction technique successfully reduced the synthesized ellipsoidal silica particles to elemental Si particles. However, there are several challenges to this approach. The magnesium vapor is inhomogeneously distributed within the reactor, which caused inhomogeneous reduction of the particles. The high degree of porosity, particle sintering, and fracturing make this technique inappropriate for the preparation of meta-atoms. Therefore, these challenges must be overcome before metallothermic reduction can be a preomising method to produce ellipsoidal silicon as meta-atoms.

## Annexe 1. Tumbling time calculation from Perrin's formula

Hydrodynamic diameter ($d_H$) = 337 nm

Aspect ratio (TEM) = 1.51

Viscosity of ethanol ($\eta$) = 0.0011941 Pa s

Boltzmann constant ($k_B$) = $1.380649 \times 10^{-23}$ $JK^{-1}$

Temperature (T) = 293 K

Radius, $r_s$ = Hydrodynamic radius = 168.5 nm

It was assumed that the hydrodynamic diameter corresponds to the diameter of a volume-equivalent sphere, so the ellipsoid has the same volume as a sphere of radius, $r_s$

For a prolate ellipsoid:

$$V = \frac{4}{3}\pi ab^2 = \frac{4}{3}\pi r_s^3 \quad (1)$$

Where $a = Rb$, ($R$ = aspect ratio; $a$ = long axis; $b$ = short axis), substituting into (1) gives:

$$b = r_s R^{-\frac{1}{3}} \quad (2)$$

*Where* $a$ = 168.5 nm*;* $b$ = 112.5 nm; and R = 1.49 ≈ 1.5

From Perrin's formula for a **prolate ellipsoid**, the rotational diffusion can be calculated along the major and minor semi-axes[27–30].

Rotational diffusion about the **minor axis**, $D_r^{\perp}$:

$$D_r^{\perp} = \frac{3k_BT}{16\pi\eta a^3} \times \frac{R^2-1}{R^3}\left[R - \frac{R^2-1}{2}\,In\left(\frac{R+1}{R-1}\right)\right]^{-1} = 13.4\ s^{-1} \quad (3)$$

Tumbling time about the minor axis:

$$\tau_r = \frac{1}{2D_r^{\perp}} = 37\ ms \quad (4)$$

Rotational diffusion about the **major axis**, $D_r^{\parallel}$:

$$D_r^{\parallel} = \frac{3k_BT}{8\pi\eta b^3} \times \frac{R^2-1}{R^3}\left[-R + \frac{R^2-1}{2}\,In\left(\frac{R+1}{R-1}\right)\right]^{-1} = 26.9\ s^{-1} \quad (5)$$

Tumbling time about the major axis:

$$\tau_r^{\parallel} = \tau_r = \frac{1}{2D_r} = 18.6\ ms \quad (6)$$

For a sphere, the rotational diffusion coefficient is given by the Stokes-Einstein-Debye relation:

$$D_r = \frac{k_BT}{8\pi\eta r_s^3} = 28.2\ s^{-1} \quad (7)$$

$$\tau_r = \frac{1}{2D_r} = 17.7\ ms \quad (8)$$

## References


(1) Wang, Z.; An, N.; Shen, F.; Zhou, H.; Sun, Y.; Jiang, Z.; Han, Y.; Li, Y.; Guo, Z. Enhanced Forward Scattering of Ellipsoidal Dielectric Nanoparticles. *Nanoscale Res. Lett.* **2017**, *12* (1), 58. https://doi.org/10.1186/s11671-016-1794-x.

(2) Fu, Y. H.; Kuznetsov, A. I.; Miroshnichenko, A. E.; Yu, Y. F.; Luk'yanchuk, B. Directional Visible Light Scattering by Silicon Nanoparticles. *Nat. Commun.* **2013**, *4* (1), 1527. https://doi.org/10.1038/ncomms2538.

(3) Hao, N.; Li, L.; Tang, F. Roles of Particle Size, Shape and Surface Chemistry of Mesoporous Silica Nanomaterials on Biological Systems. *Int. Mater. Rev.* **2017**, *62* (2), 57–77. https://doi.org/10.1080/09506608.2016.1190118.

(4) Dawi, E. A.; Mustafa, E.; Siahaan, T. Anisotropic Deformation of Colloidal Particles under 4 MeV Cu Ions Irradiation. *Mater. Res. Express* **2022**, *9* (8), 086506. https://doi.org/10.1088/2053-1591/ac87ef.

(5) Penninkhof, J. J.; Van Dillen, T.; Roorda, S.; Graf, C.; Van Blaaderen, A.; Vredenberg, A. M.; Polman, A. Anisotropic Deformation of Metallo-Dielectric Core–Shell Colloids under MeV Ion Irradiation. *Nucl. Instrum. Methods Phys. Res. Sect. B Beam Interact. Mater. At.* **2006**, *242* (1–2), 523–529. https://doi.org/10.1016/j.nimb.2005.08.116.

(6) Deng, T.; Cournoyer, J. R.; Schermerhorn, J. H.; Balch, J.; Du, Y.; Blohm, M. L. Generation and Assembly of Spheroid-like Particles. *J. Am. Chem. Soc.* **2008**, *130* (44), 14396–14397. https://doi.org/10.1021/ja805278x.

(7) Benke, D.; Feller, T.; Krüsmann, M.; Neuhöfer, A. M.; Ganster, F.; Karg, M.; Retsch, M. Prolate Spheroidal Polystyrene Nanoparticles: Matrix Assisted Synthesis, Interface Properties, and Scattering Analysis. *Soft Matter* **2023**, *19* (46), 9006–9016. https://doi.org/10.1039/D3SM01002C.

(8) Champion, J. A.; Katare, Y. K.; Mitragotri, S. Making Polymeric Micro- and Nanoparticles of Complex Shapes. *Proc. Natl. Acad. Sci.* **2007**, *104* (29), 11901–11904. https://doi.org/10.1073/pnas.0705326104.

(9) Xu, S.; Nie, Z.; Seo, M.; Lewis, P.; Kumacheva, E.; Stone, H. A.; Garstecki, P.; Weibel, D. B.; Gitlin, I.; Whitesides, G. M. Generation of Monodisperse Particles by Using Microfluidics: Control over Size, Shape, and Composition. *Angew. Chem. Int. Ed.* **2005**, *44* (5), 724–728. https://doi.org/10.1002/anie.200462226.

(10) Meoto, S.; Kent, N.; Nigra, M. M.; Coppens, M.-O. Effect of Stirring Rate on the Morphology of FDU-12 Mesoporous Silica Particles. *Microporous Mesoporous Mater.* **2017**, *249*, 61–66. https://doi.org/10.1016/j.micromeso.2017.04.045.

(11) Yu, C.; Fan, J.; Tian, B.; Zhao, D. Morphology Development of Mesoporous Materials: A Colloidal Phase Separation Mechanism. *Chem. Mater.* **2004**, *16* (5), 889–898. https://doi.org/10.1021/cm035011g.

(12) Zhang, H.; Bandosz, T. J.; Akins, D. L. Template-Free Synthesis of Silica Ellipsoids. *Chem. Commun.* **2011**, *47* (27), 7791. https://doi.org/10.1039/c1cc11787d.

(13) Travaglini, L.; De Cola, L. Morphology Control of Mesoporous Silica Particles Using Bile Acids as Cosurfactants. *Chem. Mater.* **2018**, *30* (12), 4168–4175. https://doi.org/10.1021/acs.chemmater.8b01873.

(14) Hao, N.; Li, L.; Tang, F. Facile Preparation of Ellipsoid-like MCM-41 with Parallel Channels along the Short Axis for Drug Delivery and Assembly of Ag Nanoparticles for Catalysis. *J. Mater. Chem. A* **2014**, *2* (30), 11565. https://doi.org/10.1039/C4TA01820F.

(15) Hao, N.; Nie, Y.; Tadimety, A.; Closson, A. B.; Zhang, J. X. J. Microfluidics-Mediated Self-Template Synthesis of Anisotropic Hollow Ellipsoidal Mesoporous Silica Nanomaterials. *Mater. Res. Lett.* **2017**, *5* (8), 584–590. https://doi.org/10.1080/21663831.2017.1376720.

(16) Yamada, H.; Urata, C.; Higashitamori, S.; Aoyama, Y.; Yamauchi, Y.; Kuroda, K. Critical Roles of Cationic Surfactants in the Preparation of Colloidal Mesostructured Silica Nanoparticles: Control of Mesostructure, Particle Size, and Dispersion. *ACS Appl. Mater. Interfaces* **2014**, *6* (5), 3491–3500. https://doi.org/10.1021/am405633r.

(17) Bellando, L.; Kleine, M.; Amarouchene, Y.; Perrin, M.; Louyer, Y. Giant Diffusion of Nanomechanical Rotors in a Tilted Washboard Potential. *Phys. Rev. Lett.* **2022**, *129* (2), 023602. https://doi.org/10.1103/PhysRevLett.129.023602.

(18) Gonzalez-Ballestero, C.; Aspelmeyer, M.; Novotny, L.; Quidant, R.; Romero-Isart, O. Levitodynamics: Levitation and Control of Microscopic Objects in Vacuum. *Science* **2021**, *374* (6564), eabg3027. https://doi.org/10.1126/science.abg3027.

(19) Farjadian, F.; Roointan, A.; Mohammadi-Samani, S.; Hosseini, M. Mesoporous Silica Nanoparticles: Synthesis, Pharmaceutical Applications, Biodistribution, and Biosafety Assessment. *Chem. Eng. J.* **2019**, *359*, 684–705. https://doi.org/10.1016/j.cej.2018.11.156.

(20) Catalano, F.; Pompa, P. P. Design Rules for Mesoporous Silica toward the Nanosize: A Systematic Study. *ACS Appl. Mater. Interfaces* **2019**, *11* (50), 47237–47246. https://doi.org/10.1021/acsami.9b16135.

(21) Bogush, G. H.; Zukoski, C. F. Uniform Silica Particle Precipitation: An Aggregative Growth Model. *J. Colloid Interface Sci.* **1991**, *142* (1), 19–34. https://doi.org/10.1016/0021-9797(91)90030-C.

(22) Manon Barrière. Study of Nanomaterials in Levitodynamics, 2025. https://theses.hal.science/tel-05281164v1.

(23) Amarouchene, Y.; Mangeat, M.; Montes, B. V.; Ondic, L.; Guérin, T.; Dean, D. S.; Louyer, Y. Nonequilibrium Dynamics Induced by Scattering Forces for Optically Trapped Nanoparticles in Strongly Inertial Regimes. *Phys. Rev. Lett.* **2019**, *122* (18), 183901. https://doi.org/10.1103/PhysRevLett.122.183901.

(24) Zhang, X.; Niu, Y.; Yang, Y.; Li, Y.; Zhao, J. Preparation and Magnetic Properties of γ-$Fe_2O_3$@$SiO_2$ Core Shell Ellipsoids with Different Aspect Ratios. *New J. Chem.* **2014**, *38* (9), 4351. https://doi.org/10.1039/C4NJ00389F.

(25) Wang, F.; Richards, V. N.; Shields, S. P.; Buhro, W. E. Kinetics and Mechanisms of Aggregative Nanocrystal Growth. *Chem. Mater.* **2014**, *26* (1), 5–21. https://doi.org/10.1021/cm402139r.

(26) Yokoi, T.; Wakabayashi, J.; Otsuka, Y.; Fan, W.; Iwama, M.; Watanabe, R.; Aramaki, K.; Shimojima, A.; Tatsumi, T.; Okubo, T. Mechanism of Formation of Uniform-Sized Silica Nanospheres Catalyzed by Basic Amino Acids. *Chem. Mater.* **2009**, *21* (15), 3719–3729. https://doi.org/10.1021/cm900993b.

(27) Perrin, F. Mouvement Brownien d'un Ellipsoide - I. Dispersion Diélectrique Pour Des Molécules Ellipsoidales. *J. Phys. Radium* **1934**, *5* (10), 497–511. https://doi.org/10.1051/jphysrad:01934005010049700.

(28) Happel, J.; Brenner, H. *Low Reynolds Number Hydrodynamics: With Special Applications to Particulate Media*; Moreau, R. J., Series Ed.; Mechanics of fluids and transport processes; Springer Netherlands: Dordrecht, 1983; Vol. 1. https://doi.org/10.1007/978-94-009-8352-6.

(29) Kuipers, B. W. M.; Van De Ven, M. C. A.; Baars, R. J.; Philipse, A. P. Simultaneous Measurement of Rotational and Translational Diffusion of Anisotropic Colloids with a New Integrated Setup for Fluorescence Recovery after Photobleaching. *J. Phys. Condens. Matter* **2012**, *24* (24), 245101. https://doi.org/10.1088/0953-8984/24/24/245101.

(30) Varma, V. A.; Malhotra, I.; Babu, S. B. Enhancement in the Diffusivity of Brownian Spheroids in the Presence of Spheres. *Phys. Rev. E* **2022**, *106* (1), 014602. https://doi.org/10.1103/PhysRevE.106.014602.

(31) Lai, Y.; Thompson, J. R.; Dasog, M. Metallothermic Reduction of Silica Nanoparticles to Porous Silicon for Drug Delivery Using New and Existing Reductants. *Chem. – Eur. J.* **2018**, *24* (31), 7913–7920. https://doi.org/10.1002/chem.201705818.

# General conclusions and perspectives

To fabricate a silicon-based metasurface with perfect light transmission in the visible/near-infrared region, the top-down approach of silicon nano-disks, cylinders, and pillars is usually used. An alternative to this is the self-assembly of bottom-up fabricated spherical silicon particles. In the introductory chapter, we highlighted the progress made in the bottom-up fabrication of large-area metasurfaces. However, the bottom-up fabrication of silicon-based nanostructures, which offers improved forward scattering light and scale-up potential for the production of metasurfaces, is still limited. In this project, the ambition was to experimentally explore the potential of spherical silicon-based core-shell particles and shape anisotropies to enhance forward scattering light, as theoretically revealed. In this thesis, three different predictions were considered: (i) improving the forward directional light scattering and mode hybridization with spherical silicon particles coated with plasmonic gold particles, (ii) improving the overlap between the electric and magnetic dipole resonances that enhances directional forward light scattering by ellipsoidal silicon particles, and (iii) directional light scattering by silicon nanowires.

We demonstrated the colloidal synthesis of Si@Au core-shell nanostructures. We created the shell by chemically attaching Au seeds to the Si core particles in solution. We experimentally produced both single and double coatings of AuNPs around Si spheres, finding a homogeneous thickness of ~4 and ~7 nm, respectively. The surface coverage was estimated to be ~ 50 %, based on comparison with simulated scattering spectra. While the shells were not continuous, these particulate shell particles were optically characterized with dark-field optical microscopy, single particle backscattering spectroscopy, and EELS to understand the scattering behavior and the interactions between plasmonic and Mie resonances. The optical spectra of individual core-shell particles were highly consistent between similarly-sized particles, because of the highly spherical shape of the Si core and the very thin, homogeneous Au coating. These experimental spectra could be accurately reproduced by the T-matrix simulation due to the high quality of the experimental nanostructures. We learned that the forward scattering of the particulate core-shell particles was slightly improved for all diameters within the 100 – 200 nm range, but not as much as had been previously predicted in the literature. Our study also revealed that an ideal Au shell would need to be continuous and thin ($\lesssim$ 12 nm) for the optimal forward scattering. However, even in the case of a potential continuous Au shell, the gains in dipole overlap are associated with strongly decreased resonance amplitude. This led to our

collaborators investigating other core-shell systems, in which they discovered shell materials of silver (Ag), silicon dioxide ($SiO_2$), titanium dioxide ($TiO_2$), zirconium dioxide ($ZrO_2$), and silicon nitride ($Si_3N_4$) with an optimal thickness of 4, 92, 57, 70, and 65 nm, respectively, to be suitable to enhance directional forward scattering of the Si core.

Therefore, preliminary studies on other shell materials, such as Ag and $SiO_2$, were explored. The synthesis of the Ag shell was investigated using a multi-step colloidal approach[1]. We functionalized the Si particles with a native oxide shell with $Sn^{2+}$ using a mixture of $SnCl_2$ and HCl, as described in protocol 1. The particles were functionalized with $Sn^{2+}$ to ensure a high density of Ag seeds on their surface. This is important for forming a thin homogeneous shell. Following this, the $Sn^{2+}$ functionalized particles were directly added to a concentrated Tollen's solution to directly reduce Ag seeds onto the surface of the particles (protocol 2). The formation of the Ag shell was achieved by reducing silver nitrate through the successive addition of formaldehyde and ammonia to a diluted dispersion of the Ag-seeded particles (protocol 3). From the TEM images, we observed particles with percolated and discontinuous shells (Figure 6.1a-d). Also, silver particles were observed as by-products, possibly resulting from the regrowth of the detached Ag-seeds in the dispersion. It has been reported that the regrowth of sparsely deposited Ag seeds results in large shells, which could explain why the shell was not continuous [1,2]. Another major challenge is the rapid oxidation of the Ag seeds due to their low chemical stability. Ultimately, due to the inhomogeneous shells and the rapid oxidation, we were unable to study these objects using darkfield microscopy, as we did for the particulate gold coatings. The synthesis of thin, continuous Au or Ag shells around Si core particles is thus extremely challenging. This was attributed to the poor wettability of these metals on the surface of the Si core particles.

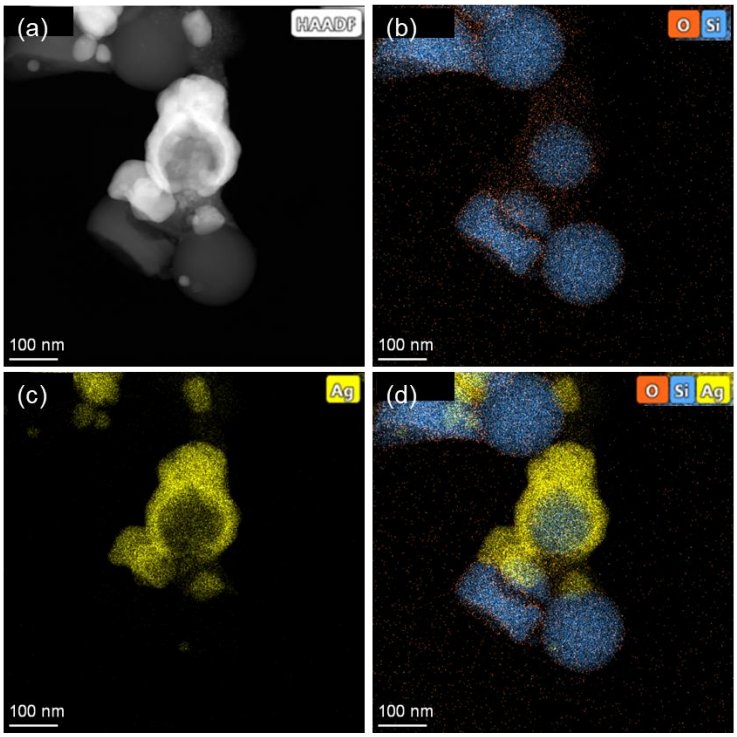



*Figure 6.1 (a) High-angle annular darkfield (HAADF) image (b-d) TEM/EDS elemental mapping of the core Si (dark-blue) and Ag shell (yellow). The scale bar represents 100 nm.*

However, a dielectric shell could be a promising alternative, as we can grow silica shells of ideal simulation-predicted thickness around the Si particles. The synthesized shell thickness ranges from 105 – 215 nm. The polydispersity of the core Si and shell thickness is suitable for studying the optical scattering properties of single particles. Compared to the known fabrication method by thermal oxidation, which faces aggregation challenges, this is the first time a batch colloidal approach has been established to fabricate core-shell Si@$SiO_2$ particles with this controlled shell thickness and morphology.

The formation of the silica shell was carried out in a single-step colloidal approach. This was based on the synthesis approach established for the regrowth of silica particles, first published by Hartlen et al.[3] and optimized by Désert et al.[4,5]. The hydrolysis and condensation of the silica precursor on the surface of the Si particles were conducted in a mixture of ethanol and ammonia. The silica precursor mixed with ethanol was added to the mixture at a specific rate. The ammonia acts as a base catalyst to enhance the hydrolysis and condensation of the silica precursor. The dilution of the silica precursor with ethanol ensures better dispersion, controlled hydrolysis, and uniform shell growth. Figures 6.2a-d show the HAADF image and elemental mapping of the sample from which we could observe core-shell particles, but also secondary nucleated silica particles. The size distribution of the sample (Figures 6.2e-f) shows

that the core Si, core-shell Si@$SiO_2$, and shell $SiO_2$ have average sizes corresponding to 171 ± 25, 418 ± 28, and 123 ± 6 nm, respectively.

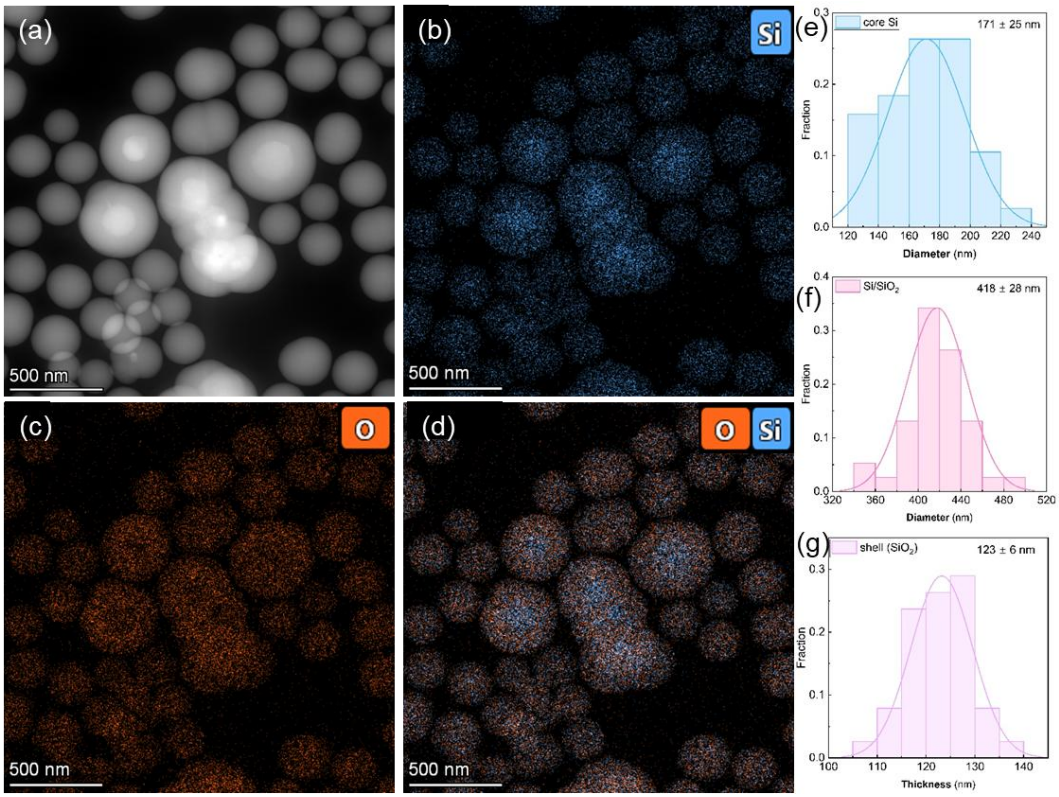



*Figure 6.2 (a) High-angle annular darkfield (HAADF) image (b-d) TEM/EDS elemental mapping of the core Si (dark-blue) and silica shell (orange). The scale bar represents 500 nm. (e-g) size distribution of the synthesized particles*

Further exploration of this approach to reduce secondary nucleation is needed, along with optical characterization of the particles to understand the extent of enhancement of the forward scattering and its potential as meta-atoms for metasurfaces. Also, other simulation-predicted dielectric materials, such as titanium dioxide ($TiO_2$) and zirconium dioxide ($ZrO_2$), can be explored as meta-atoms for forward light scattering. As these objects are isotropic, their light scattering will not depend on their orientation relative to the incident light. This makes them highly interesting meta-atoms.

We developed a two-step approach for the fabrication of silicon nanowires by the thermal annealing of a silicon-rich oxide incorporated with different metal catalysts (Au, Ag, $Fe_2O_3$) over the temperature range of 800 – 1200 °C at ambient pressure. The crystalline silicon core has a diameter between 15 – 80 nm, sheathed with an amorphous $SiO_x$ layer between 10 – 20 nm, and micrometers in length (0.5 – 3 μm). We learned that the surface area of the fabricated

precursor, along with the annealing temperature and time, is important for the formation of nanowires. Also, the choice of metal catalyst and its size influence the growth temperature and whether the nanowires have a crystalline or oxidized core. For the silicon oxide precursor incorporated with Au nanoparticles, crystalline core Si growth occurs from 800 – 900 °C. Beyond this temperature, the nanowires are completely oxidized and of smaller diameter. The choice of silver and $Fe_2O_3$ nanoparticles increased the growth temperature to > 1100 °C. Therefore, the nanowires produced are completely oxidized. Thus, other metals with a low eutectic temperature of metal/Si, such as Sn and Ga, could be a better choice for metal catalysts. However, the interest of these metals in terms of optical properties needs to be studied. While we established a bottom-up synthesis route for the fabrication of silicon nanowires, our attempts to control the monodispersity and to increase the diameter to an interesting range for Mie resonance scattering (100 – 200 nm) were unsuccessful. Perhaps the well-established CVD synthetic approach to such nanowires is more promising, or the MACE approach for wires oriented perpendicularly to a substrate.

Finally, we explore a two-step approach for the synthesis of ellipsoidal silicon particles. We fabricated ellipsoidal silica particles with a major axis of 137 ± 17 nm, a minor axis of 87 ± 13 nm, and an average aspect ratio of 1.6. In the pursuit of understanding the formation mechanism of the ellipsoidal particles, we learned that the co-surfactant pairing of L-tyrosine and CTAB acts as a critical morphology-directing agent for the ellipsoidal silica particles, with minimal influence from other reaction parameters. The mesostructure of the particles, using small-angle x-ray scattering, showed that the distance between centers of adjacent cylinders ($d_{c\text{-}c}$) is on average 4.6 nm, with a main peak at q = 1.63 $nm^{-1}$, indicating a mixture of hexagonal and wormhole structures. The dynamic light scattering analysis confirmed the reduction in particle-particle aggregation in suspension through sedimentation. The magnesiothermic reduction technique successfully reduced the synthesized ellipsoidal silica particles to elemental Si particles. However, there are several challenges to this approach, such as inhomogeneous reduction of the particles, a high degree of porosity, particle sintering, and fracturing of the morphology. Therefore, these challenges must be overcome before this approach can be a promising method to produce ellipsoidal silicon as meta-atoms. Beyond the optical properties of light scattering, we examined the drag coefficient of optically trapped ellipsoidal silica particles. This was used to measure the 3D physical dimensions of the trapped particles. A typical particle dimensions were measured to be: $d_x$ = 172 ± 11 nm, $d_y$ = 106 ± 6 nm, and $d_z$ =

117 ± 5 nm; with an aspect ratio of 1.62 and an average aspect ratio of 1.5 for multiple trapped particles.

In conclusion, this PhD work has demonstrated the potential of bottom-up fabricated silicon-based nanostructures as meta-atoms for metasurfaces. Many questions have been raised, but this thesis has also revealed promising directions for further research, particularly for spherical silicon core particles with dielectric shell materials. Colloidal fabrication techniques of nanostructures to enhance the forward light scattering of the spherical Si particles have been established. Better control over the colloidal approaches discussed in this thesis is needed to achieve precise shell thickness for optical control. However, we foresee these nanostructures, especially the dielectric shell materials, as potential meta-atoms for improved directional light scattering in the design of large-scale metasurfaces.

## Annexe 2. Experimental methods for the synthesis of silver and silica shell

### Protocol 1. Sn-functionalization of silica/silicon particles

The synthesis protocol was first optimized on silica particles and then transferred to the silicon particles. 2 mL of a 200 nm silica particle dispersion, corresponding to ~ 101.5 mg of particles, was dispersed in a 10 mL solution containing ~ 53 mM of $Sn^{2+}$ and 10 mM of HCl. The solution was stirred at 500 rpm for 30 min. The solution was centrifuged/redispersed in water at 4000 rpm (3×) for 5 min, and the particles were subsequently redispersed in a final water volume of 2 mL. Thereafter, ammonical silver was then reduced onto the surface of $Sn^{2+}$ functionalized particles. The regrowth of the seeds was carried out by the rapid reduction of silver nitrate by formaldehyde and ammonia, resulting in a shell with a diameter of ~ 20 nm[1,6].

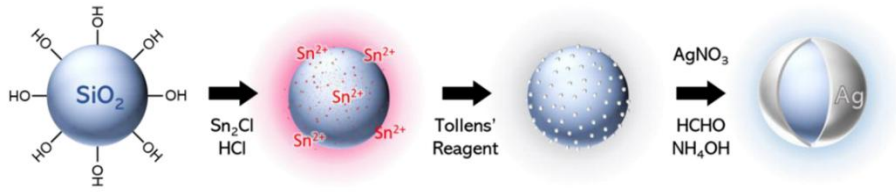



Figure 6.4 Schematic illustration of the protocol for the synthesis of an Ag shell around silica /silicon particles. Reproduced from ref.[1]

### Protocol 2. Preparation of Tollens' reagent

Tollens' reagent (270 mM) was prepared by following a previously published protocol[7]. To 10 mL of $H_2O$, 5.5 mL of 1 M $AgNO_3$, 2.5 mL of 3 M NaOH, and 2.5 mL of ammonia (28%) solution were added, and the mixture was stirred at 500 rpm. After adding NaOH, the mixture turned murky brown and later became colorless with the addition of the ammonia solution. The prepared reagent was used the same day[1].

### Protocol 3. Synthesis of Ag seeds on the Sn-functionalized particles

1.5 mL of the Sn-sensitized particles was added to 20 mL of the prepared Tollens' reagent, and the mixture was stirred vigorously. The dispersion immediately turned black. Stirring was maintained for ~ 2 min, and subsequently, the dispersion was centrifuged/redispersed at 4000 rpm (3×) for 5 min. The particles were finally redispersed in 10 mL of $H_2O$[1].

### Protocol 4. Formation of Ag shell

To 9 mL of $H_2O$, there was a subsequent addition of 1 mL of PVP solution (40,000 g/mol; 10 g/L), 75 µL of Ag seed functionalized particles, 10 – 50 µL of $AgNO_3$ (100 mM), 50 µL of formaldehyde (37% in $H_2O$), and 20 µL of ammonia (28%) solution under stirring at 500 rpm.

Between the addition of every reagent, the mixture was stirred for 4 min. After the final addition, the stirring was maintained for 2 min, resulting in a blue color. The mixture was centrifuged/redispersed in $H_2O$ (3×) at 1000 rpm for 5 min. The particles were finally dispersed in 10 mL of PVP solution (0.01 g/mL). The fabrication of the Ag-shell was based on a previously established protocol in the literature[1]. The optimized parameters with 50 µL of $AgNO_3$ (100 mM) were reproduced on silicon particles.

**Protocol 5. Synthesis of silica ($SiO_2$) shell on silicon particles**

This synthesis approach is based on the protocol established for the regrowth of silica particles (see Protocols 3.1 and 3.2), first published by Hartlen et al.[3] and optimized by Désert et al.[4,5]. We used the native silica layer, ~ 2 nm thick, on the silicon particles for this regrowth (see Figure 3.3). Silicon particles (7 mL, ~ 1 mg/mL) were added to a 30 mL round-bottom flask containing 3.3 mL of absolute ethanol and 400 µL of ammonia solution (28 wt%) under stirring at 250 rpm. The mixture was stirred for ~ 30 min to ensure good dispersity of the Si particles. Thereafter, 822 µL of TEOS precursor was mixed with 4 mL of absolute ethanol, and 2 mL of this mixture was added to the flask mixture through a syringe pump at a rate of 0.5 mL/h. The mixture was stirred overnight to ensure complete hydrolysis and condensation of the TEOS precursor. The product was centrifuged/redispersed in ethanol (3×) at 4000 rpm to remove the secondary nucleated silica particles and unreacted TEOS precursor. The final sample was redispersed in 10 mL of ethanol solution.

## References


(1) Lermusiaux, L.; Roach, L.; Lehtihet, M.; Plissonneau, M.; Bertry, L.; Buissette, V.; Le Mercier, T.; Duguet, E.; Drisko, G. L.; Leng, J.; Tréguer-Delapierre, M. Silver Nanoshells with Optimized Infrared Optical Response: Synthesis for Thin-Shell Formation, and Optical/Thermal Properties after Embedding in Polymeric Films. *Nanomaterials* **2023**, *13* (3), 614. https://doi.org/10.3390/nano13030614.

(2) Jiang, Z.; Liu, C. Seed-Mediated Growth Technique for the Preparation of a Silver Nanoshell on a Silica Sphere. *J. Phys. Chem. B* **2003**, *107* (45), 12411–12415. https://doi.org/10.1021/jp035060g.

(3) Hartlen, K. D.; Athanasopoulos, A. P. T.; Kitaev, V. Facile Preparation of Highly Monodisperse Small Silica Spheres (15 to >200 Nm) Suitable for Colloidal Templating and Formation of Ordered Arrays. *Langmuir* **2008**, *24* (5), 1714–1720. https://doi.org/10.1021/la7025285.

(4) Desert, A. Hybrid Silica/Polystyrene Colloids of Controlled Morphology, Université Sciences et Technologies - Bordeaux I, 2011. https://theses.hal.science/tel-00949569v1.

(5) Désert, A.; Chaduc, I.; Fouilloux, S.; Taveau, J.-C.; Lambert, O.; Lansalot, M.; Bourgeat-Lami, E.; Thill, A.; Spalla, O.; Ravaine, S.; Duguet, E. High-Yield Preparation of Polystyrene/Silica Clusters of Controlled Morphology. *Polym. Chem.* **2012**, *3* (5), 1130. https://doi.org/10.1039/c2py20058a.

(6) Schierhorn, M.; Liz-Marzán, L. M. Synthesis of Bimetallic Colloids with Tailored Intermetallic Separation. *Nano Lett.* **2002**, *2* (1), 13–16. https://doi.org/10.1021/nl015616g.

(7) Preston, T. C.; Signorell, R. Growth and optical properties of gold nanoshells prior to the formation of a continuous metallic layer. *ACS Nano* **2009**, 3 (11), 3696–3706. https://doi.org/10.1021/nn900883d.

# Résumé en Français des travaux de thèse

## Chapitre 1. Introduction : diffusion directionnelle dans les nanoantennes diélectriques en silicium

La nanophotonique étudie la façon dont la lumière interagit avec la matière à l'échelle nanométrique, en combinant la nanotechnologie et l'optique. Elle permet la conception de nanostructures capables de générer, de contrôler et de détecter la lumière sur l'ensemble du spectre électromagnétique, et en particulier dans le domaine du visible. Contrôler et manipuler la lumière à l'aide de dispositifs optiques consiste à modifier sa phase, son amplitude, sa polarisation et sa direction de propagation selon un schéma défini. Cela permet de façonner le front d'onde et de définir le trajet de la lumière. Ces techniques ont donné naissance à une branche de la nanophotonique appelée métamatériaux optiques. Il s'agit de matériaux artificiels composés de nanostructures métalliques ou diélectriques (appelées méta-atomes), disposées régulièrement avec des tailles caractéristiques inférieures à la longueur d'onde. La disposition de ces méta-atomes sur un substrat en deux dimensions crée des nano-dispositifs fonctionnels, fins et capables de diffuser la lumière. Ces nano-dispositifs sont désignés par le terme métasurfaces. Ils trouvent aujourd'hui de nombreuses applications dans l'imagerie, la détection, l'optoélectronique, l'éclairage et les écrans, les communications, la collecte d'énergie, le calcul, etc. (Figure 7.1)[1,2].

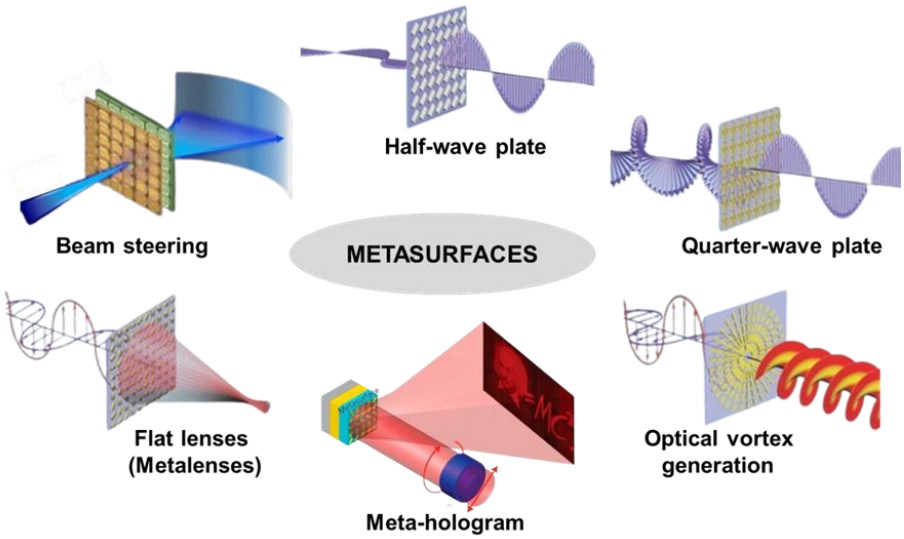



*Figure 7.1 Exemples d'applications des métasurfaces. Modifié d'après la réf.* [3]

Pour fabriquer ces métasurfaces, il est essentiel de comprendre comment chaque nanostructure contrôle l'amplitude et la phase de la lumière diffusée. La métasurface agit par la combinaison de la diffusion des différents méta-atomes pour façonner le comportement global des champs électrique et magnétique de la lumière. En conséquence, la taille, la forme et le

choix des matériaux des nanostructures doivent être soigneusement optimisés. Dans les métasurfaces de Huygens, chaque nanostructure de taille inférieure à la longueur d'onde est conçue pour se polariser à la fois suivant le champ électrique et suivant le champ magnétique de la lumière. Lorsque ces réponses sont égales en amplitude et en phase, elles permettent une transmission élevée et un contrôle complet de la phase de 0 à $2\pi$ de la lumière transmise[4].

Cependant, il est connu que les matériaux naturels ne présentent pas de propriétés magnétiques à des longueurs d'onde optiques. En effet, l'interaction directe du champ magnétique optique avec la matière est bien plus faible que celle des champs électriques. Toutefois, le magnétisme optique peut apparaître dans des structures artificielles spécialement conçues, à des échelles inférieures à la longueur d'onde. Ces structures permettent une réponse magnétique optique forte, même lorsqu'elles sont fabriquées à partir de matériaux non magnétiques[5]. La nanoantenne plasmonique la plus simple est une nanoparticule métallique sphérique (comme l'or ou l'argent), qui présente une résonance de plasmon de surface localisé. Lorsque la particule est de taille inférieure à la longueur d'onde de la lumière incidente, sa résonance ne présente que le mode de dipôle électrique (DE). En augmentant sa taille, on peut faire apparaître des modes de dipôle électrique de rang supérieur, tels que le quadrupôle électrique (QE). Une façon d'induire un dipôle magnétique consiste à utiliser un résonateur en anneau métallique divisé, où les électrons oscillent selon une boucle de courant plasmonique et donc une réponse magnétique. Cependant, le principal inconvénient des nanoantennes plasmoniques est la dissipation inévitable d'énergie sous forme de chaleur plutôt que de lumière réémise[6].

Alternativement, des nanoparticules diélectriques à indice de réfraction élevé, qui présentent des résonances électriques et magnétiques induites optiquement, devraient compléter ou même remplacer divers composants plasmoniques dans une gamme d'applications potentielles. Les matériaux diélectriques à indice élevé, à forte réponse électrique et magnétique dans la région visible, incluent le silicium (Si), le germanium (Ge) et le phosphure de gallium (GaP)[4,7]. Cependant, le Si est le plus attractif en raison de son indice de réfraction élevé et de son faible coefficient d'extinction dans la région visible (400 – 800 nm). Un indice de réfraction élevé détermine la position spectrale des résonances de la particule. Par conséquent, plus l'indice de réfraction du matériau est élevé, plus le diamètre de la particule nécessaire pour présenter des résonances de Mie dans la gamme visible/proche infrarouge est petit. Aussi, plus le coefficient d'extinction est faible, moins la particule absorbe la lumière. Ainsi, la diffusion

est plus intense. En outre, le silicium est compatible avec la plupart des technologies électroniques, respectueux de l'environnement et abondant dans la nature[6].

La Figure 7.2 présente le spectre de diffusion par résonance de Mie d'une particule sphérique simple de silicium d'un diamètre de 150 nm. Elle illustre également la décomposition du spectre de diffusion en résonances de dipôles électrique et magnétique, ainsi que leur interférence à différentes longueurs d'onde. À différentes positions spectrales indiquées sur les diagrammes de radiation, la lumière est diffusée dans toutes les directions, avec une diffusion directionnelle vers l'arrière observée à 564 nm et une diffusion vers l'avant à 660 nm. Cependant, la diffusion vers l'avant observée ne couvre qu'unegamme étroite de longueurs d'onde, l'efficacité de diffusion est faible, et elle se produit à l'extrémité de la région visible.

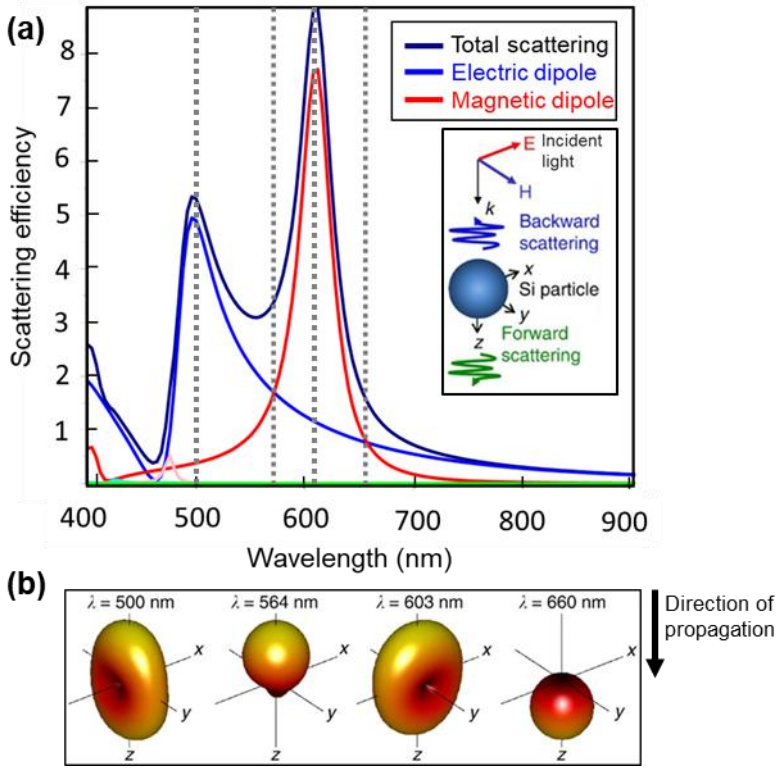



*Figure 7.2 (a) Propriétés de diffusion d'une nanoparticule de silicium (Si) d'un diamètre de 150 nm dans l'espace libre, calculées selon la théorie de Mie (b) Diagrammes de radiation de la diffusion en champ lointain à des longueurs d'onde de 500, 564, 603 et 660 nm, correspondant respectivement au dipôle électrique, à la diffusion en arrière, au dipôle magnétique et à la diffusion en avant. Modifié d'après la réf.* [8]

Une façon d'améliorer la diffusion de la lumière directionnelle vers l'avant des sphères de silicium consiste à utiliser une structure cœur–coquille, où le noyau de silicium est recouvert soit d'une fine couche plasmonique, soit d'une couche diélectrique épaisse (Figure 7.3 c). La

figure 7.3c montre les spectres simulés de diffusion avant et arrière d'une sphère de silicium nue d'un diamètre de 186 nm, dans laquelle la diffusion avant domine uniquement dans la gamme de longueurs d'onde de 750 à 800 nm. En recouvrant le noyau de silicium d'une coquille d'or de 7 nm ou d'une coquille d'argent de 4 nm (Figures 7.3c), la plage de domination de la diffusion vers l'avant s'étend sur une gamme de longueurs d'onde de 680 à 800 nm. Pour une coquille en silice diélectrique d'une épaisseur de 92 nm et un noyau de silicium de 162 nm, la diffusion vers l'avant domine sur l'ensemble du spectre visible, de 500 à 800 nm[9]. Pour une géométrie anisotrope telle qu'un ellipsoïde oblate en forme de disque (Figure 7.3d), la plage de longueurs d'onde optimale pour la diffusion directe observée se situe entre 500 et 600 nm. De même, pour un nanofil de silicium d'un diamètre de 100 nm (Figure 7.3f), une amélioration de la diffusion directe dépendant de la polarisation est observée dans la plage de longueurs d'onde de 400 à 650 nm. Cependant, le principal défi reste de développer une méthode de fabrication bottom-up évolutive pour ces nanostructures, qui pourront ensuite s'auto-assembler sur un substrat afin de créer des métasurfaces fonctionnelles (Figure 7.3a).

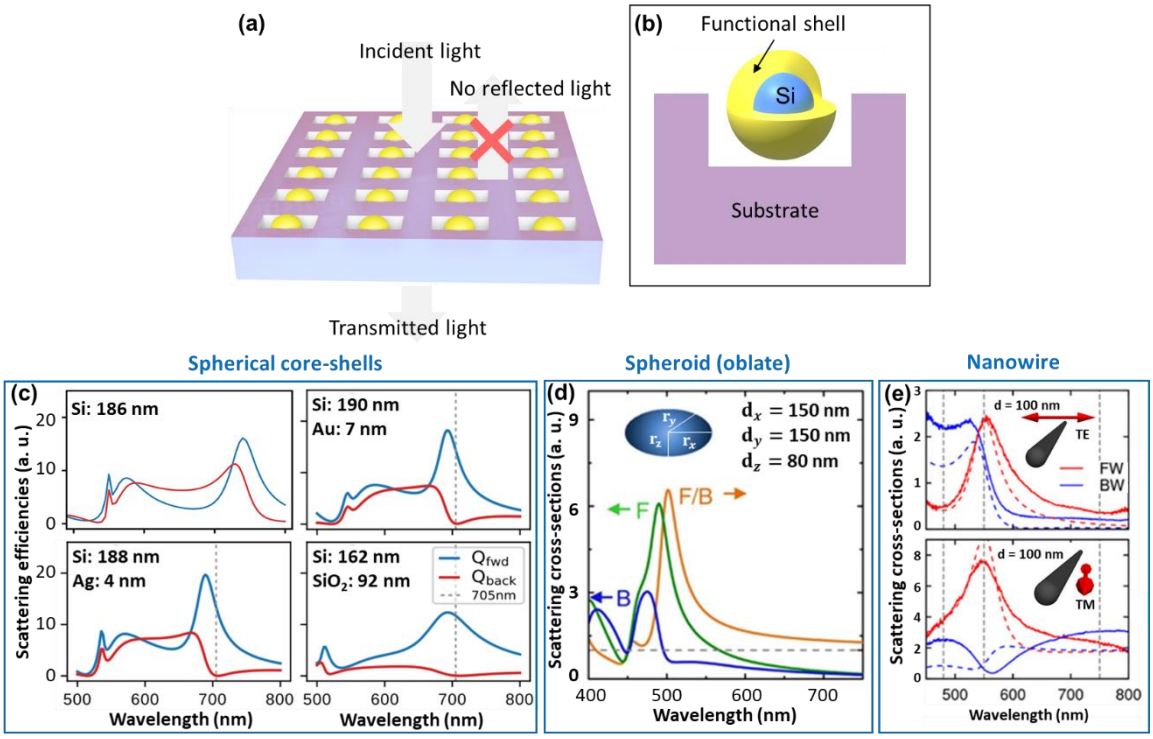



*Figure 7.3 (a) Schéma de la métasurface à transmission lumineuse parfaite (b) et du métatome avec une coque fonctionnelle. Spectres simulés de diffusion de la lumière, en avant et en arrière (c) pour différentes compositions de coquilles, (d) ellipsoïde oblate, (e) nanofils. Modifié d'après la référence.*[9]

## Chapitre 2. Méthodes expérimentales

Dans le chapitre 2, les différentes techniques de caractérisation utilisées pour analyser les particules synthétisées sont discutées. La microscopie optique et la spectroscopie de diffusion en champ sombre sur des nano-objets ont été utilisées pour étudier le comportement de diffusion optique des nanostructures cœur-coquille Si@Au synthétisées. La spectroscopie de perte d'énergie des électrons (EELS) a permis de cartographier la distribution du champ plasmonique au sein des nanostructures. De plus, la spectroscopie d'absorption optique (UV-Vis-NIR) a été employée pour étudier l'absorption des nanostructures en solution colloïdale. La morphologie des nanostructures, dont les propriétés optiques ont été étudiées, a été caractérisée à l'aide de la microscopie électronique en transmission (MET), de la microscopie électronique à balayage à émission de champ (FE-SEM) et de la spectroscopie dispersive en énergie (EDS).

Pour la fabrication des nanofils de silicium par recuit thermique d'oxyde riche en silicium, les propriétés structurelles et chimiques du précurseur synthétisé ont été examinées à l'aide de la spectroscopie infrarouge à transformée de Fourier (FTIR) et de la spectroscopie par résonance magnétique nucléaire (RMN). Les différentes liaisons chimiques présentes dans le précurseur ont été identifiées afin de prédire sa structure chimique. Les nanofils de silicium fabriqués ont été analysés par diffraction des rayons X sur poudre (DRX) et par spectroscopie Raman afin d'identifier et de quantifier les phases, de déterminer la composition chimique et d'obtenir des informations structurales. Le mécanisme de croissance a été étudié grâce à une analyse thermogravimétrique (ATG) pour évaluer les variations de masse du précurseur riche en silicium et détecter la libération de composants gazeux à l'aide d'un spectromètre de masse couplé. De plus, le mécanisme de croissance a été observé en temps réel grâce à la microscopie électronique en transmission in situ (MET in situ). De même, la morphologie et la microstructure des nanofils de silicium ont été analysées à l'aide de techniques telles que la microscopie électronique en transmission à haute résolution (MET HR), la microscopie électronique en transmission à balayage (MET STEM) et la spectroscopie de rayons X dispersion d'énergie (EDX).

Dans notre étude de particules ellipsoïdales de silice et leur évolution en silicium réduit, les morphologies ont été caractérisées à l'aide de microscopie électronique en transmission (TEM) et à balayage (MEB). Une étude mécaniquetridimensionnelle des particules a été réalisée à l'aide d'un équipement de piégeage optique en collaboration avec Manon Barrière (doctorante), Yann Louyer et Yacine Amarouchene du Laboratoire Ondes et Matière d'Aquitaine (LOMA). La diffusion dynamique de la lumière (DLS) et la diffusion de rayons X à petits angles (SAXS)

ont été réalisées au Centre de recherche Paul Pascal (CRPP) pour analyser l'agrégation des particules en solution et l'organisation de leur mésostructure. L'identification de la phase cristalline des particules réduites par magnétiothermie a été effectuée par diffraction des rayons X sur poudre (PDRX).

### Chapitre 3. Diffusion directionnelle de la lumière par des particules de silicium avec des coques ultra-fines en or, comme résonateurs de Mie

Dans le chapitre 3, nous décrivons la synthèse de particules à structure cœur-coquille Si@Au à l'aide d'une approche colloïdale. Les coeurs de silicium sont produits par le groupe de recherche de notre collaborateur, le professeur Jonathan G. C. Veinot, à l'Université de l'Alberta, au Canada. Cela est réalisé par la disproportionation thermique du silsesquioxane d'hydrogène (HSQ), un précurseur d'oxyde riche en silicium.[10]. Nous avons synthétisé la coquille particulaire en attachant chimiquement des noyaux d'or aux particules de silicium en solution (Figure 7.4a). Nous avons obtenu à la fois des revêtements simples et doubles de nanoparticules d'or autour des sphères de silicium, avec des épaisseurs homogènes d'environ ~4 et ~7 nm, respectivement. Ces particules à coque ont été caractérisées optiquement à l'aide de microscopie en champ sombre, de spectroscopie de diffusion arrière à l'échelle d'une seule particule et d'EELS pour analyser leur comportement de diffusion ainsi que les interactions entre les résonances Mie du silicium (Si) et les résonances plasmoniques de l'or (Au).

Avec l'aide de Peter R. Weicha, notre collaborateur au Laboratoire d'analyse et d'architecture des systèmes (LAAS-CNRS), nous avons pu reproduire avec précision les spectres expérimentaux à l'aide de simulations T-matrix. Nous avons estimé que la couverture de surface était d'environ 50 % pour le recouvrement simple, sur la base de la comparaison avec des spectres de diffusion simulés. Par conséquent, nous avons pu quantifier l'amélioration de la diffusion lumineuse directionnelle vers l'avant induite par la coquille de particules d'or fabriquée.

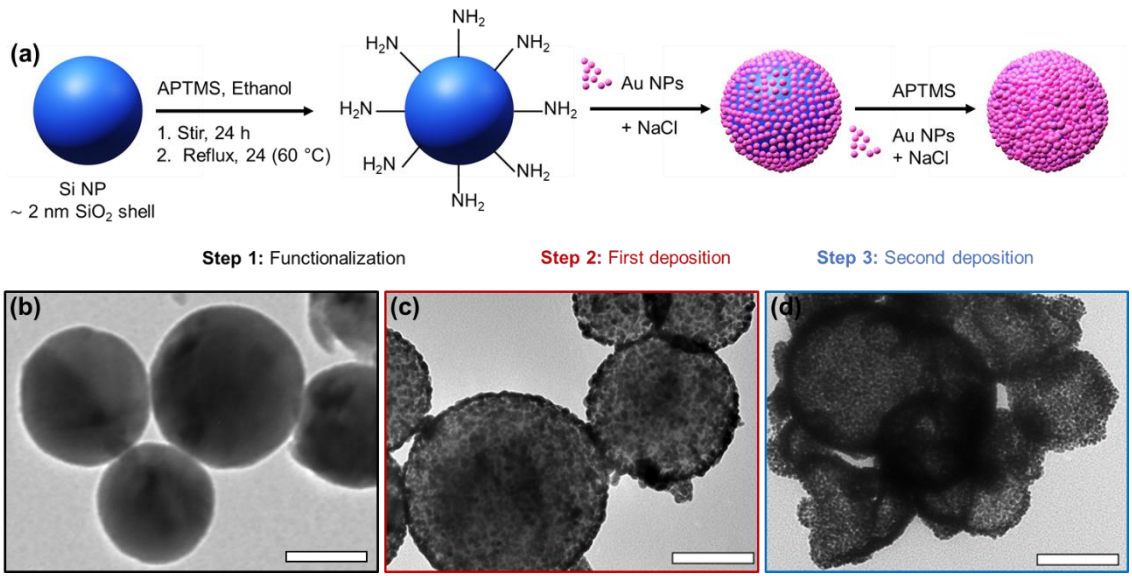



*Figure 7.4 (a) Illustration schématique du protocole de synthèse des particules de silicium décorées d'or. Images TEM permettant de comparer la densité de surface (b) des particules de silicium nues, (c) des particules de silicium décorées d'une couche de nanoparticules d'or, et (d)des particules de silicium décorées de deux couches de nanoparticules d'or. Toutes les barres d'échelle sont de 100 nm.*

D'après les simulations ajustées, nous avons constaté que la diffusion vers l'avant des particules cœur-coquille est légèrement améliorée par rapport aux simples particules de silicium, pour tous les diamètres compris entre 100 et 200 nm. Nous avons également observé que l'hybridation précédemment rapportée entre le dipôle électrique (DE) du noyau de silicium et les particules d'or qui l'entourent ne se produit pas pour des coquilles composées de particules satellites électriquement isolées.[11]. La coquille idéale en Au devrait être à la fois fine ($\lesssim$ 12 nm) et continue pour une diffusion vers l'avant optimale, ce qui n'a pas pu être réalisé avec les techniques de fabrication actuellement disponibles. Par conséquent, d'autres matériaux tels que l'Ag, $SiO_2$, $TiO_2$, $Si_3N_4$ et $ZrO_2$ doivent être explorés en tant que matériaux pour la coque des particules hybrides pour la diffusion directionnelle de la lumière. Des progrès préliminaires ont été rapportés dans la section des perspectives générales de la thèse, en se concentrant sur la synthèse en lot d'une coquille d'oxyde de silicium ($SiO_2$) homogène et continue autour des particules de silicium (Si) en tant que première étape. D'autres études sur le comportement optique de ces particules synthétisées sont nécessaires.

## Chapitre 4. Synthèse de nanofils de silicium par recuit thermique d'un précurseur d'oxyde riche en silicium contenant des nanoparticules métalliques

Une autre façon d'améliorer la diffusion de la lumière vers l'avant consiste en l'anisotropie géométrique, comme avec des sphéroïdes de silicium, des nanofils, des nanodisques et des nanocubes. Dans le chapitre 4, une technique de fabrication bottom-up a été développée pour produire des nanofils de silicium par recuit thermique d'un oxyde riche en silicium, incorporé avec différentes nanoparticules métalliques (Au, Ag, et $Fe_2O_3$) sur une plage de températures de 800 à 1200 °C et à pression ambiante (Figure 7.5a). Les nanofils produits dans des conditions optimisées possèdent un noyau cristallin d'un diamètre compris entre 20 et 40 nm, enveloppé d'une couche amorphe de $SiO_x$ de 10 à 20 nm (Figures 7.5b-c). Ils mesurent entre 0,5 et 3 µm de long. L'effet des paramètres de croissance (température, choix des catalyseurs métalliques et de leur taille, temps de recuit, surface des précurseurs, débits de gaz) sur la morphologie et la microstructure des nanofils a été étudié de manière systématique. Par exemple, les nanofils ne se forment que si la surface caractéristique des précurseurs a été augmentée par broyage avant le recuit thermique. Les précurseurs incorporant des nanoparticules d'or (Au) produisent des nanofils de silicium cristallin à 800–900 °C. Au-delà de cette température, les nanofils deviennent du $SiO_x$ amorphe, avec un diamètre plus petit et une densité plus élevée.

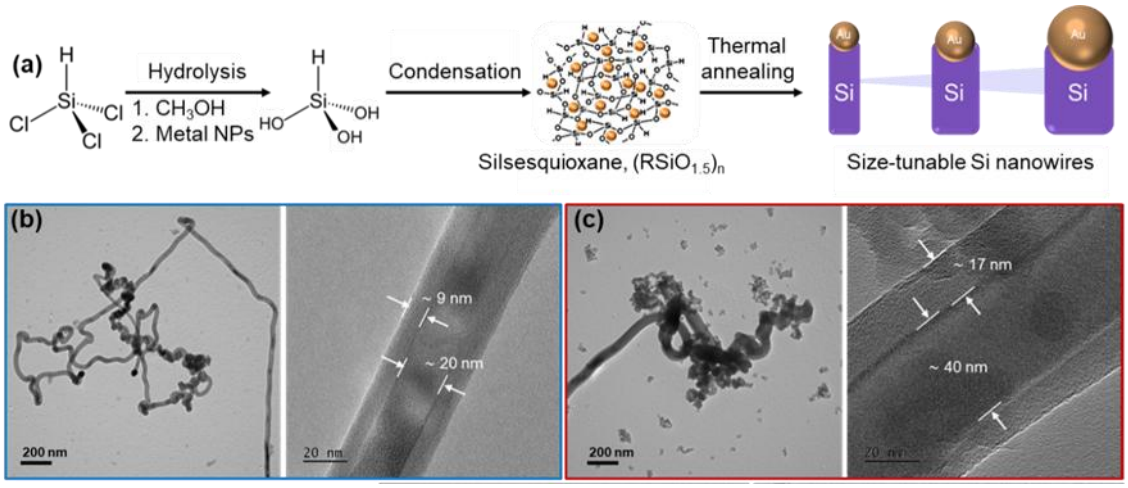



*Figure 7.5 (a) Schéma de la synthèse de nanofils de silicium à l'aide d'oxyde riche en silicium en présence de particules d'or de tailles différentes. Images TEM de nanofils de silicium synthétisés à 800 °C pendant 2 heures, avec des particules d'or de 25 nm (b) et de 95 nm (c), respectivement.*

Le changement du métal catalyseur influence la température à laquelle se forment les nanofils et leur degré d'oxydation. Le choix de nanoparticules d'argent a permis d'augmenter la

température de croissance jusqu'à 1200 °C. Dans le cas des nanoparticules de $Fe_2O_3$, une température minimale de croissance de 1000 °C est requise, et une densité élevée de nanofils est atteinte à 1100 °C. Cependant, dans les deux cas, les nanofils obtenus sont de silice amorphe ($SiO_x$). La température élevée de recuit thermique des échantillons d'argent et de $Fe_2O_3$ a été attribuée au point eutectique élevé des systèmes Si/Ag (~ 837 °C) et Si/Fe (~ 1197 °C), comparés à celui du système Si/Au (~ 363 °C). Par conséquent, d'autres métaux ayant un point eutectique plus bas avec le silicium, comme l'étain (Sn, ~ 232 °C) et le gallium (Ga, ~ 30 °C), pourraient constituer de meilleurs choix pour les catalyseurs métalliques.

La croissance des nanofils de silicium a été étudiée à l'aide de microscopie électronique en transmission *in situ* afin de mieux comprendre le mécanisme de croissance et d'optimiser les conditions de réaction. D'après les observations en temps réel lors du recuit thermique de l'oxyde riche en silicium entre la température ambiante et 1000 °C dans des conditions réductrices, les principaux phénomènes observés sont : la croissance d'une coque amorphe autour des particules d'Au, la formation de filaments, la dégradation de la matrice d'oxyde de silicium, le frittage des particules d'Au, et la perte du facettage des particules d'Au. Nous avons observé la formation d'une coque et de courts nœuds autour de la particule d'Au, phénomènes plus marqués lors du refroidissement sous $H_2$ jusqu'à la température ambiante, avec une épaisseur finale de la coquille d'environ 13 nm et une longueur d'environ 15 nm. Nous avons attribué la courte longueur du $SiO_x$ observée au faible volume de précurseur d'oxyde riche en silicium dans le système, insuffisant pour fournir le nombre d'atomes de silicium nécessaire à la croissance des nanofils. De plus, la nature amorphe de la croissance observée est cohérente avec les résultats ex situ à haute température. Cependant, d'autres études sont nécessaires pour comprendre pourquoi aucune croissance n'a été observée à des températures plus basses.

La monodispersité en taille, la morphologie uniforme et l'absence de défauts sont des paramètres cruciaux pour l'étude des propriétés optiques des nanofils de silicium. Cela n'était pas réalisable avec l'approche bottom-up développée dans cette thèse. Cette situation est similaire à celle de la plupart des méthodes bottom-up évoquées dans le chapitre 1 de cette thèse, à l'exception d'une approche de dépôt chimique en phase vapeur bien optimisée.

## Chapitre 5. Synthèse dirigée par la L-tyrosine et caractérisation 3D de particules de silice ellipsoïdales par lévitation optique

Dans le chapitre 5, nous avons exploré une autre façon de produire des particules de silicium anisotropes en étudiant la synthèse sol-gel de particules de silice ellipsoïdales, qui peuvent être réduites ensuite en particules de silicium élémentaire par réduction magnésiothermique. Ces particules ont, selon des calculs théoriques, des propriétés améliorées de diffusion de la lumière vers l'avant[12]. Les particules d'oxyde de silicium ellipsoïdales ont été synthétisées à l'aide d'un mélange de CTAB et de L-tyrosine comme agents de structuration (Figure 7.6a). En étudiant le mécanisme de formation de ces particules, nous avons établi que la L-tyrosine agit comme un agent modifiant la morphologie, avec une influence faible du cisaillement lié à l'agitation dans le milieu réactionnel et de la structure micellaire. Une synthèse typique produit des particules ellipsoïdales avec un grand axe de 137 ± 17 nm et un petit axe de 87 ± 13 nm, pour un rapport d'aspect moyen de 1.6. Ce rapport d'aspect peut varier entre 1,0 et 1,6 (Figure 7.6b-c). Les réactions menées à différentes concentrations de CTAB, en l'absence de L-tyrosine, ne forment que des particules sphériques ou en forme de bâtonnets. Avec l'augmentation de la concentration en L-tyrosine, les particules passent de sphères isotropes à des particules ellipsoïdales prolates ou oblates, de dimensions accrues.

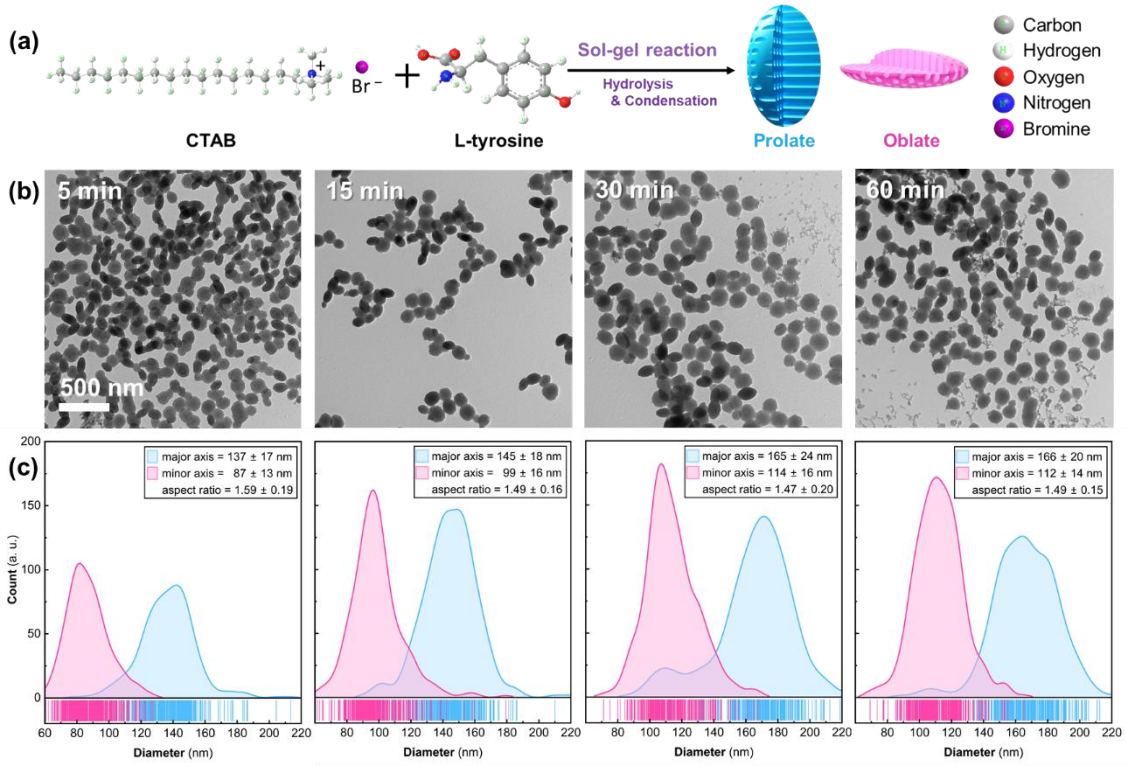


*Figure 7.6 (a) Images TEM des particules de silice synthétisées à différentes vitesses d'ajout de TEOS ($R_{TEOS}$). Les $R_{TEOS}$ (temps d'ajout) sont respectivement de 27 mL/h (5 min), 9 mL/h (15 min), 4,5 mL/h (30 min) et 2,25 mL/h (60 min), pour $V_{TEOS}$ = 2,25 mL. (b) La distribution de taille correspondante des particules synthétisées à différents taux d'ajout. [CTAB] = 3.6 mM, [l-tyrosine] = 3.7 mM, [TEOS] = 0.088 M, [$H_2O$] = 54.0 M, [$NH_4OH$] = 0.056 M ; pH = 11 – 12, temps de réaction = 1 h, T = (25 ± 2) °C, et vitesse d'agitation = 250 rpm. Les histogrammes sont basés sur 300 particules comptées.*

De plus, nous montrons que l'étude mécanique de particules en situation de piégeage optique constitue une méthode robuste et sans marquage pour la caractérisation de la forme de particules. Il s'agit d'une tâche difficile, si on ne dispose que d'images TEM/SEM, sans recourir à la tomographie. Les dimensions typiques des particules étudiées ont été mesurées comme suit : $d_x$ = 172 ± 11 nm, $d_y$ = 106 ± 6 nm, and $d_z$ = 117 ± 5 nm; avec un rapport d'aspect de 1.62. L'analyse par diffusion dynamique de la lumière a révélé que les particules colloïdales présentent un faible degré d'agrégation en suspension. Nous avons caractérisé la mésostructure des particules à l'aide de la diffusion de rayons X à petits angles, ce qui a montré que la mésoporosité de la silice a une morphologie de pores cylindriques organisés en réseau hexagonal avec une distance entre les centres des cylindres adjacents ($d_{c-c}$) de 4.6 nm, en moyenne, et un double pic de corrélation proche d'un vecteur d'onde de diffusion à q = 1.63 $nm^{-1}$, indiquant un mélange de structures hexagonales et de porosité désordonnée. Nous comprenons que la L-tyrosine interagit probablement avec la surface de la silice, sans altérer notablement l'organisation de sa mésostructure. La technique de réduction magnésiothermique a permis de réduire avec succès les particules de silice ellipsoïdales synthétisées en silicium élémentaire. Cependant, cette approche présente plusieurs défis. La vapeur de magnésium est distribuée de manière inhomogène dans le réacteur, ce qui a entraîné une réduction inégale des particules. Le degré élevé de porosité et le frittage des particules rendent cette méthode inadaptée pour la fabrication de méta-atomes.

## Conclusions générales et perspectives

En conclusion, ce travail de doctorat a démontré le potentiel de la fabrication bottom-up de nanostructures à base de silicium en tant que méta-atomes pour des métasurfaces à pertes faibles. De nombreuses questions ont été soulevées, mais cela a également mis en lumière des opportunités pour de futures recherches, notamment en se concentrant sur des particules cœur-coquille de noyau de silicium sphérique avec des coquilles de matériaux diélectriques. Bien

qu'il soit assez difficile de fabriquer une coque continue d'un matériau plasmonique autour des particules de silicium, la synthèse d'une coquille diélectrique, comme la silice, est moins exigeante. Cela a été démontré dans la section perspective de cette thèse. La synthèse colloïdale doit encore être optimisée afin de réduire la formation de particules de silice secondaires. Néanmoins, nous considérons ces nanostructures comme des méta-atomes prometteurs pour améliorer la diffusion directionnelle de la lumière incidente dans la conception de métasurfaces à grande échelle.

## Références


(1) McGurn, A. *Nanophotonics*; Springer Series in Optical Sciences; Springer International Publishing: Cham, 2018; Vol. 213. https://doi.org/10.1007/978-3-319-77072-7.

(2) Chen, H.-T.; Taylor, A. J.; Yu, N. A Review of Metasurfaces: Physics and Applications. *Rep. Prog. Phys.* **2016**, *79* (7), 076401. https://doi.org/10.1088/0034-4885/79/7/076401.

(3) Hsiao, H.; Chu, C. H.; Tsai, D. P. Fundamentals and Applications of Metasurfaces. *Small Methods* **2017**, *1* (4), 1600064. https://doi.org/10.1002/smtd.201600064.

(4) Decker, M.; Staude, I.; Falkner, M.; Dominguez, J.; Neshev, D. N.; Brener, I.; Pertsch, T.; Kivshar, Y. S. High-Efficiency Dielectric Huygens' Surfaces. *Advanced Optical Materials* **2015**, *3* (6), 813–820. https://doi.org/10.1002/adom.201400584.

(5) Kruk, S.; Kivshar, Y. Functional Meta-Optics and Nanophotonics Governed by Mie Resonances. *ACS Photonics* **2017**, *4* (11), 2638–2649. https://doi.org/10.1021/acsphotonics.7b01038.

(6) Sugimoto, H.; Fujii, M. Colloidal Mie Resonant Silicon Nanoparticles. *Nanotechnology* **2021**, *32* (45), 452001. https://doi.org/10.1088/1361-6528/ac1a44.

(7) Shima, D.; Sugimoto, H.; Assadillayev, A.; Raza, S.; Fujii, M. Gallium Phosphide Nanoparticles for Low-Loss Nanoantennas in Visible Range. *Advanced Optical Materials* **2023**, *11* (12), 2203107. https://doi.org/10.1002/adom.202203107.

(8) Fu, Y. H.; Kuznetsov, A. I.; Miroshnichenko, A. E.; Yu, Y. F.; Luk'yanchuk, B. Directional Visible Light Scattering by Silicon Nanoparticles. *Nat Commun* **2013**, *4* (1), 1527. https://doi.org/10.1038/ncomms2538.

(9) Soun, D.; Azma, A.; Roach, L.; Drisko, G. L.; Wiecha, P. R. Gradient-Based Optimization of Core-Shell Particles with Discrete Materials for Directional Scattering. *Opt. Express* **2025**, *33* (12), 25945. https://doi.org/10.1364/OE.561657.

(10) O'Connor, K. M.; Rubletz, A.; Ni, C.; He, Y.; Butler, C.; Veinot, J. G. C. High-Temperature Anomaly in the Synthesis of Large ( $d$ > 100 Nm) Silicon Nanoparticles from Hydrogen Silsesquioxane. *Chem. Mater.* **2023**, *35* (19), 7967–7973. https://doi.org/10.1021/acs.chemmater.3c01200.

(11) Sugimoto, H.; Hinamoto, T.; Kazuoka, Y.; Assadillayev, A.; Raza, S.; Fujii, M. Mode Hybridization in Silicon Core–Gold Shell Nanosphere. *Small* **2022**, *18* (45), 2204890. https://doi.org/10.1002/smll.202204890.

(12) Wang, Z.; An, N.; Shen, F.; Zhou, H.; Sun, Y.; Jiang, Z.; Han, Y.; Li, Y.; Guo, Z. Enhanced Forward Scattering of Ellipsoidal Dielectric Nanoparticles. *Nanoscale Res Lett* **2017**, *12* (1), 58. https://doi.org/10.1186/s11671-016-1794-x.

(13) Wiecha, P. R.; Cuche, A.; Arbouet, A.; Girard, C.; Colas Des Francs, G.; Lecestre, A.; Larrieu, G.; Fournel, F.; Larrey, V.; Baron, T.; Paillard, V. Strongly Directional Scattering from Dielectric Nanowires. *ACS Photonics* **2017**, *4* (8), 2036–2046. https://doi.org/10.1021/acsphotonics.7b00423.

(14) Xu, H.; Pan, H.; Yang, M.; Du, Q.; Lu, Y.; Chen, Y. Strongly Directional Fano Resonance in an Individual Silicon Nanorod. *J. Phys. Chem. C* **2020**, *124* (48), 26486–26492. https://doi.org/10.1021/acs.jpcc.0c09163.

(15) Sikdar, D.; Cheng, W.; Premaratne, M. Optically Resonant Magneto-Electric Cubic Nanoantennas for Ultra-Directional Light Scattering. *Journal of Applied Physics* **2015**, *117* (8), 083101. https://doi.org/10.1063/1.4907536.

# Fabrication de nanostructures à base de silicium : modification des propriétés optiques par la morphologie et la composition

**Résumé**

La recherche en nanophotonique vise à concevoir des nanostructures capables de diffuser la lumière de manière directionnelle afin de contrôler sa propagation à l'échelle nanométrique. Une telle diffusion présente un large éventail d'applications technologiques, notamment les revêtements optiques à transmission ou réflexion parfaite et large bande, l'amplification de la diffusion Raman, et l'optique non linéaire. Les particules de silicium (Si) de taille ous-inférieure à la longueur d'onde (100–200 nm) sont particulièrement prometteuses en raison de leurs faibles pertes optiques et de leurs fortes résonances électriques et magnétiques dans le domaine du visible et du proche infrarouge. Lorsqu'elles sont combinées, ces résonances permettent une diffusion seulement vers l'avant. Cependant, pour des sphères de Si, leur chevauchement spectral n'est que partiel, et les efficacités de diffusion qui en résultent restent relativement faibles.

Pour surmonter cette limitation, plusieurs stratégies ont été proposées, telles que l'introduction de morphologies non sphériques (par exemple ellipsoïdes, nanofils), la fabrication d'architectures cœur–coquille et l'assemblage de particules en métasurfaces. Cette thèse explore différentes approches de synthèse ascendante (bottom-up) pour développer des nanostructures à base de silicium aux propriétés optiques améliorées et étudie leur comportement de diffusion de la lumière.

Dans un premier temps, une approche en deux étapes a été développée pour préparer des particules cœur–coquille Si@Au avec une épaisseur de coquille ajustable inférieure à 10 nm. L'augmentation de la couverture en nanoparticules d'or par des étapes successives de fonctionnalisation/dépôt a permis d'améliorer la continuité de la coquille. La réponse électromagnétique de ces particules a été étudiée par spectroscopie de diffusion sur particule unique et par spectroscopie de pertes d'énergie des électrons (EELS), puis comparée à des sphères de Si de référence et à des structures cœur–coquille $SiO_2$@Au. Des simulations basées sur la méthode T-matrix ont confirmé nos observations expérimentales et mis en évidence le rôle essentiel du rapport des dimensions cœur/coquille et de la continuité de la coquille pour maximiser la diffusion en avant.

En parallèle, une voie de synthèse a également été établie pour des particules cœur–coquille Si@Ag, caractérisées avec les mêmes techniques optiques. Ce travail ouvre la voie à l'élargissement de cette bibliothèque de nanostructures cœur–coquille à des coquilles diélectriques telles que Si@$SiO_2$, Si@$ZrO_2$ ou Si@$TiO_2$.

Dans un second temps, des nanofils de silicium ont été obtenus par réaction de disproportionation thermique d'un oxyde de silicium enrichi en présence de différentes nanoparticules métalliques (Au, Ag, $Fe_2O_3$), qui jouent un rôle catalytique dans la croissance. Les nanofils obtenus présentent un cœur de silicium cristallin recouvert d'une coquille de 10–20 nm d'oxyde de silicium, et leur longueur varie de 1 à 6 µm, leur conférant des propriétés optiques fortement anisotropes. Leur formation a en outre été étudiée in situ en conditions environnementales, offrant une observation en temps réel des mécanismes de croissance. Une telle compréhension est essentielle pour améliorer le rendement, le contrôle morphologique et l'évolutivité des nanofils de silicium.

Enfin, des particules ellipsoïdales de silice mésoporeuse ont été synthétisées par voie sol-gel. Afin d'améliorer leurs performances optiques, nous avons tenté de les réduire en silicium élémentaire par réduction magnésiothermique. Toutefois, des difficultés liées au contrôle de la morphologie, à l'agrégation et à la porosité ont limité leur exploitation.

**Mots clés :** Silicium, nanoantennes, résonances de Mie, diffusion directionnelle, cœur–coquille, nanofil, nanoellipse

---

**Institut de Chimie de la Matière Condensée de Bordeaux**

[ICMCB (CNRS) – UMR5026, 87, Avenue du Docteur Schweitzer, 33608, PESSAC cedex (France)]

Fabrication of silicon-based nanostructures: altering optical properties through morphology and composition

**Abstract**

Nanophotonics research has sought to create nanostructures with strong directional optical scattering to control light propagation at the nanoscale. This directional scattered light has a range of potential technological applications, such as perfectly transmitting (or reflecting) broadband optical coatings, enhanced Raman scattering, nonlinear optics, etc. Subwavelength-sized silicon (Si) particles (100 – 200 nm) interact with visible and near-infrared light, offering low optical losses and presenting strong electric and magnetic resonances. These resonances can combine to produce pure forward scattering. However, there is only partial spectral overlap of the electric and magnetic responses, resulting in relatively weak total scattering efficiencies.

The different strategies to improve the spectral overlap of these two modes in Si particles include creating non-spherical morphologies (e.g., nanoellipse, nanowires, etc), core-shell architectures, or assembling Si particles into arrays (such as metasurfaces). Hence, this thesis aims to develop such silicon-based nanostructures via different bottom-up synthesis approaches and study their optical properties.

First, we present a two-step solution approach to prepare Si@Au core-shell particles with controllable shell thickness below 10 nm. The Au nanoparticle density around the Si particles can be increased by performing a second functionalization/deposition step. We study the electromagnetic response of the particles using single-particle scattering spectroscopy and electron energy loss spectroscopy (EELS). Our results on Si@Au core-shell particles were compared with reference Si spheres and $SiO_2$@Au core-shell particles, allowing us to establish the contribution of the Au decoration to the optical response of the hybrid particles. To further elucidate the nature of the electromagnetic response of the particles, we performed T-matrix simulations. These simulations replicated our experimental findings and showed the importance of controlling the shell/core dimensions and the need for a continuous shell to maximize forward scattering. Furthermore, a synthesis pathway was investigated for Si@Ag and Si@$SiO_2$ core-shell particles. Future work may extend this library of core-shell nanostructures to dielectric shells such as Si@$ZrO_2$ and Si@$TiO_2$.

Second, we developed a route to fabricate silicon nanowires as potential nanoantennas through the thermal disproportionation reaction of a silicon-rich oxide in the presence of different metallic nanoparticles, which we assume catalyze the wire growth. We used different metal catalysts, such as Au, Ag, and $Fe_2O_3$ nanoparticles, to grow the silicon nanowires. The silicon nanowires have a core of elemental silicon with a shell of 10–20 nm of silicon oxide. The length of the nanowires is between 1–6 µm, rendering them highly anisotropic. To achieve a higher degree of control over the morphology and to compare with other nanowire growth techniques, we performed in situ environmental studies to follow the formation of these nanowires in real time. Such knowledge can help us improve silicon nanowire yield and scalability.

Lastly, we present the sol-gel synthesis of ellipsoidal silica particles. As potential nanoantennas, we explored the reduction of these particles to elemental silicon through magnesiothermic reduction, as they would exhibit improved and asymmetric light scattering properties. However, we encountered challenges with controlling particle morphology, aggregation, and porosity.

**Keywords:** Silicon, nanoantennas, Mie resonances, directional scattering, core-shell, nanowire, nanoellipse

---

**Institut de Chimie de la Matière Condensée de Bordeaux**

[ICMCB (CNRS) – UMR5026, 87, Avenue du Docteur Schweitzer, 33608, PESSAC cedex (France)]